

The three-jets and  $Z + \text{jets}$  cross-section  
measurements in proton-proton collisions data  
collected with the ATLAS experiment  
at the LHC

Dissertation  
zur Erlangung des Doktorgrades  
des Department Physik  
der Universität Hamburg

vorgelegt von  
Aliaksei Hrynevich

Hamburg  
2023

Gutachter der Dissertation:	Prof. Dr. Peter Schleper Dr. habil. Alexandre Glazov Dr. Pavel Starovoitov
Zusammensetzung der Prüfungskommission:	Dr. habil. Alexandre Glazov Prof. Dr. Johannes Haller Prof. Dr. Sven-Olaf Moch Prof. Dr. Peter Schleper Dr. Pavel Starovoitov
Vorsitzender der Prüfungskommission:	Prof. Dr. Sven-Olaf Moch
Datum der Disputation:	16.06.2023
Vorsitzender des Fach-Promotionsausschusses PHYSIK:	Prof. Dr. Günter H. W. Sigl
Leiter des Fachbereichs PHYSIK:	Prof. Dr. Wolfgang J. Parak
Dekan der Fakultät MIN:	Prof. Dr.-Ing. Norbert Ritter

## Abstract

The thesis reports the cross-section measurements of the three-jets production and the production of jets associated with a  $Z$ -boson,  $Z + \text{jets}$ . The measurements are performed using proton–proton collision data with centre-of-mass energies of 7 and 8 TeV. The data were recorded by the ATLAS detector at the Large Hadron Collider. The cross-sections are measured double-differentially as a function of jet kinematic variables. The results probe the strong interaction dynamics at high energy scales and provide a testing ground for the theoretical models used to describe the fundamental content of matter and interactions. The measurement accuracy is consistent with or exceeds in some regions of the phase space the accuracy in the next-to-leading order calculations in perturbative Quantum Chromodynamics. Thus, the measured cross-section is one of the necessary inputs for refining the description of the parton content of the proton and constraining its uncertainties.

In addition, two measurements are reported that improve the accuracy in the jet energy measurement in the ATLAS experiment. One is the measurement of physical noise associated with the excessive energy deposits in the hadronic calorimeter due to simultaneous proton–proton interactions. Another is a jet energy measurement via the transverse momenta balance in events with a jet and a  $Z$ -boson. The results of both studies are used in the ATLAS experiment to accurately reconstruct and calibrate jets. Overall, these results provide an improved means for exploring new energy frontiers of particle interactions.

## Zusammenfassung

Diese Arbeit berichtet über die Wirkungsquerschnitt-Messungen der Drei-Jet-Produktion und der Produktion von Jets in Verbindung mit einem Z Boson, Z+Jets. Die Messungen werden unter Verwendung von Proton-Proton-Kollisionsdaten mit Schwerpunktsenergien von 7 und 8 TeV durchgeführt. Die Daten wurden vom ATLAS-Detektor am Large Hadron Collider aufgezeichnet. Die Wirkungsquerschnitte werden doppelt-differenziell als Funktion Jet-kinematischer Größen gemessen. Die Ergebnisse untersuchen die Dynamik der starken Wechselwirkung bei hohen Energieskalen und bieten ein Testfeld für die theoretischen Modelle, die zur Beschreibung des grundlegenden Aufbaus von Materie und Wechselwirkungen verwendet werden. Die Messgenauigkeit entspricht oder übertrifft in einigen Bereichen des Phasenraums die Genauigkeit der Berechnungen der nächstführenden Ordnung in der perturbativen Quantenchromodynamik. Somit ist der gemessene Wirkungsquerschnitt eine der notwendigen Beiträge, um die Beschreibung des Partongehalt des Protons zu verfeinern und seine Unsicherheiten einzuschränken.

Zusätzlich werden zwei Messungen berichtet, die die Genauigkeit der Jetenergiemessung im ATLAS-Experiment verbessern. Eine ist die Messung des physikalischen Rauschens, das mit den übermäßigen Energieablagerungen im hadronischen Kalorimeter aufgrund gleichzeitiger Proton-Proton-Wechselwirkungen verbunden ist. Eine andere ist eine Jetenergiemessung über die Querimpulsbilanz bei Ereignissen mit einem Jet und einem Z Boson. Die Ergebnisse beider Studien werden im ATLAS-Experiment verwendet, um Jets akkurat zu rekonstruieren und kalibrieren. Insgesamt bieten diese Ergebnisse ein verbessertes Mittel zur Erforschung neuer Energiebereiche von Teilchenwechselwirkungen.

Hiermit erkläre ich an Eides statt, dass ich die vorliegende Dissertationsschrift selbst verfasst und keine anderen als die angegebenen Quellen und Hilfsmittel benutzt habe.

I hereby declare upon oath that I have written the present dissertation independently and have not used further resources and aids than those stated in the dissertation.

Hamburg, 11.04.2023

## Disclaimer

The presented results are obtained in close collaboration with my colleagues. My personal contribution is as follows.

The measurement of pile-up noise in the Tile Calorimeter cells introduced in Section 3, including the development of the corresponding framework, was performed by myself under the guidance of P. Starovoitov and A. Solodkov, who also, together with S. Harkusha, helped integrating the results into the ATLAS software 1. A summary of the results has been published 2, 3.

The software framework ZeeD 4, 5 used for the  $Z + \text{jets}$  data analysis was developed at DESY under A. Glazov. The framework was adapted by P. Starovoitov to the needs of jet energy calibration. It was further refined and adapted to the Run2 ATLAS data format by myself, and to the  $Z + \text{jets}$  cross-section measurement needs together with N. Kondrashova.

The jet energy calibration using the  $Z + \text{jets}$  data described in Section 4.4 is performed by myself under the guidance of P. Starovoitov. The combination with the calibrations obtained using other event topologies is performed by the ATLAS collaboration. A summary of the results has been published 6-8.

The three-jets cross-section measurement discussed in Section 5 was performed together with P. Starovoitov and S. Yanush. I have contributed to studying systematic uncertainties, making theoretical predictions, and editing the paper 9.

The  $Z + \text{jets}$  cross-section measurement discussed in Section 5 was done by myself and N. Kondrashova with equal contributions 10, and under the guidance of A. Glazov and P. Starovoitov. I was the main editor of the paper 11.

Some studies to which I have contributed are not reflected in the thesis because they deviate from the main topic or are technical. Still, some of them demonstrate the applicability of the results and directions for their further development. For example, pile-up noise studies were necessary to evaluate the Tile Calorimeter performance in several scenarios of its upgrade 12. Some of the developments gained from the  $Z + \text{jets}$  jet energy calibration were used for similar calibration of jets reconstructed at the trigger level, which are used to search for physics beyond the Standard Model. The framework developed to study the non-perturbative correction (see Section 5.8.2) was used in other studies, like for the inclusive jet cross-section measurement 13. The results of the  $Z + \text{jets}$  cross-section measurement were used to constrain the proton content 14.

All the results are largely due to the successful performance of the LHC and the ATLAS detector, as well as due to numerous fruitful discussions with my other colleagues, friends and family, whose help, guidance and support are invaluable.

Finally, I am grateful to DESY Hamburg (Germany) and Helmholtz Association (HGF) for granted asylum, outstanding support and provided funding from the Initiative and Networking Fund under the contract number GI-001.

# Contents

<b>Introduction</b>	<b>10</b>
<b>1 Jets as a tool for addressing fundamental questions of matter</b>	<b>13</b>
1.1 The Standard Model of particle physics	13
1.2 The theory of strong interactions	15
1.2.1 Anatomy of proton–proton collision	16
1.2.2 Strong coupling	17
1.2.3 The content of proton	20
1.2.4 The hard scattering cross-section predictions	24
1.2.5 Underlying event and hadronisation	26
1.3 Jet definition algorithms	27
1.4 Previous studies of three-jets and $Z$ +jets production, and prospects for new measurements	30
1.5 Summary and outlook	34
<b>2 Experimental setup</b>	<b>35</b>
2.1 The Large Hadron Collider	35
2.2 The ATLAS detector	37
2.3 The trigger system of the ATLAS detector	39
2.4 Data quality monitoring	40
2.5 Simulation of collision data	41
2.6 Summary and outlook	42
<b>3 Pile-up noise study in the Tile Calorimeter</b>	<b>43</b>
3.1 The Tile Calorimeter segmentation	44
3.2 Energy reconstruction and noise effects in the Tile Calorimeter	46
3.3 Pile-up noise measurement	47
3.3.1 Method of pile-up noise measurement	48
3.3.2 Improving the accuracy in pile-up noise measurement using the bootstrap technique	50
3.3.3 Pile-up noise measurements in cells of the Tile Calorimeter	50
3.4 Summary and outlook	54
<b>4 Jet energy calibration</b>	<b>55</b>

4.1	Jet reconstruction	56
4.2	Jet calibration	57
4.3	Jet identification and pile-up jet rejection	60
4.4	Jet energy calibration using $Z + \text{jets}$ events	62
4.4.1	The direct transverse momentum balance technique	62
4.4.2	Electron reconstruction, energy calibration and identification	64
4.4.3	Collision data and simulated events used for jet energy calibration	66
4.4.4	$Z + \text{jets}$ event selection	67
4.4.5	Reducing the effect of collision data mis-modelling	69
4.4.6	The direct balance measurement	71
4.4.7	Systematic uncertainty evaluation	74
4.4.8	Combination with calibrations in other event topologies	80
4.5	Summary and outlook	83
<b>5</b>	<b>Measurements of the three-jets and <math>Z + \text{jets}</math> cross-sections</b>	<b>84</b>
5.1	Construction of PDF-sensitive observables	85
5.2	Collision data pre-selection	88
5.2.1	Data for the three-jets cross-section measurements	89
5.2.2	Data for the $Z + \text{jets}$ cross-section measurements	90
5.2.3	Data for the $Z + \text{jets}$ background analysis	91
5.3	Selection of events for the measurements	91
5.3.1	Selection of the three-jets events	93
5.3.2	Selection of the $Z + \text{jets}$ events	93
5.4	Backgrounds evaluation in the $Z + \text{jets}$ cross-section measurement	95
5.4.1	Simulation-based approach for background evaluation	96
5.4.2	Data-driven approach for background evaluation	97
5.4.3	Results of the background analysis	99
5.5	Comparisons between data and simulations at the detector level	101
5.6	Detector effects correction	107
5.6.1	Unfolding methods used in the cross-section measurement	107
5.6.2	Unfolding the three-jets data	110
5.6.3	Unfolding the $Z + \text{jets}$ data	114
5.7	Uncertainties in the cross-section measurements	119
5.7.1	Inaccuracy in the jet energy measurement	119
5.7.2	Inaccuracy in the electron energy measurement	123
5.7.3	Mis-modelling of the detector resolution	124
5.7.4	Mis-modelling of the detector efficiencies	126
5.7.5	Mis-modelling of pile-up effects	128
5.7.6	Inaccuracy in the background subtraction	129
5.7.7	Inaccuracy in the detector effects correction	130
5.7.8	Inaccuracy in the collider luminosity measurement	130

5.7.9	Reducing statistical fluctuations of systematic uncertainties	131
5.7.10	Statistical uncertainty	133
5.7.11	Summary on the three-jets cross-section uncertainty	134
5.7.12	Summary on the $Z + \text{jets}$ cross-section uncertainty	136
5.8	Theoretical predictions	138
5.8.1	Fixed-order QCD predictions	138
5.8.2	Non-perturbative effects and corresponding cross-section correction	143
5.8.3	QED radiation effects and corresponding cross-section correction	145
5.9	Results of the three-jets cross-section measurement	146
5.10	Results of the $Z + \text{jets}$ cross-section measurement	151
5.11	Quantitative comparison to theoretical predictions	155
5.12	Summary and outlook	158
	<b>Summary and conclusions</b>	<b>159</b>
	<b>References</b>	<b>161</b>
	<b>A The measured three-jets production cross-sections</b>	<b>178</b>
	<b>B The measured <math>Z + \text{jets}</math> production cross-sections</b>	<b>189</b>

# Introduction

Collimated sprays of hadrons, called jets, are the features produced abundantly in particle collisions at high energies. First observed in the 1970s [15], jets are used to study the fundamental content of matter and the nature of fundamental interactions. Jets confirmed the existence of elementary constituents of protons and neutrons in the nuclei of atoms. These elementary particles are called quarks. The forces that bind quarks and keep protons and neutrons inside nuclei are carried by gluons, also discovered using the jets. One of the fundamental interactions, called strong, has a remarkable property in that its strength increases with the distance between particles. This feature limits the possibility of observing free quarks and gluons. Instead, jets stemming from quarks and gluons are used to judge their properties.

Another feature of strong interactions is directly related to the structure of protons. When protons are at high energy, the complexity of their structure increases since quarks and gluons emit or decay. Studying jets in proton collisions allows for judging the structure of protons. With this in mind, jets are considered as tools to study the features of strong interactions and the content of protons.

Colliding high-energy particles is a way to unravel the fundamental questions of matter. Underlying theories are developed by studying particle collisions at ever higher energies. High energies are used to penetrate deeper into the matter and study the interactions in dynamics. Various collider experiments have been performed so far [16]. The Large Hadron Collider (LHC) [17] is a modern example of such an experiment. It is designed for proton–proton collisions at the centre-of-mass energy of 14 TeV. Among the advantages of the LHC is the high luminosity which allows rare processes to occur at a high rate. Four large experiments are being performed at four collision points. These are ATLAS [18], CMS [19], LHCb [20] and ALICE [21]. The general-purpose ATLAS detector is the core of the eponymous experiment. The study of jets is a significant part of the physics programme of the ATLAS experiment.

The object of the study at the LHC is the collision of protons at high energies. When protons collide, their constituents scatter. The scattering can occur through various physics processes. For example, it can go through the exchange of intermediate particles or annihilation. Detectors are usually placed around the scattering point, so any particle that reaches the detector is used to study the physics process that created it. An important observable to study the

scattering process is the cross-section, which is related to the probability that a given scattering process occurs. At the LHC, the predictions for the cross-section should consider the proton structure's complexity and the strength of the interactions between particles. Thus, by measuring the cross-section and solving the inverse problem, the fundamental properties of matter are revealed.

The subjects of the study in this thesis are the processes of at least three jets production and the production of jets in association with a  $Z$ -boson,  $Z + \text{jets}$ , in proton collisions at the LHC. The cross-section of both production processes are measured double differentially as a function of several kinematics variables. The measurements probe the new phase space compared to previous studies, thanks to higher proton collision energy at the LHC and larger detector acceptance. Both processes are particularly sensitive to the gluon content of proton, which so far has a rather large uncertainty, so improvements in this direction are foreseen. Apart from that, the cross-section measurements provide a new ground for testing the underlying theoretical models and tuning their parameters.

Studying jet production cross-section differentially requires accurate jet energy measurements. Moreover, since jets are used in many physics analyses, the high accuracy in their energy measurement is a common requirement. That is why techniques that satisfy this requirement are developed centrally by the ATLAS experiment. As a result, each physics analysis using jets is supplied with recommendations that guarantee the most precise measurements. Thus, in addition to the cross-section measurement, two studies are reported that contribute to the overall performance of the experiment.

One such study is related to the high detector load due to the large number of particles originating from several scattering vertices. Multiple scattering, commonly referred to as the pile-up, is due to LHC smashing bunches of billions of highly collimated protons rather than individual protons to achieve any luminosity. That is, apart from being an advantage, high luminosity brings complexity to the measurements. As a result, jets from one scattering are often affected by particles from many others, bringing an overlay of energies measured by the detector. The effect of such an energy overlay is considered in the study as a source of the detector noise, referred to as the pile-up noise. The measurement of pile-up noise provides input used to reduce the effect of energy overlay in jet energy measurements. The pile-up noise measurement in the hadronic Tile Calorimeter of the ATLAS detector is reported. The results of this study are then used indirectly in many measurements performed in the ATLAS experiment.

Another study contributes to the jet energy calibration, which brings measured energies to their true value. The calibration is necessary since jet energy measurements are affected by energy losses in inactive detector material and particles escaping the detector. A calibration of jet energy against that of a  $Z$ -boson measured precisely is reported. These results are important for many studies in the ATLAS experiment, which either use jets or veto them.

The thesis is organised as follows. The ground for measuring the three-jets and  $Z$  + jets cross-sections is set in Chapter [1](#). The experimental setup is reviewed in Chapter [2](#). The measurement of the pile-up noise is discussed in Chapter [3](#). The jet energy calibration is the topic of Chapter [4](#). Finally, the three-jets and  $Z$  + jets cross-section measurements are presented in Chapter [5](#).

# Chapter 1

## Jets as a tool for addressing fundamental questions of matter

Jets production starts from elementary constituents of matter, quarks and gluons, collectively called partons. Jets arise when these partons are at high energies, emitting gluons in an avalanche-like process. In addition to emission, gluons may create pairs of quarks. As the energy of partons decreases due to the above processes, they eventually make up composite particles called hadrons, whose collimated sprays are jets. Strong interactions confine partons with hadrons making their direct detection impossible, but jets can be detected. Jets are thus the key to studies of quarks, gluons, and many associated phenomena. The study of jet production helps to improve the description of fundamental interactions and constituents of matter. In particular, the jet production cross-section measurements are used to derive the unknowns that cannot be deduced from the first principles of the theory using existing tools, such as the strong coupling constant and the parton distribution functions within the proton.

This chapter sets the scene for the studies of jet production. The description starts by defining the Standard Model of particle physics, which describes the fundamental constituents of matter in Section [1.1](#). This is followed by key concepts of strong interactions relevant to the study in Section [1.2](#). The algorithm used to define jets in a set of elementary particles or detector signals is introduced in Section [1.3](#). Several vital studies motivating this work are discussed in Section [1.4](#). In addition, it highlights the prospects for the three-jets and  $Z +$  jets production measurements.

### 1.1 The Standard Model of particle physics

The theory of elementary particles and fundamental interactions is known as the Standard Model (SM) [\[22-24\]](#) of particle physics. The SM was established in the 1960s [\[25\]](#). Since then, the theory has successfully predicted several new particles that have been experimentally confirmed. Currently, the SM is the main theory used to predict the results of collider experiments.

There are two classes of particles in the SM. Elementary particles that constitute matter belong to a class of fermions, which includes particles with a half-integer value of intrinsic momentum called spin. Quarks and leptons are two subclasses of fermions. There are six types of quarks: up, down, charm, strange, top and bottom. These types are commonly referred to as quark **flavours**. Bound states of quarks make up composite particles known as hadrons. The best-known hadrons are the protons and neutrons that make up the atomic nuclei. Electrons from the class of leptons bond with nuclei to complete the atom's structure. Other charged leptons are muons and tau. In addition, each charged lepton in the SM has an associated neutral partner called a neutrino.

Interactions are mediated by particles from the class of bosons, which includes particles with an integer number spin. The SM describes three out of four known fundamental interactions. One is the strong interaction conducted by gluons, and responsible for nuclear bonding. Electromagnetic interactions carried by photons keep electrons inside the atom. Weak interactions represented by W and Z bosons describe various particle decays. The last fundamental interaction, gravitational, is not considered in the SM.

The mathematical framework of the SM is provided by the quantum field theory. Within this theory, the SM is the  $SU(3) \otimes SU(2) \otimes U(1)$  gauge theory, where each term represents an internal symmetry inherent to strong, weak, and electromagnetic fields, respectively. The symmetries represent conservation laws followed by the SM fields during space-time transformation. Each kind of particle is described in terms of a dynamical field that pervades space-time. The fundamental forces of physics and the parameters of elementary particles acquired their present form at the symmetry-breaking phase transitions that took place during the Universe cooling stage after the event of the Big Bang, which models the origin of the Universe. The origin of mass in the SM is described by the mechanism of symmetry breaking [26–30]. This mechanism implies another fundamental field, the Higgs field, with a nonzero potential that permeates the space. A quantum excitation of the Higgs field, known as the Higgs boson, discovered at the LHC in 2012 [31, 32], completes the elementary particle content of the SM. So, all SM particles, together with their properties such as mass, charge and spin, are summarised in Figure 1.1. This representation assumes zero neutrino masses, which are formally only negligible compared to other elementary particles.

The main equation of the SM is the Lagrangian, which describes the dynamics and kinematics properties of fields. Assuming the massless neutrino, the SM Lagrangian depends on 19 free parameters. Among these parameters are particle masses and strength of the interactions. The SM parameters are derived using many experiments carried out in the past decades. Nevertheless, new experiments, such as those at the LHC, are necessary to study the SM in new energy regimes and constrain its parameters.

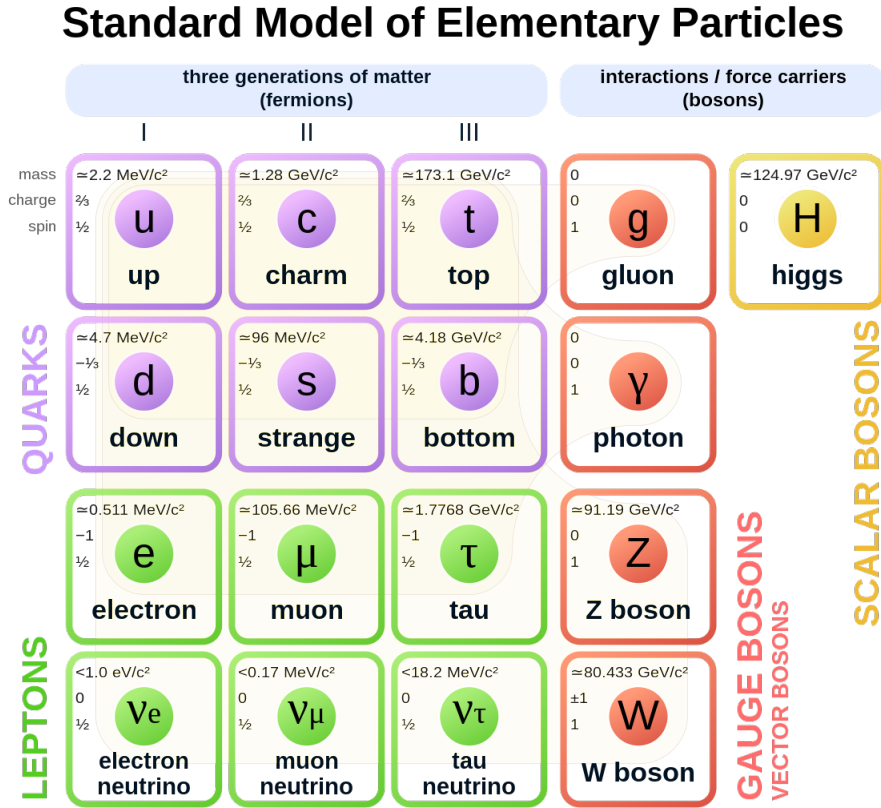


Figure 1.1 — A summary of fundamental contents of matter. The figure is taken from Ref. [33]

Apart from neglected gravity and dependence on external parameters, the SM has other fundamental shortcomings. Among them is a lack of explanation for the dominance of matter over antimatter and the nature of hypothetical substances such as dark matter and dark energy, which together make up about 95% of the entire mass-energy content of the Universe. So, in addition to the SM studies, new experiments provide new data to study these fundamental issues since any deviation from the SM predictions may indicate new phenomena.

## 1.2 The theory of strong interactions

Strong interactions are among the fundamental ones. They bind quarks into composite hadrons, and hadrons into atomic nuclei. The theory of strong interactions is Quantum Chromodynamics (QCD), a component of the SM. The QCD predictions are extensively studied in hadron collider experiments to improve the description of the content of matter and the nature of strong interactions. The QCD itself is described in many textbooks [34–36] and articles [37–41], so here a brief summary of its concepts relevant to the study is provided.

### 1.2.1 Anatomy of proton–proton collision

The proton–proton,  $pp$ , collision experiments are currently the driving force for developing QCD. These collisions encompass many complex aspects of QCD. However, a naive description of the collision is arguably a good introduction to some of the key aspects.

A sketch of a typical  $pp$  collision is shown in Figure 1.2. The protons are shown as two blobs on the sides. Three lines entering the proton represent its three constituent quarks. The quarks are bound within the proton by interaction carried by gluons (e.g. gluons  $a$  and  $b$ ). Gluons are shown by wavy lines. These gluons are mostly soft, as otherwise they would knock out the quarks. That is why gluons are often absorbed by the same quark (e.g. gluon  $c$ ).

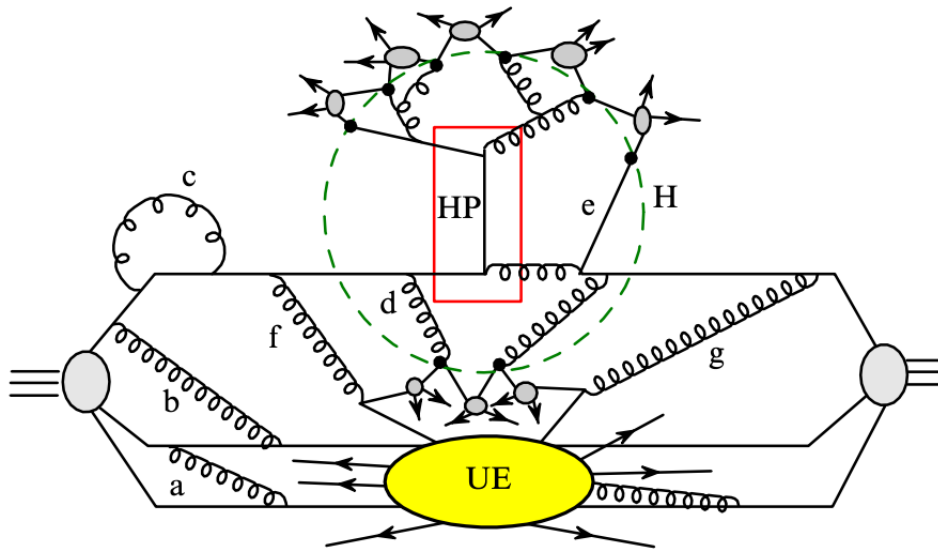


Figure 1.2 — A sketch of a typical  $pp$  collision. The description is given in the text. The figure is taken from Ref. [37].

When two partons from colliding protons interact with high momentum exchange, a **hard process** occurs (shown as  $HP$ ). In the hard process, partons either scatter or annihilate. Here, the hard process is represented by a  $qg \rightarrow qg$  scattering, where  $q$  and  $g$  are quarks and gluons, respectively. The red box insert is an example of a **Feynman diagram** used to visualise QCD calculations. The hardness of the scattering is often quantified by the transverse momenta of the outgoing partons in a plane perpendicular to the directions of colliding protons. After going through the hard process, scattered partons radiate others avalanche-like until they reach the energy of about 1 GeV (the boundary shown as  $H$ ). Below this energy, their interaction strength with neighbour ones increases asymptotically, so the partons can no longer stay isolated. This phenomenon is known as **confinement**. As a result, partons combine, making up hadrons, shown with small blobs outside  $H$ . The process of the parton-to-hadron transformation

is known as **hadronisation**. Collimated hadrons produced close to the direction of scattered partons eventually reach the detector as jets.

The  $pp$  scattering is often referred to as an **event** in collider experiments. There are two states contributing to a detector snapshot of an event. The direct outcome of a given hard process is often referred to as its **final state**. In contrast, before the scattering, partons are in the **initial state**. When other partons radiated from the initial state ones are not reabsorbed, they can contribute to the final state seen by the detector (see partons  $d$  and  $e$ ).

The  $pp$  collision is not limited to single scattering, other pairs of partons can also interact. Moreover, the larger the energy of colliding partons, the more constituent partons can be resolved (see gluons  $f$  and  $g$  that, in turn, split into quark-antiquark pairs). However, additional interactions usually undergo low momenta transfer, as the probability of simultaneous hard interactions is relatively low. Such interactions are often referred to as the **underlying event** (UE). The UE final states can also reach the detector overlapping with that of the hard process.

The hard process shown here is one of many possible processes. There can be other scattered partons or can be different intermediate particles, propagators, between the initial and final states that are allowed by the physics laws. The type of the process can often be identified by a detected final state. For example, this thesis studies the processes leading to the final states with three jets and with a  $Z$ -boson and jets. Strong interactions are involved both in the initial and final state of these processes. Thus, studying them provides a means to quantify the interaction strength. Besides that, one can deduce the actual initial state by analysing the detected final state, making it possible to study the proton content. These aspects are further revealed in the following sections.

## 1.2.2 Strong coupling

The QCD is a non-abelian quantum field theory with symmetry group  $SU(3)$ . This theory is constructed using a concept of **colour** charge inherent to quarks and gluons. The colour charge is analogous to the electric charge in the theory of electromagnetic interactions, quantum electrodynamics (QED). However, while there is only one kind of electric charge, the colour charge comes in three varieties, labelled red, green, and blue. The labelling has nothing to do with visible colours. Instead, it follows an analogy of colour neutralisation when mixing three colours. As a result, all composite particles made up of quarks are considered colourless.

Strong interactions between partons are carried by gluons like photons carry electromagnetic interactions in the QED. However, while photons are electrically neutral, gluons transfer colour charge between partons leading to colour exchange. A parameter that characterises the strength of strong interaction or, in other

words, the magnitude of its force is called strong coupling and is denoted as  $g_s$  or, more commonly,  $\alpha_S = g_s/4\pi$ .

The couplings in the SM are scale-dependent, where the **scale** is linked to a distance between interacting bodies, the distance scale, or, correspondingly, the energy scale, given that length is inversely proportional to the energy in quantum mechanics. While the QED coupling increases as a function of the energy scale, the  $\alpha_S$  tends asymptotically towards zero. This defines an important feature of strong interactions: partons behave like free particles when they are at large energy scales, i.e. small distances. This phenomenon is known as **asymptotic freedom** [42, 43], which is often assumed for partons in a proton beam at the LHC. On the other hand, at low energy scales, the  $\alpha_S$  increases, leading to the confinement of quarks within hadrons. Despite being scale-dependent, strong coupling is often referred to as strong coupling constants or running coupling.

The strong coupling is usually considered small when studying  $pp$  collisions and their final states. For example, at the  $Z$ -boson mass scale of about 91 GeV, the strong coupling is equal to  $0.1179 \pm 0.0010$  [44]. This allows using an approximate method, **perturbation theory**, for QCD calculations to predict the experiment's outcome. In perturbation theory, calculations are approximated by a convergent power series in a small parameter,  $\alpha_S$  in this case. Namely, each power of  $\alpha_S$  corresponds to the state when a parton radiates or changes its type. Each such term in the series can be illustrated by a Feynman diagram. Calculating a few leading terms in perturbative series often provides an adequate agreement with experiments.

The scale dependence of the strong coupling is formally provided in terms of the  $\beta$ -function of the renormalisation group equation

$$\mu^2 \frac{d\alpha_S(\mu^2)}{d\mu^2} = \frac{d\alpha_S(\mu^2)}{d \ln \mu^2} = \beta(\alpha_S(\mu^2)), \quad (1.1)$$

where  $\mu$  is the scale. For small  $\alpha_S$ , the  $\beta$ -function is expressed as

$$\beta(\alpha_S) = -\alpha_S^2(b_0 + b_1\alpha_S + \mathcal{O}(\alpha_S^2)), \quad (1.2)$$

where  $b_0$  and  $b_1$  are the **leading order** (LO) and **next-to-leading order** (NLO) terms, respectively. Unlike the positive sign of the  $\beta$ -function in QED, the negative sign in  $\beta(\alpha_S)$  leads to the asymptotic freedom in QCD. At the LO, the strong coupling at an arbitrary scale,  $\mu$ , is expressed as

$$\alpha_S(\mu^2) = \frac{\alpha_S(\mu_0^2)}{1 + b_0\alpha_S(\mu_0^2) \ln \frac{\mu^2}{\mu_0^2}}, \quad (1.3)$$

where  $\mu_0$  is the scale at which  $\alpha_S$  is known [45].

Parametrising QCD equations in terms of an arbitrary **renormalisation scale**  $\mu = \mu_R$  is a method of correcting theoretical divergences, which arise when

integrating infinitely high energies and momenta in the internal lines, loops, of the Feynman diagram. The  $\mu_R$  is often taken far above the QCD scale,  $\Lambda_{\text{QCD}} \sim 200$  MeV, to avoid a **non-perturbative** region where  $\alpha_S$  exceeds one. In this notation, the scale dependence of the strong coupling is expressed simply as

$$\alpha_S(\mu_R^2) = \frac{1}{b_0 \ln \frac{\mu_R^2}{\Lambda_{\text{QCD}}^2}}. \quad (1.4)$$

The strong coupling cannot be deduced from the first principles of the theory, so it is measured in experiments. The  $\alpha_S$  is determined by fitting the QCD predictions, parametrised in terms of  $\alpha_S$  as a function of the energy scale, to experimental data such as measured jet production cross-section, an observable sensitive to  $\alpha_S$ . Many experiments contribute to  $\alpha_S$  measurements [44], but results on the highest energy scale up to almost 2 TeV are obtained using  $pp$ -collisions data at the LHC, see Figure 1.3. The LHC keeps providing new data for such studies, so the  $\alpha_S$  can be probed at even higher energy scales, providing new insights into the phenomenon of asymptotic freedom. The jet cross-section measurements are among the important inputs for this.

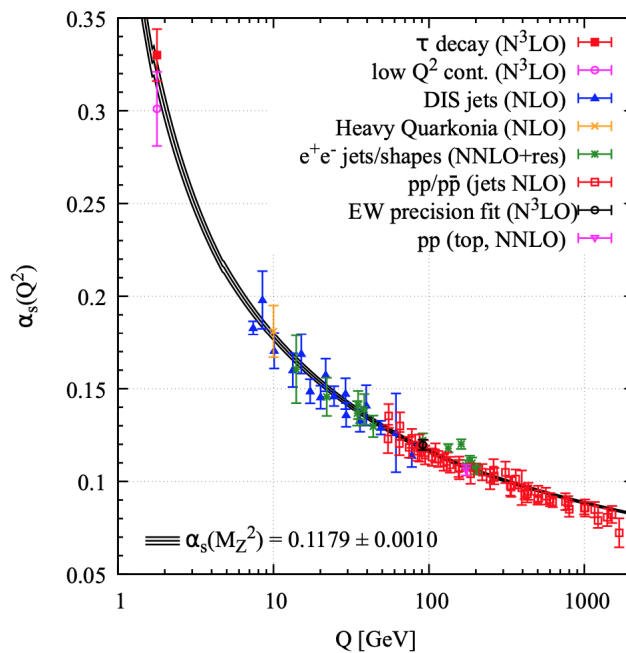


Figure 1.3 — The strong coupling,  $\alpha_S$ , measured as a function of the energy scale,  $\mu = Q$ . Data from different experiments are shown with markers, where the right-most ones, i.e. at the highest scales, are the data from the LHC, including jet cross-section measurements. The fit to the data is shown with a black line. The figure is taken from Ref. [44].

### 1.2.3 The content of proton

Proton is a composite particle. At rest, its composition is approximated by two u-quarks and one d-quark referred to as the valence quarks. The valence quarks are bound together by gluon exchange. However, more than this approximation is required when protons are accelerated. The composition of a proton fluctuates as quarks emit gluons, which emit other gluons or create quark-antiquark pairs and so on, see Figure 1.4. As a result, its composition is better approximated by valence quarks surrounded by a parton sea.

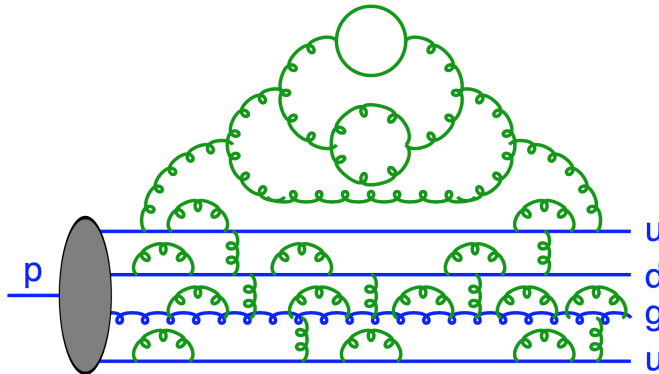


Figure 1.4 — Illustration of parton fluctuations, appearing as wavy green lines, inside a high-energy proton. Valence quarks are shown as straight blue lines. The figure is taken from Ref. [39].

The probability of finding a parton of flavour  $i$  carrying a fraction of the proton momentum  $x$  at a given energy scale  $\mu$  is given by the non-perturbative **parton distribution function** (PDF),  $f_i(x, \mu^2)$ . In this notation, the quark content of the proton obeys the quark number sum rules

$$\int_0^1 (f_u(x, \mu^2) - f_{\bar{u}}(x, \mu^2)) dx = 2, \quad (1.5)$$

$$\int_0^1 (f_d(x, \mu^2) - f_{\bar{d}}(x, \mu^2)) dx = 1, \quad (1.6)$$

$$\int_0^1 (f_{\text{sea}}(x, \mu^2) - f_{\bar{\text{sea}}}(x, \mu^2)) dx = 0, \quad (1.7)$$

where the subscripts indicate quark flavour, upper bars denote antiquarks, and *sea* means other than valence quark flavours. Together with gluons,  $g$ , the content of a proton obeys the momentum sum rule:

$$\int_0^1 (u_v(x, \mu^2) + d_v(x, \mu^2) + f_{q/\bar{q}}(x, \mu^2) + f_g(x, \mu^2)) x dx = 1, \quad (1.8)$$

where  $u_v$  and  $d_v$  are the PDFs of the valence u- and d-quark,  $f_{q/\bar{q}}$  are the PDFs of other quarks from a sea, and  $f_g$  is the gluon PDF. These sum rules are vital when determining the PDFs.

The proton PDFs for various parton types, as well as their change with scale, are shown in Figure 1.5. The most probable fraction of the proton momentum carried by valence quarks is about 20% at  $\mu^2 = 10 \text{ GeV}^2$ . More than half of the proton momentum is carried by gluons. The fraction of the proton momentum carried by sea quarks is considerably smaller than valence quarks. However, at higher scales, the fraction of the proton momenta carried by sea quarks increases while that of the valence quarks decreases to about 10% at  $\mu^2 = 10^4 \text{ GeV}^2$ .

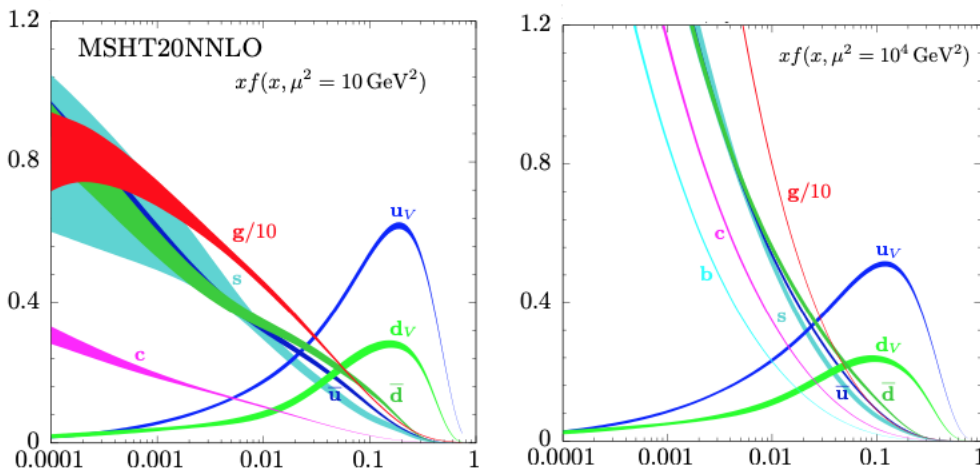


Figure 1.5 — The proton PDFs for various parton types at scales  $\mu^2 = 10 \text{ GeV}^2$  (left) and  $\mu^2 = 10^4 \text{ GeV}^2$  (right). The abscissa is the fraction of the proton momentum  $x$ , while the ordinate is  $x$  times the PDF  $f_i(x, \mu^2)$ . For convenience, the gluon PDF is scaled by 1/10. The figure is taken from Ref. [44].

The scale dependence of the PDFs is described by Dokshitzer, Gribov, Lipatov, Altarelli and Parisi (DGLAP) [46–49] evolution equations, which read

$$\mu^2 \frac{\partial f_i(x, \mu^2)}{\partial \mu^2} = \frac{\partial f_i(x, \mu^2)}{\partial \ln \mu^2} = \sum_j \frac{\alpha_S(\mu^2)}{2\pi} \int_x^1 \frac{dy}{y} \sum_j P_{ij}\left(\frac{x}{y}\right) f_j(y, \mu^2), \quad (1.9)$$

where  $P_{ij}$  are the parton splitting functions describing the probability of a given parton  $i$  to carry a momentum fraction  $x$  after parton  $j$  carrying a momentum fraction  $y$  splits [44]. The DGLAP equations are said to describe the evolution of partons across energy scales. The splitting functions can be calculated order-by-

order in perturbative QCD. Examples of splitting functions at LO are

$$P_{qq}(x) = C_F \left[ \frac{1+x^2}{(1-x)_+} + \frac{3}{2} \delta(1-x) \right], \quad (1.10)$$

$$P_{gq}(x) = C_F \left[ \frac{1+(1-x)^2}{x} \right], \quad (1.11)$$

$$P_{qg}(x) = \frac{1}{2} [x^2 + (1-x)^2], \quad (1.12)$$

$$P_{gg}(x) = 2C_A \left[ \frac{1-x}{x} + x(1-x) + \frac{x}{(1-x)_+} \right] + \left[ \frac{11}{2} - \frac{n_f}{3} \delta(1-x) \right], \quad (1.13)$$

where the singularities that arise at  $x = 1$  are regularised by means of the plus prescription defined for  $[g(x)]_+$  as

$$\int_0^1 [g(x)]_+ f(x) dx = \int_0^1 g(x) [f(x) - f(1)] dx, \quad (1.14)$$

the  $C_F = 4/3$  and  $C_A = 3$  are the quark and gluon colour factors, which can be thought of as the colour-charge squared, and  $n_f$  is the number of quark flavours [44]. The  $P_{qq}$ ,  $P_{gq}$ ,  $P_{qg}$  and  $P_{gg}$  correspond to the  $q \rightarrow qq$ ,  $g \rightarrow gq$ ,  $g \rightarrow q\bar{q}$  and  $g \rightarrow gg$  splittings, respectively. The splitting functions make up a core of an algorithm of successive parton emissions making up parton showers [41].

The sum over PDFs of all parton flavours is used to predict the outcome of  $pp$  collisions. However, by themselves, the PDFs cannot be deduced from the theory. So, experiments are used to determine them by fitting the predictions for hard scattering processes to the existing data. But once the PDFs are derived in a given process, they can be used to predict the outcome of other processes, as the PDFs are universal, i.e. they are process-independent.

Data from various experiments are used to determine PDFs over a wide range in  $x$  and  $\mu^2$ , and to constrain their uncertainties. Among such experiments are fixed target ones, lepton–hadron collider HERA, proton–antiproton collider TEVATRON, and finally proton–proton collider LHC [50]. The kinematic domain of different experiments used for PDF determination is summarised in Figure 1.6. The data on jet production cross-section at the LHC are used to determine the PDF at the highest energy scales.

Several global collaborations determine the PDFs using existing experimental data. The most known collaborations are CT [51]<sup>1</sup>, MSHT [52]<sup>2</sup> and NNPDF [53]. These collaborations perform ‘global fits’ in the sense of using the widest available set of data from various experiments to determine PDFs. Other popular PDFs used to predict the outcome of experiments are obtained by HERA-PDF [54], ABMP [55] and GJR [56] collaborations. The difference between PDFs

<sup>1</sup>Former CTEQ.

<sup>2</sup>Former MRST, MSTW and MMHT.

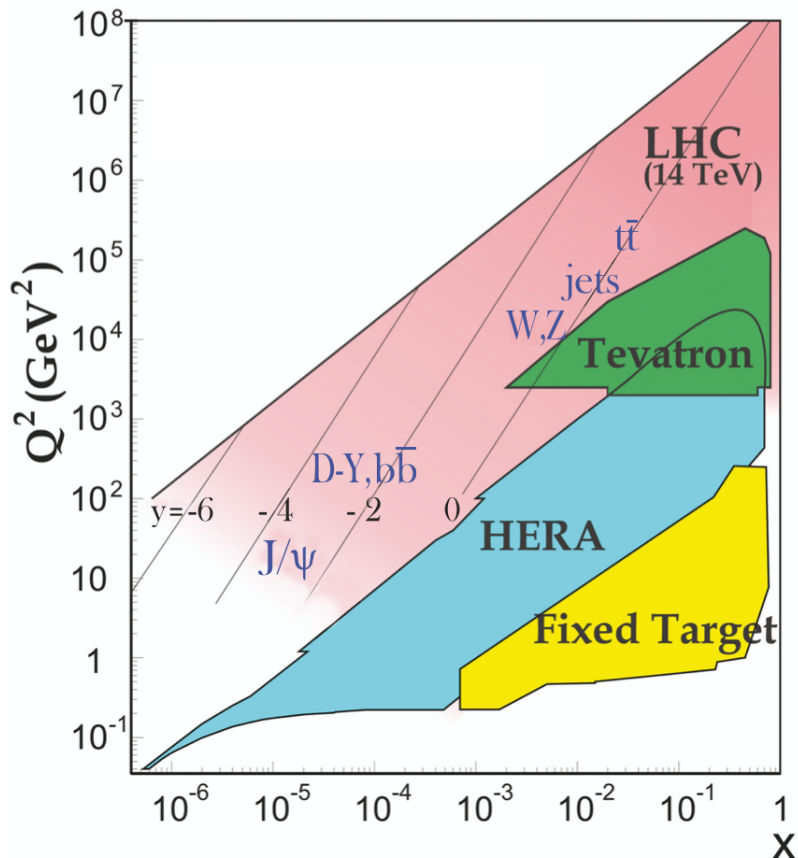


Figure 1.6 — Kinematic domain in  $x$  and  $\mu^2 = Q^2$  probed by fixed-target and collider experiments, whose data are used for the PDF determination. The data on jet production at the LHC populate the upper right region. The figure is taken from Ref. [44].

is mainly in their parametrisations. For example, CT and MSHT collaborations use restricting functional forms with several dozen free parameters to describe PDFs. At the same time, the NNPDF combines a Monte Carlo representation of the probability measure in the space of PDFs with the use of neural networks, which effectively correspond to parametrisation using hundreds or even thousands of free parameters. The other sources of difference are associated with the selection of data fitted, the accuracy in theory calculations, the fitting assumptions and the approaches to assessing uncertainties [44]. The collaborations periodically update their PDFs with new data and more accurate approaches, which is usually indicated by a newer version of the PDF. So most modern PDFs mainly agree within uncertainties. However, further reducing PDF uncertainty is necessary, especially when searching for deviations from the experimental data, whose accuracy improves progressively as more data are recorded.

## 1.2.4 The hard scattering cross-section predictions

The hard scattering cross-section is the quantity commonly used in particle physics to describe the probability of occurrence of a given reaction. This quantity is sensitive to fundamental properties of interactions, resilient against some theoretical divergences, and can be measured experimentally. The latter feature is widely used to probe state-of-the-art theoretical predictions, tune phenomenological models of the theory and determine theoretical parameters and unknowns, such as strong coupling and PDFs.

The calculation of the hard scattering cross-section in  $pp$  collisions is based on the concept of collinear **factorisation** in QCD. This implies splitting the process into two parts. One of them is a perturbatively calculated short-distance, high-energy scale, part representing a hard process. The other is a non-perturbative long-distance part encoded in PDF  $f(x, \mu^2)$ . Factorising these parts, the cross-section of producing a final state  $n$  is calculated as

$$\sigma_{h_1, h_2}^n = \sum_{a, b} \int_0^1 dx_a dx_b \int f_a^{h_1}(x_a, \mu_F^2) f_b^{h_2}(x_b, \mu_F^2) d\hat{\sigma}_{a, b \rightarrow n}(\mu_F, \mu_R), \quad (1.15)$$

where the summation is carried out over all partons  $a$  and  $b$  inside the colliding protons  $h_1$  and  $h_2$ , respectively. The  $\mu_F$  is the arbitrary **factorisation scale**, which effectively denotes a boundary between the short and long-distance parts. The  $\hat{\sigma}_{a, b \rightarrow n}$  is the cross-section at the level of scattered partons representing a short-distance part of the  $pp$  collision. The  $\hat{\sigma}_{a, b \rightarrow n}$  can be expressed as

$$d\hat{\sigma}_{a, b \rightarrow n} = \frac{1}{2\hat{s}} |\mathcal{M}_{a, b \rightarrow n}|^2 d\Phi_n, \quad (1.16)$$

where the  $\mathcal{M}_{a, b \rightarrow n}$  is the scattering matrix element averaged over initial-state spin and colour degrees of freedom and evaluated at given factorisation and renormalisations scales  $\mu_F$  and  $\mu_R$ , respectively. The  $1/2\hat{s}_{ab} = 1/(2x_a x_b s)$  is the parton flux, where  $s$  is the squared centre-of-mass energy of the  $pp$  collision. The  $d\Phi_n$  is the differential phase-space element over the  $n$  final-state particles,

$$d\Phi_n = \prod_{i=1}^n \frac{d^3 p_i}{(2\pi)^3 2E_i} (2\pi)^4 \delta(p_a + p_b - \sum_{i=1}^n p_i), \quad (1.17)$$

where  $p_a$  and  $p_b$  are the initial-state partons momenta [41].

The parton-level cross-section calculations are often approximated by their perturbative series expansion in powers of  $\alpha_S$ , where each term can be illustrated using Feynman diagrams. Such calculations are usually truncated at a given order of  $\alpha_S$  as each subsequent order significantly increases the number of involved equations. Thus, they are often referred to as the **fixed-order** calculations. The LO in  $\alpha_S$ , Born-level, describes the production of the  $n$  final-state partons from

initial state partons  $i$  and  $j$ . The NLO correction, in addition to the LO, includes two contributions referred to as real and virtual corrections. The real correction accounts for emission from Born-level partons resulting in the  $n + 1$  final states. The virtual correction includes the internal loop contributions to the  $n$  parton final state. The higher-order corrections are calculated in a similar fashion.

The fixed-order calculations are complicated due to contributions that lead to infinities, often referred to as divergences. There are two types of divergences. The **ultraviolet** one is associated with infinitely large momenta that may appear in loop calculations. These divergences are cured by renormalisation. Another type is **infrared**, which appears in the loop and phase-space integrals when the energy or angle of emission tends to zero, so this divergence is often referred to as soft (energy close to zero) and collinear (angles energy close to zero). Soft and collinear divergences are cured by the Kinoshita-Lee-Nauenberg (KLN) theorem [57, 58], according to which the divergences cancel out when real and virtual corrections are summed order by order in the perturbation theory.

The calculations for most scattering processes up to the NLO corrections are automated. For example, the NLO calculations for three-jets and  $Z + \text{jets}$  cross-section predictions can be obtained using publicly available NLOJET++ [59] and MCFM [60] programs, respectively. Calculating corrections above the NLO is subject to additional difficulties due to additional emissions and corresponding divergences. Thus, the calculation of NNLO and higher-order corrections for many scattering processes are currently state-of-the-art.

The fixed-order calculations provide reasonable predictions for scattering processes with a few well-separated hard partons in the final state. However, in reality, the final state partons undergo multiple emissions followed by hadronisation. Multiple soft and collinear emissions add logarithmic terms to each power of  $\alpha_s$  in the perturbative expansion due to the  $\alpha_s$  scale dependence. Large logarithmic terms make the fixed-order calculations divergent and so inapplicable. However, more realistic final states can be generated using the parton shower algorithm, which models successive parton emissions according to the parton splitting functions, see Section 1.2.3. The algorithm starts by randomly generating the phase space for any required hard process. This is followed by the so-called evolution of the parton shower from the high scale of the hard process to the low scale of the order of  $\Lambda_{\text{QCD}}$  where hadronisation takes place. This parton shower evolution is described by an iterative probabilistic process developed using the Monte Carlo (MC) numerical calculation techniques [41]. The parton showering accounts only for the contribution of leading logarithmic terms to all orders of perturbative series expansion. Accordingly, its accuracy is often referred to as leading logarithmic (LL), next-to-leading logarithmic (NLL) and so on. The drawback of the parton shower approach is that it may not reproduce hard and wide-angle emissions accurately.

The parton showering is performed using general-purpose Monte Carlo generators such as PYTHIA [61–63], HERWIG [64–67] and SHERPA [68, 69], which have different implementation and settings adjusted to different scattering processes. These generators provide reasonable predictions for a plethora of particle collision final states.

Given that fixed-order and parton shower approaches to cross-section calculations have their merits and shortcomings, they are often combined to get the best of both. However, this requires special approaches to avoid double counting of contributions calculated by each approach. Several prescriptions exist to overcome this issue. The CKKW [70, 71] and MLM [72] prescriptions split the phase space into the regions of hard and soft radiations thus factorising the problem. These strategies are collectively referred to as merging strategies, as they use an arbitrary merging scale to distinguish contributions from different calculation techniques. The other set of strategies, such as MC@NLO [73], POWHEG [74, 75] and their combination MENLOPS [76], collectively referred to as matching strategies, deal with double-counting using an additive fixed-order correction which supplements the parton shower predictions. As a result, using any of the combination strategies results in the most accurate cross-section predictions.

Predictions obtained so far describe the idealistic parton-level final state of the scattering. However, this final state cannot be observed due to the confinement phenomenon. The realistic particle-level predictions must account for hadronisation and UE effects, discussed in the following section.

### 1.2.5 Underlying event and hadronisation

Accounting for the effects of UE and hadronisation is necessary to obtain realistic particle-level predictions. However, these effects take place at the energy scale, which is much smaller than that of hard scattering. At this scale, the strong coupling is large enough, so methods of perturbation theory are inapplicable for their description. Therefore, these effects are often referred to as non-perturbative.

The term UE combines all contributions to the final state that are not associated with a hard process, including its initial and final states. Thus, the UE mainly implies interactions between other partons of colliding protons that occur simultaneously with the hard scattering. These interactions are commonly referred to as multiple-parton interactions (MPI). Partons produced in MPI increase the overall multiplicity of the  $pp$  collision final state, making the hard scattering final state difficult to identify. In addition, they create additional energy deposits in the detector. So it is important to take them into account to obtain realistic predictions. However, MPI are usually soft enough, so the perturbative calculations diverge. That is why they are described using phenomenological models. These models are governed by many parameters that are adjusted or often said

to be tuned to make predictions better fit the data. Various MPI models are included in all general-purpose parton shower generators, but their implementation and the data used for tuning are usually different [41].

The term hadronisation refers to a process that transforms a set of coloured partons into colourless hadrons. High-energy partons are usually showered perturbatively until their energy reaches the non-perturbative scale of about 1 GeV, so the hadronisation takes over to describe a non-perturbative phase transition. Two phenomenological models are often used to describe hadronisation. One is the Lund model [77, 78], also known as a string model, making the hallmark of PYTHIA. The model is usually illustrated in terms of colour flow tubes stretched like strings between various partons. The string's tension increases as partons move apart, so it can break, producing a new parton pair. It can also break into a pair of diquarks, each being a pair of quarks, which are needed to create particles made up of an odd number of quarks. The process continues recursively for new parton pairs until their invariant mass is of the order of a typical hadron, which eventually confines them. In this view, each gluon is considered as the energy and momentum-carrying transverse kink on the string, which grows, stretching connected strings until the gluon's kinetic energy has been used. The breaking of a string and the production of hadrons are probabilistic processes. The probabilities are governed by model parameters that are tuned to match predictions with data.

Another hadronisation model is the so-called cluster model [79], which is the hallmark of HERWIG, but also alternatively implemented in SHERPA. The model implies preconfinement of showered quarks, which are close to each other, into colour-singlet subsystems called clusters. In addition, gluons are forced to split into quark-antiquark pairs that also enter the clusters. The clusters then decay into hadrons aiming to reproduce the distribution of hadrons in data, where the decay is governed by tuned parameters, whose number is fewer compared to the string model.

As a result, a model of hard scattering, which is supplemented with UE and hadronisation, leads to a realistic particle-level final state of  $pp$  collision.

### 1.3 Jet definition algorithms

The scattering final states are usually represented by moving away partons, parton showers or particles, depending on the level of approximation. In experiments, the final states are described by the measured signals in the detector. So, there are various objects on which jets must be defined. The algorithms that map these objects based on their topology into jets are called jet definition algorithms.

The general criteria for a jet definition algorithm were formulated at the Snowmass conference in 1990 [80]. According to them, the algorithm must be simple for implementation in experimental analysis and theory calculations, be determined at any order of perturbation theory, yield finite cross-section, i.e. it must be insensitive to the soft and collinear emissions, and be relatively insensitive to non-perturbative effects like hadronisation and UE. These are the baselines for modern jet definition algorithms.

There are two general classes of jet definition algorithms that were used in various experiments: cone and sequential recombination algorithms [81, 82]. Cone algorithms were the first to be used for jet definition [83]. The idea behind the cone algorithm is that jets represent a dominant energy flow in an event. The general cone algorithm starts with a seed particle  $i$ . It sums the momenta of close-by particles  $j$  within a cone of opening-angle  $R$ , using a geometrical distance  $\Delta R_{ij}$  in the rapidity<sup>3</sup>-azimuth plane  $y$ - $\phi$  defined as

$$\Delta R_{ij} = \sqrt{(y_i - y_j)^2 + (\phi_i - \phi_j)^2} < R. \quad (1.18)$$

The  $R$  parameter is dimensionless and is often referred to as **jet radius**. The algorithm redefines the seed by the vector sum of particle  $i$  and  $j$  directions and iterates until the cone direction is stable. The differences between the types of cone algorithms lie in the seed particle definition and handling cases when jets overlap. Most cone algorithms are slow, infrared unsafe and currently outdated. Although an issue of infrared unsafety is resolved in a modern variant of a seedless cone algorithm, the SISCone [84].

The sequential recombination algorithms follow a QCD-inspired idea of successive parton branching. The core of these algorithms is based on the inversion of the parton branching process by sequential pairwise recombination of the input objects. The algorithms of this class were initially developed aiming to overcome infrared unsafety. The most widely used algorithms are generalised as follows [85]. First, the list of input objects is created. Then, the distance between various pairs of input objects  $i$  and  $j$  is calculated as

$$d_{ij} = \min(p_{T,i}^{2p}, p_{T,j}^{2p}) \frac{\Delta R_{i,j}^2}{R^2}, \quad (1.19)$$

where  $p_T$  is the transverse momentum inherent to the input object and  $p$  is a free parameter of the algorithm. In addition, the so-called distance from each object to the beamline is calculated as

$$d_{i,B} = p_{T,i}^{2p}. \quad (1.20)$$

---

<sup>3</sup>Rapidity  $y$  (and pseudorapidity  $\eta$ ) is the standard variable in collider experiments. It is defined as the  $y = \frac{1}{2} \ln \frac{E+p_z}{E-p_z}$  ( $\eta = -\ln \tanh \frac{\theta}{2}$ ), where  $E$  is the particle energy and  $p_z$  is the momentum along the beam-line  $z$  ( $\theta$  is the angle with respect to the beam-line). Rapidity is equal to the pseudorapidity in the case of massless particles.

Finally, the objects  $i$  and  $j$  are recombined if  $d_{ij} < d_{i,B}$ , while otherwise, particle  $i$  is called a jet and removed from the list of entities. The distances are recalculated, and the procedure is repeated until no entities are left.

The generalised description combines the three most known sequential recombination algorithms depending on the value of the parameter  $p$ . The value of  $p = 1$  corresponds to the so-called  $k_t$  algorithm [86, 87]. The  $k_t$  algorithm clusters the input objects starting from low transverse momenta. The case of  $p = 0$  leads to the Cambridge/Aachen [88, 89] algorithm, which does not depend on the transverse momenta of input objects. Finally, the case of  $p = -1$  leads to the **anti- $k_t$  algorithm**, which is the default in modern experiments. The anti- $k_t$  algorithm starts from the hardest input objects and provides perfect cone-shaped hard jets. The  $R$  parameter in anti- $k_t$  has a straightforward interpretation of a radius of a cone in the  $y$ - $\phi$  plane. Although, if several jets overlap, a softer jet will be truncated. Each algorithm has its own prescription for the truncation of overlapping jets.

Several types of recombination schemes specify how the kinematic properties of input objects are combined to make up jets. The most commonly used is the four-vector recombination scheme which simply sums the components of the four vectors resulting in massive jets.

The behaviours of different jet algorithms are illustrated in Figure 1.7. The input to the algorithm is provided by a sample parton-level event generated with HERWIG. The  $k_t$  and Cambridge/Aachen algorithm result in heterogeneous borders representing an attempt of the algorithm to adapt to a complex distribution of the soft particles in the event. The irregular shapes of jets from these algorithms complicate the experimental analysis of jet final-states and leads to certain implications in theoretical calculations with respect to the algorithms resulting in regular shapes [85]. The SIScone algorithm results in regular single-particle jets, but it becomes irregular in the case of composite jets. Finally, the anti- $k_t$  provides circular hard jets, while only the softer jets have a complex shape.

The relative simplicity of the anti- $k_t$  jet definition algorithm, its resilience to infrared and collinear singularities, high speed of recombination of input objects, and the conical representation of jets simplifying the experimental and theoretical analyses are its main advantages over other algorithms. These advantages have made anti- $k_t$  the default algorithm in many modern experiments.

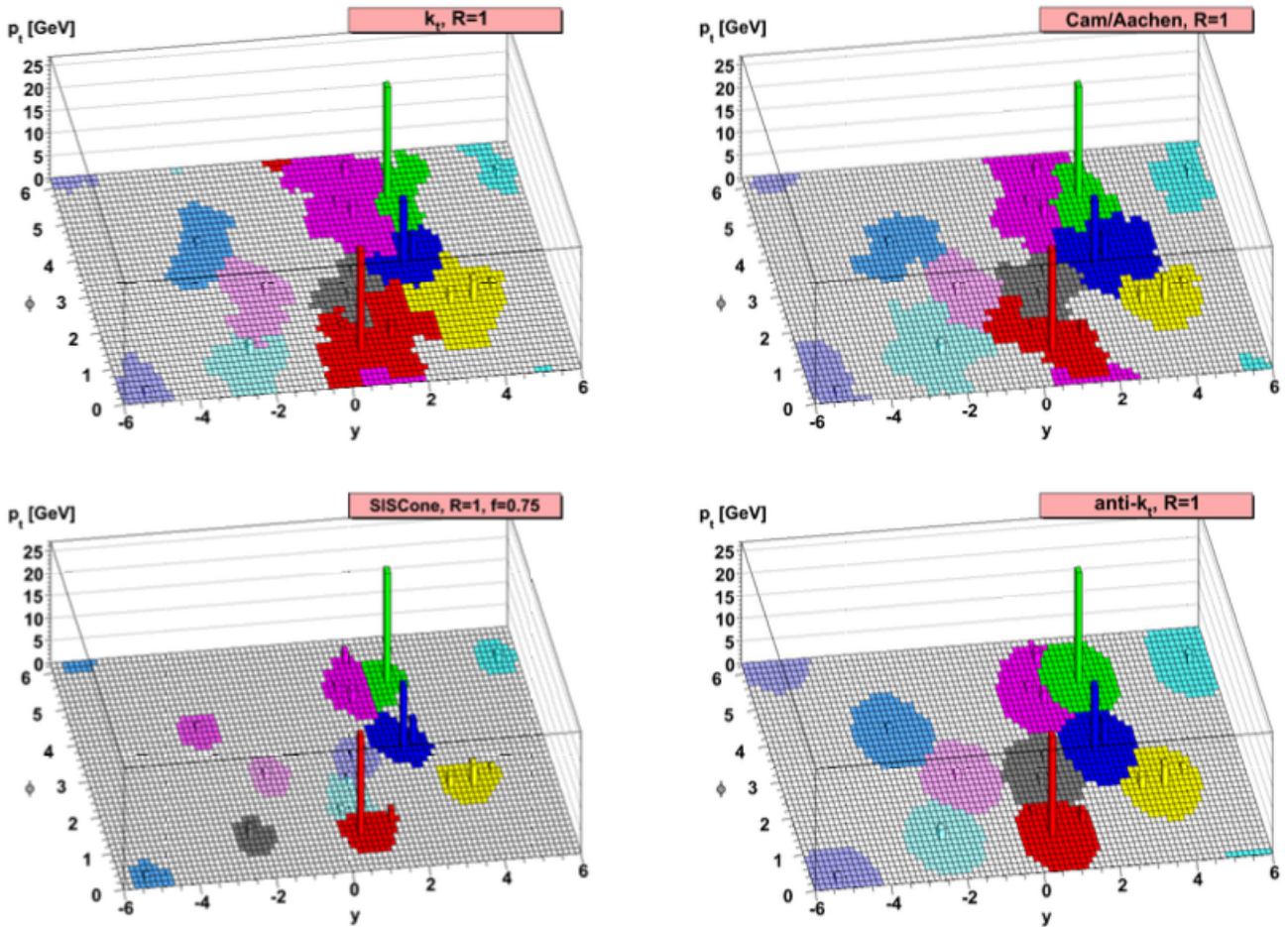


Figure 1.7 — A representation of the behaviour of different jet algorithms on an  $y$ – $\phi$  plane. Different jet definition algorithms run on the same showered parton-level input. The defined jets are shown in colour. The default in modern experiments is the anti- $k_t$  algorithm shown at the bottom left. The figure is taken from Ref. [85].

## 1.4 Previous studies of three-jets and $Z + \text{jets}$ production, and prospects for new measurements

The current state of the theory of strong interactions would be impossible without the study of jets in collider experiments [16]. The first evidence of the two jet production in electron–positron,  $ee$ , collisions at the SPEAR [90] in 1975 was an important confirmation of the quark model of matter. One of the first confirmations of the existence of a gluon was an observation of a three-jet topology in the final state of  $ee$  collisions at the PETRA in 1979 [91–94]. Larger interaction scales for jet production in  $ee$  collisions were probed at the LEP [95]. The experiments at  $ee$  colliders lead to measurements of the QCD parameters such as  $\alpha_S$ , colour factors and properties of heavy quarks. Jets in hadron collisions were indicated for the first time at ISR [96], before being unambiguously isolated at

$Spp\bar{p}S$  [97]. The hadron collision experiments extend the use of jets to study the hadron structure. For example, jets from lepton–hadron collisions at the HERA helped to derive the PDFs in a wide range of partons momenta [98]. The jet data from the HERA were also used for further constraints of the uncertainty in strong coupling [99]. Jets are also used to search for new phenomena in larger energy regimes, an example of which is the top-quark discovery in  $p\bar{p}$  collisions at the TEVATRON [100].

Experiments at the LHC go beyond the energy frontiers of previous experiments. For example, in the case of  $pp$  collisions, the LHC explores the energy scales of the order of ten TeV. Such high energies make available many physical processes that were previously inaccessible. A variety of processes, whose production cross-sections are measured by the ATLAS experiment at the LHC, are summarised in Figure 1.8. Many of them include jets in their final states. Even the Higgs boson studies are carried out extensively using jets, for example, those initiated by bottom quarks, which are often produced by the decay of the Higgs boson. [101]. Besides the Higgs boson studies, the cross-section measurements of other production processes are equally important. Among these are the cross-section measurements of the three-jet production and the  $Z$ -boson productions together with jets, which are described in this thesis. Jets are produced abundantly at the LHC as their cross-section is large. Even though their cross-section decreases gradually depending on the number of jets in the final states, the three-jets production cross-section exceeds that of many other processes. The  $Z + \text{jets}$  production cross-section is several orders of magnitude below that of jets but still higher than many other processes, so the  $Z + \text{jets}$  are also produced in abundance at the LHC. As a result, high-energy  $pp$  collisions at the LHC provide ample opportunities for precision measurements of the three-jets and  $Z + \text{jets}$  cross-sections.

The three-jets and  $Z + \text{jets}$  cross-section measurements provide valuable inputs for the strong coupling and PDF determination. The sensitivity to these quantities is evident directly from their LO Feynman diagrams, shown in Figures 1.9 and 1.10. These processes are produced predominantly by the quark-gluon interactions in the initial state, so a high sensitivity is expected to the gluon PDF, which is currently known with greater uncertainty than that of quarks. Moreover, a valuable contribution to the gluon PDF analysis is expected from the gluon-gluon interactions in the three-jets initial states but not in the  $Z + \text{jets}$  since gluons do not interact directly with the  $Z$ -boson. The fraction of the quark-quark initial states is relatively small in the total production rate of these processes, so a lower sensitivity to quark PDF is expected. As for the final states, the multi-jet production is described by high-order terms in perturbative series expansion in  $\alpha_s$ , so high sensitivity to  $\alpha_s$  is expected. For example, the three-jets production is directly sensitive to  $\mathcal{O}(\alpha_s^3)$  term, so the measured cross-section can be used to constrain  $\alpha_s$ . Besides this, the three-jets and  $Z + \text{jets}$  cross-section measure-

ments provide an important input for testing high-order theoretical predictions and tuning phenomenological models.

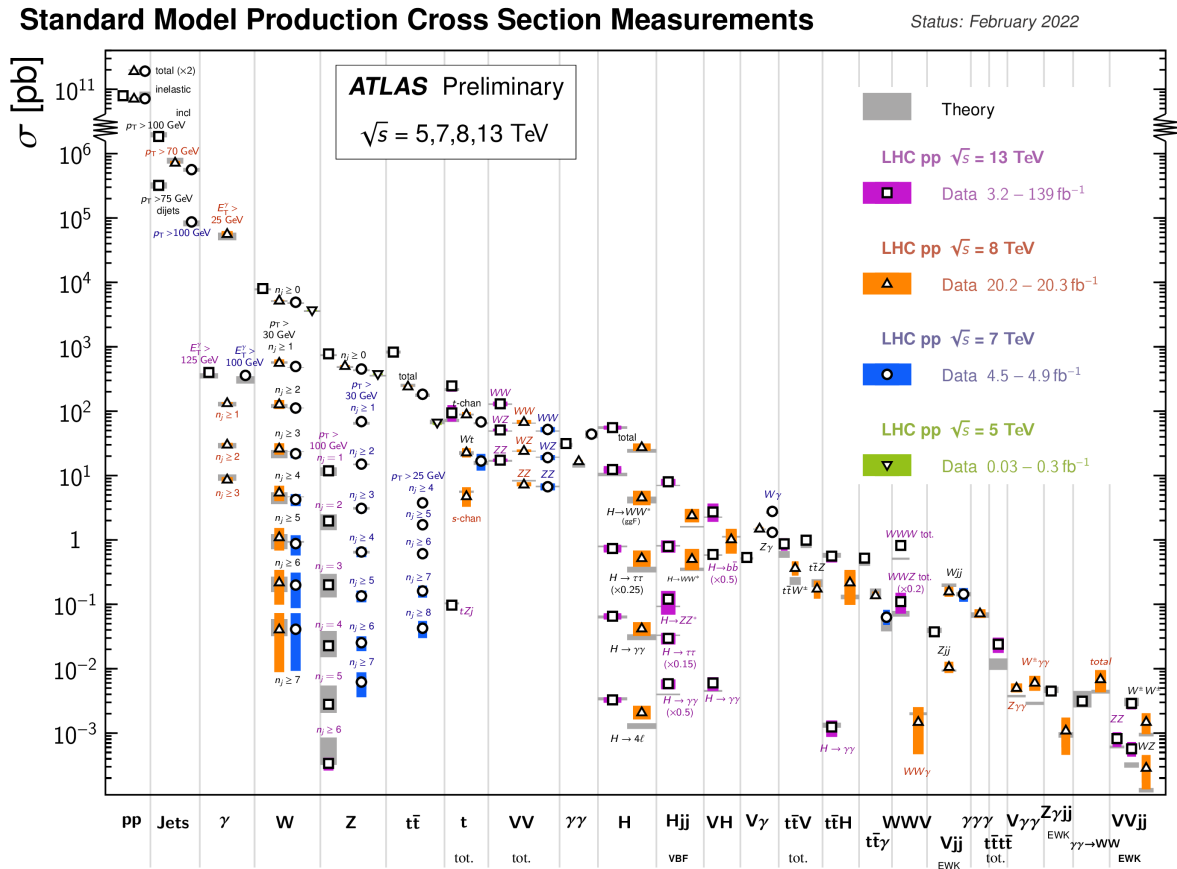


Figure 1.8 — A summary of several SM cross-section measurements in the ATLAS experiment at the LHC. The figure is taken from Ref. [102].

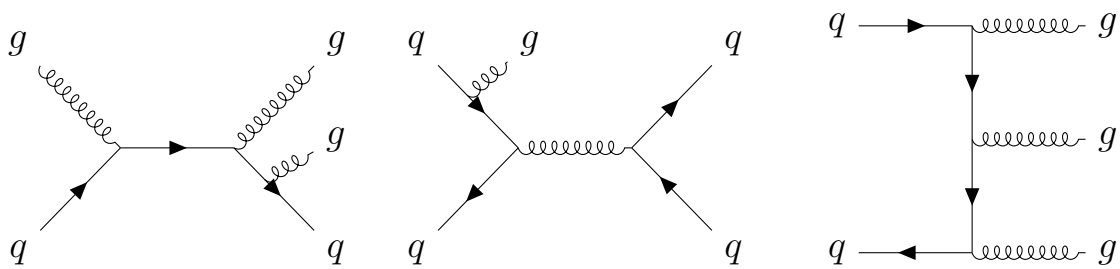


Figure 1.9 — Examples of Feynman diagrams for three-jet production in the leading-order of perturbative QCD.



Figure 1.10 — Examples of Feynman diagrams for  $Z + \text{jets}$  production in the leading-order of perturbative QCD.

Various properties of jet production, particularly the three-jets and  $Z + \text{jets}$  cross-section, were thoroughly studied in experiments at hadron colliders. For example, the three-jets cross-section was measured differentially as a function of three-jet mass for the first time using  $\sqrt{s} = 1.96$  TeV  $p\bar{p}$  collisions data in 2011 [103]. However, experiments at the LHC explore the largest energy scales. For example, inclusive jet and dijet cross-sections were measured in  $pp$  collisions with  $\sqrt{s} = 2.76$  TeV [104], 7 TeV [13, 105–107], 8 TeV [108] and 13 TeV [109]. Several measurements were performed to test cross-section predictions for jets of different radii [106, 108, 110]. The means for determining the strong coupling constant were provided by measuring the ratio between the three-jet and two-jet cross-sections [111]. Theoretical predictions for the multi-jet production have been tested by measuring their cross-sections using 7 TeV  $pp$  collisions data [112, 113].

As for the  $Z + \text{jets}$  production, its various properties have been measured in  $p\bar{p}$  collisions [114–117]. These include differential  $Z + \text{jets}$  cross-section measured as functions of the  $Z$ -boson transverse momentum, the jets' transverse momenta and rapidities, and as the function of the angular separation between the  $Z$ -boson and jets in final-states with different jet multiplicities. The data on measured  $Z + \text{jets}$  cross-section was expanded by measurements at the LHC using  $pp$  collisions at different centre-of-mass energies [118–127] that have an increased phase space compared by the previous experiments.

This thesis describes the three-jets and  $Z + \text{jets}$  cross-section measurements performed double-differentially as a function of jet kinematics, which became possible thanks to high statistics collected by the ATLAS experiments at the LHC. Moreover, they explore larger energy regimes compared to previous experiments using  $\sqrt{s} = 7$  TeV and 8 TeV  $pp$  collisions data, respectively. Compared to the previous ATLAS measurement, the new results make use of the superior description of the uncertainties in the jet energy measurement. These cross-section measurements are especially valuable for the PDF analysis, as they describe multiple regions in  $x-Q^2$  plane, see Figure 1.6. So new constraints for gluon PDF can be determined. In addition, the results can be used to constrain  $\alpha_s$ . Despite this, the results allow a refined test of the most up-to-date theoretical predictions, such as those for  $Z + \text{jet}$  productions at NNLO [128, 129].

## 1.5 Summary and outlook

The studies of jet production in  $pp$  collisions are important components of particle physics development. They probe the fundamental structure of protons and the nature of strong interactions. Particularly, they allow determining the strong coupling and parton distribution functions, quantities that cannot be deduced from the first principles of the theory.

New experiments, such as those at the LHC, are pushing the energy scale boundaries towards those of the early Universe aiming to uncover new phenomena. However, even if there is nothing new, the studies of the jet production make an important contribution to improving the accuracy in the existing theory.

## Chapter 2

# Experimental setup

The study in this thesis is carried out within the framework of the ATLAS experiment at the LHC. The core of the experiment is an eponymous general-purpose detector. The detector is located at the crossing point of high-energy particle beams. It detects particles produced in the collisions at the LHC. The proton–proton collisions are the object of the study in this thesis.

This chapter introduces the experiment’s details relevant to the study. The LHC is discussed in Section [2.1](#). The ATLAS detector is reviewed in Section [2.2](#). The trigger system which prevents the overflow of the ATLAS data stream is described in Section [2.3](#). Data quality monitoring necessary to reject data affected by the detector malfunctions is presented in Section [2.4](#). A chain of several simulation stages used to model the data is reviewed in Section [2.5](#). A summary is provided in Section [2.6](#).

## 2.1 The Large Hadron Collider

The LHC is the two-ring accelerator and collider of protons and ions. It is installed in a 26.7 km tunnel running 45–170 m under the Franco-Swiss border near Geneva. The underground location effectively suppresses the impact of cosmic rays on any physics studies. The collider is operated by the European Organisation for Nuclear Research (CERN).

The LHC is designed for proton–proton collisions at the centre-of-mass energy of  $\sqrt{s} = 14$  TeV [\[17\]](#). To achieve such record energy, the CERN accelerator complex developed over its 70-year history is used. So, the particle beams are successively accelerated by a linear accelerator, followed by three synchrotron rings with increasing diameters. When in the LHC, the particle beams circulate contrariwise in separate rings. The beams are governed by superconducting magnets. The collisions are performed in four distant points, where large particle detectors are installed. Among them, the ATLAS detector is the largest in size.

Collisions with high luminosity, a quantity that describes the accelerator’s ability to produce a given number of collisions, are necessary for studying rare events. More formally, the luminosity is the quantity proportional to the rate of

inelastic collisions and inversely to their cross-section. The design peak luminosity of proton collisions at the LHC is  $10^{34} \text{ cm}^{-2} \text{ s}^{-1}$ . This is achieved, among other things, by colliding bunches of  $1.1 \times 10^{11}$  protons with a nominal collision frequency of 40 MHz, i.e. one collision every 25 ns. High luminosity is one of the advantages of the LHC compared to previous experiments.

The LHC is approaching its design parameters through several data-taking campaigns. The first one, **Run 1**, took place from 2010 to 2012. During Run 1 proton bunches collided every 50 ns with centre-of-mass energy of  $\sqrt{s} = 7$  TeV in 2011 and  $\sqrt{s} = 8$  TeV in 2012. The second data-taking campaign, **Run 2**, took place from 2015 to 2018. During Run 2 proton bunches collided every 25 ns with a centre-of-mass energy of  $\sqrt{s} = 13$  TeV. The integral of the luminosity delivered to the ATLAS detector as a function of time is shown in Figure 2.1. The data correspond to the conditions when proton beams are considered stable. Most of the delivered data, except for a small fraction related to the detector problems [130], are recorded. The total integrated luminosity of about  $180 \text{ fb}^{-1}$  is about two-thirds of the initial goal at the LHC.

The high luminosity is achieved at the expense of dozens of simultaneous interactions per bunch crossing, referred to as a pile-up, whose debris overwhelms the detector. The distribution of a mean number of such interactions averaged over about a minute of data-taking is shown in Figure 2.2. This number reaches 40 in Run 1 and 70 in Run 2. That is why the pile-up suppression techniques are emphasised in the text.

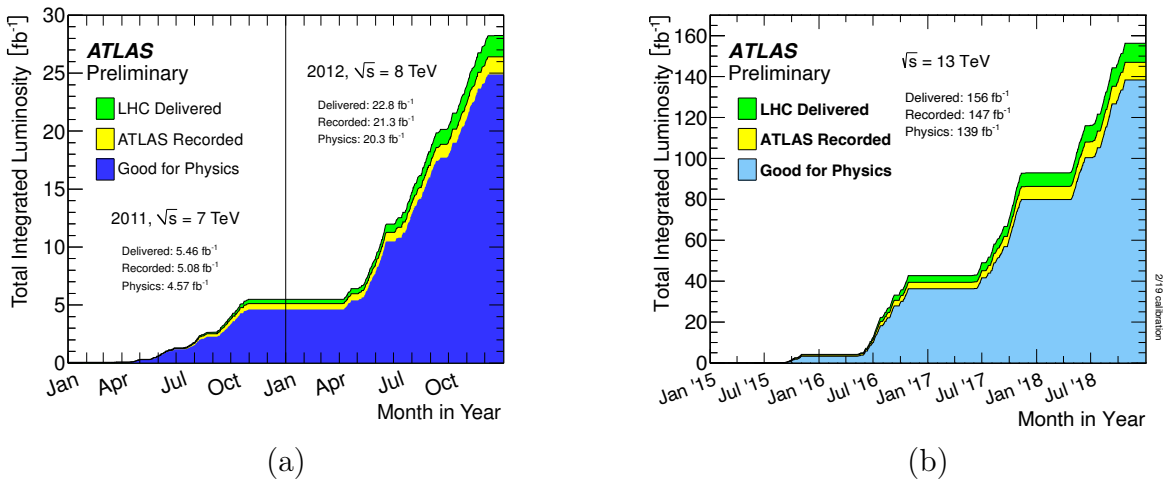


Figure 2.1 — Total integrated luminosity delivered by the LHC (green), recorded by the ATLAS (yellow), and certified for physics analysis (blue) as a function of time in (a) Run 1 [131] and (b) Run 2 [132].

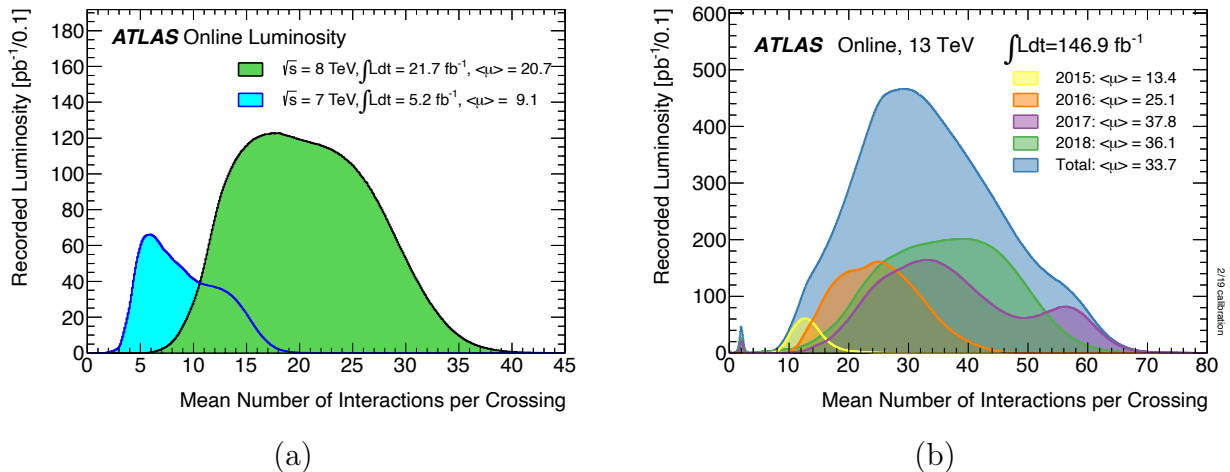


Figure 2.2 — Mean number of interactions per bunch crossing in the ATLAS experiment in (a) Run 1 [131] and (b) Run 2 [132].

## 2.2 The ATLAS detector

The ATLAS (A Toroidal LHC ApparatuS) is a general-purpose particle detector with a forward-backwards symmetry, which covers nearly the entire solid angle around the collision point<sup>1</sup> [18]. The research program of the ATLAS detector is broad. It spreads over precision measurements of the SM model parameters and searches for new phenomena in the TeV regime. The detector thus consists of many components necessary to achieve its experimental goals. Among the key components are the inner tracking detector surrounded by the thin superconducting solenoid, electromagnetic and hadron calorimeters, and the muon spectrometer incorporating three large superconducting air-core toroidal magnets. They are shown schematically in Figure 2.3.

The inner-detector system (ID) is immersed in a 2 T axial magnetic field and provides charged-particle tracking in the range  $|\eta| < 2.5$ . The high-granularity silicon pixel detector covers the vertex region and typically provides three measurements per track, the first hit normally being in the innermost layer. It is followed by the silicon microstrip tracker (SCT), which usually provides eight measurements per track. These silicon detectors are complemented by the transition radiation tracker (TRT), which enables radially extended track reconstruction up to  $|\eta| = 2.0$ . The TRT also provides electron identification information based on the fraction of hits (typically 30 in total) above a higher energy-deposit threshold corresponding to transition radiation.

<sup>1</sup>ATLAS uses a right-handed coordinate system with its origin at the nominal interaction point (IP) in the centre of the detector and the  $z$ -axis along the beam pipe. The  $x$ -axis points from the IP to the centre of the LHC ring, and the  $y$ -axis points upward. Cylindrical coordinates  $(r, \phi)$  are used in the transverse plane,  $\phi$  being the azimuthal angle around the  $z$ -axis.

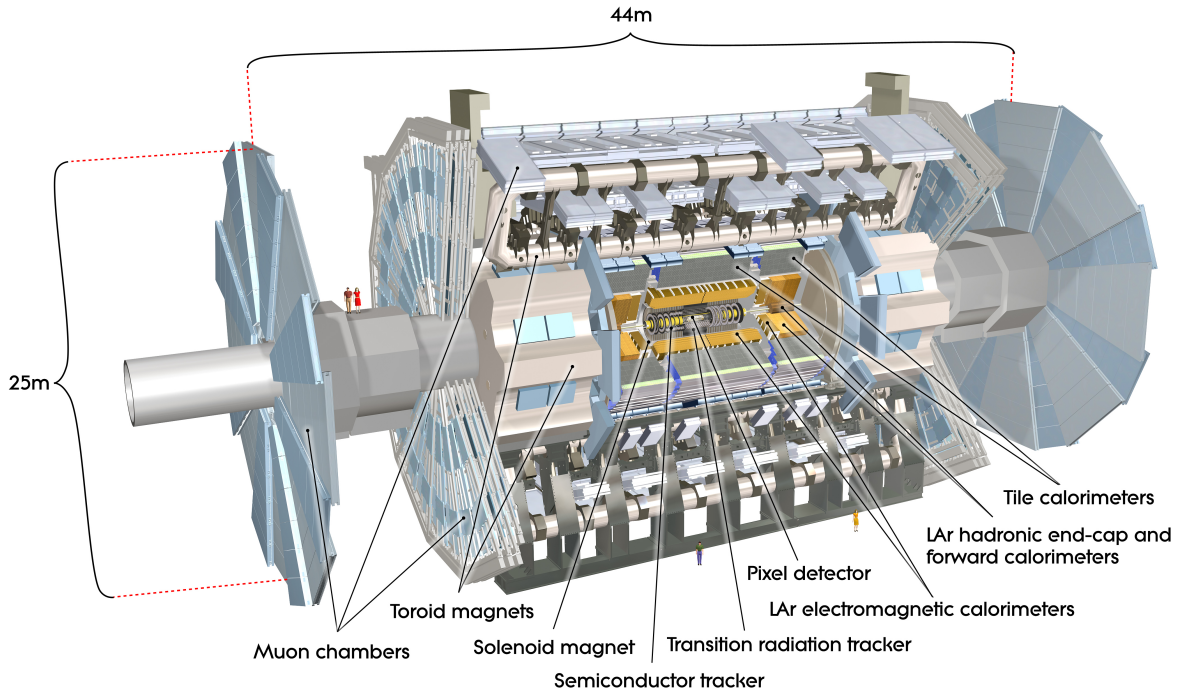


Figure 2.3 — The ATLAS detector composition [133].

The calorimeter system covers the pseudorapidity range  $|\eta| < 4.9$ . Within the region  $|\eta| < 3.2$ , electromagnetic calorimetry is provided by barrel and endcap high-granularity lead/liquid-argon (LAr) calorimeters, with an additional thin LAr presampler covering  $|\eta| < 1.8$  to correct for energy loss in material upstream of the calorimeters. Hadron calorimetry is provided by the steel/scintillator Tile Calorimeter, segmented into three barrel structures within  $|\eta| < 1.7$ , and two copper/LAr hadron endcap calorimeters. The solid angle coverage is completed with forward copper/LAr and tungsten/LAr calorimeter modules optimised for electromagnetic and hadronic energy measurements, respectively.

The muon spectrometer (MS) comprises separate trigger and high-precision tracking chambers measuring the deflection of muons in a magnetic field generated by the superconducting air-core toroidal magnets. The field integral of the toroid, quantified by particles originating at the interaction point and propagating outward in a straight line, ranges between 2.0 and 6.0 Tm across most of the detector. A set of precision chambers covers the region  $|\eta| < 2.7$  with three layers of monitored drift tubes, complemented by cathode-strip chambers in the forward region, where the background is highest. The muon trigger system covers the range  $|\eta| < 2.4$  with resistive-plate chambers in the barrel, and thin-gap chambers in the endcap regions.

## 2.3 The trigger system of the ATLAS detector

The LHC collides particles at a high rate to collect information about rare physics processes. However, not all collision data can be preserved. The limitations are mainly due to the finite bandwidth of the data acquisition system, available processing resources and storage capabilities. The trigger system is used to overcome these limitations. It analyses partial detector information online at the collision rate to identify events of the primary interest, such as those with a large momentum transfer. The trigger system accepts selected events at the maximal possible rate. The rest of the events are discarded.

A three-level trigger system is used in Run 1 [134]. The first-level (L1) triggers are implemented in hardware. They use a subset of detector information to analyse and accept the most interesting events at a rate of 75 kHz. In addition, the L1 trigger identifies the regions of interest within the detector, so higher trigger levels do not require scanning the entire detector for high-energy signatures. Events accepted by the L1 are processed by the Level-2 (L2) and Event Filter (EF) triggers. The L2 triggers execute fast custom algorithms within the region of interest and reduce the event rate before the EF. The EF, whose algorithms most closely resemble those used in offline data processing, revises full event information and reduces the event rate to about 400 Hz, which satisfies the detector read-out capability.

During the LHC shutdown between Run 1 and Run 2, the detector and trigger systems were upgraded to accommodate the expected increase in the collision energy and luminosity [135]. This upgrade also improved the offline event processing capabilities, so triggers were updated accordingly. The L1 acceptance rate was increased to 100 kHz. The L2 and EF triggers were merged into a high-level trigger (HLT), improving resource sharing and simplifying hardware and software. As a result, the average acceptance rate of the trigger system was increased to 1000 Hz.

Interesting events include various objects produced in the final state of  $pp$  collision. Examples of such objects are electrons, muons and jets. Multiple triggers with different reconstruction algorithms and selection criteria are developed to account for various physics analysis needs. Since the decision on event acceptance is made by a chain of L1 and high-level triggers, several hundred trigger chains run in parallel to maximise the physics output of the experiment.

Some final states occur at a rate that exceeds the detector's readout capabilities. For example, jets are produced abundantly, but their production cross-section decreases sharply as a function of the hardest jet transverse momentum. Therefore, a set of jet trigger chains selecting jets with different kinematics is used to record events efficiently. That is, events with the hardest jet  $p_T$  are recorded without any exceptions, while below a certain jet  $p_T$  threshold, only a fraction of events is recorded. This strategy is referred to as the trigger **prescale**. The

fraction of accepted events is adjusted by the prescale factor, whose magnitude depends on the detector read-out capability. As a result of prescale, the statistics along the jet  $p_T$  are often uniform.

Some tasks require datasets with events recorded unconditionally or at least with a minimal bias due to the selection requirements. Such datasets are used to develop trigger algorithms, test predictions of the total scattering rate, or study detector noise. Triggers that serve this purpose make decisions based on the signals in specific detector components sensitive to low-energy deposits, such as the Minimum Bias Trigger Scintillators [134]. Another approach is to trigger random events. An example of the latter is implemented in the **ZeroBias** trigger [135, 136]. This trigger accepts events occurring in a fixed number of bunch crossings after an event with a high-energy electron or photon is accepted by the L1 trigger, so their rate scales linearly with the luminosity. In this case, the contribution of hard scattering events is minimised since their cross-section is much smaller than the total inelastic cross-section. This strategy is used in this thesis to study the effect of the calorimeter noise associated with pile-up.

## 2.4 Data quality monitoring

The ATLAS detector consists of various subsystems. Each subsystem reads out information about particle collision products from thousands of electronic channels. The overall readout consists of over 100 million channels. These channels and larger detector elements made up of them are subject to malfunctions affecting the recorded data. For example, the measurement error can be due to high-voltage trips, noise bursts, and detector misconfigurations. That is why the data are continuously monitored to ensure high-quality input for physics research [130].

The data quality monitoring is carried out online automatically and by a crew of shifters. If a significant problem in any subsystem occurs, immediate actions are taken to minimise the data loss.

Another inspection is performed offline when the data-taking is over. The offline monitoring proceeds in two stages. First, the quality is assessed in a subset of data processed parallel to the data-taking, so these data are quickly available. These data already contain information on reconstructed physics objects, e.g. jets. Any uncovered misconfigurations or miscalibrations affecting the data quality are corrected where possible. Otherwise, the corresponding subsystems are flagged. The performance of individual readout channels is also checked, so the channels containing issues that cannot be calibrated are also flagged. The flags are recorded in the detector conditions database and used in the upcoming processing of the full dataset, so channels whose information cannot be recovered are excluded. The processing of the full data set starts after this stage of data quality monitoring is

over. The second round of quality assessment is then performed to ensure that the discovered issues are fixed. Otherwise, reprocessing may be required.

If a significant detector failure affects the data quality, a so-called defect flag is set into the database. The defects are assigned to the affected interval of the data-taking, which are usually, but not always, rejected during the data analysis. The smallest interval considered during the data quality assessment corresponds to about a minute of data-taking. This interval is a so-called luminosity block or **lumiblock**, within which the accelerator, detector and trigger configurations are considered constant. As a result of the data quality monitoring, the list of lumiblocks certified for physics analysis is obtained. This list is referred to as the **Good Run List (GRL)**. The absence of the data in the GRL is often a sufficient reason to exclude them from physics analysis.

## 2.5 Simulation of collision data

Simulating collision data is essential for the ATLAS data analysis. The simulation is performed in a chain [137] that starts with generating particle collision events and results in an output similar to that of the real detector. These results are then used, for example, to correct measured particle properties to their true values. The simulation also allows direct comparisons between the data and theoretical predictions. So, the main aspects of simulation in ATLAS need to be introduced.

The simulation in ATLAS is performed using a dedicated software suite, ATHENA [1], which is designed for reconstruction and analysis of real and simulated data, as well as to ensure the operation of the detector, trigger and data acquisition systems of the experiment.

The first step in the simulation chain is the modelling of the hard scattering. At this step, the kinematics of the final-state particles is generated. This implies a realistic final state, including the modelling of effects such as parton showering, hadronisation, particle decays and emissions where appropriate. This step is often done with general-purpose particle generators interfaced to the ATHENA. The stable particles obtained at this step represent a so-called **particle level** state, which assumes that the particle properties are measured precisely using an ideal detector. These results are usually retained despite the other steps of the simulation chain so that the effect of the real detector on particle properties can be evaluated later.

In the second step, the generated particles are propagated to the ATLAS detector simulation. Here, the path of particles through the detector and their interactions with the active detector materials are simulated. The detector simulation is performed using the GEANT4 [138] framework interfaced to the ATHENA. The GEANT4 uses the most accurate detector description, including all materials,

even glue, traversed by particles, alignment of various subsystems, known detector malfunctions, and the magnitude of the magnetic field within the detector volume. The output of the simulation is the list of records of particle energy depositions, with their position and time.

Finally, the results of the detector simulation are propagated to the digitisation step, which generates detector signals, such as voltages and currents in the detector electronics. Signal readout features, such as electronics noise, cross-talks between the detector subsystems, and channel-dependent variations in the detector response, are also modelled. The inputs to the digitisation step are not limited to the hard scattering events. The most realistic readings are obtained when backgrounds accompanying the hard scattering are overlaid at a user-specified rate just prior to digitisation. The main backgrounds considered at this stage are due to simultaneous  $pp$  interactions and non-collision-related sources, such as those from cosmic ray particles, proton beam interactions with residual gas along the beam pipe and beam-halo events caused by interactions in the tertiary collimators located in the beam line far away from the ATLAS detector. The decisions of hardware-based L1 triggers are also simulated at the digitisation step. As a result, the digitisation output is similar to that of the real detector.

Further processing of digitised data implies reconstructing particles and jets that traverse the detector. The same reconstruction algorithms are used both in real and simulated data, including the high-level trigger algorithms. The reconstructed particles and jets are usually referred to as those at the **detector-level**. Contrary to those at the particle level, their properties are distorted by detector effects, such as finite resolution, limited acceptance and inefficiencies of the detector. Despite this, the reconstructed particles are inputs for physics studies in ATLAS.

## 2.6 Summary and outlook

The LHC and the ATLAS detector are complex scientific instruments. The complexity of their subsystems requires huge scientific collaborations to ensure their operation. Only through a joint effort can discoveries be made, among which the Higgs bosons discovery is the most known. Examples of several contributions to the studies performed by the ATLAS collaboration are revealed in the following chapters. However, the physics programme of the ATLAS experiment has not yet been completed. The experiment is ongoing. The discoveries are still possible, given that the designed  $pp$  collision energy has not yet been reached. Furthermore, many scientific problems may find solutions by considering the ever-growing amount of data.

## Chapter 3

# Pile-up noise study in the Tile Calorimeter

The Tile Calorimeter (TileCal) [3, 139] provides hadronic calorimetry in the central part of the ATLAS detector. It is designed for precise energy measurements of hadrons, jets, and  $\tau$ -leptons. The precision is particularly relevant for jets, up to a third of whose energy is measured in the TileCal. In addition, the TileCal supplements a variety of other measurements. For example, it is used to improve the electromagnetic calorimeter performance by measuring the energies of particles that pass through the latter. The TileCal also complements the measurements of transverse momentum imbalance caused by weakly-interacting particles, such as neutrinos or various hypothetical particles. This kind of measurement is necessary for W-boson and top-quark mass reconstruction, as well as for various Higgs-boson studies, such as those exploring the  $H \rightarrow WW$  and  $H \rightarrow \tau\tau$  decay channels [140].

One of the TileCal design goals is the energy resolution for jets of  $dE/E = 50\%/\sqrt{E} \oplus 3\%$ , which is a prerequisite for accurate jet cross-section measurements and searches for new physics phenomena in the range of energies from GeV to several TeV. However, the energy resolution degrades significantly due to simultaneous  $pp$  interactions, known as the pile-up interactions, whose number goes as high as 40 in Run 1 and 70 in Run 2. A high flux of low-energy particles originating from pile-up interactions distorts the energy measurements. This effect is particularly relevant to jets whose constituents are distributed over a significant part of the calorimeter volume. Apart from that, pile-up complicates extracting signals from hard interactions and makes up a source of transverse momentum imbalance affecting the studies of weakly-interacting particles. The complexity associated with the pile-up is expected to increase in the next generation of the LHC, high luminosity LHC (HL-LHC), where up to 200 simultaneous interactions are expected. So the study of pile-up effects is essential.

Various techniques are developed to minimise the pile-up contribution to the jet energy measurements. Some of them minimise pile-up contribution when the particle energy deposited in the calorimeter is reconstructed [141]. According to another, the clusters of calorimeter energy deposits rather than individual

cells are used to reconstruct high-level objects, such as jets [142], so the pile-up contribution is suppressed by the clustering algorithm [142]. Finally, the pile-up contribution to reconstructed jets is evaluated and subtracted by the jet energy scale calibration [143].

This chapter reports on a helper method developed in the TileCal to provide input to the energy clustering algorithm. According to this, the pile-up contribution to the calorimeter energies is treated as a component of the calorimeter noise. This kind of noise is referred to as the **pile-up noise** or, since it is associated with the physics of collisions between particles, it is also called physics noise. Together with another component of the calorimeter noise, electronics noise, the pile-up noise measured using  $pp$  collisions data allows one to estimate how significant the energy is relative to the noise. As a result, energies that do not exceed noise are usually suppressed by the clustering algorithm.

The content of the chapter is as follows. The TileCal segmentation into cells is introduced in Section 3.1. A brief description of the energy reconstruction algorithm used in the TileCal that minimises noise is presented in Section 3.2. The pile-up noise measurement performed in the TileCal cells is discussed in Section 3.3. This includes the description of the method and demonstrates its performance using the 8 TeV  $pp$  collisions data and simulation, as well as the HL-LHC simulation. The chapter is summarised in Section 3.4.

## 3.1 The Tile Calorimeter segmentation

The TileCal is a composite sampling detector. It is made of tile-shaped plastic scintillators, which are the active medium. The scintillators are interleaved with steel tiles to absorb particle showers within an adequate detector's volume. The energies deposited by incident particles in scintillators are read out. The smallest structural elements of the TileCal in which energy is measured are cells. So the pile-up noise is also studied at the cell level, which is why the TileCal cell structure must first be introduced. The structure used during the Run 1 LHC operations is reported here. The same structure is used during the Run 2 and Run 3 operations, but with minor differences associated mainly with special cells.

Starting from the largest structural elements, the TileCal consists of three large cylinders. This design was chosen to simplify the assembly and provide space for the power and services of the other detectors closest to the beam line. The central cylinder of the TileCal, Long Barrel (LB), has a length of 5.8 m and spans the pseudorapidity range of  $|\eta| < 1.0$ . Two cylinders on the sides, Extended Barrels, cover the  $0.8 < |\eta| < 1.7$  pseudorapidity range. The inner and outer radii of the cylinders are 2.28 m and 4.25 m, respectively. The instrumented part with a radius of up to 3.865 m in these modules establishes the nuclear interaction length for protons of  $7.4\lambda$  at  $\eta = 0$ . The signal readout design splits the LB into

two **partitions**, the LBA in the  $\eta > 0$  region and LBC in the  $\eta < 0$  region. The same naming scheme is used for the EBs, which make up the EBA and EBC partitions, respectively.

The TileCal cylinders are modular in design, making them easy to assemble and maintain. Each cylinder consists of 64 wedge-shaped **modules** with a width of  $\Delta\phi = 2\pi/64 = 0.098$  rad. Scintillator and absorber tiles are placed within the modules radially and perpendicular to the beamline. The light produced in scintillators by ionising particles is read out by optical fibres attached to both sides of the scintillation tile. The optical fibres route scintillating light to the detector electronics located at the outer edge of each module. Such a readout scheme results in almost seamless calorimeter coverage in azimuth.

The modules are further segmented in longitude and pseudorapidity by grouping the optical fibres connected to the scintillators into bundles. The longitudinal segmentation is necessary to establish the linearity of the energy response along the depth of the hadron showers. So there are three longitudinal **layers**, approximately  $1.5\lambda$ ,  $4.1\lambda$  and  $1.8\lambda$  thick at  $\eta = 0$ . These layers are called A, BC and D, counting from the beamline outwards. The pseudorapidity segmentation follows the transverse profile of hadron showers and exceeds the granularity of the electromagnetic calorimeter. In the TileCal it is  $\Delta\eta = 0.1$  in the first two layers and  $\Delta\eta = 0.2$  in the third layer. The segmentation results in the three-dimensional readout **cells** providing an approximately projective detector geometry. The TileCal segmentation scheme in the  $\eta > 0$  region is shown in Figure 3.1. This structure is symmetrical about the centre of the detector.

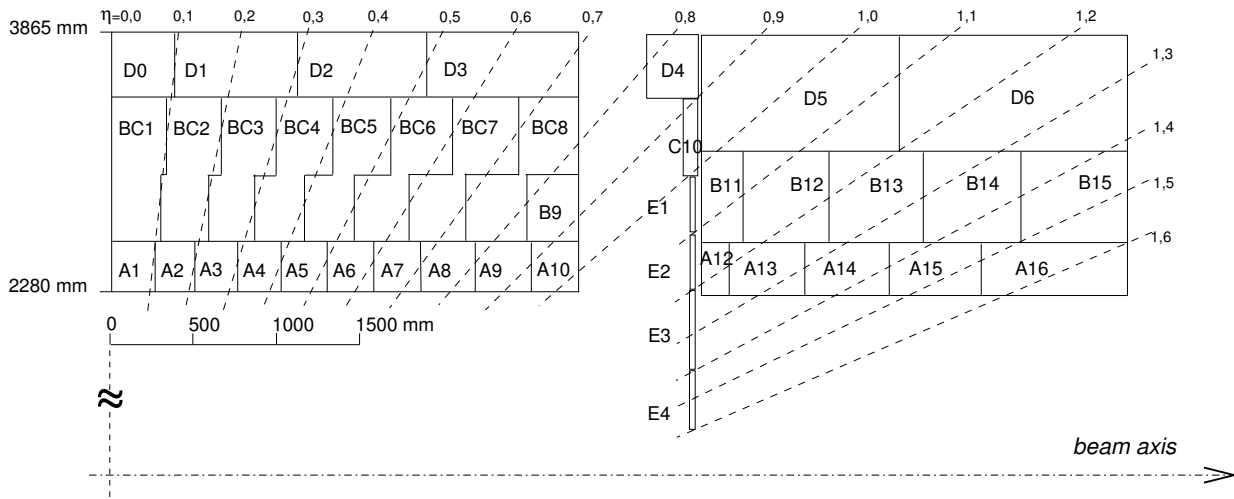


Figure 3.1 — Schematic representation of the TileCal segmentation into cells. The  $\eta > 0$  region of the detector is shown [139].

Most of the space between the LB and EBs is occupied by the services of the innermost detectors. However, there is some free space into which the fourth layer of cells is installed. This layer is called the Intermediate Tile Calorimeter

(ITC) and consists of cells D4, C10 and E1–E4. The E cells are made up entirely of scintillator material and serve primarily to assess energy losses in passive materials between calorimeter barrels. The D4 and C10 cells have a standard steel-scintillator structure in most modules. However, in some modules, the ITC cells have features, so they are called special. First, the D4 cells in four modules and C10 cells in eight modules have a reduced thickness or consist entirely of scintillator material, respectively. It should be noted that the fibres of one of the special D4 cells are coupled to the adjacent D5 cell of the EB due to the truncated readout, while the signal from the three remaining special D4 cells is read out separately. Finally, the E3 and E4 cells in eight modules are removed to free up the readout for minimum bias scintillator counters used by the trigger system [139]. It is also important to note, that this configuration was used only in Run 1, since in Run 2 the removed E cells were placed back, while their readout was combined with the adjacent E cells. All mentioned special cells are the features that exist in both gaps between the LB and EBs.

In total, there are 5182 signal readout cells in 192 TileCal modules.

## 3.2 Energy reconstruction and noise effects in the Tile Calorimeter

Energies measured in calorimeter cells are the input for jet reconstruction. However, energy measurements are often distorted by noise, which deteriorates the jet reconstruction performance. The energy reconstruction algorithm used in the TileCal mitigates the noise contribution partially. This algorithm is discussed here, along with the main noise sources.

The energy measurement starts from the light emitted by incident particles interacting with scintillators, which is transmitted to photomultipliers (PMT). The PMTs respond to the input light by a current pulse of about 18 ns full width at half maximum. The amplitude of the pulse is proportional to the deposited energy. To measure the amplitude, the pulse is shaped to a width of 50 ns, amplified and sampled by analogue-to-digital converters at the LHC bunch crossing rate of 40 MHz. Thus, seven digital samples obtained within a time window of 150 ns centred at the peak of the shaped pulse are used for cell energy reconstruction.

There are two main sources of noise that distort the pulse shape. One is the thermal noise in the detector readout electronics, electronics noise. Another is due to the overlay of energies deposited by particles from pile-up  $pp$  interactions. Although the rate of pile-up interactions is high, they mainly produce low-energy particles resulting in small energy deposits. These particles are distributed uniformly over the detector. These features allow treating the effect of energy overlays as the source of noise, referred to as the pile-up noise. The pile-up noise is further factorised into two contributions. One is due to the overlay

of energies from particles originating from the triggered bunch crossing. This is the so-called **in-time pile-up noise**. Another is due to the subsequent and consecutive bunch crossings since the shaped pulse covers several of them. This contribution is referred to as the **out-of-time pile-up noise**. As a result, the total noise is an interplay of all these components.

The cell energy reconstruction is performed using an optimal filter (OF) algorithm [141], which minimises the amplitude variance associated with noise. The choice of the algorithm is also due to the simplicity of its implementation in the detector hardware. The algorithm restores the pulse's amplitude by linearly combining digital samples. The samples are weighted using known pulse shape and noise autocorrelation matrix. Apart from the amplitude, the algorithm also computes the time phase and the amplitude's pedestal. These quantities are used in variance minimisation. As a result, the average amplitude reconstructed by the OF algorithm equals zero when no hard particles traverse the detector cells.

The reconstructed amplitude is converted to the energy deposited by particles using a set of multiplicative calibration coefficients. Most of the coefficients are evaluated using three dedicated calibration systems integrated into the TileCal. These are the caesium system probing the scintillator light yield, the laser system probing the PMT response, and the charge injection system probing the post-PMT electronics. These systems help to correct the effects of irradiation, ageing, PMT gain drift and faults in the hardware and electronics. But the main one is a coefficient correcting the energy scale. This coefficient is derived in experiments with about 1/8 of the final production calorimeter modules exposed to an electron beam [144]. So the calibration maintains the overall electromagnetic (EM) energy scale in the TileCal.

### 3.3 Pile-up noise measurement

The variance of the energies measured in the TileCal cells is not zero, although the energy reconstruction algorithm minimises it. So, there is always a probability that the measured energy is solely due to noise. When such energies enter the jet reconstruction, they deteriorate jet energy resolution. That is why noise measurements are required to identify how significant is the measured energy relative to the noise.

The electronics noise in the TileCal cells is measured under collision-free conditions. For this purpose, the energy distributions measured in each cell are used. Each energy distribution is fitted by a model that combines two gaussian distributions with different widths. A narrow gaussian distribution fits the core of the energy spectrum, while a second wide gaussian distribution fits the tails of the spectrum. As a result of the fit, the electronics noise is evaluated as an

effective width of the combined gaussians containing 68.3% of the area of the fit function [139].

In  $pp$  collisions, even without hard scattering, the width of the energy distribution measured in the TileCal cells increases due to pile-up noise. The positive tail of the energy distribution is pulled mostly by the in-time pile-up noise. Conversely, the negative tail is pulled mostly by the out-of-time pile-up noise under the influence of which the amplitude's pedestal shifted due to high activity in nearby bunch crossings can result in negative reconstructed amplitude. The pile-up noise is an interplay of these two effects, and its measurement in the TileCal is further revealed in this section.

### 3.3.1 Method of pile-up noise measurement

The pile-up noise is measured using  $pp$  collisions data that are minimally biased by the event selection. Suppose the data are selected by the trigger that does not require hard scattering events explicitly. In that case, most events are due to soft interactions, normally treated as the pile-up in the studies of hard scattering. An example of such a trigger in ATLAS is the ZeroBias trigger [135, 136]. As a result of such triggering, the energy distribution measured in the TileCal cells is still centred around zero as a feature of the energy reconstruction algorithm. However, in addition to electronics noise, the width of the energy distribution includes the pile-up noise contribution. As a result, the total noise can be expressed as

$$\sigma_{\text{total}} = \sqrt{\sigma_{\text{electronics}}^2 + \sigma_{\text{pile-up}}^2}, \quad (3.1)$$

where  $\sigma_{\text{electronics}}$  and  $\sigma_{\text{pile-up}}$  are the electronics and pile-up noise components. Thus, pile-up noise can be extracted by measuring total noise, given that the electronics noise is known.

The width of the TileCal cell energy spectrum is quantified by the standard deviation. The narrow core of the energy spectrum can still be described by the gaussian distribution, as in the case of the electronics noise measurement. However, the tails of the energy spectrum are non-gaussian, and the double gaussian fit model fails. So the standard deviation describes the total noise better.

The total noise varies with the collider luminosity, as the pile-up noise can differ. As shown in Ref. [141], the pile-up noise scales as

$$\sigma_{\text{pile-up}} = \sqrt{\frac{\mathcal{L}}{\mathcal{L}_0}} \sigma_{\text{p}0}, \quad (3.2)$$

where  $\sigma_{\text{p}0}$  is the reference pile-up noise at a given reference luminosity  $\mathcal{L}_0$ . Using this equation, the total noise at any luminosity can be calculated by measuring pile-up noise at a given luminosity, assuming a constant electronics noise.

The luminosity changes significantly during the data taking. However, conditions with stable luminosity are required for pile-up noise measurement. The LHC luminosity can be expressed as

$$\mathcal{L} = \frac{\langle \mu \rangle n_b f_r}{\sigma_{\text{inelastic}}}, \quad (3.3)$$

where  $\langle \mu \rangle$  is the average number of inelastic interactions per bunch crossing,  $n_b$  is the number of bunch pairs colliding per LHC revolution,  $f_r$  is the revolution frequency,  $\sigma_{\text{inelastic}}$  is the total inelastic cross-section. The luminosity is measured in fixed time intervals during the data-taking, so the  $\langle \mu \rangle$  averaged over the lumiblock is usually known. Within the given  $\langle \mu \rangle$ , the luminosity is assumed to be constant, which provides a stable reference for pile-up noise measurement. Since  $\langle \mu \rangle$  is averaged over lumiblock, it is sensitive to both the in-time and out-of-time pile-up noise, which makes it an advantage for the pile-up noise study over using the number of reconstructed vertices, which is less susceptible to out-of-time pile-up noise. So Equation (3.3) is parametrised as a function of  $\langle \mu \rangle$

$$\sigma_{\text{pile-up}} = \sqrt{\frac{\langle \mu \rangle}{\langle \mu_0 \rangle}} \sigma_{p0}, \quad (3.4)$$

assuming that other LHC parameters are unchanged.

The total noise measurement is affected by high-energy outliers in the Tile-Cal cell energy spectra if there are accidentally accepted hard scattering events. Thus, the pile-up noise extracted from a single measurement of the total noise can be inaccurate. To reduce the uncertainty associated with outliers, the pile-up noise is extracted from the total noise measured as a function of  $\langle \mu \rangle$ . This measurement can be performed using a single LHC run as the beam intensity decreases over time, so a range of  $\langle \mu \rangle$  is often available. Then, a function

$$\sigma_{\text{total}} = \sqrt{\sigma_{\text{electronics}}^2 + \frac{\langle \mu \rangle}{\langle \mu_0 \rangle} \sigma_{p0}^2}, \quad (3.5)$$

that describes total noise as a function of  $\langle \mu \rangle$ , is fit to the measurement results. This function is obtained by combining Equations (3.1) and (3.4). The electronics noise is known, so it is fixed in the fit. As a result, the  $\sigma_{p0}$  is a single unknown in Equation (3.5). The  $\sigma_{p0}$  obtained from the best fit provides the pile-up noise measure, which is robust against the high energy outliers.

Equation (3.5) is integrated into the ATLAS software providing the ability to calculate total noise at any luminosity when the  $\sigma_{\text{electronics}}$  and  $\sigma_{p0}$  are known. The implementation requires  $\sigma_{p0}$  that corresponds to  $\mathcal{L}_0 = 10^{33} \text{ cm}^{-2} \text{ s}^{-1}$  which is hardcoded<sup>1</sup>. That is why the pile-up noise corresponding to this luminosity is stored in the ATLAS software database.

<sup>1</sup>According to the LHC design, the luminosity of  $10^{34} \text{ cm}^{-2} \text{ s}^{-1}$  is achieved at 23 simultaneous  $pp$  interactions with  $\sigma_{\text{inelastic}}$  of about 65 mb [145]. So  $\mathcal{L}_0 = 10^{33} \text{ cm}^{-2} \text{ s}^{-1}$  corresponds to  $\langle \mu_0 \rangle = 2.3$ . In

### 3.3.2 Improving the accuracy in pile-up noise measurement using the bootstrap technique

Even though the effect of high-energy outliers in the TileCal cell energy spectra is minimised by fitting the total noise as a function of  $\langle\mu\rangle$ , an additional intermediate step is used to improve the accuracy in the pile-up noise measurement. To do this, the statistical uncertainty in the total noise measurement is evaluated using the bootstrap technique [147, 148].

The bootstrap technique is based on toy pseudo-experiments that mimic several data-taking attempts. In each pseudo-experiment, each data event is counted  $n$  times, where  $n$  is a pseudo-random number drawn from a Poisson distribution with a mean of one. Any measurement performed using the data is repeated using pseudo-experiments, so there is an ensemble of the measurement results. The standard deviation computed along this ensemble estimates the statistical uncertainty in the measurement.

The more pseudo-experiments are performed, the more accurate the estimate of statistical uncertainty. However, this requires significant computing resources. So, in many cases, a hundred pseudo-experiments are enough since a further increase in the number of pseudo-experiments does not change the results. However, a cross-check with more pseudo-experiments is a rule of thumb.

Coming back to the pile-up noise study, evaluating the statistical uncertainty improves the precision of the fit to the total noise measured as a function of  $\langle\mu\rangle$ . In particular, the improved precision is associated with a lower contribution of rare high-energy outliers, which are either suppressed or amplified in pseudo-experiments, leading to large statistical uncertainty. As a result, the total noise with large statistical uncertainty is counted with a lower weight in the fit.

### 3.3.3 Pile-up noise measurements in cells of the Tile Calorimeter

The measurement of the pile-up noise in the TileCal cells using  $\sqrt{s} = 8$  TeV  $pp$  collisions data is reported. The data were obtained in the Run 1 LHC campaign. The bunch crossing intervals are 50 ns, which is twice the design value. As a result, these data are less affected by the out-of-time pile-up. The data accepted by the ZeroBias trigger are used for the measurement. The results are compared to the simulation, which includes only soft pile-up interactions. Up to 200 simultaneous  $pp$  interactions are generated to simulate the HL-LHC conditions.

---

the case of 50 ns bunch crossing intervals in Run 1, which is twice the design value, the luminosity of  $\mathcal{L}_0 = 10^{33} \text{ cm}^{-2}\text{s}^{-1}$  corresponds to  $\langle\mu_0\rangle = 4.6$ . During Run 2, the luminosity of  $\mathcal{L}_0 = 10^{33} \text{ cm}^{-2}\text{s}^{-1}$  is assumed at  $\langle\mu_0\rangle = 2.9$  taking into account the measured  $\sigma_{\text{inelastic}}$  of about 80 mb [146].

The pile-up noise is measured in all TileCal cells. The measurement is  $\phi$  agnostic, assuming that particles from pile-up interactions are distributed uniformly across  $\phi$ , while the TileCal modules within a given partition are similar. That is, the noise is studied using cell energy spectra populated by measurements in cells of a given type, irrespective of the TileCal module. The exceptions are special cells studied separately from normal cells of the same type. Cells with failed readout, identified by the data quality monitoring, are excluded from the measurement to avoid errors associated with mismeasured energy.

The cell energy distribution is the primary input for the pile-up noise measurement. An example of such distribution is shown in Figure 3.2. This distribution is measured in cell A12, one of the most exposed cells in the TileCal. This cell experiences extreme particle flux since it is located close to the gap between detectors, so there is less dense material in front of it than in other cells. The energy distributions are measured in two  $\langle\mu\rangle$  intervals,  $\langle\mu\rangle = 20 \pm 0.5$  and  $30 \pm 0.5$ . Despite many simultaneous  $pp$  interactions, both distributions peak around zero. The width of the energy distributions increases with  $\langle\mu\rangle$  due to larger pile-up noise. The contribution of the in-time and out-of-time pile-up to the energy distribution is asymmetric, which is a feature of the energy reconstruction algorithm in the TileCal. The simulation describes positive energies above 200 MeV well, but closer to the peak, the difference reaches two times. It also tends to underestimate the negative energy tail by up to 50%. Approximately the same features are observed in energy distributions measured in other cells.

The total noise evaluated as the standard deviation of the cell energy distributions as a function of  $\langle\mu\rangle$  is shown in Figure 3.3. These are the results obtained using HL-LHC simulation. Two sets of cells are shown, one from LBA and another from EBA. Each set contains cells from the same  $\eta$  region but different layers. In all cells, the total noise increases as a function of  $\langle\mu\rangle$ . This increase is well described by Equation (3.5) up to  $\langle\mu\rangle = 200$ . In most cells, the total noise at high  $\langle\mu\rangle$  is dominated by pile-up noise since electronics noise of about 20 MeV is approximately the same in all cells and is almost independent of  $\langle\mu\rangle$ . Thus, the largest pile-up noise is in the A and E layers closest to the beam pipe. The next largest pile-up noise is the BC layer. The smallest pile-up noise is in the D layer, even though the cell size is the largest in this layer, which means larger susceptibility to the pile-up noise. However, the D layer is the farthest from the beam pipe, so particles from pile-up interactions are largely absorbed in front of it. In this layer, the total noise is mostly due to the electronics noise. The statistical uncertainties in the total noise are evaluated using the bootstrap technique with a hundred replicas, but they are small enough that they are not visible behind the markers.

The pile-up noise is derived by fitting Equation (3.5) to the total noise versus  $\langle\mu\rangle$ . In addition to the simulation, the pile-up noise is measured similarly using the data, where the  $\langle\mu\rangle$  varies between 9 and 35. The  $\sigma_{p0}$  obtained from the fits

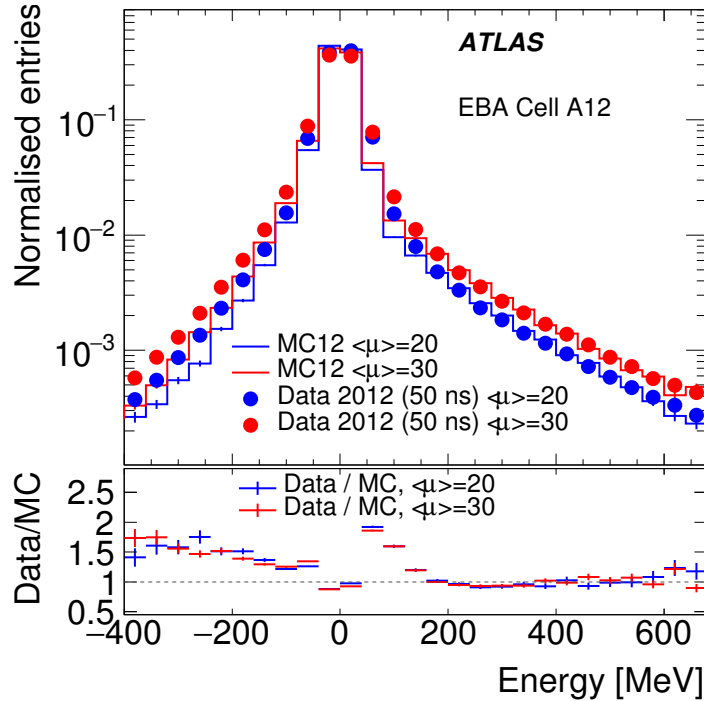
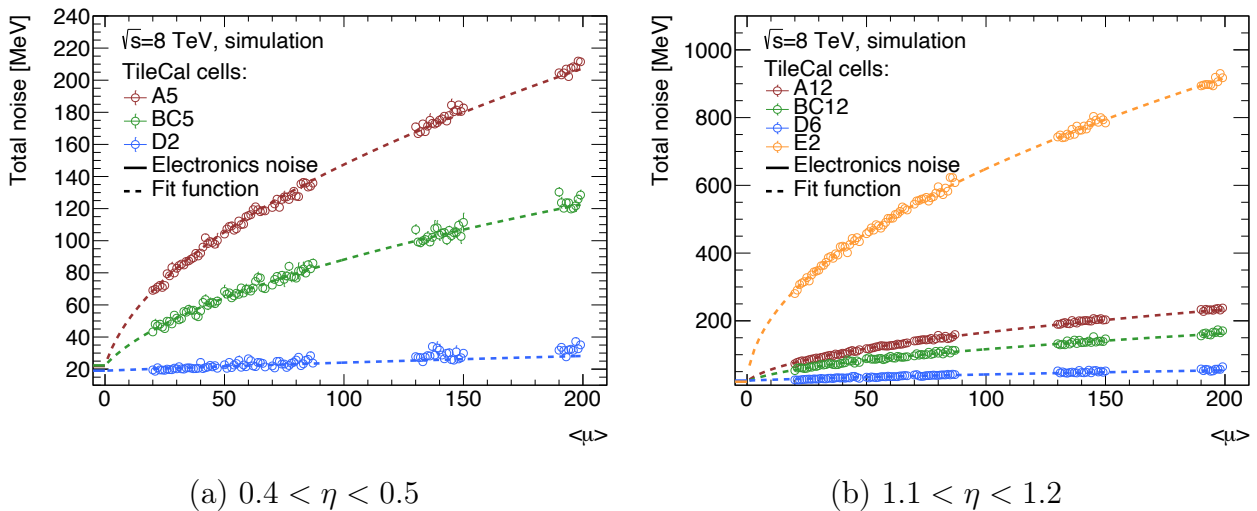


Figure 3.2 — Area-normalised energy distribution in cells A12. Markers depict data. Lines represent simulation. Different colours are used for different pile-up conditions,  $\langle\mu\rangle = 20$  (blue) and 30 (red).



(a)  $0.4 < \eta < 0.5$

(b)  $1.1 < \eta < 1.2$

Figure 3.3 — Total noise as a function of  $\langle\mu\rangle$ . Simulation with  $\langle\mu\rangle$  up to 200 is shown. Markers depict total noise in cells located in the regions (a)  $0.4 < \eta < 0.5$  and (b)  $1.1 < \eta < 1.2$ . Different colours are used for different cell layers. Dashed lines represent fits used to derive pile-up noise. Solid horizontal lines extended into the region  $\langle\mu\rangle < 0$  are used to represent electronics noise contribution.

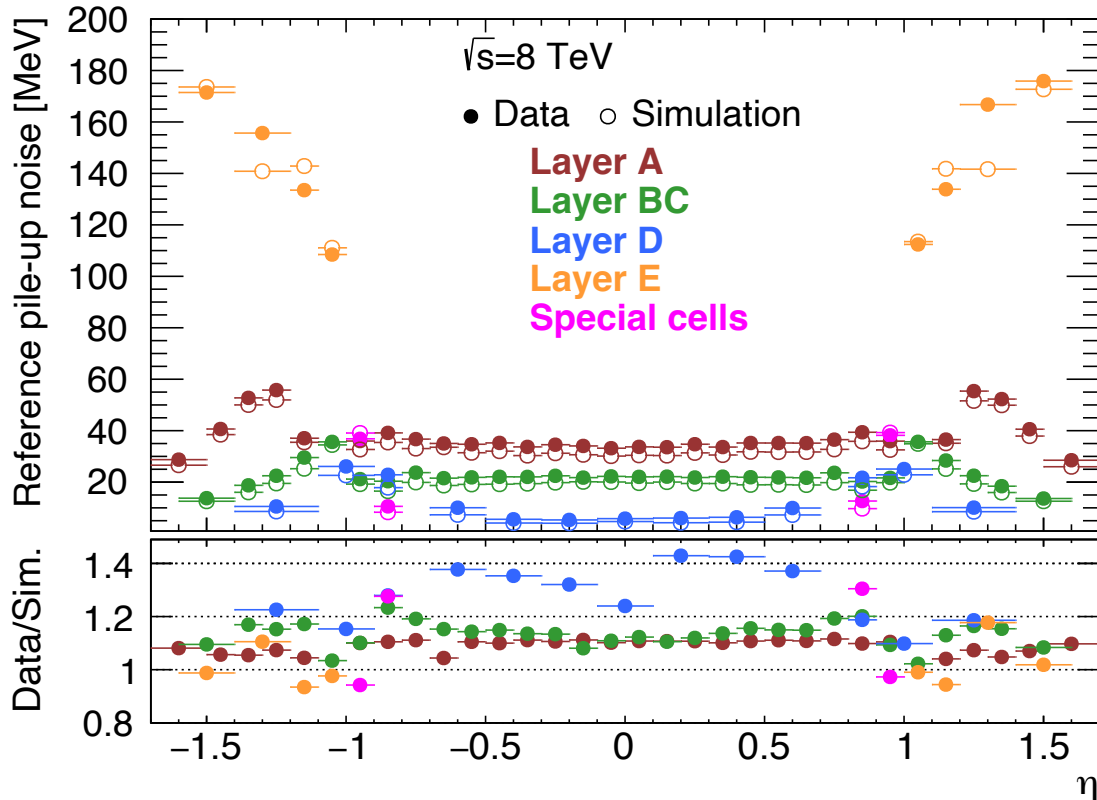


Figure 3.4 — The measured reference pile-up noise in all TileCal cells. The results are shown as a function of  $\eta$  of each cell. The reference pile-up noise corresponds to  $\mathcal{L}_0 = 10^{33} \text{ cm}^{-2}\text{s}^{-1}$ . Different colours are used for different cell layers. Closed (open) markers depict data (simulation). The lower panel shows the ratio between data and simulation.

is shown in Figure [3.4](#). The results are shown as a function of  $\eta$  corresponding approximately to the cell centre. Both the data and simulation results are shown. The measured reference pile-up noise corresponds to  $\mathcal{L}_0 = 10^{33} \text{ cm}^{-2}\text{s}^{-1}$  as required by the ATLAS software. In terms of  $\langle\mu_0\rangle$ , the measured  $\sigma_{p0}$  corresponds to  $\langle\mu_0\rangle = 4.6$ . The pile-up noise is mainly flat in the LB cells. It is about 35 MeV in the A layer, 20 MeV in the BC layer and 4 MeV in the D layer. In the EB cells near the gap between barrels, the measured noise exceeds that of the LB. It is then decreases as a function of  $\eta$  as more pile-up initiated particles are absorbed in front of the corresponding cells. This is different in the E layer, where pile-up noise increases as a function of  $|\eta|$  since the E cells with larger  $\eta$  are closer to the beam pipe. The pile-up noise is similar on both sides of the calorimeter owing to its  $\eta$ -symmetry. The simulation underestimates pile-up noise by about 10% in most TileCal cells due to a difference in the negative side of cell energy distribution. The largest difference is in the D layer, where the pile-up noise is the smallest, so it is more affected by outliers in the energy distributions.

The measured pile-up noise is loaded into the ATLAS software database and used by the jet reconstruction algorithm in the 8 TeV data.

### 3.4 Summary and outlook

Energy measurements in the TileCal cells are used to reconstruct jets in ATLAS. However, these measurements are affected by overlapping signals from low-energy particles creating pile-up noise, which increases with the LHC luminosity. The pile-up noise measurement is used to determine which energy deposits are significant compared to the noise and allows for improved jet reconstruction performance.

A method for measuring pile-up noise in the TileCal cells is presented. The method accounts for pile-up noise dependence on the collider luminosity. The method is currently the default for pile-up noise analysis in the TileCal cells. Once the pile-up noise is determined, the total noise can be calculated on an event-by-event basis for any luminosity. Such calculations estimate the total noise well up to  $\langle\mu\rangle = 200$  expected at the HL-LHC.

The pile-up noise measurement is reported using the  $pp$  collision data and simulation. The measured pile-up noise is a dominant contributor to the total noise in most TileCal cells, but its contribution decreases in the outer calorimeter layers. The measurement results are underestimated by simulation by about 10% in most of the TileCal cells, so an improved soft physics modelling is required to reduce the uncertainty in the jet energy measurement since the pile-up noise determined using the simulation is used to reconstruct jets in both the data and simulation.

# Chapter 4

## Jet energy calibration

Footprints that particles leave when they interact with the detector materials are used to identify jets. An algorithm that associates patterns in the detector signals with traces of jets is called jet reconstruction. However, the energy of the reconstructed jet often diverges from the true one. Among the reasons for that is the different nature of electromagnetic and strong interactions in the detector, detector inhomogeneity, energy losses in the passive components of the detector, and detector signal distortions due to pile-up. A calibration based on a set of corrections is used to restore the true energy of reconstructed jets. Accurate reconstruction and calibration of jets are vital ingredients of the ATLAS physics program.

The LHC experiments consistently face new challenges since the collision energy and beam intensity increase gradually. Therefore, the methods of jet reconstruction and calibration are constantly being improved. Despite the difficulties along the way, the accuracy in the jet energy measurement increases [6, 149–152]. This chapter introduces the techniques used for jet reconstruction and calibration at the beginning of Run 2, where the calibration of reconstructed jet energy against well-measured  $Z$ -bosons is studied. However, the techniques related to the cross-section measurements discussed in this thesis, that are based on the Run 1 data, are built on the same principles.

The chapter starts with an introduction to the general aspects of the jet reconstruction and calibration in the ATLAS experiment. These are the topics of Sections 4.1 and 4.2, respectively. The identification of jets originating from hard scattering is introduced in Section 4.3. Section 4.4 is dedicated to the main topic of this chapter, which is the jet energy calibration using  $Z + \text{jets}$  events. It is important to note that the calibration is performed using the same detector signature used in the cross-section measurement. Therefore, some subsections may seem overly detailed for the jet energy calibration alone, but these details are necessary to understand the cross-section measurement. Namely, these subsections are related to electron reconstruction and collision data mis-modelling. Despite this, they are integral parts of the calibration study. Finally, the chapter is summarised in Section 4.5.

## 4.1 Jet reconstruction

Jets in the ATLAS experiment are usually defined using the anti- $k_t$  [85] algorithm. The input to the algorithm is either a set of particle energy deposits reconstructed in the calorimeter or charge particle tracks reconstructed in the inner detector. The most recent approach implies using as input the combined objects made up of energy deposits and tracks [153]. But many Run 1 and Run 2 jet studies, including those in this thesis, are carried out using mainly the calorimeter data.

The jet reconstruction algorithm is designed to suppress noise contribution to the jets. Therefore, it uses clusters of topologically connected calorimeter cells, **topoclusters** [142], rather than individual cells as an input to the anti- $k_t$  algorithm. The cell clustering algorithm follows the spatial spread of the particle shower. The algorithm combines calorimeter cells with significant energy deposits relative to the total noise. The clustering starts with energy deposits four times the noise level. Cells satisfying this condition make up the topocluster seed. When all seeds are defined, the cluster expands onto adjacent cells with energy twice the total noise. The expansion proceeds iteratively in both longitudinal and lateral directions. The last step is to add an additional layer of adjacent cells to complete the topocluster. This final step allows for the retention of cells with energies about the noise level while maintaining overall noise suppression. Some topoclusters split if they include several local energy maxima. This takes into account the presence of close-by particles. Overall, the clustering algorithm follows the so-called 4-2-0 clustering scheme. There are other options, but this scheme is optimal based on the results of charged pion beam experiments with the ATLAS calorimeter prototypes [142].

The topoclusters are three-dimensional objects. It is assumed that each topocluster is a massless pseudo-particle hitting the calorimeter. The energy of a cluster is the sum of the energies of its constituent cells. The cluster direction is calculated as the energy-weighted barycentre of the cell positions about the detector centre.

The energies of calorimeter cells and hence the clusters are calibrated at the electromagnetic (EM) scale. The calibration is derived by studying the energy response of the calorimeter prototype to the electron beam. However, the ATLAS is the non-compensating calorimeter. This means that the calorimeter energy response to hadrons is smaller than to electrons. In addition, there are other sources of difference between the true energy of a particle and the energy of a cluster. Among them are particle energy losses due to finite cluster size and inactive detector materials. The local cell weighting (LCW) [142, 154] calibration is designed to correct for all these differences. A set of corrections is evaluated by simulating pion interactions in various detector regions. The corrections are applied to clusters classified as hadronic-like based on dominant energy deposits

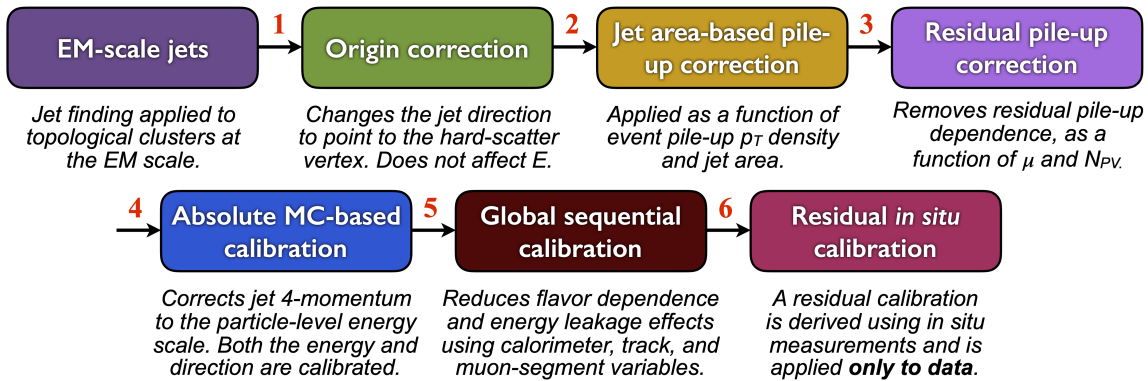


Figure 4.1 — Jet energy scale calibration scheme. Jets are calibrated sequentially. Each calibration step is numbered to be referenced along the text. The figure is taken from Ref. [6].

in different calorimeter regions. The LCW calibration leads to an improved jet energy resolution. The LCW is often used in Run 1 jet studies but slightly less often in Run 2 as almost the same effect is achieved with jet energy calibration.

The topoclusters calibrated at either the EM or LCW scale are inputs to the anti- $k_t$  jet algorithm. Only topoclusters with positive energies are used for a meaningful jet formation. The four-momenta of the jets are defined as the sum of constituting clusters four-momenta. Thanks to the underlying noise suppression, using the topoclusters instead of individual calorimeter cells improves the jet reconstruction performance. Nevertheless, jet calibration is necessary.

## 4.2 Jet calibration

Jet calibration is a prerequisite for many studies in the ATLAS experiment. The calibration brings the reconstructed jet energy scale (JES) to that of true jets. It ensures correct measurements of the average jet energy across the detector, reduces the dependence of measured jet energies on pile-up activity and equalises JES between data and simulation.

The calibration consists of a set of corrections applied sequentially to jets. The principle calibration scheme used in the ATLAS experiment is depicted in Figure 4.1. Even though it starts with jets at the EM scale, based on the topocluster's energy scale, jets built on topoclusters at the LCW scale are calibrated similarly.

The first step of the calibration is the jet origin correction. The topoclusters and hence the jets point to the detector centre when reconstructed. Thus, the jet four-vector needs a correction so that it points to the hard-scatter vertex. The hard-scatter vertex is found among many primary vertices<sup>1</sup> reconstructed using

<sup>1</sup>Primary vertices are points in space where  $pp$  interactions occur. Reconstruction of a primary vertex usually requires at least two associated tracks reconstructed in the inner detector.

charged particle tracks. The vertex with the largest sum of associated tracks transverse momenta, as measured in the inner detector, defines the hard scatter. This hard-scatter vertex is used as the jet origin. The origin correction does not change the jet energy, as the topocluster energies are unaffected.

The second and third steps subtract pile-up contribution from the jet energy. The pile-up contribution is estimated per jet on an event-by-event basis using the median  $p_T$  density [155] of jets in the event and the jet areas [156] defined in  $(y, \phi)$ -space. The event  $p_T$  density is calculated using jets defined with the  $k_t$  algorithm as it clusters more soft radiation than the anti- $k_t$ . The  $k_t$ -jets are less conical, so their area  $A$  is calculated using a fraction of simulated ghost particles of infinitesimal momentum distributed uniformly in the event. The  $p_T$  density of each  $k_t$ -jet is then defined as  $p_T/A$ . The distribution of densities is used to calculate the median  $p_T$  density per event, thus reducing the method's sensitivity to the hard-scatter activity. The median  $p_T$  density is calculated only within highly granular calorimeter regions,  $|\eta| < 2$ . Outside this region, the pile-up jets are suppressed more strongly, making the method meaningless [143]. The pile-up contribution per the anti- $k_t$  jet is calculated as a product of the median  $p_T$  density and the area of the jet. This contribution is subtracted from any reconstructed jet. However, the residual pile-up contribution, mainly to jets with  $|\eta| > 2$ , remains. To mitigate this, additional corrections parametrised in terms of  $\langle \mu \rangle$  and the number of primary vertices,  $N_{PV}$ , are derived using simulation. The corrections are evaluated as the absolute  $p_T$  difference between the reconstructed detector-level jet and its particle-level counterpart, which is insensitive to the pile-up. These corrections are considered independent of jet  $p_T$ . The derived corrections are used to subtract the residual pile-up contribution from jets.

The fourth step of the calibration restores the true energy of the reconstructed jet. This step corrects for detector non-compensation and various sources of energy loss. The correction is obtained using the jet production simulation. Isolated particle-level jets are used for calibration purposes. Only stable particles with a lifetime  $\tau$  defined by  $c\tau > 10 \text{ mm}$ <sup>2</sup>, excluding muons and neutrinos<sup>3</sup>, enter the particle-level jet definition. To derive the correction, the closest particle-level jet is matched to the reconstructed detector-level jet. That is, it is expected that the same jet is taken at different levels. The correction is then defined by the relative difference between their energies. The derived correction establishes the absolute energy scale of jets.

The reconstructed jet coordinates can be affected by poorly instrumented detector regions and variations in calorimeter granularity across the detector. For example, jet coordinates are shifted if part of their energy is missing due to detector effects since calorimeter energies are used to determine the topocluster's

---

<sup>2</sup>Particles with a lower lifetime curl up by magnetic field and do not reach the detector.

<sup>3</sup>Muons and neutrino deposit negligible energy in the calorimeter. Including these particles in the particle-level jets definition can distort the calibration if their energy deposits are poorly modelled.

directions. Such effects are most relevant to jet pseudorapidity, as the calorimeter is uniform across  $\phi$ . The contribution of these effects is corrected using the same simulated data as for the absolute energy scale correction. An  $\eta$ -correction is derived as the average difference between pseudorapidities of the matched particle-level and detector-level jets. This correction varies as the function of the jet energy and pseudorapidity relative to the detector centre,  $\eta_{\text{det}}$ <sup>4</sup>. When applied, the jet coordinates are corrected. Overall, the fourth calibration step is often called the absolute MC-based calibration, as the simulation is largely based on the Monte Carlo methods.

Detector response to jets varies due to different fragmentation of the quark and gluon-initiated jets. Those quarks and gluons that initiate jets are sometimes referred to as the source of the **jet flavour**. Gluon-initiated jets usually have a wide transverse profile of the shower and many low-energy particles. Quark-initiated showers are usually thinner, and their particles often hit the farthest calorimeter layers. Thus, a correction that accounts for the detector response variations is necessary. The correction is derived using simulation. For this, the jet energy response, defined as the relative difference between energies of matched detector-level and particle-level jets, is studied as a function of global jet properties correlated with the jet flavour. Namely, those properties that describe the longitudinal and transverse components of the jet's profile are studied. The longitudinal component is characterised by the jet energy deposits in different calorimeter layers and the number of muon spectrometer segments hit by the jet remnants. The transverse component is specified by the number of reconstructed tracks and their energy-weighted dispositions from the jet axis. The corrections are designed to remove the jet energy response dependence on the listed properties without changing the average energy of the jets. Thus, the absolute jet energy scale is unaffected. The corrections are derived sequentially, so the calibration is referred to as the Global Sequential Calibration (GSC). The corrections reduce the detector response variations associated with the jet flavour. In addition, they lower the uncertainty in the jet energy measurement and improve the jet energy resolution. The GSC is the fifth step of the calibration.

The above corrections are mostly simulation-based. Thus, it is necessary to account for the differences between the energies of jets reconstructed in data and simulation. These differences are due to response variations in different detector regions and detector non-uniformities not accounted for by the simulation. The differences can also be related to mis-modelling of hard interactions, initial and final-state radiation, parton shower evolution, hadronisation, underlying event and pile-up. Therefore, the final step of the JES calibration is designed to eliminate these differences. For this, the detector response to jets is studied *in situ*

---

<sup>4</sup>The  $\eta_{\text{det}}$  is used instead of the calibrated jet rapidity because the calibration requires a robust connection to a specific detector region.

both in data and simulation. The response is estimated by balancing the transverse momentum of a jet against that of an accurately measured reference object. The ratio between responses in data and simulation is used to derive jet energy correction.

Several *in situ* techniques are used in ATLAS. One is the  $\eta$ -intercalibration technique. It uses dijet production events to explore the pseudorapidity dependence of jet response. Jets reconstructed in a uniform, well-instrumented detector centre are used as reference objects relative to which the JES calibration in the forward regions of the detector is performed. As a result, the JES in data and simulation is equalised across  $\eta$ . This calibration is often referred to as the relative *in situ* JES.

The absolute *in situ* JES calibration follows the  $\eta$ -intercalibration. Events of the associated productions of jets and  $Z/\gamma$ -bosons are used for this purpose. The transverse momenta of the  $Z/\gamma$ -bosons are reconstructed with high accuracy from their decay products. These bosons serve as a calibration reference for jets. However, the scope of the calibration is limited since  $Z/\gamma + \text{jets}$  production cross-section decreases rapidly as the function of jets  $p_T$ . So, only jets with transverse momenta below about 1 TeV are calibrated using the  $Z/\gamma + \text{jets}$  events. Jets with higher momenta are calibrated using multi-jet production events. So, high- $p_T$  jets are calibrated against systems of well-calibrated low- $p_T$  jets. As a result, the JES in data and simulation is equalised across jet  $p_T$ .

The corrections entering the jet calibration are centrally derived in the ATLAS experiment. So, many data analyses use the same jet calibration. Most of the calibration steps but the *in situ* are applied to jets reconstructed in both data and simulation. By ATLAS convention, the *in situ* corrections are used only for jets reconstructed in data. Fully calibrated jets are referred to as EM+JES or LCW+JES jets.

### 4.3 Jet identification and pile-up jet rejection

Jets originating other than from hard scattering are usually considered to be the background. The dominant backgrounds are associated with non-collision sources and pile-up interactions. Identifying jets from hard scattering and rejecting background jets is necessary for many physics studies. This is relevant for both the jet energy calibration and jet production cross-section measurements discussed in this thesis. Thus, a brief introduction to the jet identification techniques used in the ATLAS experiment is provided.

There are various sources of the non-collision background. Among them are cosmic ray particles reaching the detector, noise bursts seeding the clusters in the calorimeter, beam-gas events due to beam interactions with residual gas along the beam pipe, and beam-halo events caused by interactions in the tertiary

collimators in the beam line far away from the ATLAS detector [150, 157]. Jet identification criteria are used to distinguish between jets from hard scattering and non-collision backgrounds. The identification is based on the quality of energy reconstruction in the calorimeter cells, topology of jet energy deposits across the detector and momenta of tracks matched to jets. There are several sets of jet identification criteria called *looser*, *loose*, *medium*, and *tight*. They are developed centrally in the ATLAS experiment. The criteria are listed in ascending order of the background rejection strength. However, this strength is achieved at the cost of decreasing hard-scatter jet selection efficiency. It is assumed that the jets whose properties do not meet the identification criteria are due to background. Such jets are usually rejected.

Another source of background is associated with pile-up interactions. These interactions produce copious jets since the jet production cross-section is large in  $pp$  collisions. The pile-up jets are predominantly soft. The pile-up jet rejection techniques rely on the precision tracking system used to determine the origin of the jets. Among the quantities used for pile-up jet rejection is the **jet vertex fraction (JVF)** [143]. The JVF is calculated for all pairs between jets and primary vertices. Tracks matched to each jet are used for this purpose. The scalar sum of the track's transverse momenta is calculated. The JVF is then calculated as the ratio, where tracks matched to a jet and associated with a given vertex make up the numerator, while all tracks matched to a jet enter the denominator. Thus, the JVF varies between zero and one. Jets with high JVF are assumed to originate from the hard scatter. The operating point at which the JVF is assumed to be high enough is optimised for the effective rejection of pile-up jets while retaining high selection efficiency for jets from hard scattering. The use of the JVF is a prerequisite in many Run 1 studies.

The JVF is developed in relatively low pile-up conditions observed at the start of the data-taking. However, the pile-up in Run 2 is higher than in Run 1, so there is some jet selection inefficiency increased as a function of  $N_{PV}$ . That is why an improved pile-up jet rejection is developed for Run 2. Essentially there are two improvements. First, an explicit  $N_{PV}$  dependence is included in the JVF denominator. Second, an additional quantity, the charged  $p_T$  fraction, is introduced, which is defined as the  $p_T$  sum of hard-scatter tracks matched to a jet and divided by jet  $p_T$ . The updated JVF and the charged  $p_T$  fraction are used to construct a likelihood-based discriminator between jets from hard scattering and pile-up, the **jet vertex tagger (JVT)**. The operating point used for discrimination is optimised such that the jet selection efficiency is above 90% at any  $N_{PV}$ .

Both the JVT and JVF have a limited scope. They are used within the tracker acceptance of  $|\eta| < 2.5$ . Apart from this, both criteria are mainly used in the low jet  $p_T$  regions to avoid inefficient selection of high- $p_T$  jets. Typically, a jet  $p_T$  threshold of 50 GeV is used. It is assumed that the contribution of pile-up

jets above this threshold is negligible in the limit of high statistics. Apart from this, the JVF and JVT are effective tools for pile-up jet rejection.

## 4.4 Jet energy calibration using $Z + \text{jets}$ events

The last step of the JES calibration is derived *in situ*. This step resolves differences between the measured and simulated jet energies, which is necessary since other calibration steps are based on simulation.

There are three different production processes used to calibrate JES *in situ* in ATLAS. These processes are the  $Z + \text{jets}$ ,  $\gamma + \text{jets}$  and multijet ones. In them, jets are produced back-to-back with the other object whose energy is well-measured. This is either the  $Z$ -boson,  $\gamma$  or a system of low- $p_T$  jet, respectively. Each of these processes has its optimal scope for JES calibration. For example, the  $Z + \text{jets}$  takes precedence over  $\gamma + \text{jets}$  for low  $p_T$  jets calibration, where the latter process suffers from more background. However, due to steeply falling cross-section, the reach of the  $Z + \text{jets}$  is limited to jets below 500 GeV, which is about half that of the  $\gamma + \text{jets}$ . Multijet events are used above the  $Z/\gamma + \text{jets}$  reach.

In this section, the JES calibration is derived using the  $Z + \text{jets}$  events. Among several techniques developed in ATLAS, the direct transverse momentum balance between a jet and a  $Z$ -boson decaying into electrons is used. The technique is introduced in Section [4.4.1](#). The electron reconstruction, energy calibration and identification are discussed in Section [4.4.2](#). The data and simulation events samples used for the calibration are defined in Section [4.4.3](#). Several corrections are used in simulated events to reduce calibration errors associated with the data mis-modelling, as discussed in Section [4.4.5](#). Selecting the  $Z + \text{jets}$  events from the data and simulation samples is the topic of Section [4.4.4](#). The calibration is then derived by measuring the direct transverse momentum balance in the data, as discussed in Section [4.4.6](#). The uncertainty in the measurement is evaluated in Section [4.4.7](#). Finally, the derived calibration is combined with the results obtained using other methods, as discussed in Section [4.4.8](#).

### 4.4.1 The direct transverse momentum balance technique

The direct transverse momentum balance (DB) technique is based on the assumption that the momenta of some final state objects balance exactly in the transverse plane. This assumption, in turn, is based on the leading order approximation in perturbative QCD, where the  $2 \rightarrow 2$  scattering leads to the production of two final state objects whose directions are back-to-back. In this approximation, the transverse momenta of the jet and a  $Z$ -boson in the  $Z + \text{jets}$  events follow the momentum conservation rule. Assuming that the  $Z$ -boson's transverse

momentum is accurately measured, the  $Z + \text{jets}$  event topology is a tool for JES calibration.

A  $Z$ -boson is a reliable reference object for the JES calibration since its transverse momentum measurement is highly precise. If the  $Z$ -boson decays into electrons, then its four-momentum is reconstructed from them. The electron energy, in turn, is measured to a sub-percent accuracy [158] due to relatively narrow electron showers and precision electromagnetic calorimeter. In addition, electrons are effectively identified from other particles by matching the calorimeter energy deposits to tracks reconstructed in the inner detector. Thus, events with detector signatures like  $Z + \text{jets}$ , which can mess up the JES calibration, are easily suppressed.

The real proton scattering is more complex than its leading order representation. The parton radiation creating additional jets in an event spoils the exact balance between a  $Z$ -boson and leading- $p_T$  jet. There are several ways to minimise the effect of additional parton radiation on the JES calibration. One is to reject events with hard sub-leading- $p_T$  jets. Another is to impose a criterion on an azimuthal angle separation between a leading- $p_T$  jet and  $Z$ -boson per event to ensure they are back-to-back. Finally, the component of the  $Z$ -boson's  $p_T$  perpendicular to the jet axis is ignored by defining the reference

$$p_T^{\text{ref}} = p_T^Z \times |\cos \Delta\phi(Z, \text{jet})|, \quad (4.1)$$

where the  $\Delta\phi(Z, \text{jet})$  is the azimuthal angle between the  $Z$ -boson and jet. In this notation, the jet response defined as the  $p_T^{\text{jet}}/p_T^{\text{ref}}$  is used for the JES calibration purposes.

There are other causes of the transverse momentum imbalance between the jet and  $Z$ -boson. Among them is the uncertainty in the electron energy measurements, the energy carried away by particles outside of the jet cone (OOC), and the additional energy due to particles originating from underlying event and pile-up. These effects are difficult to minimise. This is why the DB technique is used only to correct the differences between the average jet response in data,  $\langle p_T^{\text{jet}}/p_T^{\text{ref}} \rangle_{\text{data}}$ , and simulation,  $\langle p_T^{\text{jet}}/p_T^{\text{ref}} \rangle_{\text{sim}}$ , rather than correcting the measured jet response itself. So that the correction is derived as

$$c = \frac{\langle p_T^{\text{jet}}/p_T^{\text{ref}} \rangle_{\text{data}}}{\langle p_T^{\text{jet}}/p_T^{\text{ref}} \rangle_{\text{sim}}}. \quad (4.2)$$

The  $c$  is inverted to calibrate the JES in the data [159].

The JES calibration depends on the jet  $p_T$ . This dependence is accounted for by deriving the calibration as a function of  $p_T^{\text{ref}}$ , which is more reliable than the uncalibrated jet  $p_T$ . The derived calibration is then reparametrised to a function of  $p_T^{\text{jet}}$  by mapping the average  $p_T^{\text{ref}}$  to the average  $p_T^{\text{jet}}$  using the data so that it better represents the mismeasured jet to which the calibration should be applied.

## 4.4.2 Electron reconstruction, energy calibration and identification

The JES calibration derived using the  $Z + \text{jets}$  events is based on an accurate measurement of the  $Z$ -boson momentum, which is determined by the momentum of the electrons<sup>5</sup> it decays into. Electrons are also used in the  $Z + \text{jets}$  cross-section measurements presented in this thesis. Therefore, an overview of electron reconstruction and energy scale calibration techniques is provided. In addition, techniques used to identify prompt electrons, like those produced in a  $Z$ -boson decay, from electrons originating from various background sources, like from photon conversions, are discussed. The discussions are mainly based on the techniques used at the beginning of Run 2 [158, 160]. However, the techniques used in the Run 1 are built on the same principles [161–163].

The studies discussed in this thesis use electrons reconstructed in the precision central detector region,  $|\eta| < 2.5$ . This region corresponds to the acceptance of the inner detector and high segmentation of the electromagnetic calorimeter. The reconstruction of electrons starts from energy deposits in the calorimeter cells. First, a sliding-window algorithm [164] scans the electromagnetic calorimeter volume to seed three-dimensional clusters. The window has a size of  $3 \times 5$  in units of  $0.025 \times 0.025$  in  $\eta$ - $\phi$  space, which is optimised to the electron shower width. The seed clusters are required to have the sum of energies in the constituent calorimeter cells greater than 2.5 GeV. Then, an electron candidate is reconstructed if the cluster is matched to at least one track originating from the primary vertex. The energy of the reconstructed electron candidate is given by the energy of a cluster that is enlarged to a size of  $3 \times 7$  ( $5 \times 5$ ) in  $\eta$ - $\phi$  space in the central (endcap) electromagnetic calorimeter. This is done to account for the electromagnetic shower shape difference across the calorimeter. The  $\eta$  and  $\phi$  coordinates of a reconstructed electron candidate are taken from the matched track.

A multistep calibration is used to correct the energy scale of reconstructed electrons to that of the true electrons. The calibration starts by equalising the energy scale between the data and simulation layer-by-layer in the calorimeter to account for the miscalibration of the calorimeter readout electronics. In addition, the electron energy variations due to pile-up are eliminated in data cell-by-cell by computing the average expected pile-up contribution as a function of bunch position in a train. A residual pile-up contribution obtained using the data selected by the random event trigger as a function of  $\langle \mu \rangle$  is corrected for at the cluster level. These corrections are followed by the simulation-based cluster energy correction that accounts for energy lost in the material upstream of the electromagnetic calorimeter, outside the cluster and behind the electromagnetic

---

<sup>5</sup>Electrons and positrons are collectively referred to as electrons. This is done so because of the similarity in most of their properties, except for the charge.

calorimeter. Then, a correction is used that accounts for the non-uniformity of the cluster energy response due to high-voltage inhomogeneities throughout the detector volume, high-voltage variations over time, and differences in the size of the interelectrode gap, which increases at the edges of the electromagnetic calorimeter modules. This correction is obtained using the ratio between the cluster's energy and the electron track's momentum. Finally, the absolute energy scale of reconstructed electrons is adjusted *in situ* so that the  $Z \rightarrow ee$  mass distributions in the data better match the simulation.

The identification of electrons originating from prompt decay of particles such as the  $Z$ -boson rather than from various background sources, such as photon conversions, jets that mimic the signature of prompt electrons, and semileptonic heavy-hadron decays, is a prerequisite of many studies. The likelihood-based identification is used in ATLAS for this purpose. A likelihood-based discriminant is obtained for each electron candidate using the information from the calorimeter and inner detector. This information includes the probability density functions of energy deposited in various calorimeter layers, lateral energy distribution within the cluster, number of hits in the inner detector per electron track and the track-to-cluster matching properties. These functions are evaluated separately for prompt and background electrons using the simulation. The prompt electron is identified if the value of the discriminant exceeds a given operating point. There are several operating points, such as *very loose*, *loose*, *medium* and *tight*. They are listed in ascending order of the background rejection strength but descending electron selection efficiency. So that various analysis needs are covered. These operating points are designed so that the electrons that satisfy each subsequent one make up a subset of those selected by the previous.

The background suppression can be improved by using electrons isolated from nearby activity. This is particularly relevant for suppressing the backgrounds due to jets and heavy-hadron decays, which are characterised by a dense environment around the reconstructed electron. So, the non-isolated electrons are assumed to originate from the background. The isolation is quantified by other energy deposits or tracks within a cone of a typical size  $\Delta R = 0.2$  around that of the electron. Using too high isolation to suppress all backgrounds is disadvantageous because it reduces the true electron selection efficiency. For example, low-energy electrons are usually less isolated than more energetic ones due to the greater fractional contribution of other energies and tracks around the electron. Therefore, several isolation operating points are developed in ATLAS. Most of them imply a flexible isolation threshold. The *Loose* operating point is designed to ensure that the selection efficiency is uniform in electron energies and pseudorapidities and exceeds 98%. The *Gradient* operating point improves the background rejection strength, but the selection efficiency threshold is reduced to 90%. The uniformity in the electron pseudorapidity is still required. Finally, the *Fixed* operating point implies a fixed isolation threshold resulting in the best

background suppression. However, the cost of this is the lowest selection efficiency among other operating points. The use of isolation is optional in many studies.

### 4.4.3 Collision data and simulated events used for jet energy calibration

The transverse momentum balance between the jet and a  $Z$ -boson is measured using the  $\sqrt{s} = 13$  TeV  $pp$  collisions data collected during the 2015 and 2016 data-taking campaigns. Two data samples are studied separately from each other, resulting in independent sets of the JES calibrations.

Collision data are pre-selected using triggers requiring events with electrons. The triggers imply minimum selection criteria applied to electrons to match the finite bandwidth of the data acquisition system and storage capabilities. These criteria differ in the 2015 and 2016 data pre-selection due to different instantaneous luminosity and pile-up conditions.

The high-level triggers used for event pre-selection are seeded by the L1 triggers. The L1 triggers require events with electron candidates reconstructed in the precision central detector region of  $|\eta| < 2.5$ . The event acceptance rate is optimised by requiring electron candidates with an  $\eta$ -dependent energy threshold, so the variation of the electron energy scale across the detector is considered. The electron candidates with the hadronic calorimeter energy deposits exceeding 1 GeV are assumed to be background-like and rejected. Apart from rejecting background electrons, the latter criterion helps to maintain a high event acceptance rate at a lower electron energy threshold.

The 2015 data are pre-selected with a high-level trigger requiring at least one reconstructed electron. The optimal event recording rate is reached when the electron satisfies the *medium* identification operating point and has energy exceeding 24 GeV.

The 2016 data-taking is carried out at a much higher luminosity and pile-up conditions. Thus, the same event recording rate would require triggering events with higher electron energies. To avoid increasing the energy threshold, a trigger requiring at least two electrons per event is used. This requirement also rejects more events with background electrons. As a result, the trigger accepts events if two electrons satisfy the *very loose* operating point and have energy exceeding 17 GeV.

The studies are performed using the data certified by quality monitoring. These data are pre-selected using events that satisfy the GRL.

The  $Z + \text{jets}$  simulation required for the JES calibration is performed centrally by ATLAS. The simulation follows each data-taking campaign individually to account for different pile-up conditions.

The baseline simulation is based on events generated using the POWHEG-BOX v. 2.0 [74, 75, 165] that is accurate to the next-to-leading order (NLO) in perturbative QCD. The predictions are convolved with the CT 10 [166] PDF set. The POWHEG predictions are supplemented by parton showers from PYTHIA8 [62]. The simulation parameters of the parton showering, underlying event and hadronisation are set according to the AZPHINLO [167] set. Overall, this sample of events is referred to as the POWHEG+PYTHIA.

An alternative sample of events necessary for the systematic uncertainty evaluation is generated using the SHERPA v. 2.1 [68]. These predictions incorporate multi-leg  $2 \rightarrow N$  matrix elements calculations with up to 4 partons in the final state. The default SHERPA parton showering and event tune are used to evolve partons to the final state particles. As a result, using the SHERPA predictions in the JES studies allows taking into account the differences in both the hard scattering and parton shower modelling, as well as in the hadronisation and underlying event.

Pile-up effects in both samples are modelled by the soft jet production in inelastic  $pp$  scattering events generated using PYTHIA8 with the A2 [168] tune. These events are overlaid onto the generated  $Z + \text{jets}$  events. The number of pile-up events is drawn from a Poisson distribution around the average number of interactions per bunch crossing in the data. The out-of-time pile-up effects are also modelled following the LHC's bunch train structure.

The detector-level predictions are obtained by propagating the generated events through the ATLAS detector simulation based on the GEANT4 [138] program.

#### 4.4.4 $Z + \text{jets}$ event selection

The data pre-selected by the triggers contain many events other than  $Z + \text{jets}$ . These events must be rejected to allow for the study of the direct transverse momentum balance between the jet and a  $Z$ -boson decaying in the electron channel. In addition, the DB technique requires that the leading- $p_T$  jet and the  $Z$ -boson are produced back-to-back to minimise the effect of additional parton radiation. The event selection is designed to meet these requirements.

The event selection starts by rejecting events associated with the non-collision background. These events are identified by the absence of any reconstructed primary vertex compatible with the beam spot. The vertices are reconstructed by extrapolating the charge particle tracks reconstructed in the inner detector. At least three reconstructed tracks are expected in the  $Z + \text{jets}$  events. Namely, two tracks of electrons and one of a jet. The reconstructed tracks with  $p_T$  less than 1 GeV are not considered due to sub-optimal reconstruction and high mis-modelling under high pile-up conditions of the Run 2. Events missing a primary vertex with at least three associated tracks are rejected. If there are several

primary vertices, the one with the largest sum of associated tracks  $p_T$  defines the hard scatter.

The electron selection requirements imply two reconstructed electrons with opposite charges per event. Fully calibrated electrons are used. The electron kinematics must be in the region of high trigger efficiency to avoid the associated measurement errors. That is, electrons with  $p_T > 25$  GeV and  $|\eta_e| < 2.47$  are required. In addition, electrons reconstructed in the detector transition region of  $1.37 < |\eta_e| < 1.52$ , where the accuracy of measuring the electron energy degrades, are rejected. The reconstructed electrons must satisfy the *medium* [160] identification and *Gradient* [160] isolation operating points to avoid backgrounds associated with non-prompt particle decays, discussed in Section 4.4.2. To minimise other backgrounds, such as the  $Z \rightarrow \tau\tau$ , dibosons,  $W$ +jets, multi-jet and top-quark productions, that result in the  $Z$ +jets-like detector signatures when there are misidentified or undetected electrons, a requirement for the electron pair invariant mass is used, so that it is within the  $66 \text{ GeV} < m_{ee} < 116 \text{ GeV}$  window, in which the  $Z$ -boson decays predominate. A stronger requirement of  $80 \text{ GeV} < m_{ee} < 116 \text{ GeV}$  is used when analysing the 2016 data, thanks to larger statistics, so that the purity of the  $Z$ +jets sample improves.

At least one reconstructed jet is required per event. Jets are calibrated with all steps up to the absolute *in situ* calibration, which is being derived in this study. The detector performance for jets other than in the  $p_T > 10$  GeV and  $|y_{\text{jet}}| < 4.5$  region is considered sub-optimal, so they are rejected. Jets associated with a non-collision background are rejected using the *medium* jet identification operating point [150, 157]. Jets originating from pile-up are rejected using the JVT, whose operating point above 0.59 is required. To avoid the selection inefficiency associated with the JVT, it is used only for jets within the  $p_T < 60$  GeV and  $|y_{\text{jet}}| < 2.4$  region, beyond which the contribution of pile-up jets is considered low. Finally, jets reconstructed in the vicinity of electrons are rejected to avoid their energy overlap. Namely, only jets with  $\Delta R(\text{jet}, e) > 0.35$  are used in the study.

Some additional requirements apply to the first two highest- $p_T$  jets, **jet1** and **jet2**, to minimise the effect of additional parton radiation affecting the DB measurements. First, events with the  $\Delta\phi(Z, \text{jet1}) > 2.8$  rad are required to ensure that the  $Z$ -boson and **jet1** are back-to-back. Secondly, the **jet2**  $p_T$  should not exceed the maximum between 15 GeV and  $0.1 \times p_T^{\text{ref}}$  to ensure that the balance between the  $Z$ -boson and **jet1** is not spoiled by hard parton radiation. Numerically, both of these criteria are compromises between the sample statistics and the strength of parton radiation suppression. Finally, the  $|\eta_{\text{det}}^{\text{jet1}}| < 0.8$  is required to ensure that the jet being calibrated is within the most precise central detector region. This is necessary because these central jets are used to calibrate the forward ones by the  $\eta$ -intercalibration.

All criteria used for the  $Z$ +jets event selection are summarised in Table 4.1.

Table 4.1. — The  $Z + \text{jets}$  event selection criteria.

Object	Selection criteria
Vertex	$N_{\text{tracks}} \geq 3$ $p_{\text{T}}^{\text{tracks}} > 1 \text{ TeV}$
Electrons	$N_{\text{e}} = 2$ identification = <i>medium</i> isolation = <i>Gradient</i> excluded region: $1.37 <  \eta_{\text{e}}  < 1.52$ $p_{\text{T}}^{\text{e}} > 25 \text{ GeV}$ , $ \eta_{\text{e}}  < 2.47$ $66 (80) \text{ GeV} < m_{\text{ee}} < 116 \text{ GeV}$
Jets	$N_{\text{jets}} \geq 1$ identification = <i>loose</i> $p_{\text{T}}^{\text{jet}} > 10 \text{ GeV}$ , $ y_{\text{jet}}  < 4.5$ $\text{JVT} > 0.59$ if $p_{\text{T}}^{\text{jet}} < 60 \text{ GeV}$ and $ y_{\text{jet}}  < 2.4$ $\Delta R(\text{jet}, \text{e}) > 0.35$
Jet1	$ \eta_{\text{det}}^{\text{jet1}}  < 0.8$ , $\Delta\phi(Z, \text{jet1}) > 2.8 \text{ rad}$
Jet2	$p_{\text{T}}^{\text{jet2}} < \max(15 \text{ GeV}, 0.1 \times p_{\text{T}}^{\text{ref}})$

## 4.4.5 Reducing the effect of collision data mis-modelling

Simulation is widely used in the ATLAS experiment. For example, it helps to interpret the results of measurements and searches. Also, the simulation is necessary for the JES calibration. These tasks require high-quality data modelling since the mis-modelling generates measurement errors. For example, the mis-modelling leads to overcorrected data in the absolute *in situ* JES calibration. The cross-section measurements are also affected since the simulation is used to correct the detector effects distorting the measurements. That is why the simulation is often adjusted to data to minimise the effect of mis-modelling. The quantities that bring the greatest improvement are usually studied first. Among them are the quantities describing the pile-up activity, detector efficiencies and resolution. Reducing their mis-modelling is the topic of this section. Improvements in the modelling of the detector efficiencies and resolution are discussed in the context of electrons since those of jets are considered to be well-modelled.

### 4.4.5.1 Reducing the effect of pile-up conditions mis-modelling

Pile-up events are often generated separately from the hard scattering. This is a prerequisite for the effective use of computing resources. Once generated, pile-up events are overlaid onto each hard-scatter event following the average pile-up activity in data. However, pile-up activity in a sub-sample of data that is studied may differ from that used for overlays. Therefore, a correction is used to equalise

the simulated  $\langle\mu\rangle$  distribution with the actual data. This is done by assigning the generated events a  $\langle\mu\rangle$ -dependent multiplicative event weight calculated as

$$\omega_{\text{pile-up}} = \frac{\mathcal{L}_i/\mathcal{L}}{N_i/N}, \quad (4.3)$$

where  $\mathcal{L}_i/\mathcal{L}$  ( $N_i/N$ ) is the fraction of the integrated luminosity in the data (the sum of the generator event weights in simulations) in the given bin  $i$  of the  $\langle\mu\rangle$  distribution.

The  $\langle\mu\rangle$  distributions in the data and simulation are similar after reweighting events. However, the differences remain in  $N_{\text{PV}}$  distributions, also characterising pile-up activity. This is due to the different sensitivity of  $\langle\mu\rangle$  and  $N_{\text{PV}}$  to the in-time and out-of-time pile-up effects. The difference between the data and simulation in  $N_{\text{PV}}$  distribution is reduced by scaling the  $\langle\mu\rangle$  in each generated event by an empirically determined factor of 1.09. Such a scaling improves the agreement with data in  $N_{\text{PV}}$  distribution but introduces a slight mismatch in that of  $\langle\mu\rangle$ .

#### 4.4.5.2 Reducing the effect of electron reconstruction, identification, isolation and trigger efficiencies mis-modelling

The ability to effectively reconstruct prompt electrons, identify and isolate them from various background sources, and trigger electrons during data-taking is a prerequisite of many measurements. The corresponding algorithms are designed to be highly efficient for most of the electrons with different kinematics. Still, full efficiency within the phase space defined by the event selection requirements is rarely reached. The total electron efficiency is factorised as

$$\epsilon_{\text{total}} = \epsilon_{\text{reco}} \times \epsilon_{\text{id}} \times \epsilon_{\text{iso}} \times \epsilon_{\text{trig}}, \quad (4.4)$$

where the multipliers are the electron reconstruction, identification, isolation and trigger efficiencies, respectively. It is desirable that the detector simulation models the observed electron efficiency well to avoid measurement error. Since this is not always the case, corrections are used to minimise the effect of mis-modelling on the measurements.

The electron efficiencies are measured using the  $Z$  and  $J/\psi$  production data, where two electrons are produced. The tag-and-probe technique [160] is used for this purpose. In this technique, one of the decay electrons must meet strict selection criteria, while the second is a probe for measuring the efficiency. The efficiencies are evaluated as the fraction of probe electrons satisfying the tested criteria. The results are compared to the simulation.

The differences between the observed and simulated electron efficiencies are eliminated by assigning a multiplicative event weight to each generated event.

The event weight is calculated as

$$\omega_{\text{efficiency}} = \frac{\epsilon_{\text{reco}}^{\text{data}}}{\epsilon_{\text{reco}}^{\text{sim}}} \times \frac{\epsilon_{\text{id}}^{\text{data}}}{\epsilon_{\text{id}}^{\text{sim}}} \times \frac{\epsilon_{\text{iso}}^{\text{data}}}{\epsilon_{\text{iso}}^{\text{sim}}} \times \frac{\epsilon_{\text{trig}}^{\text{data}}}{\epsilon_{\text{trig}}^{\text{sim}}}, \quad (4.5)$$

where  $\epsilon_i^{\text{data}}$  and  $\epsilon_i^{\text{sim}}$  are the corresponding efficiencies in the data and simulation. This weight is normally close to one. Using this event weight in the simulation improves the data modelling.

#### 4.4.5.3 Reducing the effect of electron energy resolution mis-modelling

The electron energy resolution is often underestimated in simulation due to simplified detector descriptions. The differences between the resolution in the data and simulation are the subject of improvement so that the mis-modelling does not propagate to the measurement results.

The electron energy resolution is measured in test-beam experiments using the ATLAS calorimeter prototypes [169] and validated in different data-taking campaigns using the  $Z \rightarrow ee$  [158]. The observed electron energy resolution is usually modelled up to a Gaussian constant term  $c$ . As a result, the observed resolution,  $\mathcal{R}^{\text{data}}$ , can be represented as

$$\mathcal{R}^{\text{data}} = \mathcal{R}^{\text{sim}} \oplus c, \quad (4.6)$$

where  $\mathcal{R}^{\text{sim}}$  is the simulated electron energy resolution. The  $\oplus$  sign denotes the sum in quadrature. The  $c$  is  $\eta$ -dependent due to differences in the detector segmentation. The  $c$  is derived by minimising the differences in  $Z \rightarrow ee$  invariant mass distribution between the data and simulation [158]. The derived  $c$  is used to improve the data modelling.

The differences between the observed and simulated electron energy resolution are eliminated by smearing the reconstructed electron energy in the simulation. To do this, the electron energy is scaled event-by-event by a factor drawn from Gaussian distribution with a mean of one and a standard deviation of  $c$ . This increases the electron energy resolution, so the agreement with the data improves.

#### 4.4.6 The direct balance measurement

The  $Z + \text{jets}$  DB measurement using the 2016 data is discussed in this section. A similar measurement, published in Ref [6], is performed using the 2015 data, where the statistics are much lower, so the results are less illustrative. Despite this, the results of both studies are mainly similar.

The transverse momentum balance between a  $Z$ -boson and the jet is measured as a function of  $p_{\text{T}}^{\text{ref}}$ , which is proportional to the  $Z$ -boson's transverse

momentum. The measurement is performed using the  $p_T^{\text{ref}}$  above 17 GeV, where the associated jets are reconstructed efficiently enough [149], so the average jet response is evaluated reliably. The  $Z + \text{jets}$  production cross-section falls steeply as a function of  $p_T^{\text{ref}}$ , so the measurement is statistically limited by the  $p_T^{\text{ref}}$  of 500 GeV. This  $p_T^{\text{ref}}$  range is split into 13 regions, whose sizes are optimised for uniform statistics in the data.

The DB technique implies evaluating the average jet response,  $\langle p_T^{\text{jet}}/p_T^{\text{ref}} \rangle$ , in each of the  $p_T^{\text{ref}}$  regions. The jet response distributions obtained in the regions of low and intermediate  $p_T^{\text{ref}}$  are shown in Figure 4.2. Only simulated distributions are shown as the data is less illustrative due to fewer statistics, but the shape is the same in both cases. The purpose is to demonstrate the asymmetry that complicates decreasing the  $p_T^{\text{ref}}$  threshold used in the measurement. This asymmetry is due to a lack of low  $p_T$  jets. The asymmetry decreases as a function of  $p_T^{\text{ref}}$  so that the distribution becomes almost Gaussian at some point. To derive the average jet response, a fitting is used that takes into account the features of the distributions. The fit is preferable to the arithmetic mean, which is sensitive to the effect of soft parton radiation on the tails of the distributions. The fitting is performed using the Poisson distribution function extended to non-integer values [150, 151], that describes the shape of the jet response distribution well. In addition, this function captures asymmetries at low- $p_T^{\text{ref}}$  regions and behaves Gaussian-like at high- $p_T^{\text{ref}}$  regions. The fitting range is limited to twice the spread of the distributions to minimise the effect of the data mis-modelling at the tails. At low- $p_T^{\text{ref}}$  regions, this range is truncated by the linear turn-on function that reduces the effect of the asymmetry when computing the average. As a result, the fit is robust across all  $p_T^{\text{ref}}$  regions. The mean value derived from the fit is used for the JES calibration.

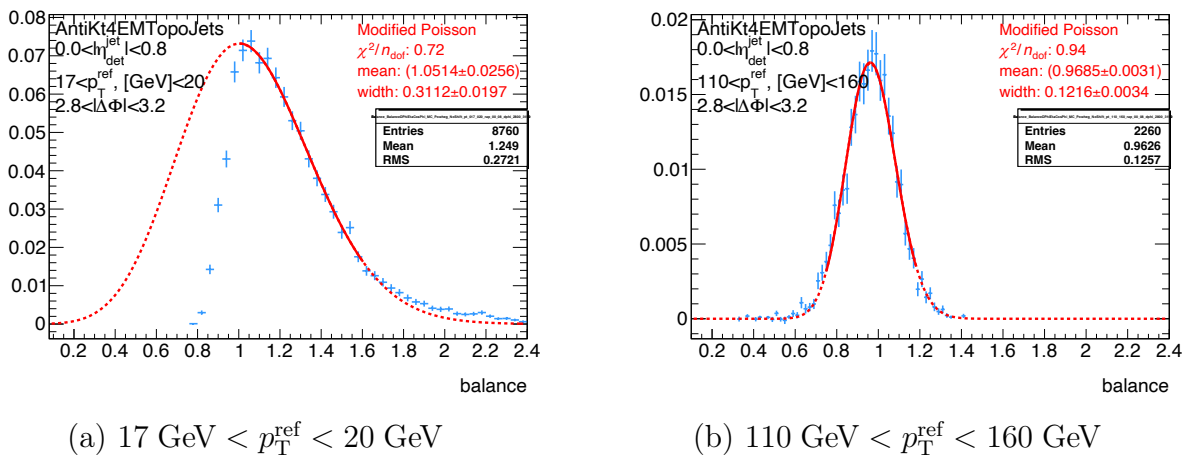


Figure 4.2 — Jet response distributions at a) low and b) intermediate  $p_T^{\text{ref}}$ . The distributions are obtained using simulation. The dashed red line represents the functions fitted to the jet response to derive the average. The function is represented by a solid red line in the range used for fitting.

The average jet response obtained as a function of  $p_T^{\text{ref}}$  is shown in Figure 4.3. The results are generally below one since part of the jet energy is usually carried by particles that are outside the jet cone. The fraction of energy outside the jet cone decreases with jet  $p_T$ , as the particles making up jets are collimated more strongly, that is why the jet response improves as a function of  $p_T^{\text{ref}}$ . The behaviour is different in the  $p_T^{\text{ref}} < 30$  GeV region, where the average jet response is shifted towards larger values due to the asymmetry in the jet response distribution. Despite this, the simulation reasonably models the features observed in the data, so the JES correction is derived as the ratio between the data and simulation. The JES correction is about 7% at low- $p_T^{\text{ref}}$  regions and 2% at high- $p_T^{\text{ref}}$  ones.

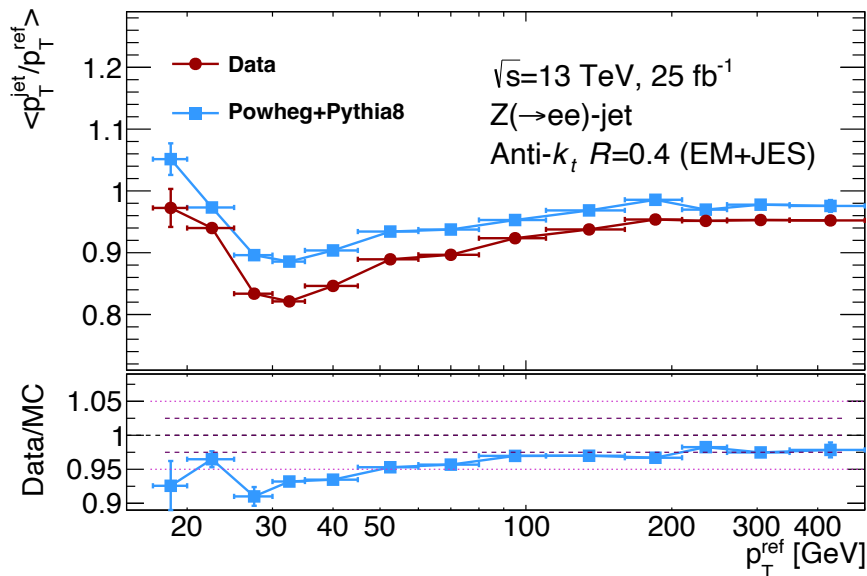


Figure 4.3 — Jet response as a function of  $p_T^{\text{ref}}$ . The data and simulation are shown in colour. The lower panel shows the ratio between them, that determines the JES correction.

The derived corrections are reparametrised to a function of  $p_T^{\text{jet}}$ , which better represents jets to be calibrated. To do this, the average jet  $p_T$  is computed in each  $p_T^{\text{ref}}$  region. The ratios between the average jet  $p_T$  and the average  $p_T^{\text{ref}}$  in data are used as conversion factors from  $p_T^{\text{ref}}$  to  $p_T^{\text{jet}}$ . These ratios are shown in Figure 4.4. The  $\langle p_T^{\text{jet}} \rangle$  is larger than  $\langle p_T^{\text{ref}} \rangle$  by about 25% at low- $p_T^{\text{ref}}$  region and by 5–10% lower at high- $p_T^{\text{ref}}$ . The  $\langle p_T^{\text{jet}} \rangle / \langle p_T^{\text{ref}} \rangle$  dependence on  $p_T^{\text{ref}}$  is reasonably well modelled, while the differences are mostly consistent with the miscalibration. As a result, the  $p_T^{\text{ref}}$ -to- $p_T^{\text{jet}}$  conversion narrows the derived JES calibration validity range.

The derived corrections are combined with the results obtained using other *in situ* techniques before being used for the final JES calibration.

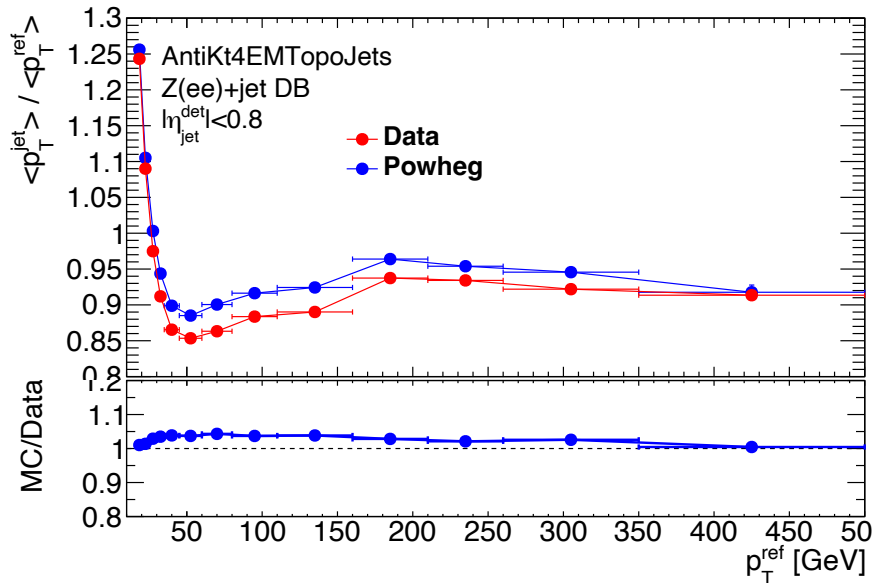


Figure 4.4 — Relationship between the average  $p_T^{\text{jet}}$  and average  $p_T^{\text{ref}}$  as a function of  $p_T^{\text{ref}}$ . Data and simulation are shown in colours. The lower panel shows the ratio between them.

#### 4.4.7 Systematic uncertainty evaluation

The DB technique is approximate. It incorporates several assumptions that are sources of systematic uncertainty. Evaluating this uncertainty is essential to ensure the reliability of the calibration.

There are several sources of systematic uncertainty. Each uncertainty is evaluated by introducing variations in the direct balance measurement. Deviations from the nominal JES correction are used to estimate uncertainties unless otherwise stated. The description of uncertainty sources and variations used to estimate the uncertainty is the topic of this section.

The data and simulation samples used for the calibration are statistically limited. So some uncertainties are due to fluctuations rather than systematic effects. To determine whether the systematic uncertainty is significant, estimating its statistical component is necessary. The statistical components are evaluated using the bootstrap technique, see Section [3.3.2](#). To do this, a set of pseudo-calibrations is derived using pseudo-experiments with the data and simulation. Systematic uncertainties are then evaluated for each pseudo-calibration. As a result, each systematic uncertainty source is described by a set of deviations from the nominal calibration. A standard deviation calculated along them quantifies the statistical component of a given systematic uncertainty. A systematic uncertainty is considered significant if it is twice the corresponding statistical component.

Systematic uncertainties experiencing large fluctuations are often over or underestimated. Besides that, their statistical components are counted multiple times when evaluating total uncertainty. Therefore, a reduction of these compo-

nents is necessary. To do this, adjacent  $p_{\text{T}}^{\text{ref}}$  regions are iteratively combined if necessary until the associated systematic uncertainty becomes statistically significant or until all regions have been merged. All systematic uncertainties are then quoted in the original  $p_{\text{T}}^{\text{ref}}$  regions but with the values defined by the combined ones.

#### 4.4.7.1 Inaccuracy in the electron energy measurement

Electrons are used for the  $Z$ -boson four-momentum reconstruction. However, the electron energy is measured with uncertainty. Although the electron energy scale calibration is largely based on simulation, the uncertainty is evaluated using the  $Z \rightarrow ee$  data. The dominant components of the uncertainty are associated with mis-modelling of the  $Z \rightarrow ee$  decays and inaccuracies in the detector simulation. The total uncertainty in the electron energy scale is generally below 1% across the reconstructed electron kinematics [158]. To evaluate the associated uncertainty in the JES calibration, the energy of reconstructed electrons is varied within its total uncertainty.

#### 4.4.7.2 Electron energy resolution mis-modelling

The electron energy reconstructed using the simulation is smeared to reduce the difference between electron energy resolutions in the data and simulation, see Section 4.4.5. The amount of smearing is known with uncertainty, evaluated using the  $Z \rightarrow ee$  data [158]. The amount of smearing is varied within its total uncertainty to estimate its effect on the JES.

#### 4.4.7.3 Soft parton radiation mis-modelling

The effect of soft parton radiation altering the  $Z + \text{jets}$  DB technique is minimised by the event selection. The event selection limits the tolerable  $\Delta\phi$  between a  $Z$ -boson and the jet and the  $p_{\text{T}}$  of the second-hardest jet in the event. However, some residual effects remain, but they are largely cancelled in the data-to-simulation ratio that defines the calibration. This assumes that soft parton radiation is well-modelled. The effect of potential mis-modelling is studied by varying the event selection criteria. The  $\Delta\phi$  is varied by  $\pm 0.1$  around its nominal value. The  $p_{\text{T}}^{\text{jet}2}$  criterion is tightened to  $\max(10 \text{ GeV}, 0.05 \times p_{\text{T}}^{\text{ref}})$  and loosened to  $\max(20 \text{ GeV}, 0.15 \times p_{\text{T}}^{\text{ref}})$ . With these variations, the effect of soft parton radiation either increases or decreases. The ability of the simulation to describe these extreme variations determines the systematic uncertainty.

#### 4.4.7.4 Pile-up jets mis-modelling

Pile-up jets are largely rejected by limiting the tolerable JVT in the data and simulation. However, the pile-up jet rejection implies certain inefficiency [143]. Thus, a mis-modelling of pile-up jets can affect the JES calibration. To study the effect of mis-modelling, the JVT requirement is varied around its nominal value using  $\text{JVT} > 0.11$  and  $\text{JVT} > 0.91$ . These variations increase and decrease the amount of accepted pile-up jets, respectively. They also account for a few per cent change in the hard-scatter jet selection efficiency. Thereby, the variations allow accounting for the mis-modelling of the pile-up effect and JVT efficiency as the JES systematic uncertainty.

#### 4.4.7.5 $Z + \text{jets}$ production mis-modelling

The JES calibration is derived by comparing the jet response between the data and simulation. Thus, a dependency on the underlying physics model implemented in an event generator producing the  $Z + \text{jets}$  events is expected. The systematic uncertainty in the JES is evaluated using an alternative event generator. Among the requirements is different modelling of the hard scattering, parton showers, hadronisation, and the underlying event effect. As a result, the alternative JES corrections are derived. The differences between the nominal and alternative corrections are treated as the JES uncertainty.

#### 4.4.7.6 Out-of-cone effect mis-modelling

Jets are defined by the anti- $k_t$  algorithm, which clusters calorimeter energy deposits inside a cone of fixed size. However, the width of the jet can exceed the size of the cone, which leads to the loss of part of the energy associated with the jet outside of the cone. This affects the balance between the transverse momenta of the jet and a  $Z$ -boson. This effect is known as the OOC radiation effect. The effect is expected to cancel in the data-to-simulation jet response ratio if the OOC radiation is well-modelled. Otherwise, the JES calibration may be inaccurate. Therefore, the mis-modelling of the OOC radiation is considered as a source of uncertainty.

The quality of the OOC radiation modelling is probed using charged particle tracks reconstructed around the jet axis. To do this, the average transverse momentum density of the charged particle tracks is measured. Neutral particles are neglected in this study as their track momenta are not measured. It is assumed that the quality of their modelling outside of the jet cone is similar to that of charged particles. The charged particle tracks momenta are studied both in data and simulation. Only the tracks associated with the hard-scatter vertex are used to disentangle the effect of pile-up. Tracks associated with electrons from the  $Z$ -boson decay are rejected. The average track  $p_T$  density is measured as a

function of angular track disposition from the jet axis,  $\Delta R$ . The results of the measurement in one of the  $p_T^{\text{ref}}$  regions are shown in Figure 4.5. The density decreases as a function of  $\Delta R$  to a constant pedestal level at  $\Delta R > 2$ , representing the underlying event contribution. So, the mis-modelling of the underlying events is investigated along with the OOC radiation effect.

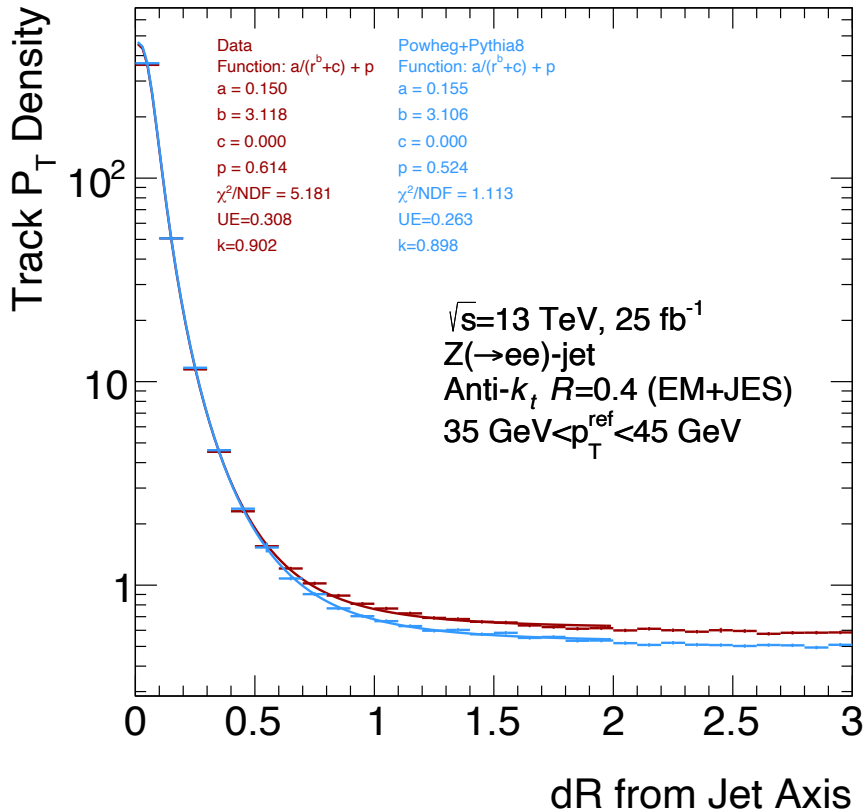


Figure 4.5 — Average transverse momentum density of tracks as a function of the angular distance between a track and the jet axis. The measurement is performed in the  $35 \text{ GeV} < p_T^{\text{ref}} < 45 \text{ GeV}$  region. Data and simulation are shown in colours. Solid lines represent fits whose parameters are quoted at the top of the figure.

The average track  $p_T$  density measured as a function of  $\Delta R$  is used to quantify the effects of the OOC radiation and the underlying event. To reduce the impact of statistical fluctuations on this study, the measured density is fit by a four-parameter function

$$f(r) = \frac{a}{r^b + c} + p, \quad (4.7)$$

where the  $a$ ,  $b$ ,  $c$  and  $p$  are free parameters of the fit. Here, the  $\Delta R$  is represented by  $r$  to avoid confusion with the jet radius. The parameters derived from the fit are used to quantify the  $p_T$  densities of the hard-scatter-initiated plus underlying-event-initiated tracks inside the jet cone,  $p_T^{\text{HS+UE,IC}}$ , only the underlying-event-initiated tracks inside the jet cone,  $p_T^{\text{UE,IC}}$ , and only the hard-scatter-initiated

tracks but outside of the jet cone,  $p_{\text{T}}^{\text{HS,OC}}$ . These quantities are estimated as

$$p_{\text{T}}^{\text{HS+UE,IC}} = \int_0^R \left( \frac{a}{r^b + c} + p \right) 2\pi r dr, \quad (4.8)$$

$$p_{\text{T}}^{\text{UE,IC}} = \int_0^R p 2\pi r dr, \quad (4.9)$$

$$p_{\text{T}}^{\text{HS,OC}} = \int_R^2 \frac{a}{r^b + c} 2\pi r dr, \quad (4.10)$$

where  $R$  is the jet radius. Finally, the fraction of the jet energy inside the cone is obtained from these quantities as

$$k_{\text{IC}} = \frac{p_{\text{T}}^{\text{HS+UE,IC}}}{(p_{\text{T}}^{\text{HS+UE,IC}} - p_{\text{T}}^{\text{UE,IC}}) + p_{\text{T}}^{\text{HP,OC}}}. \quad (4.11)$$

The  $k_{\text{IC}}$  is thus an interplay of both the OOC radiation and the underlying event effects. The  $k_{\text{IC}}$  decreases under the effect of the OOC radiation and increases by the underlying event effect. This quantity is used to probe the modelling quality.

The  $k_{\text{IC}}$  obtained in both the data and simulation is shown as a function of  $p_{\text{T}}^{\text{ref}}$  in Figure 4.6. The  $k_{\text{IC}}$  is always below one, which means that the OOC radiation effect dominates over the underlying event. The OOC radiation effect is the largest for low- $p_{\text{T}}$  jets populating the low- $p_{\text{T}}^{\text{ref}}$  regions. The effect decreases for strongly collimated jets at the high- $p_{\text{T}}^{\text{ref}}$ . The simulation reasonably describes the  $k_{\text{IC}}$  in the data. So, the effects of the OOC radiation and the underlying event are assumed to be well-modelled. Although, a few per cent difference between the data and simulation is observed in the region below  $p_{\text{T}}^{\text{ref}} = 25$  GeV. Some differences are also seen in the highest  $p_{\text{T}}^{\text{ref}}$  region in which the statistics are the lowest. The relative differences between  $k_{\text{IC}}$  in the data and simulation determine the JES uncertainty.

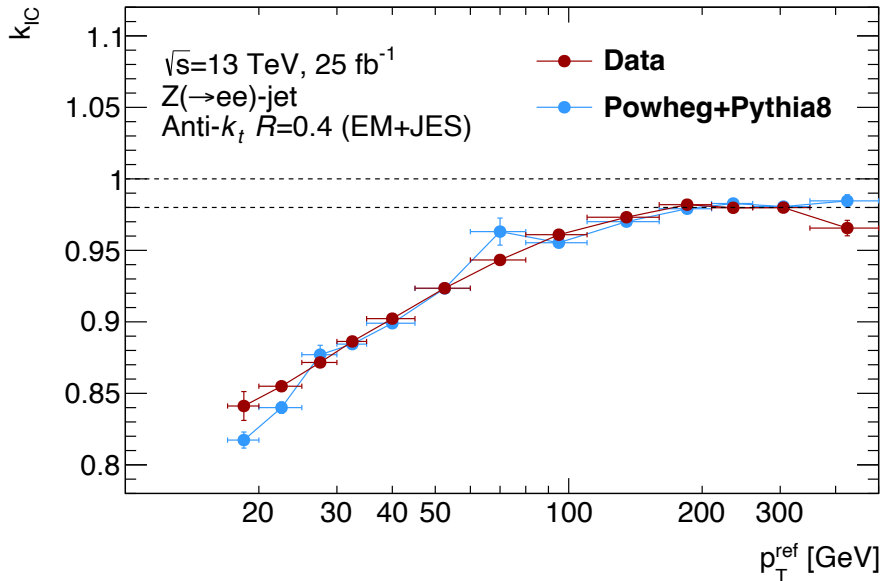


Figure 4.6 — Fraction of jet energy inside the cone given by the anti- $k_t$  jet clustering algorithm with  $R = 0.4$ . The results are shown as a function of the reference object’s transverse momentum. Data and simulation are shown with coloured markers.

#### 4.4.7.7 Summary of uncertainties

The total systematic uncertainty in the DB measurement is described by seven components. Their estimate shows that the  $35 \text{ GeV} < p_T^{\text{ref}} < 350 \text{ GeV}$  region is the most accurate in the measurement. The total systematic uncertainty is within 1–1.5%. The largest contributions of 0.5–1% are due to the mis-modelling of soft parton radiation and  $Z + \text{jet}$  production. Other systematic uncertainties are negligible.

Systematic uncertainties increase significantly at the edges of the kinematic phase space. The largest uncertainty is in the  $p_T^{\text{ref}} < 35 \text{ GeV}$  region, which is affected by the asymmetry of the jet response distribution. In this region, there are several components with a contribution exceeding 1%. They are due to the mis-modelling of soft parton radiation, pile-up jets and out-of-cone effects. These uncertainties are up to 5% at the lowest  $p_T^{\text{ref}}$ . Other systematic uncertainties in this region are negligible.

Systematic uncertainty increases up to 2% in the  $p_T^{\text{ref}} > 350 \text{ GeV}$  region mainly due to out-of-cone effects mis-modelling.

Statistical uncertainty in the measurement is estimated using the bootstrap technique. This uncertainty is negligible over most of the phase space, except at the edges. It reaches several per cent in the  $p_T^{\text{ref}} < 35 \text{ GeV}$  region and about 1% in the  $p_T^{\text{ref}} > 350 \text{ GeV}$ .

As a result, the calibration performed using the  $Z + \text{jets}$  DB technique is accurate to a per cent level in most of the probed jet kinematics.

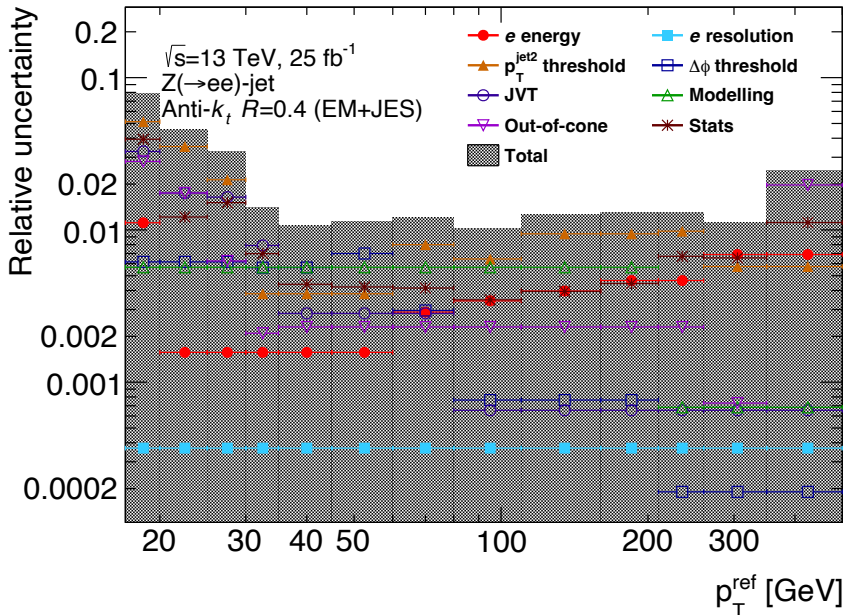


Figure 4.7 – Uncertainties in the  $Z + \text{jets}$  DB measurement. Individual uncertainties are shown in colour. Statistical fluctuations of systematic uncertainties are not shown. The shaded region represents the total uncertainty, the sum in quadrature of all uncertainties.

#### 4.4.8 Combination with calibrations in other event topologies

The calibration derived using the  $Z + \text{jets}$  events is combined with the results obtained using other event topologies to cover the full range of the measured jet energies. However, different calibrations overlap in several regions of jet  $p_T$ . The combination procedure is designed to minimise the uncertainty in the final JES calibration given the uncertainties in individual measurements.

Several cross-checks are performed before the combination. First, the derived calibration is compared to the  $Z + \text{jets}$  DB results obtained in the  $Z \rightarrow \mu\mu$  decay channel. The results are consistent within the uncertainty. The uncertainties in the  $Z + \text{jets}$  calibration using the  $Z \rightarrow \mu\mu$  decay channel have the same origins, except the muon energy scale and resolution uncertainties. As in the  $Z \rightarrow ee$  case, these uncertainties are negligible compared to others. These additional uncertainties are taken into account in the combination.

Secondly, the  $Z + \text{jets}$  DB results are compared to that obtained using the missing projection fraction (MPF) technique [149]. The MPF studies are performed using the same  $Z + \text{jets}$  events but balancing the transverse momentum of the  $Z$ -boson against that of the full hadronic recoil of an event rather than a single jet. The  $Z + \text{jets}$  DB and MPF techniques are complementary as each has advantages and disadvantages [149]. The results of both techniques are consistent within the uncertainties.

The combination with the calibrations obtained using the  $\gamma + \text{jets}$  and multi-jet events is performed in several steps [149, 150]. First, second-order polynomial splines interpolate all calibrations into common fine- $p_{\text{T}}^{\text{jet}}$  regions. Then, each calibration is assigned a  $p_{\text{T}}^{\text{jet}}$ -dependent weight through the  $\chi^2$  minimisation. The minimisation favours the calibration with the smallest uncertainty in each  $p_{\text{T}}^{\text{jet}}$  region. The combined calibration is determined as a weighted average of different calibrations. Finally, a minimal amount of smoothing using a sliding Gaussian kernel [150] is performed to reduce statistical fluctuations in the combined calibration.

Each uncertainty component in the individual calibrations is propagated to the combined result. To do this, each calibration is coherently shifted by a given uncertainty. The  $p_{\text{T}}^{\text{jet}}$  interpolation and combination with other calibrations are then repeated using the same averaging weights as in the nominal combination. The difference between the obtained combined calibration and the nominal one is considered the uncertainty. It is assumed that each uncertainty represents the  $1\sigma$  variation of the calibration. The final JES calibration is described by several dozens of independent uncertainty components. Each uncertainty is treated as fully correlated across the combined  $p_{\text{T}}^{\text{jet}}$  range.

The individual and combined JES calibrations are shown in Figure 4.8. These results are obtained using the 2015  $pp$  collisions data and published [6]. Despite this, the following is generally true for the results obtained using the 2016 data. A good overlap between *in situ* measurements using different topologies is observed. The consistency of the measurements is quantified by the  $\chi^2$  divided by the number of degrees of freedom, whose result is generally below one over most of the  $p_{\text{T}}^{\text{jet}}$  range. The combined *in situ* JES correction is about 4% at low- $p_{\text{T}}^{\text{jet}}$ , decreasing as a function of  $p_{\text{T}}^{\text{jet}}$  to 2% near 2 TeV.

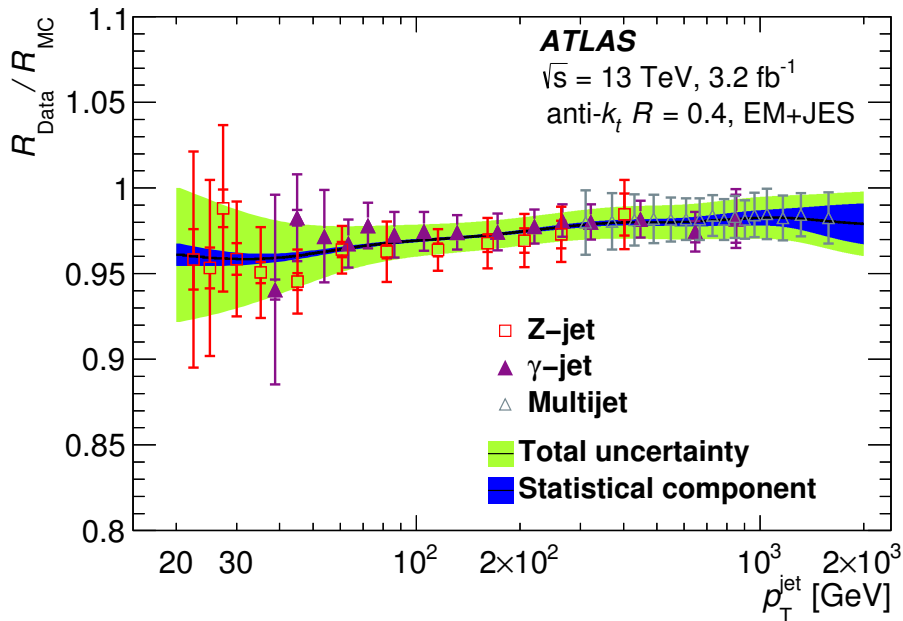


Figure 4.8 — The JES calibrations derived *in situ* in different event topologies [6]. The  $Z$  + jets,  $\gamma$  + jets and multi-jet calibrations are shown with coloured markers. Combined calibration is shown with the solid black line. The statistical and total uncertainties are shown as shaded bands around the combined calibration.

The total JES calibration uncertainty is shown in Figure 4.9. In addition to the absolute *in situ* JES calibration uncertainty, there are other uncertainty sources. Among them are the uncertainties associated with the relative *in situ* JES calibration, jet flavour composition in the inclusive jet sample and the flavour-related jet response differences, pile-up corrections, and punch-through effect from jets hitting the muon spectrometer. More details about these uncertainties are provided when describing the cross-section measurement. Here, it is important to note that the uncertainty in the absolute *in situ* JES calibration dominates the total JES calibration uncertainty. The total uncertainty is about 4.5% at low- $p_T^{\text{jet}}$ , decreasing to about 1% within the 200–1000 GeV region. A sharp increase at high- $p_T^{\text{jet}}$  is due to the statistical limitation of the multi-jet topology used to calibrate jets. Thus, the uncertainty for jets with the largest- $p_T$  is estimated by studying the detector response to single-hadrons that make up jets [6]. The single-hadron studies serve as another cross-check that confirms the reliability of the JES calibrations obtained *in situ*.

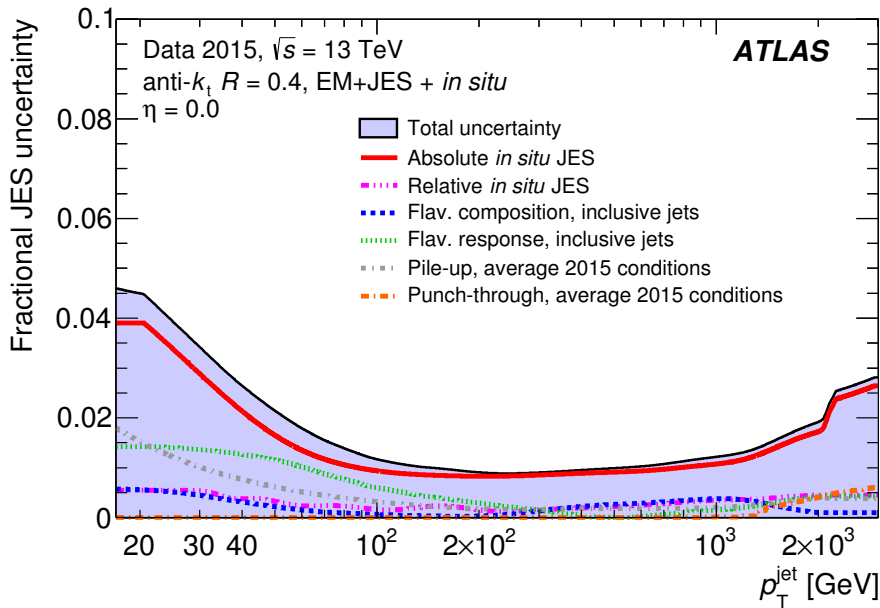


Figure 4.9 — Total JES uncertainty as the function of jet  $p_T$  at  $\eta = 0$  [6]. The uncertainty in the absolute *in situ* JES calibration is shown in red. Other uncertainty components are shown with different colours.

## 4.5 Summary and outlook

Accurate calibration of the jet energy scale is a prerequisite for many physics studies in the ATLAS experiment. The calibration is first derived using the simulation. After that, the jet response is studied *in situ* to correct for the remaining differences between the data and simulation. In connection with the latter, the transverse momentum balance between the jet and  $Z$ -boson is measured using the  $pp$  collisions data collected during the 2015 and 2016 data-taking campaigns. The result is a calibration of the jet energy scale for jets with transverse momenta below 500 GeV. The calibration restores the jet response to unity from 0.93–0.98% depending on the transverse momentum of the jet. A thorough study of the measurement uncertainties is reported. The uncertainty is mainly due to mis-modellings of various physics effects. For example, the mis-modelling of the soft parton radiation in the  $Z + \text{jets}$  events is among the largest uncertainties. The total uncertainty is below 1.5% for most probed jet transverse momenta. The measurement results are combined with those obtained using other event topologies, providing a means for accurate jet energy and hence the differential cross-section measurements.

## Chapter 5

# Measurements of the three-jets and $Z + \text{jets}$ cross-sections

The large instantaneous luminosity of the LHC provides an excellent opportunity to study rare processes. However, three-jets and  $Z + \text{jets}$  productions are not uncommon in  $pp$  collisions. Their production cross-sections are among the largest. Despite this, there are multiple reasons for measuring their cross-sections. The measurements provide a high-statistics benchmark for fixed-order QCD calculations and predictions from various event generators. This is necessary because the modelling of the three-jets and  $Z + \text{jets}$  production processes is often used for the SM backgrounds estimation, which is a prerequisite for the search for new phenomena. Apart from that, their production cross-sections are sources of new data necessary to constrain SM parameters such as the PDF and  $\alpha_S$ . These parameters are not deduced from the first principles of the theory, which is why experiments are required. So, the measurements are vital for theory improvements.

Similar measurements were performed previously, see Section [1.4](#), but the ones presented in the thesis offer new details. First, particles at the LHC collide with energies greater than at previous colliders. This explores the three-jets and  $Z + \text{jets}$  cross-sections in new energy regimes. Secondly, the cross-section are measured double-differentially as a function of several kinematic quantities. Thus, the results probe theory predictions in different regions of phase space. This verifies the ability of the theory to interpolate between these regions. In addition, the sliced phase space provides new details needed for PDF and  $\alpha_S$  constraints. Finally, the measurement uses an advanced jet energy scale calibration whose accuracy exceeds earlier measurements in the ATLAS experiments. In addition, the uncertainty in the calibration is known in more detail. Overall, these improvements are essential because the jet energy scale uncertainty dominates in such measurements.

The three-jets and  $Z + \text{jets}$  productions have different detector signatures. However, techniques used for the cross-section measurements have many similarities. That is why both measurements are described simultaneously. Both measurements start by constructing observables sensitive to PDF. These observables

are discussed in Section 5.1. The data used in the measurements are described in Section 5.2. The event selection criteria are introduced in Section 5.3. There is certain inefficiency in event selection leading to background contamination that must be subtracted as discussed in Section 5.4. An intermediate comparison between the data and simulation at the detector level is performed in Section 5.5. The simulation is then used to correct for detector effects distorting the measurement as discussed in Sections 5.6. The measurement is mostly completed after the correction, so this is immediately followed by a thorough evaluation of the uncertainty, which is the topic of Section 5.7. Before moving on to the result, the most advanced theoretical predictions that need to be probed by the data are obtained in Sections 5.8. Finally, the results of the three-jets and  $Z + \text{jets}$  cross-section measurements, along with qualitative comparisons to the theoretical predictions, are presented in Sections 5.9 and 5.10, respectively. The quantitative comparisons are discussed in Section 5.11. The chapter is summarised in Section 5.12.

## 5.1 Construction of PDF-sensitive observables

The cross-section measurements aim at providing refined information for PDF constraints. The production cross-sections are PDF-sensitive by default since they depend on the flavour of interacting partons and their energies. Since PDFs are scale-dependent, the refined information for their constraints is obtained by measuring the cross-section as a function of the hard scattering scale rather than measuring total production cross-section. The hard scattering scale determines the final state kinematics, so measuring the cross-section as a function of kinematic quantities that correlate with the hard scattering scale is necessary to meet the measurement goals.

The hard scattering scale of the three-jets production is probed by measuring the cross-section as a function of the three highest- $p_T$  jets invariant mass

$$m_{\text{jjj}} = \sqrt{(p_1 + p_2 + p_3)^2}, \quad (5.1)$$

where  $p_i$  are the four-momenta of the 1st, 2nd and 3rd leading- $p_T$  jets. A large invariant mass of the three-jet system can result either from high- $p_T$  jets or jets with large rapidity separation. These different production mechanisms are separated by studying the cross-section in six equidistant regions of absolute rapidity separation

$$|Y^*| = |y_1 - y_2| + |y_2 - y_3| + |y_1 - y_3|, \quad (5.2)$$

where  $y_i$  are the rapidities of the  $i$ th leading- $p_T$  jets. In this notation, the double-differential three-jets cross-section is defined as

$$\frac{d^2\sigma}{dm_{\text{jjj}}d|Y^*|} = \frac{1}{\mathcal{L}} \frac{N_{\text{events}}^{\text{data}}}{\Delta m_{\text{jjj}} \Delta |Y^*|}, \quad (5.3)$$

where  $N_{\text{events}}^{\text{data}}$  is the number of three-jets events measured in each of the  $\Delta m_{\text{jjj}}$  and  $\Delta|Y^*|$  regions, and  $\mathcal{L}$  is the integrated luminosity of the data sample.

The hard scattering scale of the  $Z + \text{jets}$  production is probed by measuring the cross-section as a function of absolute jet rapidity,  $|y_{\text{jet}}|$ , in five regions of the jet transverse momentum,  $p_{\text{T}}^{\text{jet}}$ . The  $Z + \text{jets}$  cross-section is measured inclusively against jets, so each jet selected for the analysis is counted separately. The inclusive cross-section is calculated with greater precision than the exclusive one, thus allowing for more sophisticated tests of the theory. The double-differential  $Z + \text{jets}$  cross-section is defined as

$$\frac{d^2\sigma}{d|y_{\text{jet}}|dp_{\text{T}}^{\text{jet}}} = \frac{1}{\mathcal{L}} \frac{N_{\text{jets}}^{\text{data}}}{\Delta|y_{\text{jet}}|\Delta p_{\text{T}}^{\text{jet}}}, \quad (5.4)$$

where  $N_{\text{jets}}^{\text{data}}$  is the number of jets in each of the  $\Delta|y_{\text{jet}}|$  and  $\Delta p_{\text{T}}^{\text{jet}}$  regions.

The  $N_{\text{events}}^{\text{data}}$  and  $N_{\text{jets}}^{\text{data}}$  are corrected for detector effects that distort the measurements. Among the effects are those related to the finite resolution, limited acceptance and inefficiencies of the detector. As a result, the measured cross-sections are provided at the particle level so that theoretical predictions can be probed directly with no need for detector simulation. A separate section of this chapter is devoted to this correction.

The sizes of kinematic regions where the cross-sections are measured are optimised according to the available statistics in the data. In addition, to reduce migrations of events between neighbouring regions, the sizes of  $m_{\text{jjj}}$  regions are optimised to be twice the detector resolution. The resolution is determined by the spread of the ratios between the reconstructed and true  $m_{\text{jjj}}$  obtained as a function of true  $m_{\text{jjj}}$  using the simulation.

Both measurements are performed using the anti- $k_t$   $R = 0.4$  jets. The three-jets cross-section is additionally measured using  $R = 0.6$  jets to provide data for the tests of the modelling of parton showers and effects of hadronisation and underlying event.

To ensure that the selected observables meet the measurement goals, they are checked for PDF sensitivity. The check is performed using the cross-section predictions obtained at the next-to-leading order accuracy in perturbative QCD and containing the information about the fractional contributions of various initial states, such as gluon-gluon, quark-gluon and quark-quark. In this test, the cross-section predictions are convolved with PDFs provided by the CTEQ [170, 171] collaboration. The fraction contributions of various initial states of the three-jets and  $Z + \text{jets}$  productions are shown in Figure 5.1. The three-jets with small  $m_{\text{jjj}}$  are produced mainly by gluon-gluon and quark-gluon interactions, while for high  $m_{\text{jjj}}$  the fractions of quark-gluon and quark-quark initial states are about 50% each. The  $Z + \text{jets}$  are produced mainly by quark-gluon interactions over the entire measurement range. However, the fractional contribution of this initial

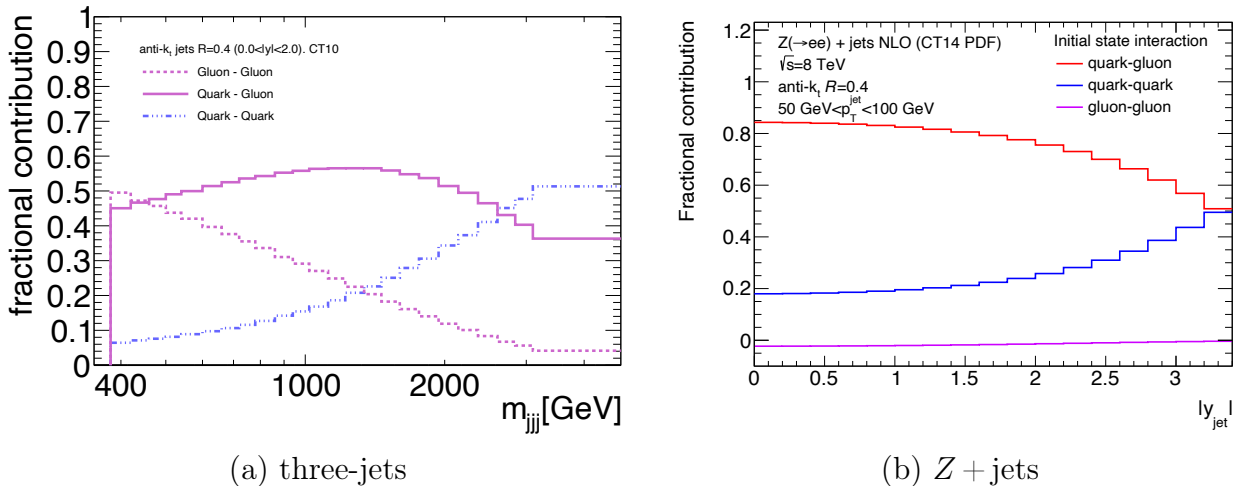


Figure 5.1 — Fractional contributions of gluon-gluon, quark-gluon and quark-quark initial states to the (a) three-jets and (b)  $Z + \text{jets}$  cross-section. Different initial states are represented by colour. The results for the three-jets are presented as a function of  $m_{jjj}$  in the  $|Y^*| < 2$  region. The results for the  $Z + \text{jets}$  are shown as a function of  $|y_{\text{jet}}|$  in the  $50 \text{ GeV} < p_{\text{T}}^{\text{jet}} < 100 \text{ GeV}$  region. The gluon-gluon initial state is suppressed in the  $Z + \text{jets}$  production.

state decreases as a function of  $|y_{\text{jet}}|$  until it becomes equal to the quark-quark one near  $|y_{\text{jet}}| = 3.2$ , which is about the boundary of the studied kinematics. The gluon-gluon initial state is suppressed in the  $Z + \text{jets}$  production. Despite this, the initial-state gluons are effectively probed by both measurements through either the gluon-gluon or quark-gluon interactions. As a result, both cross-section measurements are clearly PDF-sensitive.

In addition, the correlation between the fraction  $x$  of the proton momentum carried by a parton and the hard scattering scale is investigated. The same cross-section predictions are used for this purpose but convolved with the PDFs provided by the NNPDF [172] collaboration. The PDFs are provided with an ensemble of replicas representing a collection of equally likely PDF sets derived by fluctuating their input data within experimental uncertainties. So, an ensemble of cross-section predictions is obtained. These predictions are used to calculate correlation coefficients

$$\rho(x, Q^2) = \frac{N_{\text{rep}}}{N_{\text{rep}} - 1} \frac{\langle \frac{d^2\sigma}{dm_{jjj}/d|Y^*}| f_i(x, Q^2) \rangle - \langle \frac{d^2\sigma}{dm_{jjj}/d|Y^*}| \rangle \langle f_i(x, Q^2) \rangle}{\Delta_{\frac{d^2\sigma}{dm_{jjj}/d|Y^*}|} \Delta_{f_i(x, Q^2)}}, \quad (5.5)$$

where  $N_{\text{rep}}$  is the number of PDF replicas,  $f_i$  is the PDF for parton flavour  $i$ ,  $Q$  is the hard scattering scale,  $\Delta_{d^2\sigma/dm_{jjj}/d|Y^*}|$  and  $\Delta_{f_i(x, Q^2)}$  are the standard deviations of the ensembles of cross-sections and PDFs, respectively. Examples of correlation coefficients calculated using the three-jets predictions in the  $|Y^*| < 2$  region are shown in Figure 5.2. The hard scattering scale is determined by the invariant mass of the three-jets system. The strongest correlations are between the  $m_{jjj}$  and

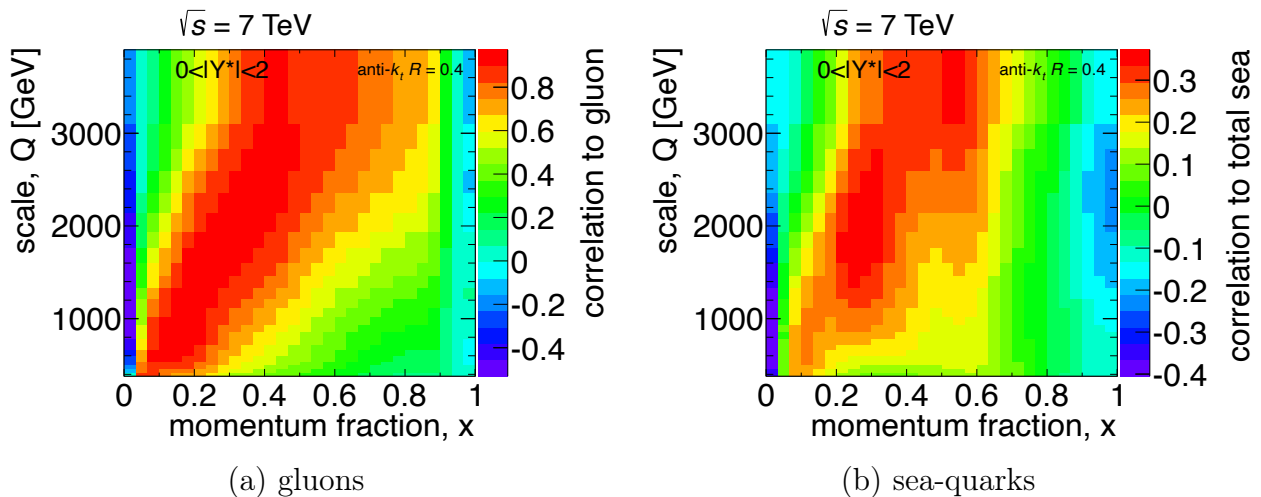


Figure 5.2 — Correlations between the hard scattering scale of the three-jets production and the fraction  $x$  of the proton momentum carried by (a) gluons and (b) sea-quarks. The hard scattering scale is determined by the  $m_{\text{jjj}}$ . The  $|Y^*| < 2$  region is shown.

gluon momentum fraction. The  $m_{\text{jjj}}$  correlations with the sea-quark momentum fraction are half as large. The  $m_{\text{jjj}}$  correlations with the strange and valence quarks momentum fractions are much lower. Approximately the same level of correlations are observed in other  $|Y^*|$  regions. A similar study is performed for the  $Z + \text{jets}$  production, where high correlations with the gluon and sea-quark momentum fractions are also observed.

Therefore, the cross-section measurements are highly sensitive to the gluon PDF, which is currently known with greater uncertainty than quarks. There is also sensitivity to other parton flavours, though not as pronounced. So the measurements look promising in terms of PDF constraints.

## 5.2 Collision data pre-selection

The measurements are performed using  $pp$  collision data collected during the Run 1 campaign. The data used for the three-jets cross-section measurement were collected in 2011, while those for the  $Z + \text{jets}$  were in 2012. The  $pp$  collisions were performed at the centre-of-mass energy of 7 TeV in 2011 and 8 TeV in 2012. The latter data are affected by a larger pile-up of  $\langle \mu \rangle = 20.7$  relative to  $\langle \mu \rangle = 9.1$  in the former. That is why there are differences in the treatment of pile-up contributions, which are revealed later in the event selection.

Collision data are pre-selected by triggers that optimise the event recording rate according to the detector's readout capabilities. So, the most interesting events are identified and stored, while the rest of the events is discarded. The triggered events are then checked against the GRL, so those affected by significant detector failures are rejected.

The triggers that select events for the cross-section measurements are introduced in this section. In addition, a special set of data for the background analysis in the  $Z + \text{jets}$  cross-section measurement is presented.

### 5.2.1 Data for the three-jets cross-section measurements

The production of jets has the largest cross-section among other processes in  $pp$  collisions at the LHC. Though, not all events can be recorded due to detector readout and storage limitations. Thus, several triggers are used to optimise the event recording rate. They all select events with at least one jet reconstructed in the  $|y| < 3.2$  region. But each trigger has a different jet energy threshold above which they accept events. Triggers with energy thresholds of 40, 55, 75, 100, 135, 180 and 240 GeV are used in the three-jets cross-section measurement. Trigger with the lowest energy threshold has the largest prescale. That is, only a fraction of events accepted by the trigger is recorded. The prescale factor decreases in triggers with larger jet energy threshold since the jet production cross-section falls steeply with energy. The trigger with a threshold of 240 GeV operates with zero prescale, so all events are kept. As a result, several data sets are recorded.

Statistics across the entire jet energy range is maximised by combining the data pre-selected by different triggers. However, there are overlaps in the data since no upper energy threshold is used per trigger. So, the regions of jet kinematics populated by the trigger with the lowest prescale need to be identified to avoid event double-counting when combining the data. In the ideal case, the lower end of these regions would be defined by the trigger's energy threshold, while the upper one would be the lower end of the next trigger. However, the pre-selection is inefficient near the trigger threshold due to the jet energy smearing associated with the finite resolution of the detector. Therefore, before combining the data, it is necessary to determine the lower ends of the regions of full trigger efficiency.

The efficiency of each trigger is measured as the fraction of selected events relative to the trigger with a lower energy threshold. The latter trigger is considered fully efficient above the threshold of the trigger under study. The efficiencies are measured as a function of  $m_{\text{jjj}}$  in each  $|Y^*|$  region. The trigger efficiencies measured in the  $|Y^*| < 2$  region are shown in Figure 5.3. The efficiencies increase gradually as a function of  $m_{\text{jjj}}$ . As a result, the triggers are fully efficient well above their energy thresholds. The  $m_{\text{jjj}}$  threshold at which a trigger is considered fully efficient is determined by the smallest  $m_{\text{jjj}}$  above which the efficiency exceeds 99%.

The efficiencies are measured separately for  $R = 0.4$  and  $R = 0.6$  jets. Due to larger energy smearing, the  $m_{\text{jjj}}$  thresholds are significantly higher for  $R = 0.6$  jets. Therefore, different  $m_{\text{jjj}}$  thresholds are used when combining data with different jet radii since the same ones would reduce the number of events in the case of  $R = 0.4$  jets.

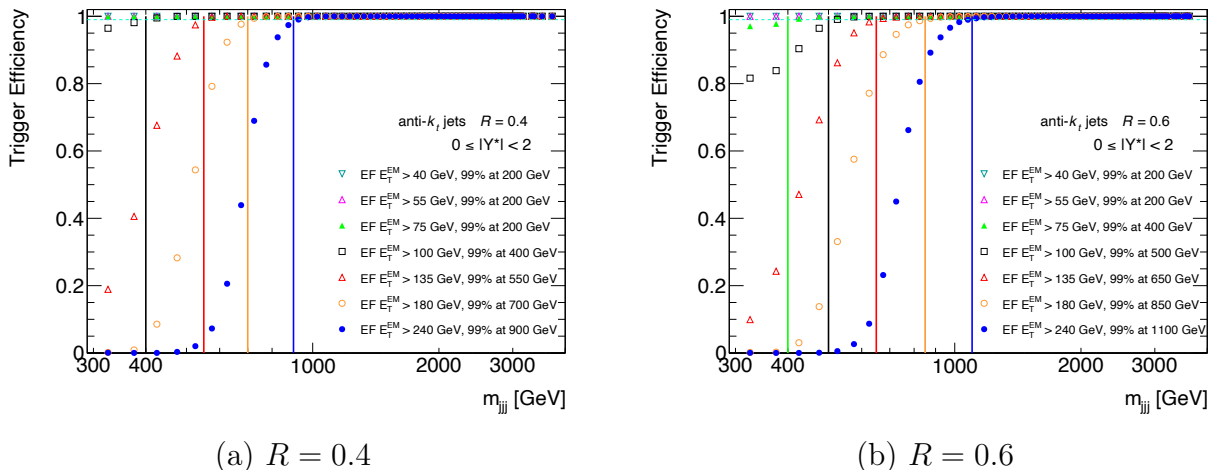
(a)  $R = 0.4$ (b)  $R = 0.6$ 

Figure 5.3 — Trigger efficiencies measured as the function of  $m_{jjj}$  in  $|Y^*| < 2$  region. The results are shown for (a)  $R = 0.4$  and (b)  $R = 0.6$  jets. Different triggers are shown in colours. The lowest  $m_{jjj}$  where trigger efficiency exceeds 99% is shown with vertical lines. These values of  $m_{jjj}$  in different triggers are listed in the legend. Each trigger’s energy threshold is also listed.

Finally, the data recorded by different triggers are combined. However, the  $m_{jjj}$  threshold where the trigger is considered fully efficient is additionally shifted up by 15%. As a result, the  $m_{jjj}$  threshold is far enough from the region where efficiency drops, giving more room for analysis variations when assessing systematic uncertainties. The increase in the statistical error of the measurement due to this shift is negligible.

## 5.2.2 Data for the $Z + \text{jets}$ cross-section measurements

The  $Z + \text{jets}$  production cross-section is several orders of magnitude smaller than that of three-jets. So events are selected by a trigger that meets the readout and storage capabilities of the detector without prescaling. However, minimal selection criteria are applied. The trigger requires at least two electrons per event. At trigger, the reconstructed electron candidates must satisfy  $p_T > 12$  GeV and  $|\eta| < 2.47$ . Those electron candidates whose energy deposits in the hadronic calorimeter exceed 1 GeV are assumed as background-like and rejected. The electrons must satisfy the *loose++* identification operating point [173] for background rejection. The identification implies constraining the electron candidate’s shower and track properties that are considered tolerable, as opposed to using the likelihood-based discriminant discussed in Section 4.4.2. Despite these differences, both approaches for electron identification are based on the same principles [163].

### 5.2.3 Data for the $Z + \text{jets}$ background analysis

There are several background processes that spoil the cross-section measurement by creating the  $Z + \text{jets}$ -like detector signature. That is when two electrons and at least one jet are reconstructed per event, but the  $Z + \text{jets}$  is not their origin. Most such backgrounds are studied using simulation, except for the  $W + \text{jets}$  and multi-jet ones. These processes are the backgrounds if either one or two jets are identified as electrons, respectively. Other jets supplementing the  $Z + \text{jets}$ -like signature are produced abundantly in  $pp$  collisions. These backgrounds are normally suppressed by the trigger requiring two electrons. Therefore, to study them, a special data sample is used, where the data selected for the  $Z + \text{jets}$  cross-section measurement are expanded with auxiliary events selected by two additional triggers.

The first trigger requires at least one electron per event. The  $p_T$  of the electron is required to be greater than 24 GeV to keep the trigger unprescaled. Several other criteria ensure that the selected electron candidates are likely to be true electrons. Among them, the electron energy deposit in the hadronic calorimeter should not exceed 1 GeV. Also, the candidate must satisfy the *medium++* [173] identification, a tightened subset of *loose++*. Finally, the electron's track must be isolated from other tracks in the event. This implies a rejection of an event if there are other tracks whose scalar sum  $p_T$  within  $\Delta R = 0.2$  exceeds 10% of the electron's track  $p_T$ . As a result, this trigger selects many background-like events since the second electron is not explicitly required but can exist. So, events with an electron either from  $W$  decay or jet misidentification are accepted by the trigger.

Electrons with high- $p_T$  are less likely to be misidentified but can fail the isolation requirement of the first trigger. So the trigger becomes inefficient for events with high- $p_T$  electrons. Therefore, events selected by a second trigger are used to avoid inefficiency. The second trigger requires events with an electron that has  $p_T$  greater than 60 GeV and satisfies the *medium++* identification.

A logical OR between the decisions of any of the triggers is used when combining events to avoid double-counting.

## 5.3 Selection of events for the measurements

Designing event selection criteria is an essential part of the measurements. The event selection is performed on top of the data pre-selected by the triggers. The selection criteria are designed based on the final state expected from a particular process using the reconstructed and calibrated physics objects as the input. The problem is that many physics processes have similar final states either at the particle or detector level. In addition, some objects are poorly reconstructed, for

example, when they hit the detector acceptance boundary. So, to avoid measurement errors, the selection should preserve events associated with a process under study while minimising the contribution of background and problematic events.

The main objects used in both measurements are jets. Jets are reconstructed using the anti- $k_t$  algorithm with  $R = 0.4$ . In addition, the  $R = 0.6$  jets are used in the three-jets cross-section measurement. The input objects are topoclusters calibrated to the LCW scale, see Section 4.1. Both measurements use the JES calibration scheme shown in Figure 4.1. However, there are two exceptions in the three-jets cross-section measurement. First, the pile-up subtraction strategy is based only on what is referred to as the residual pile-up correction in Section 4.2, which is an event-based average pile-up subtraction rather than the jet-by-jet one. This strategy has shown to be efficient under low pile-up in the 7 TeV data [150], so the area-based pile-up correction is not used in this measurement. Secondly, the GSC step is dropped because it did not produce a visible gain in the jet energy resolution. The rest is unchanged.

Jets are identified using the *medium* set of identification criteria, see Section 4.3. The identification suppresses background jets caused by cosmic ray particles, calorimeter noise bursts, and beam interactions with the collimator and residual gas along the pipe. There are also other identifications, but the *medium* one leads to the best background suppression with minimal inefficiency.

Jets falling into the Tile Calorimeter modules that are either temporarily or permanently off throughout the data taking [150] are assumed to be poorly reconstructed. The list of such modules is known. Events with such jets are rejected to avoid measurement errors.

Apart from jets, the  $Z + \text{jets}$  cross-section measurement requires exactly two reconstructed and calibrated electrons, see Section 4.4.2. Electrons are identified using the *medium++* set of identification criteria. These criteria limit the tolerable shower shape and track properties of electrons instead of using the likelihood-based discriminant introduced previously.

All events are required to have a reconstructed hard scattering vertex. Otherwise, they are treated as background-like and rejected. The vertices are determined by extrapolating at least two tracks reconstructed in the inner detector [174] with transverse momenta above 500 MeV. In the case of the  $Z + \text{jets}$  cross-section measurement, a minimum of three reconstructed tracks is required to reject more background. In addition, a looser criterion on their transverse momenta of 400 MeV is used due to improved track reconstruction efficiency [175, 176]. Among the reconstructed primary vertices, the hard scattering vertex is determined as the one with the largest sum of the transverse momenta of the associated tracks.

Other selection criteria used in the measurements are process specific.

### 5.3.1 Selection of the three-jets events

The main requirement in the three-jets cross-section measurement is the reconstruction of at least three jets per event. Jets with transverse momenta above 50 GeV are used to ensure low pile-up contribution and avoid a phase-space region affected by the jet identification inefficiency. Jets must be within the  $|y| < 3.0$  region to ensure that the core of the jet energy is far enough from the jet rapidity threshold imposed by the trigger. The first three leading- $p_T$  jets are required to satisfy  $p_T > 150$  GeV,  $p_T > 100$  GeV and  $p_T > 50$  GeV, respectively. This reduces pile-up contribution when two overlapping dijet events are misidentified as a three-jets event. So, no additional pile-up rejection techniques are necessary. In addition, these asymmetric criteria on the jets  $p_T$  improve the stability of the fixed-order QCD calculations being probed by the measurement [177].

The data used for the measurement are affected by a failure in a part of the electromagnetic calorimeter. The region constrained by  $0.0 < \eta < 1.475$  and  $-0.791 < \phi < -0.595$  was affected by malfunctioning due to problems with the readout electronics during the 2011 data-taking. Thus, events with any of the three leading jets falling in the region  $-0.88 < \phi < -0.5$  are rejected regardless of their rapidity. This avoids errors associated with mismeasured jet energy while measuring the cross-section double-differentially. Therefore, a lack of phase space associated with rejected jets is corrected later using the simulation. The correction is performed along with other detector effects.

The three-jets event selection criteria are summarised in Table 5.1. More than  $5.3 \times 10^6$  events with  $R = 0.4$  jets and  $2.5 \times 10^6$  events with  $R = 0.6$  jets are selected for the cross-section measurement.

Table 5.1. — The three-jets selection criteria.

Object	Selection criteria
Vertex	$N_{\text{tracks}} \geq 2$ $p_T^{\text{tracks}} > 500$ GeV
Jets	$N_{\text{jets}} \geq 3$ identification = <i>medium</i> excluded region: $-0.88 < \phi_{\text{jets}} < -0.5$ $p_T^{\text{jet}} > 50$ GeV, $ y_{\text{jet}}  < 3.0$ $p_T^{\text{jet1}} > 150$ GeV, $p_T^{\text{jet2}} > 100$ GeV, $p_T^{\text{jet3}} > 50$ GeV

### 5.3.2 Selection of the $Z + \text{jets}$ events

The  $Z + \text{jets}$  cross-section measurement requires events with at least one jet and exactly two electrons. The electrons must be oppositely charged as expected from the  $Z$ -boson decay. Their transverse momenta must exceed 20 GeV, while

absolute pseudorapidities must be below 2.47. This is a region where the detector performance is optimal. In addition, electrons falling into the detector transition region,  $1.37 < |\eta_e| < 1.52$ , are excluded due to a large amount of inactive material between the barrel and endcap electromagnetic calorimeters, which leads to a large uncertainty in electron energy measurements. Finally, the electron-pair invariant mass,  $m_{ee}$ , is required to be within the  $66 \text{ GeV} < m_{ee} < 116 \text{ GeV}$  range. This criterion minimised the contribution of backgrounds with the  $Z + \text{jets}$ -like detector signatures.

At least one reconstructed jet is required per event. Jets with transverse momenta above 25 GeV and rapidity within  $|y_{\text{jet}}| < 3.4$  are used to avoid the regions of inaccurate JES calibration. These restrictions are necessary because, for example, an inaccuracy in the forward jets calibration, found when validating the JES using the  $Z + \text{jets}$  data [178], blows up the error of the detector effects correction.

Jets originated from pile-up interactions are suppressed using the JVF [143]. The JVF above 0.25 is required for jets reconstructed within the region of  $p_{\text{T}}^{\text{jet}} < 50 \text{ GeV}$  and  $|\eta_{\text{det}}| < 2.4$ , since its scope is limited by the inner detector acceptance and inefficiency affecting high- $p_{\text{T}}$  jets, see Section 4.3. Because of this, the region of  $p_{\text{T}}^{\text{jet}} < 50 \text{ GeV}$  and  $2.4 < |y_{\text{jet}}| < 3.4$  has a high number of pile-up jets that spoil the detector effects corrections since these jets are poorly modelled. That is why this region is not reported in the cross-section measurement.

Finally, jets reconstructed within  $\Delta R = 0.4$  of selected electrons are rejected to avoid their energy overlap.

The  $Z + \text{jets}$  event selection criteria are summarised in Table 5.2. About  $1.5 \times 10^6$  events with at least one  $R = 0.4$  jet are selected for the cross-section measurement. Each jet that meets the selection requirements is used in the measurement.

Table 5.2. — The  $Z + \text{jets}$  selection criteria.

Object	Selection criteria
Vertex	$N_{\text{tracks}} \geq 3$ $p_{\text{T}}^{\text{tracks}} > 400 \text{ GeV}$
Electrons	$N_e = 2$ identification = <i>medium</i> excluded region: $1.37 <  \eta_e  < 1.52$ $p_{\text{T}}^e > 20 \text{ GeV}$ , $ \eta_e  < 2.47$ $66 \text{ GeV} < m_{ee} < 116 \text{ GeV}$
Jets	$N_{\text{jets}} \geq 1$ identification = <i>medium</i> $\text{JVF} > 0.25$ if $p_{\text{T}}^{\text{jet}} < 50 \text{ GeV}$ and $ y_{\text{jet}}  < 2.4$ $p_{\text{T}}^{\text{jet}} > 25 \text{ GeV}$ , $ y_{\text{jet}}  < 3.4$ $\Delta R(\text{jet}, e) > 0.4$

## 5.4 Backgrounds evaluation in the $Z + \text{jets}$ cross-section measurement

Event selection is designed to reduce background contribution to the measurement. However, some backgrounds are irreducible by the selection requirements. These are the backgrounds from processes with final states similar to the measured ones. Other types of backgrounds are accepted due to reconstruction inaccuracy or limited detector acceptance. All backgrounds are counted along with the events of the process being studied, thus distorting the cross-section measurements. Therefore, evaluating and subtracting the backgrounds are important tasks when measuring cross-section.

There are no significant backgrounds in the three-jets cross-section measurement since no other process with a final state similar to the QCD production of jets occurs at a comparable rate. So, background analysis beyond that of non-collision-related sources, which is reduced by the jet identification, is unnecessary.

The background analysis is performed in the  $Z + \text{jets}$  cross-section measurement. The backgrounds are expected from the  $Z \rightarrow \tau\tau$ , dibosons ( $WW$ ,  $ZZ$ ,  $WZ$ ),  $W + \text{jets}$ , multi-jet,  $t\bar{t}$  and single top-quark production. The  $Z \rightarrow \tau\tau$  is a background if both  $\tau$ -leptons decay into an electron and neutrinos. Diboson production makes up a background if a pair of electrons from  $W$  and/or  $Z$ -boson decays is detected while other decay products are not. The  $W + \text{jets}$  background is due to an electron from  $W$  boson decay and a jet misidentified as another electron. Multi-jet production constitutes a background when two jets are misidentified as electrons. The  $t\bar{t}$  and single top-quark events form a background since top-quarks decay predominantly via the  $t \rightarrow Wb$ . So the electrons can be from  $W$  bosons

decay or jet misidentification. The detector signature is indistinguishable from a  $Z + \text{jets}$  one when the reconstructed electron pair is associated with the above processes and is complemented by any jet produced either from initial or final state parton radiation or pile-up. These backgrounds must be subtracted from the  $Z + \text{jets}$  events selected for the cross-section measurements.

Two approaches are used for background evaluation. One is simulation-based, and another is data-driven. Both approaches are introduced first. The results of the background analysis follow immediately after.

### 5.4.1 Simulation-based approach for background evaluation

A simulation-based approach is used to evaluate the  $Z \rightarrow \tau\tau$ , diboson,  $t\bar{t}$  and single top-quark backgrounds. These processes are sufficiently well-modelled, as is known from previous studies. [179–186]. The entire ATLAS simulation chain introduced in Section 2.5 is used to obtain the detector-level predictions of these processes. Simulated events are propagated through the  $Z + \text{jets}$  selection requirements to assess their contribution to the measurement. The data contamination by each of these backgrounds is then evaluated as

$$N_{\text{ev}}^{\text{bkg}} = N_{\text{ev}}^{\text{sel}} \mathcal{L} \sigma / N_{\text{ev}}^{\text{tot}}. \quad (5.6)$$

where  $N_{\text{ev}}^{\text{tot}}$  is the total number of simulated events,  $N_{\text{ev}}^{\text{sel}}$  is the number of selected events,  $\sigma$  is a given process production cross-section and  $\mathcal{L}$  is an integrated luminosity of the data set. The cross-sections used for normalisations are calculated at fixed-order accuracy in QCD and shown in Table 5.3. As a result, the luminosity-normalised yields of each background are obtained.

Table 5.3. — Simulated background processes and their total production cross-sections calculated at fixed-order accuracy in QCD. The cross-sections are taken from Refs. [179–186].

Process	order in QCD	$\sigma$ [pb]
$Z \rightarrow \tau\tau$	NNLO	$1122 \pm 56$
$WW$	NLO	$58.7^{+3.0}_{-2.7}$
$WZ$	NLO	$20.3 \pm 0.8$
$ZZ$	NLO	$7.2^{+0.3}_{-0.2}$
$t\bar{t}$	NNLO+NNLL	$252.9^{+13.3}_{-14.5}$
$t_{s\text{-chan}}$	NLO+NLL	$5.6 \pm 0.2$
$Wt$	NLO+NLL	$22.4 \pm 1.5$
$t_{t\text{-chan}}$	NLO+NLL	$87.8^{+3.4}_{-1.9}$

## 5.4.2 Data-driven approach for background evaluation

A data-driven approach is used to evaluate the multi-jet and  $W$ +jets backgrounds. This approach is preferential over the simulation-based one for at least two reasons. First, billions of simulated events are needed to obtain reasonable statistics on jets faking two electrons at the same event. This is especially true for the two-dimensional observable being explored in the measurement. Simulating and keeping such a vast sample of events is impractical. Second, the multi-jet production is expected to be a dominant background in the  $Z$ +jets cross-section measurements. Thus, the measured cross-section becomes sensitive to the modelling of the multi-jet production if the simulation-based approach is used. The data-driven approach reduces the sensitivity to the modelling. Therefore, a data-driven approach is necessary, at least for the multi-jet background.

The absolute number of the multi-jet events in the data sample used for the  $Z$ +jets cross-section measurement is low. Therefore, a special data sample is used for the background analysis. This data sample includes events used for the  $Z$ +jets cross-section measurement plus additional ones selected by single-electron triggers. These triggers accept many background events normally rejected by the  $Z$ +jets selection requirements. Thus, the number of multi-jet events is increased. Besides that, the special data set naturally includes  $W$ +jets events, where a true electron originates from the  $W$  decay. Thus, to gain more statistics in the regions where either of the two backgrounds is small, they are studied combined. The combined background of multi-jet and  $W$ +jets events is referred to as the multi-jet plus  $W$ +jets background.

The data-driven background study requires an orthogonal approach to event selection. That is, the  $Z$ +jets events must be suppressed while preserving the multi-jet plus  $W$ +jets background. However, following the nominal  $Z$ +jets selection requirements closely is necessary to keep the background representative of the  $Z$ +jets data. This is achieved by modifying only some of the electron selection requirements. By default, the measurement requires two reconstructed electrons. So, the  $Z$ +jets events are vastly suppressed by requiring electrons to be equally charged, not oppositely. An electron faked by a jet is identified when it satisfies the *medium++*, but not *tight++* set of criteria. Finally, no identification is imposed on the second reconstructed electron so that it can be either a true electron in  $W$ +jets events or another electron-faking jet. Other  $Z$ +jets selection requirements remain untouched. As a result, the event sample is mainly populated by the multi-jet plus  $W$ +jets. The resulting event sample is referred to as the control sample, as opposed to the nominal one used in the cross-section measurement.

In addition to the multi-jet and  $W$ +jets events, the control sample is expected to be contaminated by other events. These are the  $Z$ +jets events and the backgrounds evaluated using a simulation-based approach. The simulation is

also used to estimate their contribution to the control sample. To do this, events that simulate any of these processes are checked against the requirements of the control sample. The resulting event samples are normalised to data according to Equation 5.6. As a result, the luminosity-normalised event yields are obtained. Their contribution to the control sample is relatively low. These yields are subtracted from the data providing a pure yield of the multi-jet plus  $W$ +jets events. The results of this study are shown in Figure 5.4. The purity of the background selection is evaluated as the fraction of the multi-jet plus  $W$ +jets events in the control sample. The purity is about 98% in the tails of the  $m_{ee}$  distribution and 80% near the  $m_{ee}$  peak at 91 GeV. It is above 90% as a function of  $|y_{\text{jet}}|$  and  $p_{\text{T}}^{\text{jet}}$ . Thus, the resulting multi-jet plus  $W$ +jets yields are weakly dependent on the simulations used to derive them, so they are considered model-independent.

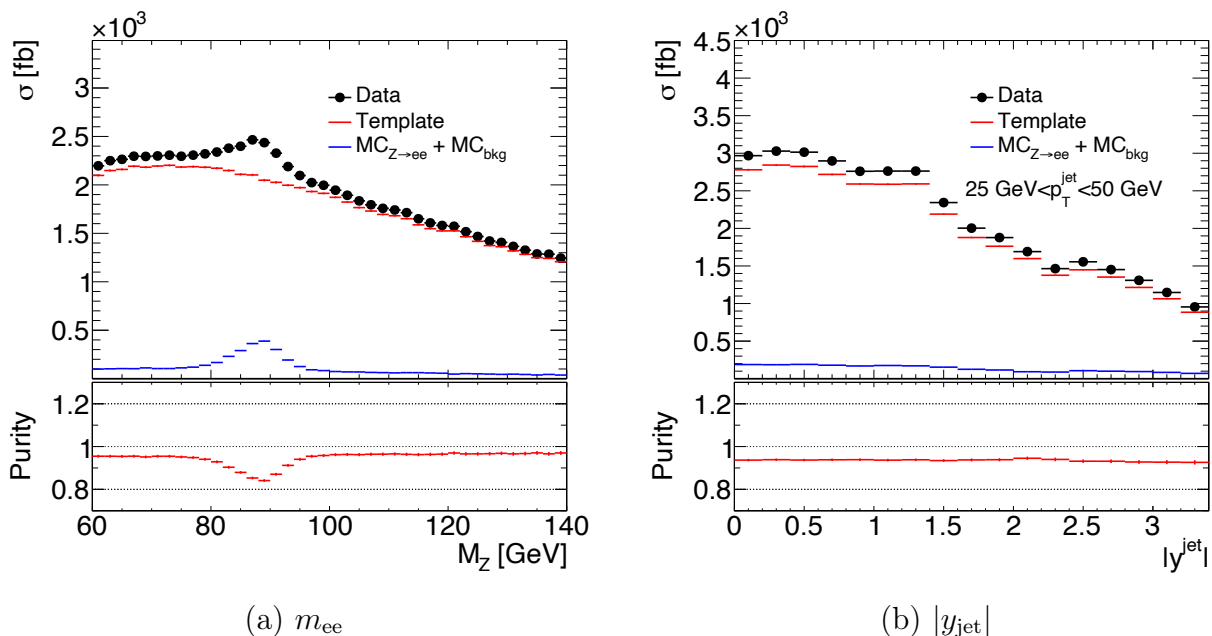


Figure 5.4 — Luminosity-normalised event yields used in the combined multi-jet plus  $W$ +jets background analysis. The yields are shown as a function of (a)  $m_{ee}$  and (b)  $|y_{\text{jet}}|$  in the  $25 \text{ GeV} < p_{\text{T}}^{\text{jet}} < 50 \text{ GeV}$  region. The control sample data are shown in black markers. Combined contaminations by the  $Z$ +jets and other backgrounds are shown in blue. The multi-jet plus  $W$ +jets yields are shown in red. The lower panel shows the purity of the control sample.

Besides many similarities, the requirements used for the nominal and control sample selections are different, so the derived multi-jet plus  $W$ +jets yields describe only the shape of the background, whose normalisation is yet inconsistent with the nominal  $Z$ +jets sample. This shape is used as the template, which requires fitting to the data to obtain correct normalisation. The  $m_{ee}$  distribution is used for this purpose as it discriminates well the region where the multi-jet background is large. The largest fractional contribution of the background is expected at the tails of the  $m_{ee}$  distribution, decreasing towards the  $Z$ -boson

mass peak near 91 GeV. These tails are underestimated by the  $Z + \text{jets}$  predictions, even when combined with other backgrounds obtained using simulation. The difference is attributed to the lack of a multi-jet background. Therefore, the template is adjusted to the data to compensate for this difference. This is done using a maximum-likelihood fit. The fitting is done using an extended  $m_{ee}$  window of  $60 \text{ GeV} < m_{ee} < 140 \text{ GeV}$  to access larger backgrounds in the tails, thereby improving the fit reliability. The region of  $80 \text{ GeV} < m_{ee} < 100 \text{ GeV}$  is excluded from the fit to avoid the region where the background contribution is small. The predictions for the  $Z + \text{jets}$  and other backgrounds are fixed, so only the template normalisation is varied by the fit. Instead of being normalised by the cross-section, the  $Z + \text{jets}$  predictions are scaled to data to give the same yields in the  $90 \text{ GeV} < m_{ee} < 92 \text{ GeV}$  region. This is done to improve the accuracy of the template fit since it can be affected by the inaccuracy of the  $Z + \text{jets}$  cross-section calculation. The best fit estimates the normalisation required to bring the template to the  $Z + \text{jets}$  data.

The results of the best fit are shown in Figure 5.5. The fit quality is estimated using

$$\chi^2 = \sum_i \frac{(N_i^{\text{data}} - N_i^{\text{bkg MC}} - K_s N_i^{\text{signal MC}} - K_t N_i^{\text{template}})^2}{(\delta_i^{\text{data}})^2 + (\delta_i^{\text{bkg MC}})^2 + (\delta_i^{\text{signal MC}})^2 + (\delta_i^{\text{template}})^2}, \quad (5.7)$$

where  $\delta_i^{\text{data}}$ ,  $\delta_i^{\text{bkg MC}}$ ,  $\delta_i^{\text{signal MC}}$ ,  $\delta_i^{\text{template}}$  are the statistical uncertainties in the data, simulated backgrounds, simulated  $Z + \text{jets}$  and template, respectively. The statistical uncertainties are calculated in each interval  $i$  of the  $m_{ee}$  distribution. The best fit quality is  $\chi^2/(\text{n.d.f.}) = 337.1/30$ , where n.d.f. is the number of the  $m_{ee}$  spectrum bins. This definition of  $\chi^2$  is used to identify the best fit and ignores the systematic uncertainty in the measurement. However, when the systematic uncertainties are considered, the  $Z + \text{jets}$  predictions combined with all backgrounds are consistent with the data.

The normalisation of the combined multi-jet plus  $W + \text{jets}$  background obtained by fitting its template of the  $m_{ee}$  distribution to the data is used to normalise its templates of  $|y_{\text{jet}}|$  distributions obtained in various  $p_{\text{T}}^{\text{jet}}$  regions.

### 5.4.3 Results of the background analysis

Most of the backgrounds to the  $Z + \text{jets}$  cross-section measurement are studied using the simulation-based approach. Among them are the processes of the  $Z \rightarrow \tau\tau$ , diboson,  $t\bar{t}$  and single top-quark productions. The combined multi-jet plus  $W + \text{jets}$  background is estimated using the data-driven approach. The results of the background analysis are shown in Figure 5.6. The distribution of jets in the  $Z + \text{jets}$  data is shown as a function of  $|y_{\text{jet}}|$  in different  $p_{\text{T}}^{\text{jet}}$  regions. The dominant background is from the  $t\bar{t}$  events. Its contamination is within 0.7–3%

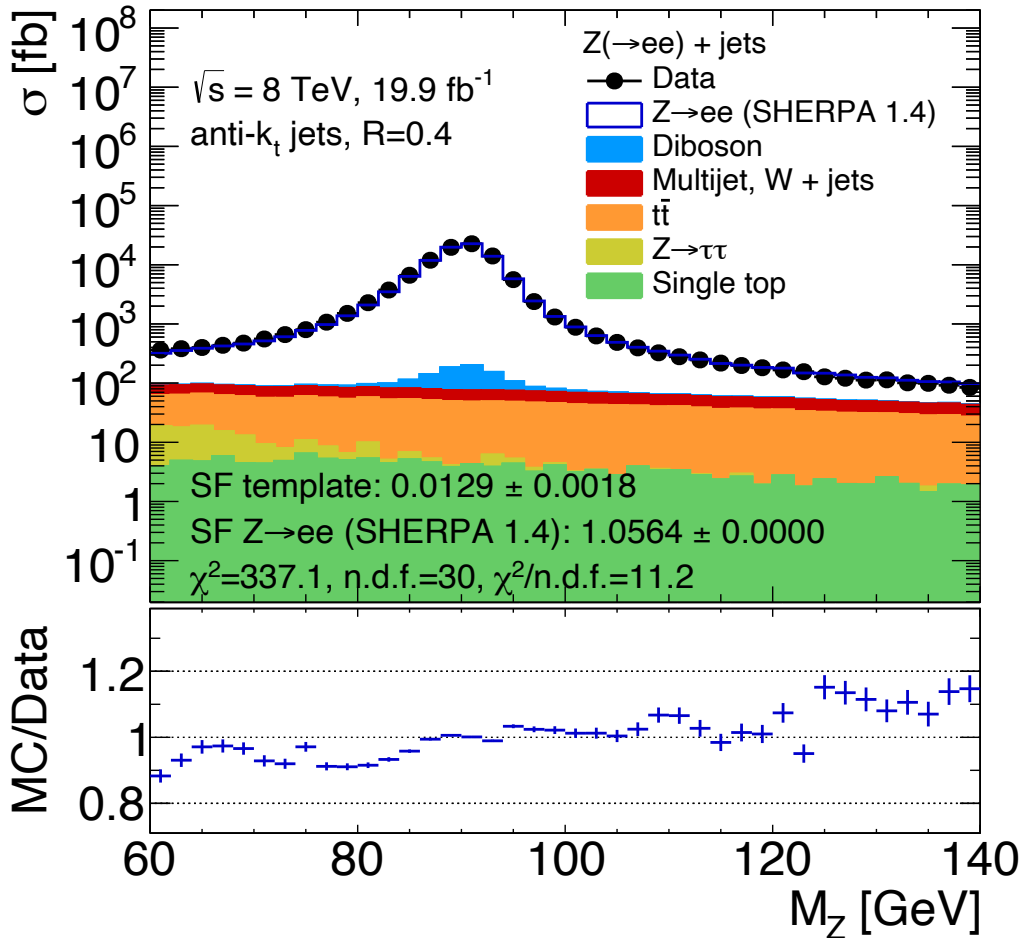


Figure 5.5 — Luminosity-normalised  $Z + \text{jets}$  yields as a function  $m_{ee}$ . Data are shown in black markers. The filled areas correspond to the stack of backgrounds listed in the legend. The simulated  $Z + \text{jets}$  prediction combined with all backgrounds is shown in blue. The simulated  $Z + \text{jets}$  prediction is scaled by a factor of 1.056. The multi-jet plus  $W + \text{jets}$  template is scaled by a factor 0.0129 obtained from the fit to data. The fit quality parameters are shown in the bottom part of the plot. The lower panel shows a ratio between the simulated  $Z + \text{jets}$  prediction combined with all backgrounds and data.

in most bins of the measurement. This is expected as the  $t\bar{t}$  cross-section is relatively high. The next largest is the combined multi-jet plus  $W + \text{jets}$  background and the diboson background, which are approximately the same size. The contributions of these backgrounds are 0.5%–1%. The  $Z \rightarrow \tau\tau$  and single-top-quark backgrounds are below 0.1%.

The  $Z + \text{jets}$  simulation combined with the backgrounds predicts data well. The agreement is within the uncertainty in electron and jet energy measurements, although the total uncertainty is expected to be greater. There is a visible sensitivity to the  $Z + \text{jets}$  modelling. However, this does not affect the backgrounds.

All derived backgrounds are subtracted from the  $Z + \text{jets}$  data.

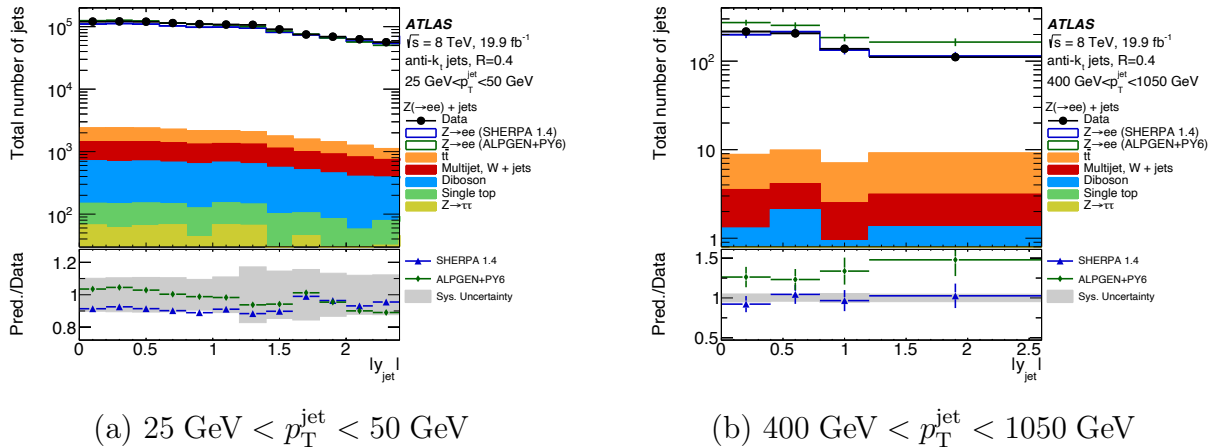


Figure 5.6 — The total number of jets in  $Z + \text{jets}$  events as a function of  $|y_{\text{jet}}|$  in  $p_T^{\text{jet}}$  bins. Data are presented with markers. The filled areas correspond to the stack of backgrounds. All backgrounds are added to the simulated  $Z + \text{jets}$  predictions. Lower panels show ratios between the  $Z + \text{jets}$  predictions and data. The grey band shows the sum in quadrature of the electron and jet uncertainties. The statistical uncertainties are shown with vertical error bars. The total data + simulation statistical uncertainty is shown in the lower panels.

## 5.5 Comparisons between data and simulations at the detector level

High-quality simulation is a prerequisite for the measurements. The simulation is used for detector effects correction and systematic uncertainty evaluation. There are many event generators providing predictions for a given process production. However, it is unclear which one predicts the data better. Therefore, comparisons between data and simulations at the detector level are performed to identify the best model to use in the measurement.

The detector-level predictions are obtained using the simulation chain described in Section 2.5. It is assumed that the difference between generators is larger than the uncertainty in the detector simulation. Therefore, the differences are explored between several main event generators, which have proven themselves in previous studies. The generators encode different physics models providing means for systematic uncertainty evaluation. The following predictions for the three-jets productions are explored:

- the PYTHIA6 [61] is used to calculate  $2 \rightarrow 2$  matrix elements at the LO accuracy in perturbative QCD supplemented by leading-logarithmic calculations of parton showers ordered in  $p_T$ . The matrix elements are convolved with the CTEQ5L [170] PDF. A simulation of the underlying event, including multiple parton interactions, is also included. The generator is tuned

according to the PERUGIA 2011 [187] prescription for an optimal description of high-energy particle collisions based on data from previous colliders;

- the ALPGEN [188] is used to calculate multi-leg matrix elements for up to six final state partons at LO accuracy. The matrix elements are convolved with the CTEQ6L1 [171] PDF. The calculations are supplemented by parton showers generated using HERWIG [65] with the AUET2 [168] set of tuned parameters.

Three predictions are explored in the  $Z$  + jets cross-section measurement:

- the SHERPA v.1.4 [68] is used to calculate multi-leg matrix elements for the inclusive  $Z$ -boson production at NLO accuracy and up to five partons in the final state at LO accuracy. The matrix elements are convolved with the CT10 [166] PDF. The calculations are supplemented by the SHERPA's parton showers matched according to the CKKW [70] prescription. Different parton multiplicities in matrix elements and parton showers are combined according to the MENLOPS [76] prescription. The predictions are normalised to the inclusive  $Z$ -boson production cross-section calculated at NNLO accuracy [189–191] for better agreement with data;
- the ALPGEN v. 2.14 [188] is used to calculate matrix elements for the inclusive  $Z$ -boson production and up to five final state partons at LO accuracy. The matrix elements are convolved with the CTEQ6L1 [171] PDF. The parton showers are generated using the PYTHIA v. 6.426 with the PERUGIA 2011C [187] set of tuned parameters. The ALPGEN matrix elements are matched to the parton showers following the MLM [72] prescription. The predictions are also normalised to the cross-section calculated at the NNLO accuracy. These predictions are referred to as the ALPGEN+PYTHIA;
- the POWHEG-BOX v. 1.0 [74, 75, 165] is used to calculate matrix elements for the inclusive  $Z$ -boson production at NLO accuracy. The matrix elements are convolved with the CT10 PDF set. The calculations are supplemented by parton showers generated using the PYTHIA8 [62] with the AU2 [168] set of tuned parameters. These predictions are referred to as the POWHEG+PYTHIA8.

The PHOTOS [192] and TAUOLA [193] programs are interfaced with the two latter predictions to model electromagnetic final state radiation and  $\tau$ -lepton decays, respectively.

Pile-up  $pp$  interactions are generated using the PYTHIA8. The pile-up events are randomly overlaid on the hard scattering events to reproduce the  $\langle\mu\rangle$  distribution in the data. The effects of both the same and neighbouring bunch crossings are modelled.

The simulated electron and jet four-momenta are calibrated to the same energy scale as in the data. Simulated events are checked against the selection requirements used in the data. Finally, a set of corrections discussed in Section 4.4.5 is used in the  $Z + \text{jets}$  simulation. These corrections reduce the effect of mis-modelling associated with pile-up and electron-related quantities. Electron isolation is not used in the cross-section measurement in favour of larger statistics. So the associated correction is unnecessary. The three-jets cross-section measurement is insensitive to the shape of  $\langle \mu \rangle$  distribution since pile-up is low in the data. Given that this measurement does not require electrons, none of the above corrections is needed.

Several kinematics quantities are used to probe the level of agreement between the data and simulation. In the three-jets cross-section measurement, it is important to model well the jet transverse momenta and rapidities that determine the  $m_{\text{jjj}}$ . It is also necessary that the  $\Delta R$  between the pairs of the three leading- $p_{\text{T}}$  jets be well modelled when the cross-section is measured as a function of  $|Y^*|$ . The distributions of these quantities are shown in Figure 5.7. There is a good agreement between the data and PYTHIA6 predictions. The ALPGEN predictions deviate from the data at high transverse momenta and rapidity. The  $\Delta R$  modelling is also worse than in PYTHIA6.

In the  $Z + \text{jets}$  cross-section measurement, the important quantities are related to both jets and electrons. The electrons are used to define the  $Z$ -boson four-momentum. Therefore, good modelling of electrons  $p_{\text{T}}$  and  $\eta$  in the  $Z + \text{jets}$  events is necessary. The modelling of the  $Z$ -boson  $p_{\text{T}}$  and rapidity defined by the kinematics of the electron pair is also probed. Finally, the distributions of several properties of jets are checked. Namely, these are the jet  $p_{\text{T}}$ , rapidity, number of reconstructed jets, and  $\Delta R$  between the jet and electron. The luminosity-normalised  $Z + \text{jets}$  yields as functions of listed quantities are shown in Figures 5.8 and 5.9. The study shows that the electron and  $Z$ -boson kinematics is predicted well within the uncertainty in the electron and jet energy measurements. However, this does not apply to jets. The jet properties are reasonably well predicted only by the SHERPA. The ALPGEN+PYTHIA predictions overestimate the transverse momenta of jets. The opposite is in the POWHEG+PYTHIA8 predictions underestimating the jet  $p_{\text{T}}$ . In addition, they significantly underestimate the number of reconstructed jets. Although, all simulations predict the angular properties of the jets well.

As a result, the models that best predict the data are identified. These are the ones obtained with the PYTHIA6 in the three-jets analysis and SHERPA in the  $Z + \text{jets}$  analysis. These predictions are used for the detector effects correction and systematic uncertainty evaluation. The SHERPA is also used in the data-driven background evaluation in the  $Z + \text{jets}$  cross-section measurement. The other predictions are kept to estimate the uncertainty in the detector effects cor-

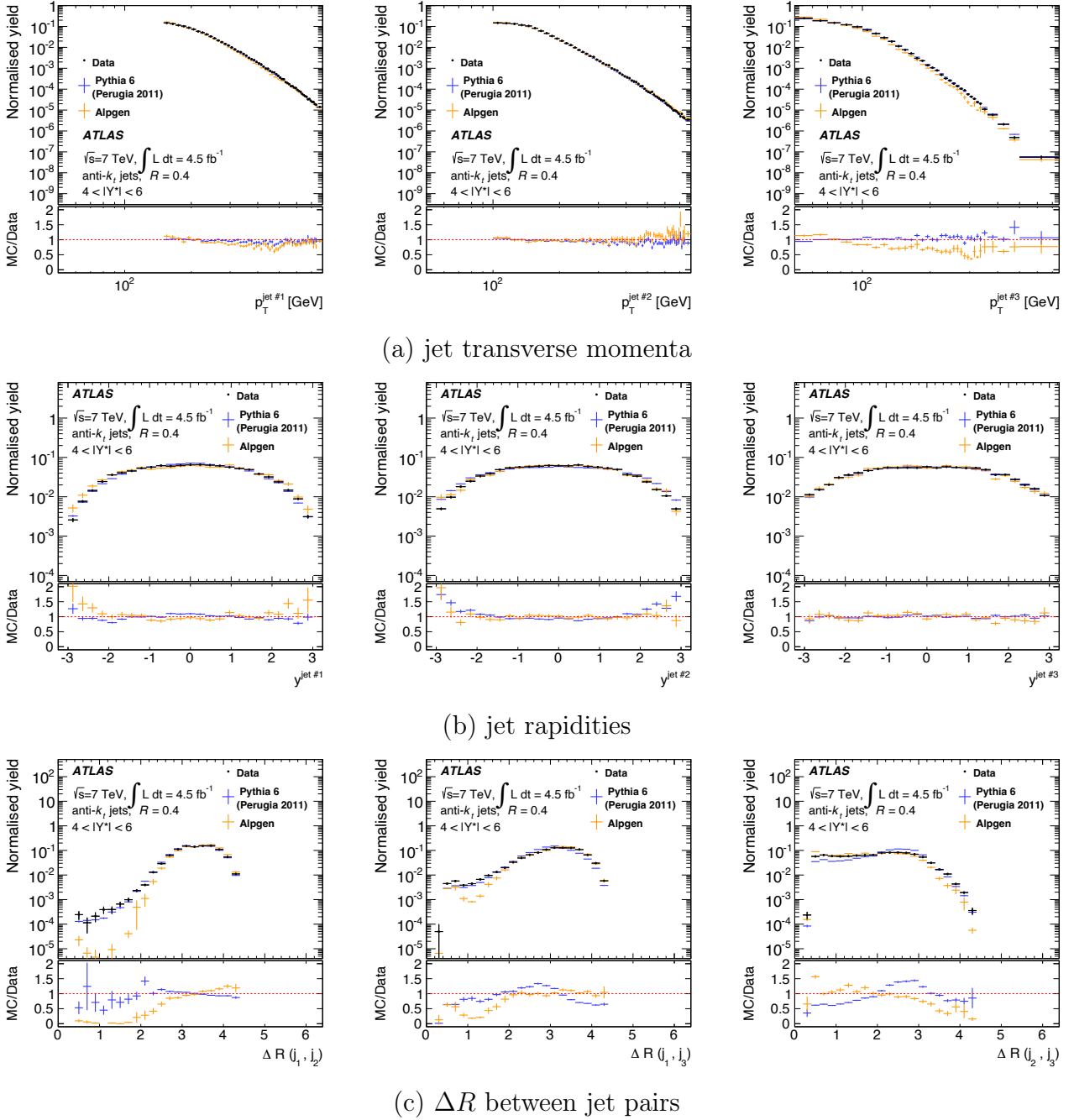


Figure 5.7 – Detector-level distributions of the first three leading- $p_T$  jets transverse momenta and rapidities, and the  $\Delta R$  between the jet pairs in the three-jets analysis. The  $4 < |Y^*| < 6$  region is shown. Different predictions are shown in colours. Statistical uncertainties are depicted with the vertical error bars. Lower panels show ratios between the three-jets predictions and data.

rection. The exception is the POWHEG+PYTHIA8 prediction which is not used in the measurements at all due to poor agreement with data.

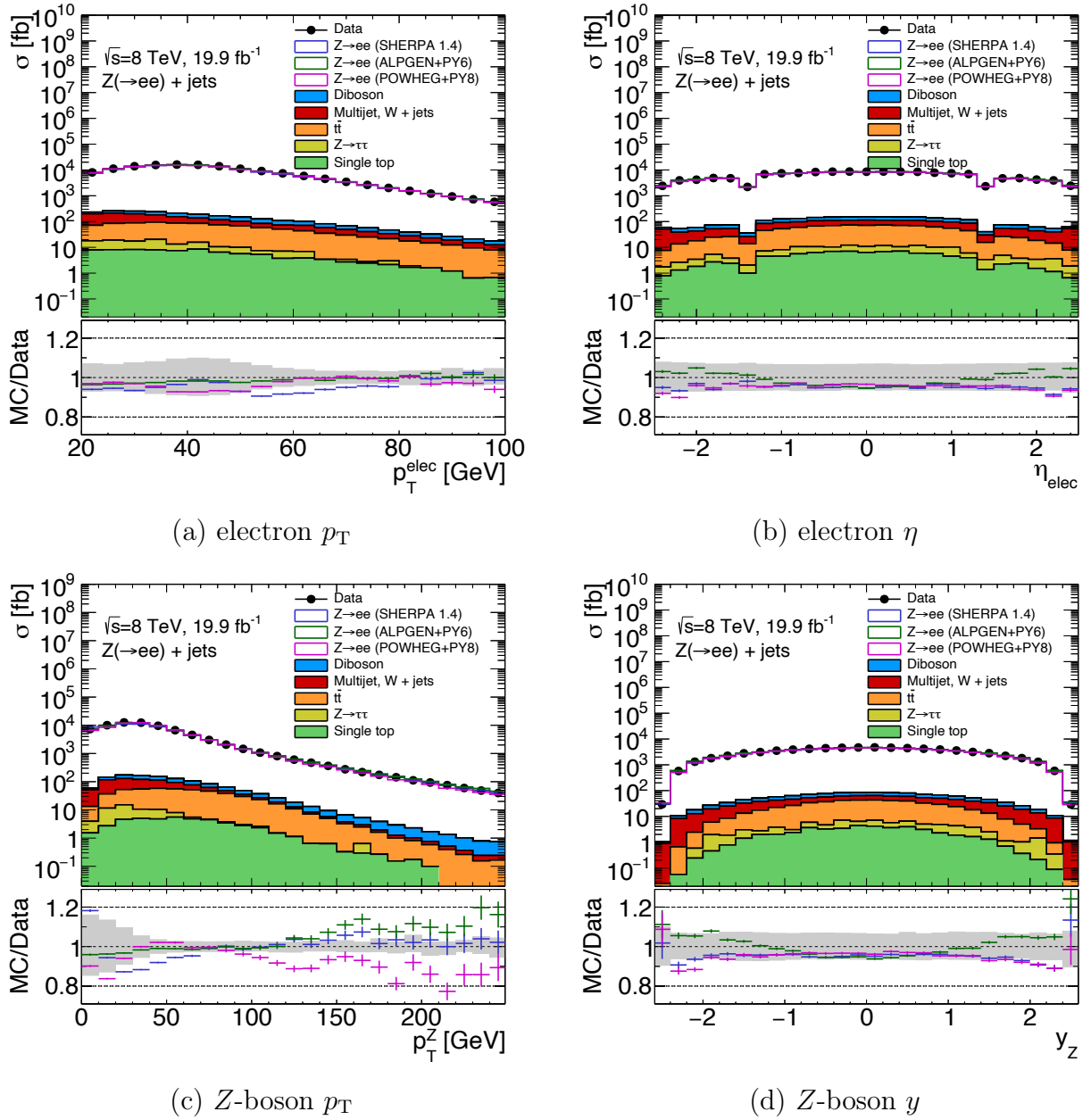
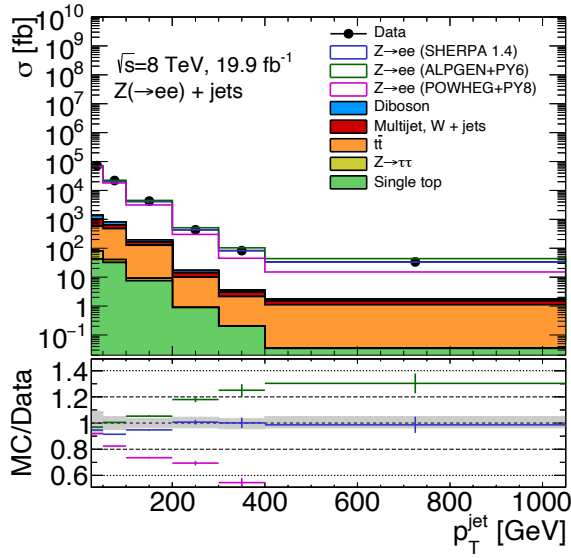
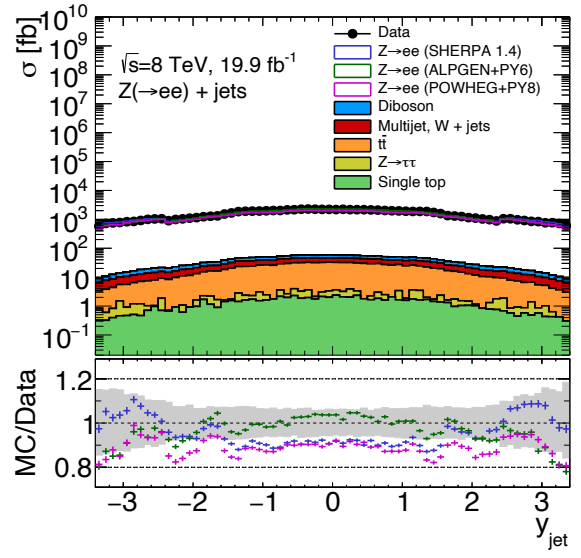
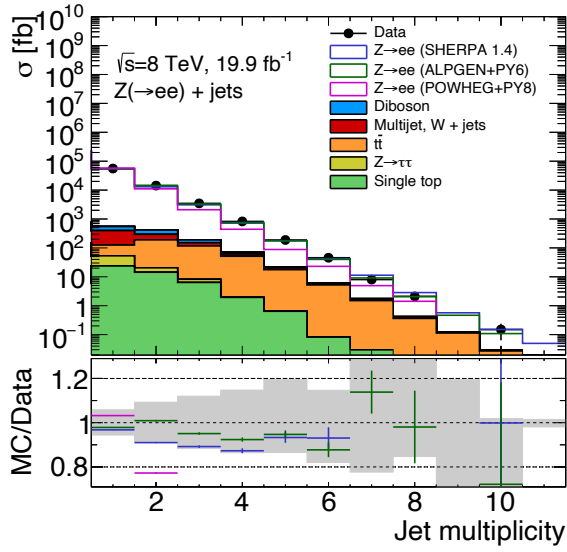


Figure 5.8 — Luminosity-normalised  $Z$  + jets yields as a function of electron's  $p_T$  and  $\eta$ , and  $Z$ -boson's  $p_T$  and  $y$ . Data are presented with markers. The filled areas correspond to the stack of backgrounds. All backgrounds are added to the simulated  $Z$  + jets predictions shown as coloured lines. Lower panels show ratios between the  $Z$  + jets predictions and data. The grey band shows the sum in quadrature of the electron and jet uncertainties. The statistical uncertainties are shown with vertical error bars.

(a) jet  $p_T$ (b) jet  $y$ 

(c) number of jets

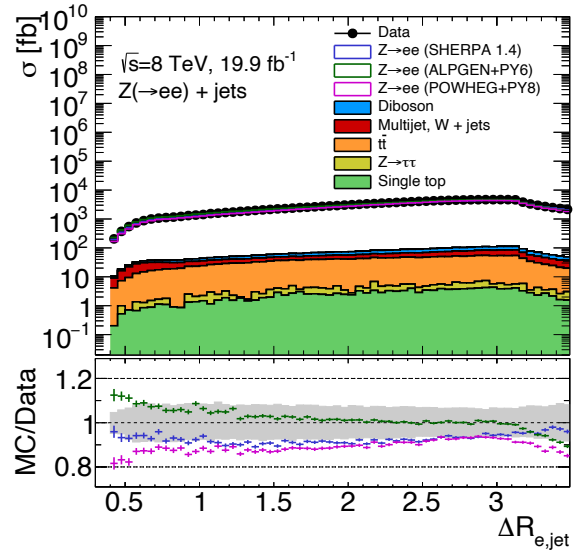
(d)  $\Delta R(\text{jet}, \text{electron})$ 

Figure 5.9 — Luminosity-normalised  $Z + \text{jets}$  yields as a function of jet  $p_T$ ,  $y$ , number of reconstructed jets and  $\Delta R$  between the jet and electron. Data are presented with markers. The filled areas correspond to the stack of backgrounds. All backgrounds are added to the simulated  $Z + \text{jets}$  predictions shown as coloured lines. Lower panels show ratios between the  $Z + \text{jets}$  predictions and data. The grey band shows the sum in quadrature of the electron and jet uncertainties. The statistical uncertainties are shown with vertical error bars.

## 5.6 Detector effects correction

The experiments are affected by the detector effects that distort the measurement. Among the sources of distortions are finite resolution, limited acceptance and inefficiencies of the detector. For example, the measured energies and angles of the reconstructed final state objects can fluctuate event by event due to the resolution. These fluctuations lead to migrations across the measured spectra, thus distorting the measured cross-sections. Due to the limited acceptance and inefficiencies of the detector, some particles may go undetected, or the particle's energy may only be measured partially. Influenced by the detector effects, the measured spectrum can be seen as if the true spectrum were folded with the detector response function describing all possible detector effects. As a result, these distortions complicate the direct comparisons between the measurements and theoretical predictions. They also make the comparisons between different experiments difficult. That is why a correction that unfolds the detector effects from the measured spectra is necessary.

### 5.6.1 Unfolding methods used in the cross-section measurement

There are various unfolding methods [194], that rely on simulations linking particle-level and detector-level information. These methods assume that the simulation describes the detector response well. The simulations performed by ATLAS are suitable for unfolding as they agree with the detector-level data and preserve the particle-level information. The unfolding methods used in the three-jets and  $Z + \text{jets}$  cross-section measurement are briefly introduced below.

The preparatory step of any method is the particle-level definition [195]. This establishes the ground to which the measured spectra are to be corrected. Compared to the detector level, the particle level can include particles that have been produced but not seen by the detector. Apart from that, at the particle level, there is no need to exclude the kinematics regions affected by the detector failures. So the unfolding will correct the detector level's shortcomings. As a result, the unfolded data can then be compared with theoretical predictions obtained using the same particle-level definition.

The simplest unfolding method estimates the correction factors as

$$C_i = N_i^{\mathcal{P}, \text{sim}} / N_i^{\mathcal{D}, \text{sim}}, \quad (5.8)$$

where  $N_i^{\mathcal{P}, \text{sim}}$  and  $N_i^{\mathcal{D}, \text{sim}}$  are the numbers of simulated events with the final state generated and reconstructed in the  $i$ -th region of the phase space, respectively. Thus, the number of events,  $N_i^{\mathcal{D}}$ , measured in the region  $i$  is unfolded to the particle-level using

$$N_i^{\mathcal{P}} = C_i N_i^{\mathcal{D}}, \quad (5.9)$$

where  $N_i^{\mathcal{P}}$  is the unfolded number of events. This method is referred to as the bin-by-bin correction, where the bin, in turn, refers to the intervals that subdivide the spectrum. The result of the bin-by-bin unfolding strongly depends on the quality of the modelling of the true distribution. In addition, the uncertainty in the method increases when significant migrations occur in the measured spectra. This motivates the use of wider phase space regions to reduce the impact of migrations.

Another class of methods aim for a more reliable unfolding when migrations are unavoidable. The methods use an unfolding probability matrix  $U$  that accounts for migrations better than  $C_i$ . The unfolding matrix connects the number of events with final states reconstructed in the region  $j$  to that caused by final states within  $i$ . The inputs to this class of unfolding methods are:

- the transfer matrix,  $A$ , with elements  $A_{ij}$  defined by the number of events with the final state generated in the region  $i$  but reconstructed in  $j$ . The matrix  $A$  is determined by matching the generated and reconstructed final states using simulations. Both final states are expected to be within the phase space predefined by the event selection criteria. When normalised by the number of events, the transfer matrix converts to the response matrix,  $\hat{A}$ . Thus, it provides means for an inverse problem solution that determines the unfolding matrix  $U$ ;
- the particle-level matching efficiency,  $\mathcal{E}_i^{\mathcal{P}}$ . It is calculated as a fraction of generated events with the final state in the region  $i$  matched to any reconstructed final state. The latter is limited only by the predefined phase space. The  $\mathcal{E}_i^{\mathcal{P}}$  is below one when there are final states reconstructed outside of the predefined phase space, that is when no matching occurs;
- the detector-level matching efficiency,  $\mathcal{E}_j^{\mathcal{D}}$ . It is calculated as a fraction of reconstructed events with the final state in the region  $j$  matched to any generated final state. The latter is limited only by the predefined phase space. The  $\mathcal{E}_j^{\mathcal{D}}$  is below one when there are reconstructed final states generated outside of the predefined phase space, that is when no matching occurs. The  $\mathcal{E}_j^{\mathcal{D}}$  can also be affected by the background events like pile-up having no particle-level preserved.

As a result, the unfolding can be expressed as

$$N_i^{\mathcal{P}} = \frac{1}{\mathcal{E}_i^{\mathcal{P}}} \sum_j U_{ij} \mathcal{E}_j^{\mathcal{D}} N_j^{\mathcal{D}}. \quad (5.10)$$

Calculating  $U$  by inverting the  $A$  is an often ill-defined problem. The solution results in highly oscillating unfolded spectra since the data and simulation have finite statistics. However, some methods overcome this issue through

regularisation. This involves using some a priori information about the unfolded spectrum. Such methods are Singular Value Decomposition (SVD) [196], D'Agostini [197] and Iterative Dynamically Stabilised (IDS) [198] unfolding.

The SVD method performs a decomposition of the matrix  $\hat{A}$  through  $\hat{A} = WSV^T$ , where  $W$  and  $V$  are orthogonal matrices, and  $S$  is diagonal. The  $U$  is evaluated by inverting the  $WSV^T$ . Small diagonal elements  $S_{ij}$  leading to high oscillations are suppressed by minimising the difference between the unfolded and true distribution in the simulation. The minimisation uses a regularisation term favouring unfolded spectra with the smallest curvature. However, the regularisation introduces long-range constraints that can lead to over-smoothed results.

The D'Agostini method justifies using Bayes' theorem to determine  $U$  from  $A$ , assuming that  $A$  encodes the a priori probability of the occurrence of an event and the conditional probability of its reconstruction. The unfolding results are iteratively improved by updating the inputs based on the results of each iteration. Thus, the effect of the true distribution mis-modelling is minimised. However, iterations increase the statistical uncertainty. The number of iterations is essentially a regularisation parameter. At least several iterations are often required.

In the IDS method, the unfolding matrix is defined as  $U_{ij} = A_{ij} / \sum_k A_{kj}$ . The key feature of the method is that only a statistically significant fraction of events are transferred. These events are defined bin-by-bin using a smooth monotonous function proportional to  $\Delta x / (\lambda \delta)$ , where  $\Delta x$  is the absolute difference between data and simulation,  $\delta$  is the corresponding error, and  $\lambda$  is a regularisation parameter. The unfolding results are also improved with iterations, thus avoiding bias due to the true distribution mis-modelling. However, the number of iterations required is usually less than in the D'Agostini method.

There are different assumptions behind the unfolding methods, so it is not obvious which method is the most accurate. To address this uncertainty, the measured distributions are unfolded using several methods, and the best one is selected. To determine the best method, two closure tests are performed. A data-driven test evaluates the effect of mis-modelling the shape of the particle level spectrum of the observable being measured. To do this, the transfer matrix is reweighted bin-by-bin until it provides the detector level distribution that matches the  $\mathcal{E}_j^{\mathcal{D}}$ -corrected data. In this case, the particle level distribution provided by the reweighted matrix is assumed to describe the true distribution better. The detector level distribution of the reweighted matrix is unfolded using the original transfer matrix as an input. The unfolded distribution is compared to the particle-level one of the reweighted matrix. The differences are treated as unfolding errors.

Another is the simulation-based closure test. It evaluates the impact of mis-modelling the particle-level spectral shape in quantities that are different from those being measured but which affect the detector response. Such quantities are often referred to as the hidden variables. For example, a certain bias may be asso-

ciated with mis-modelling of quark and gluon jet composition. So, an alternative simulation obtained using a different event generator is used for unfolding. A new transfer matrix is obtained using this simulation. This matrix is reweighted until it provides the detector-level distribution that matches the original simulation, so only the effect on detector response rather than the difference between the predictions will be evaluated by the test. Then, the detector-level distribution of the original simulation is unfolded using the reweighted transfer matrix of the alternative simulation. The unfolded distribution is compared to the particle-level one of the original simulation. The differences are treated as another source of unfolding errors.

Apart from evaluating the unfolding performance, closure tests are used to determine the optimal number of unfolding iterations in methods for which this is relevant. The number of iterations at which the statistical uncertainty in the unfolded data exceeds the unfolding error is usually considered optimal.

As a result of the tests, the unfolding method leading to the smallest uncertainty is used to correct detector effects in the data.

## 5.6.2 Unfolding the three-jets data

The performance of several unfolding methods is evaluated in the three-jets cross-section measurement to identify the best one. The bin-by-bin, SVD and IDS methods are explored.

The measured detector-level spectra are unfolded to the particle level, which is defined by three jets clustered on any final-state particle, including the undetected presence of muons and neutrinos from hadron decays in jets. The clustering is performed using the anti- $k_t$  jet algorithm. The phase space is defined by that of the jets selected for the measurement, see Table 5.1. No exclusion of the  $\phi$  region associated with the detector failure is used at the particle level. Thus, a correction for undetected events is performed by the unfolding.

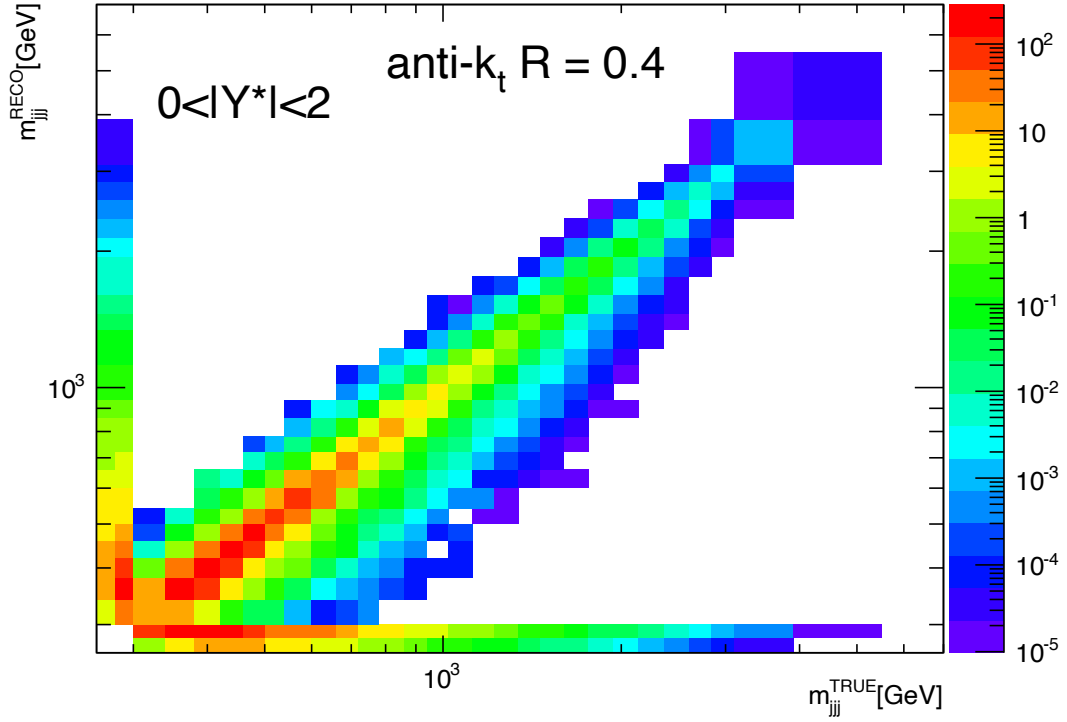
Preparing inputs for the unfolding requires matching the detector-level to particle-level final states to ensure that three leading- $p_T$  jets at both levels are identical. The matching is done in the  $m_{jjj}-|Y^*|$  plane. That is, for each  $|Y^*|$  region, only a three-jets system is required that meets the event selection conditions. This is sufficient to conclude that the three leading- $p_T$  jets are identical at both levels. However, the detector-level jets displaced significantly from their particle-level counterparts can cause larger migrations in the transfer matrix. The distance between the particle-level and detector-level jets is studied to ensure this is not the case. As a result, it was found that three leading- $p_T$  jets at the detector level are always within the jet radius of that at the particle level. Thus, geometrically matching jets per event is equivalent to event-wide matching when measuring three-jets cross-section.

Events with matched three jets make up inputs for the unfolding. The transfer matrix and matching efficiencies obtained using matched events in the  $|Y^*| < 2$  region are shown in Figure 5.10. The transfer matrix represents significant migrations of events across the three-jets mass spectrum. These migrations are mainly due to jet energy smearing. Migrations associated with the jet angular resolution occur less often. That is why unfolding is performed separately in each  $|Y^*|$  bin. The measurement starts at  $m_{\text{jjj}} = 380$  GeV within the  $|Y^*| < 2$ , thus avoiding the region of phase space affected by the jet  $p_{\text{T}}$  cuts. This lowest  $m_{\text{jjj}}$  increases to 1180 GeV for the  $8 < |Y^*| < 10$  range. However, events with lower  $m_{\text{jjj}}$  are also kept for the unfolding to account for migrations.

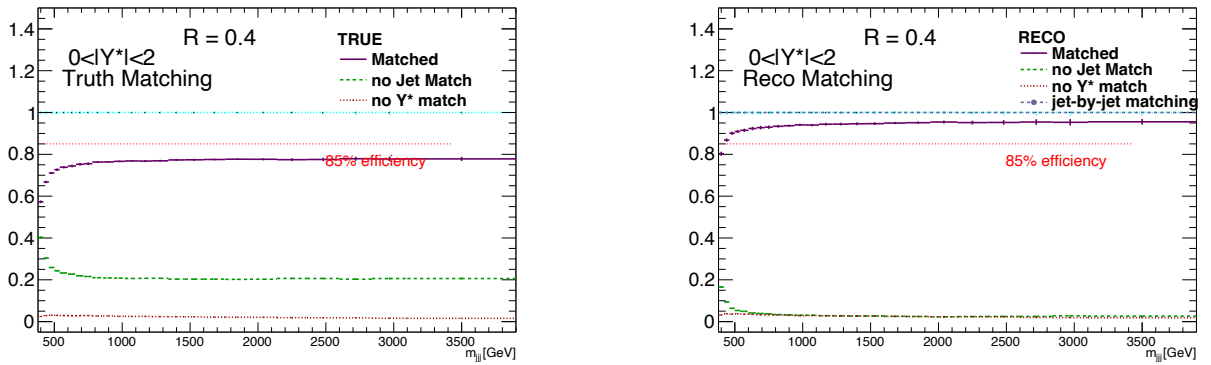
The particle-level and detector-level matching efficiencies are above 80% and 95%, respectively, in most bins of the measurement. A relatively large particle-level inefficiency is due to an excluded region of  $\phi$  at the detector level. Other inefficiencies are due to events generated or reconstructed outside of the allowed kinematics.

The unfolding is performed using the derived transfer matrices and matching efficiencies. The errors of all three unfolding methods are estimated using a data-driven closure test. The results of the test are shown in Figure 5.11. The error of the bin-by-bin unfolding is negligible in most bins of the measurements. However, in the region of the highest  $m_{\text{jjj}}$  and  $|Y^*|$ , the error is about 1%. The SVD unfolding is the least reliable of the probed methods. It results in an error that increases as a function of  $m_{\text{jjj}}$  reaching 7%. The IDS unfolding without iterations also results in an error that increases as a function of  $m_{\text{jjj}}$ . However, this error is smaller than in the SVD. The IDS performance is significantly improved after one iteration of the unfolding. As a result, the estimated error is almost zero in all bins of the measurement. These conclusions are valid both when measuring the three-jets cross-section with  $R = 0.4$  and  $R = 0.6$  jets.

The IDS unfolding with one iteration is adopted for the three-jets cross-section measurement.



(a) The transfer matrix in the three-jets cross-section measurement. The particle-level  $m_{\text{jjj}}$  is on the x-axis, while the detector-level  $m_{\text{jjj}}$  is on the y-axis. The z-axis represents the number of events. The non-diagonal elements represent migrations of events across the  $m_{\text{jjj}}$  spectrum. The first two columns and rows represent the mismatch probabilities. The first column (row) represents the probability of mismatch only due to a different  $|Y^*|$  on the particle level (detector level). The second column (row) represents the probability of mismatch only due to a failed jet  $p_{\text{T}}$  requirement on the particle level (detector level). Events below the lowest  $m_{\text{jjj}}$  defined by the three jet  $p_{\text{T}}$  requirements are also shown.



(b) The (left) particle-level and (right) detector-level matching efficiencies as a function of  $m_{\text{jjj}}$ . The matching efficiencies are shown in violet. The inefficiencies due to a different  $|Y^*|$  on the other level are shown in red. The inefficiencies due to a failed jet  $p_{\text{T}}$  requirement on the other level are shown in green. The horizontal lines represent the 85% and 100% efficiency levels. The three leading- $p_{\text{T}}$  jets at the detector level are always within the jet radius of their particle-level counterparts, as shown with dark blue.

Figure 5.10 — Inputs to the unfolding in the three-jets cross-section measurement in the  $|Y^*| < 2$  region.

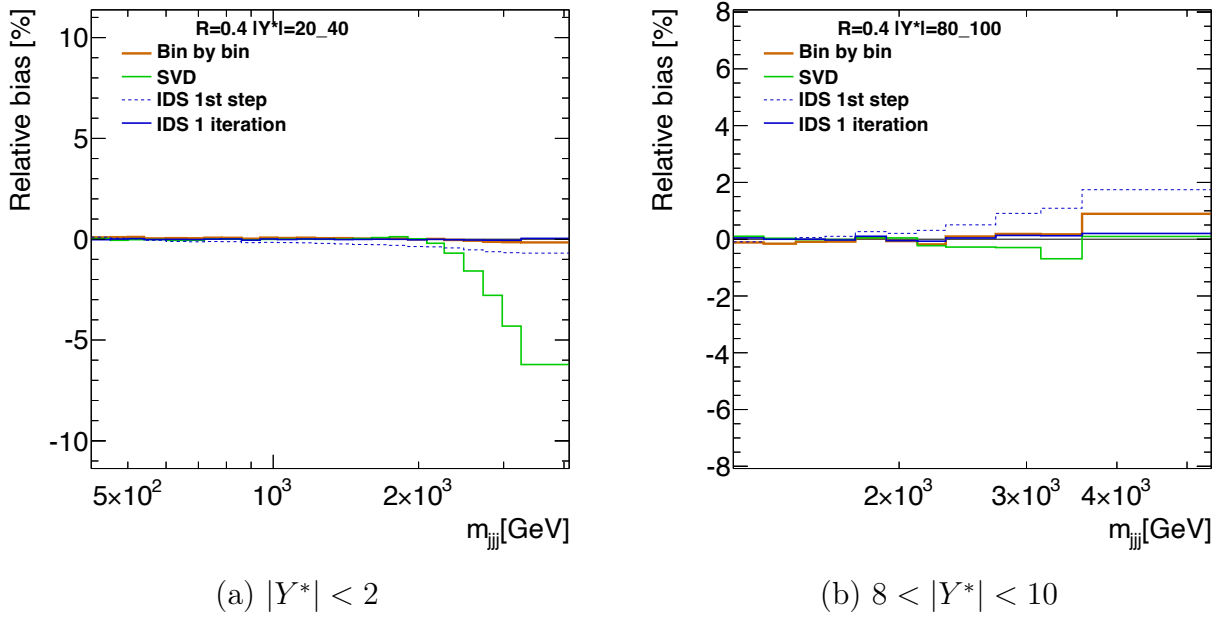


Figure 5.11 — The bias of unfolding performed by the bin-by-bin, SVD and IDS methods in the three-jets cross-section measurement. Different unfolding methods are shown in colour. The errors are estimated using a data-driven method. The dotted line depicts the error of the IDS unfolding without iterations. This error becomes negligible after the first iteration.

### 5.6.3 Unfolding the $Z + \text{jets}$ data

Two unfolding methods are probed in the  $Z + \text{jets}$  cross-section measurement. These are the bin-by-bin and D’Agostini methods.

The unfolding is performed to the particle level defined by two electrons and at least one jet. The phase space is defined by that of the electron and jets selected for the measurement, as presented in Table 5.2. However, it includes two important assumptions. The first is associated with the photons radiated by an electron. By design, the reconstruction of electrons partially accounts for the energy carried by these photons. However, only photons that follow the electron direction closely are accounted for due to finite cluster size. Mis-modelling of photon emissions outside the cluster brings significant uncertainty to the unfolding. To reduce this uncertainty, the photon emission at the particle level is also considered. The four-momenta of any photons within a cone of  $\Delta R = 0.1$  around the electron axis are added to the four-momentum of the particle-level electron. Such electrons are referred to as the dressed ones as opposed to the bare electrons, where the energy of radiated photons is neglected. However, these electrons are softer than those at the lowest order in QED, referred to as the born electrons. The second assumption implies including electrons falling into the detector transition region. Thus, the undetected events are corrected by the unfolding.

The particle-level jets are clustered using the anti- $k_t$  algorithm on the stable final-state particles with a decay length of  $c\tau > 10 \text{ mm}$ <sup>1</sup>, excluding muons and neutrinos. The same particle-level jet definition is used in the jet energy calibration. As a result, the unfolded cross-section avoids errors due to the mismodelling of these particles.

The simulated  $Z + \text{jets}$  final state at the detector level match that at the particle level if the selection requirements are met at both levels. In addition, a geometric requirement is imposed to ensure that each detector-level jet corresponds to its particle-level counterpart. The closest jets at different levels match if  $\Delta R$  between their axes satisfies  $\Delta R < 0.4$ .

The matched jets make up the unfolding inputs. The derived transfer matrix and matching efficiencies are shown in Figure 5.12. Migrations across different regions of  $|y_{\text{jet}}|$  and  $p_{\text{T}}^{\text{jet}}$  are studied simultaneously. A linear transformation function converting the two-dimensional observable into a one-dimensional is used for this purpose. This function attaches the cross-section measured as a function of  $|y_{\text{jet}}|$  in a subsequent  $p_{\text{T}}^{\text{jet}}$  region to the previous one until they are all represented as a wide one-dimensional histogram. Given a good jet angular resolution, the migrations in the  $|y_{\text{jet}}|$  spectra are less than a few per mille. They are barely visible along the main diagonal of the transfer matrix, in which the dotted-lined

---

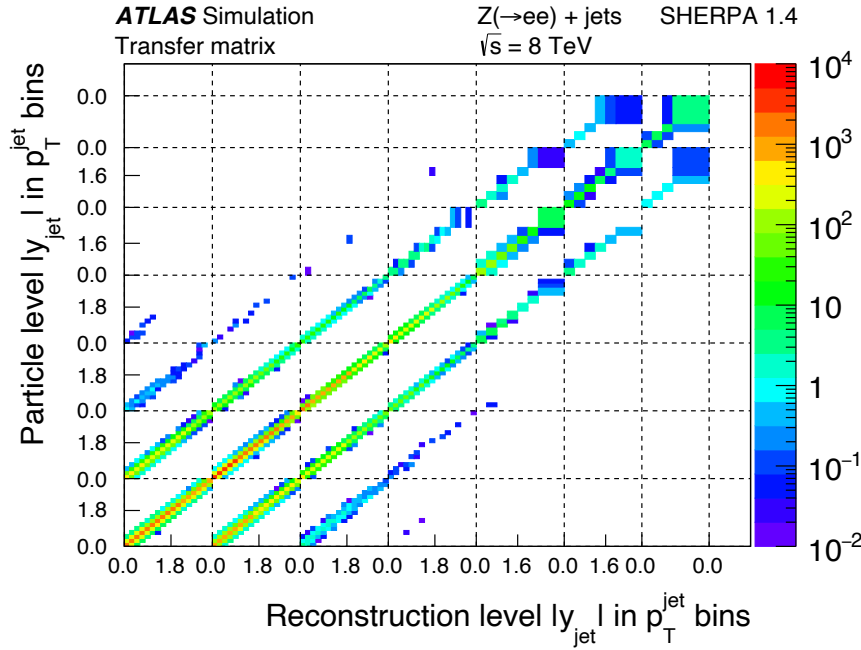
<sup>1</sup>Particles outside of  $c\tau > 10 \text{ mm}$  range curl up by magnetic field and do not reach the detector.

squares represent different  $p_T^{\text{jet}}$  regions. The elements at superdiagonals and sub-diagonals represent significant migrations between different  $p_T^{\text{jet}}$  regions. These migrations are associated with finite jet energy resolution. Two additional  $p_T^{\text{jet}}$  regions are kept to account for migrations outside of a measured range. These regions are limited by  $17 \text{ GeV} < p_T^{\text{jet}} < 25 \text{ GeV}$  and  $p_T^{\text{jet}} > 1050 \text{ GeV}$ . As a result, the unfolding takes migrations to and from these regions into account.

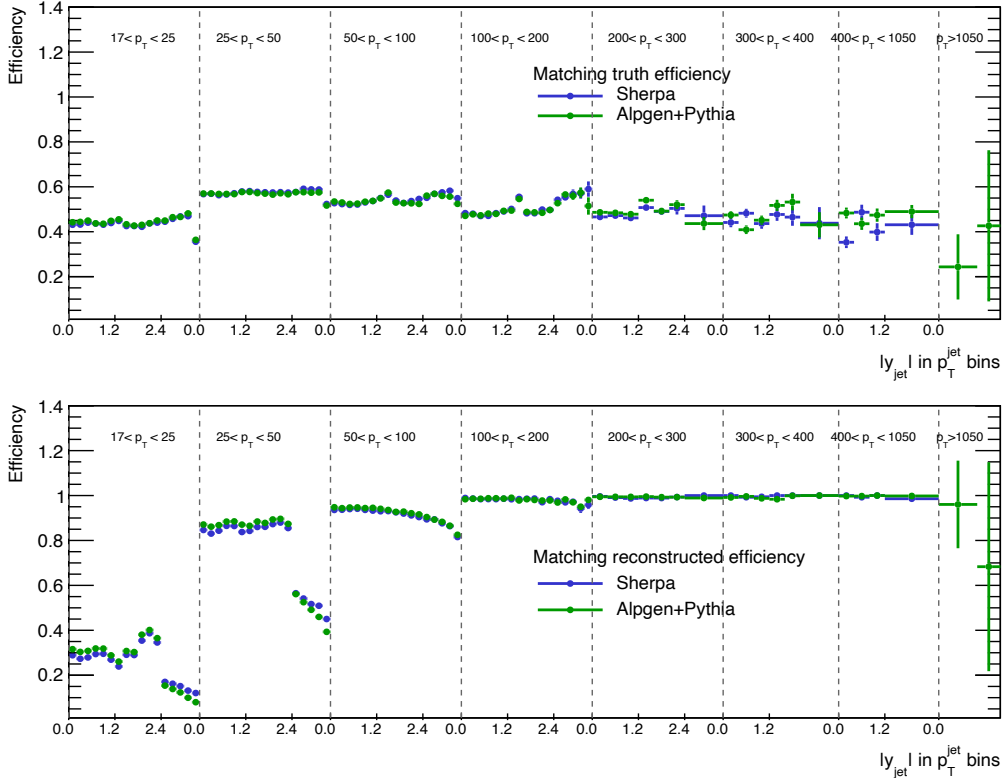
The particle-level and detector-level matching efficiencies are above 45% and 80%, respectively. A relatively large matching inefficiency at the particle level is attributed to an inefficient  $Z$ -boson reconstruction known from previous ATLAS studies. Despite this, the particle level efficiency is approximately flat across the entire range of the jet kinematics, so the unfolding is straightforward. The detector-level matching efficiency is close to 100% in the  $100 \text{ GeV} < p_T^{\text{jet}} < 1050 \text{ GeV}$  range, which also simplifies the unfolding. However, there is significant inefficiency in the  $25 \text{ GeV} < p_T^{\text{jet}} < 100 \text{ GeV}$  range, which is attributed to migrations between different  $p_T^{\text{jet}}$  regions and residual contribution from pile-up that survived suppression. The largest inefficiency is within the phase space region of  $2.4 < |y_{\text{jet}}| < 3.2$  and  $25 \text{ GeV} < p_T^{\text{jet}} < 50 \text{ GeV}$ , which is outside of the JVF coverage, so this region is largely affected by pile-up jets. These jets are poorly modelled, which negatively affects the detector effects correction, which is why this region is not reported in the cross-section measurement. The efficiency is even lower in the  $17 \text{ GeV} < p_T^{\text{jet}} < 25 \text{ GeV}$  region, where the effects of migration and pile-up increase. However, this region is also not reported in the cross-section measurement since its only purpose is to account for migrations.

The derived transfer matrix and matching efficiencies are used to unfold the  $Z + \text{jets}$  data. The performance of the D'Agostini unfolding with up to ten iterations is probed. The unfolding errors are estimated using the data-driven and simulation-based closure tests. The errors after three unfolding iterations are mainly compatible with the data statistical uncertainty, as shown in Figure 5.13. A larger number of iterations does not significantly improve the unfolding performance but results in greater statistical uncertainty. The errors in the additional  $p_T^{\text{jet}}$  regions used to account for migrations outside of a measured range are ignored when evaluating the unfolding performance. In the  $25 \text{ GeV} < p_T^{\text{jet}} < 50 \text{ GeV}$  region, the effect of the true distribution mis-modelling reaches up to 5%, as shown by the data-driven closure test. The unfolding error in this region exceeds the statistical uncertainty. Since the true distribution modelling is imperfect, the D'Agostini's unfolding is preferred over the bin-by-bin one, as the latter relies more on the modelling quality. Another error of the bin-by-bin unfolding is estimated using the simulation-based closure test is shown in Figure 5.14. The error is compatible with that of the D'Agostini unfolding in most of the phase space. But, the error of the bin-by-bin is larger in the  $25 \text{ GeV} < p_T^{\text{jet}} < 50 \text{ GeV}$  region by several per cent. That is why the D'Agostini unfolding is favoured.

The D'Agostini unfolding with three iterations is adopted for the  $Z + \text{jets}$  cross-section measurement.



(a) The transfer matrix in the  $Z + \text{jets}$  cross-section measurement. The detector-level  $|y_{\text{jet}}|$  is on the x-axis, while the particle-level  $|y_{\text{jet}}|$  is on the y-axis. The dotted-lined squares enclose  $|y_{\text{jet}}|$  obtained in different  $p_{\text{T}}^{\text{jet}}$  regions, whose magnitude increases sequentially along the main diagonal starting from the lower left bottom corner. The first and last squares along the main diagonal are additional  $p_{\text{T}}^{\text{jet}}$  regions used to account for migrations outside of a measured range. The z-axis represents the number of jets. The non-diagonal elements represent migrations. Close to the main diagonal are the migrations in the  $|y_{\text{jet}}|$  spectra. The elements at superdiagonals and subdiagonals represent migrations between  $p_{\text{T}}^{\text{jet}}$  intervals.



(b) The (top) particle-level and (bottom) detector-level matching efficiencies as a function of  $|y_{\text{jet}}|$ . The dotted vertical lines designate transitions between  $p_{\text{T}}^{\text{jet}}$  regions. The first and last  $p_{\text{T}}^{\text{jet}}$  regions are used to account for migrations outside of a measured range and are not reported in the measurement. The matching efficiencies obtained using different event generators are shown in colour.

Figure 5.12 — Inputs to the unfolding in the  $Z + \text{jets}$  cross-section measurement.

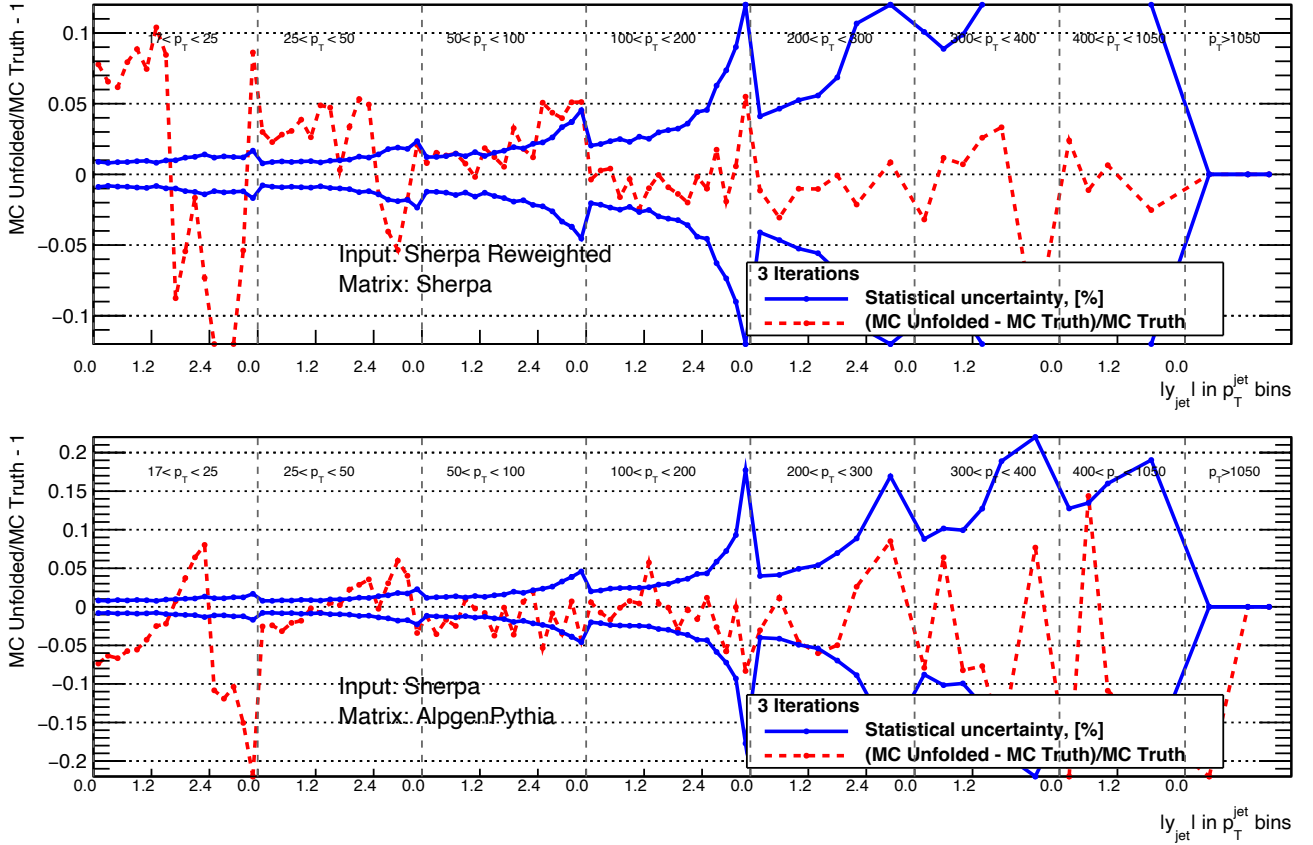


Figure 5.13 — The (top) data-driven and (bottom) simulation-based closure test of the D’Agostini unfolding with three iterations. The unfolding errors are shown in red as a function of  $|y_{\text{jet}}|$ . The data statistical uncertainty is shown in blue. The dotted vertical lines designate transitions between  $p_T^{\text{jet}}$  regions. The first and last  $p_T^{\text{jet}}$  regions are used to account for migrations outside of a measured range and are not reported in the measurement.

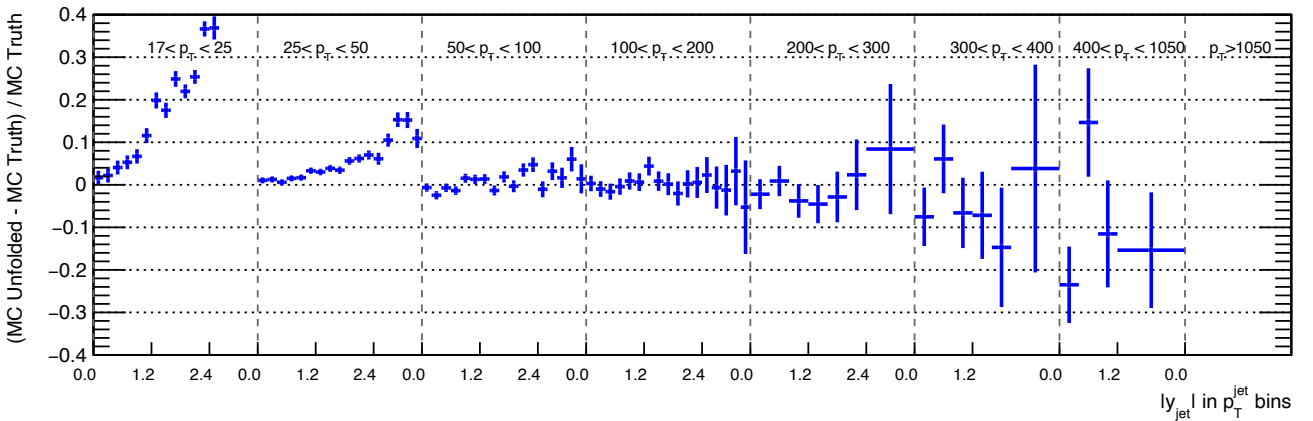


Figure 5.14 — The simulation-based closure test of the bin-by-bin unfolding. The unfolding bias is shown as a function of  $|y_{\text{jet}}|$ . The dotted vertical lines designate transitions between  $p_T^{\text{jet}}$  regions. The first and last  $p_T^{\text{jet}}$  regions are used to account for migrations outside of a measured range and are not reported in the measurement.

## 5.7 Uncertainties in the cross-section measurements

Uncertainty evaluation is an inherent part of any measurement. The sources of uncertainty in the three-jets and  $Z + \text{jets}$  cross-section measurements are discussed in this section. Many of the uncertainties in both measurements have the same origins. Therefore, when individual uncertainty sources are introduced, it is explicitly specified to which measurement the uncertainty belongs.

Individual uncertainties are evaluated by introducing systematic variations to the analysis. For example, the reconstructed jet energy or an event weight can be shifted up and down. The property being varied is explicitly specified for each source of uncertainty. The amount by which a given property is shifted is usually equal to the size of the uncertainty unless otherwise stated. The variations are performed using simulation to reduce the effect of limited statistics in the data. A new transfer matrix and matching efficiencies are calculated for each systematic variation, and the data unfolding is performed. The deviation from the originally unfolded data is assigned as the systematic uncertainty in the measured cross-section.

Despite using simulation to reduce the effect of statistical fluctuations, it is impossible to avoid them completely since simulated event samples are also finite. Thus, a technique is introduced to reduce statistical fluctuations in systematic uncertainties.

Right after this, the statistical uncertainties in the measurements are discussed.

The uncertainties in each measurement are quantified at the end of the section.

### 5.7.1 Inaccuracy in the jet energy measurement

Jet energy is measured with limited precision. This affects any measurement using jets in the final state. It is among the dominant uncertainties in previous measurements of the three-jets and  $Z + \text{jets}$  cross-sections in ATLAS. Therefore, this uncertainty is discussed in detail.

More than fifty components describe the uncertainty in the jet energy measurement. Each uncertainty component is independent of the others and fully correlated across jet  $p_{\text{T}}$  and  $\eta$ . The uncertainties are propagated to the measured cross-section by varying the reconstructed jet energy. Each component is propagated separately to keep information about the correlations. The individual uncertainty components are discussed in this section.

### 5.7.1.1 Inaccuracy in the jet energy calibration in the central detector region

Jet energy calibration in the central detector region of  $|\eta| < 0.8^2$  is established *in situ* using  $Z + \text{jets}$ ,  $\gamma + \text{jets}$  and multi-jet events. The calibration equalises the jet response in data and simulation, where the jet response is defined relative to the transverse momentum of a reference object whose energy is measured precisely. Uncertainties in the calibration using  $Z + \text{jets}$  events are detailed in Section 4.4. They are associated with inaccuracies in measuring the energy of the reference object and mis-modelling of physics effects relevant to the calibration. Similar uncertainty sources are inherent in the calibrations using the other two event topologies.

The combination of different *in situ* calibrations ensures that each contributes to a region of jet energy where it is most accurate. The combination procedure introduces correlations between different regions of jet  $p_T$ . Thus, a fluctuation of the calibration in any region causes a systematic shift in the others. Therefore, statistical uncertainties in jet calibrations are treated as systematic uncertainty components in the cross-section measurement.

As a result, the inaccuracy in the jet energy calibration in the central detector region is described by 54 systematic uncertainty components [150]. These uncertainties are propagated to the three-jets cross-section measurement.

The jet energy calibration in the data used for the  $Z + \text{jets}$  cross-section measurements is described by 56 systematic uncertainty components [151]. The number of components is larger due to different treatments of the uncertainty associated with the electron energy resolution mis-modelling, which was previously neglected. In addition, the phase space slicing differs between the calibrations. However, using a large number of systematic uncertainties complicates the analysis. Therefore, a reduced set is used to describe these uncertainties. The reduction is performed by combining uncertainties in a way that minimises the loss of correlations. This is done by calculating a total covariance matrix using all uncertainty components. An eigenvector decomposition is performed on this matrix to determine a new set of effective uncertainty components. The largest of the resulting orthogonal terms are kept separate, while others are combined quadratically. As a result, the reduced set of six effective uncertainty components is obtained. The loss of information on correlations does not exceed a few per cent. These uncertainties are propagated to the  $Z + \text{jets}$  cross-section measurement.

---

<sup>2</sup>The  $|\eta| < 1.2$  region is used when calibrating jets in the 7 TeV data to obtain more statistics.

### 5.7.1.2 Inaccuracy in the jet energy calibration in the forward detector region

The  $\eta$ -intercalibration extends the jet energy calibration towards the forward detector regions. The dijet production events are used for this purpose. The dominant systematic uncertainty is the difference to a calibration obtained with an alternative event generator. This uncertainty accounts for the dijet production mis-modelling. There are other systematic uncertainties [150], but they are relatively small. Thus, they are combined in quadrature with the modelling uncertainty. The loss of correlation information due to the summation is assumed to be negligible. The resulting uncertainty is propagated to both measurements.

Another uncertainty source is associated with the statistical uncertainty in the calibration. This uncertainty is non-zero in the central detector region, where the modelling uncertainty is zero by the design of the  $\eta$ -intercalibration. The statistical uncertainty is propagated separately to both measurements.

### 5.7.1.3 Inaccuracy in subtracting pile-up contribution

The pile-up contribution is subtracted from jets at an early stage of the JES calibration. The method used for pile-up energy subtraction has the associated systematic uncertainty. The uncertainty is described by four components. One is due to the event  $p_T$  density dependence on the event topology. It is evaluated as the largest difference between the average  $p_T$  densities in  $Z + \text{jets}$ ,  $\gamma + \text{jets}$  and multi-jet events.

Two other components are due to the mis-modelling of the corrections for residual pile-up contribution. These uncertainties are estimated *in situ* by re-evaluating the  $\langle\mu\rangle$  and  $N_{PV}$  corrections using pile-up insensitive reference objects in the data. These reference objects are the jets clustered on reconstructed tracks and  $Z$ -bosons in the  $Z + \text{jets}$  events. The differences between the corrections evaluated in the data and simulation are treated as uncertainties.

Finally, an uncertainty is used that accounts for jet  $p_T$  dependence of the residual pile-up correction. To evaluate this uncertainty, the correction is studied as a function of the jet  $p_T$  using the  $Z + \text{jets}$  events. The largest difference between the corrections derived from the data and simulation is treated as uncertainty.

These uncertainties are propagated to the  $Z + \text{jets}$  cross-section measurements.

The three-jets cross-section is measured in the data with a relatively low pile-up contribution. Only what is referred to as the residual pile-up correction in Section 4.2 is used in the jet calibration. The area-based pile-up correction is not used in the measurement as it does not improve the performance of pile-up subtraction. Therefore, two components describe the uncertainty associated with the  $\langle\mu\rangle$  and  $N_{PV}$  corrections. The uncertainty in the jet  $p_T$  dependence of the residual pile-up correction is very small and can be neglected.

### 5.7.1.4 Difference between the detector response to quark-initiated and gluon-initiated jets

Jets initiated by quarks and gluons respond differently in the detector. The energy response of calibrated jets is higher when they are initiated by quark than by gluon [150]. These differences are associated with the radiation characteristics of quarks and gluons. However, an uncertainty that accounts for these differences depends on the fraction of quark and gluon initiated jets in a given sample of events. Thus, it is necessary to determine the fraction of gluon-initiated jets  $f_g$  based on the analysis. The fraction of quark-initiated jets is estimated by  $(1 - f_g)$ . As a result, the jet flavour-related uncertainty has two components. One component accounts for the jet energy response difference with some uncertainty  $u_g$  on the  $f_g$  in the sample. This is the so-called flavour composition uncertainty estimated as

$$u_{\text{composition}} = u_g \frac{|r_q - r_g|}{f_g r_g + (1 - f_g) r_q}, \quad (5.11)$$

where  $r_q$  and  $r_g$  are the energy responses of jets initiated by quarks and gluons. Another component accounts for the mis-modelling of the response of gluon initiated jets from different event generators. The generators modelling parton showers, hadronisation and underlying event differently are taken. This component, known as the flavour response uncertainty, is thus estimated as

$$u_{\text{response}} = f_g (r_g^{\text{PYTHIA}} - r_q^{\text{HERWIG}}). \quad (5.12)$$

The mis-modelling of the response of quark initiated jets is small, so it is neglected.

The  $f_g$  is determined using the three-jets and  $Z$  + jets simulations. The flavour of each jet is assigned by the parton with the highest energy within the jet cone. The  $f_g$  is obtained as a function of jet kinematics probed by each measurement. The spread between different predictions is used to estimate  $u_g$ . Thus, the flavour composition and response uncertainties relevant to each event sample used in the measurements are derived. These uncertainties are propagated to the measured cross-sections.

### 5.7.1.5 Inaccuracy in the calibration for jets with the highest transverse momenta

The *in situ* methods are used to calibrate jets with  $p_T$  up to 1 TeV and 1.5 TeV in the 7 TeV and 8 TeV  $pp$  collisions data, respectively. These upper limits are due to a kinematic and statistical limitation of the multi-jet calibration used for high- $p_T$  jets. However, there are jets with a higher  $p_T$ . They use the calibration of the highest- $p_T$  jet probed *in situ* but with greater uncertainty. This uncertainty is estimated by that of single hadrons that make up jets. Single hadrons are calibrated at the test-beam experiments [150]. Convolution of their

uncertainties is used as an estimate of the jet uncertainty. This uncertainty is propagated to both measurements.

#### 5.7.1.6 Mis-modelling of close-by jets

Jet energy scale calibration is derived using isolated jets. However, jets in the analysis selection are often produced in a busy environment, so the energies of close-by jets overlap. A mis-modelling of close-by activity may lead to inaccuracy in the jet energy calibration. The uncertainty is estimated *in situ* using jets reconstructed using inner-detector tracks. The resulting uncertainty accounts for the jet response difference between data and simulation for overlapping jets. This uncertainty is propagated to the three-jets cross-section measurements. This uncertainty is negligible in jet calibration obtained using the 8 TeV data, so it is not used in the  $Z + \text{jets}$  cross-section measurement.

#### 5.7.1.7 Mis-modelling of punch-through jets

High-energy jets carry away some of the energy when they leave the calorimeter. The associated punch-through effect is accounted for in the jet calibration if such jets are well-modelled. The modelling quality is estimated by evaluating missing transverse momentum pointing towards the direction of the jet or using muons spectrometer segments hit by the jets. The punch-through is well-modelled in jet calibration obtained using the 7 TeV data [149], so uncertainty is neglected when measuring the three-jets cross-section. However, a non-negligible uncertainty is obtained in the calibration using 8 TeV data [151], which is propagated to the  $Z + \text{jets}$  cross-section measurement.

#### 5.7.1.8 Inaccuracy in the detector description

The description of the detector is constantly being improved. The effect of the improved detector description on the jet calibration is treated as uncertainty. This uncertainty, referred to as the MC non-closure, is generally negligible [151]. However, it is propagated to the  $Z + \text{jets}$  cross-section measurement.

### 5.7.2 Inaccuracy in the electron energy measurement

Electrons are used for event selection in the  $Z + \text{jets}$  cross-section measurement. Thus, the inaccuracy in the electron energy measurement affects the measured cross-section mainly through the number of selected events.

There are many uncertainty sources when measuring the energy of electrons. Among them are the inaccuracy in the detector electronics calibration, mis-modelling of the detector noise and electromagnetic shower energy losses in front of the calorimeter, behind it, and outside of the reconstructed calorimeter

clusters. However, the total uncertainty is within 1% [162]. Since the cross-section measurement examines mostly the jet properties, the effect of this uncertainty is small. Therefore, the total uncertainty is propagated to the cross-section measurement. For this, the variations of reconstructed electron energy are performed.

### 5.7.3 Mis-modelling of the detector resolution

The energies and angles of the reconstructed particles fluctuate around their most probable value due to finite detector resolution. This applies both to electrons and jets used in the measurements. These fluctuations cause migrations of events across the measured spectra, thereby distorting the measurement. The distortions are corrected by the unfolding. However, the unfolding is based on simulation, so the detector resolution mis-modelling distorts the measurement through this correction. This is usually not the case since the simulation is often adjusted to model the resolution in the data well. However, the resolution is measured with uncertainty. Thus, it is necessary to propagate this uncertainty to the measured cross-section to account for a potential mis-modelling of the resolution.

The uncertainty is propagated by smearing a given property rather than by shifting as elsewhere. The smearing is designed to reproduce a resolution increased by the uncertainty. The scale factors varying from event to event are used to do this. These scale factors are drawn from Gaussian distribution with a mean of one and standard deviation  $\mathcal{R}_{\text{smear}}$ . The  $\mathcal{R}_{\text{smear}}$  is calculated as

$$\mathcal{R}_{\text{smear}}^2 = (\mathcal{R}_{\text{nom}} + u_{\mathcal{R}})^2 - \mathcal{R}_{\text{nom}}^2, \quad (5.13)$$

where  $\mathcal{R}_{\text{nom}}$  is the nominal resolution and  $u_{\mathcal{R}}$  is the uncertainty. The smeared property depends on the resolution in question. The uncertainty is symmetrised at the cross-section level to account for the resolution decreased by the uncertainty.

There are several detector resolution components whose uncertainties are propagated to the measurements. These components are discussed along with their uncertainties in this section.

#### 5.7.3.1 Jet energy resolution

The jet energy resolution (JER) causes migrations mainly across the spectra of  $m_{\text{jjj}}$  in the three-jets cross-section measurement and  $p_{\text{T}}^{\text{jet}}$  in the  $Z + \text{jets}$  cross-section measurement. The JER is measured *in situ* as a function of jet  $p_{\text{T}}$  and  $\eta$  using the dijet,  $Z + \text{jet}$  and  $\gamma + \text{jet}$  events [151, 199]. It decreases as a function of  $p_{\text{T}}^{\text{jet}}$  from 20% at  $p_{\text{T}}^{\text{jet}}$  near 25 GeV to 3% near 1 TeV. The total uncertainty in the JER measurement is about 10–20% across the  $p_{\text{T}}^{\text{jet}}$ . The JER in simulation reproduces the data generally well within this uncertainty, so no JER adjustments are performed. This uncertainty is propagated to the measured cross-section by smearing the reconstructed jet energy.

### 5.7.3.2 Jet angular resolution

The jet angular resolution (JAR) affects both the  $m_{\text{jjj}}-|Y^*|$  and  $|y_{\text{jet}}|-p_{\text{T}}^{\text{jet}}$  planes in the cross-section measurements. The migrations across the angular spectra in the cross-section measurements are small, so the JAR uncertainty is irrelevant. However, the migrations across the  $m_{\text{jjj}}$  are significant. These migrations are partly JAR-related since the directions of the three leading jets are used to reconstruct  $m_{\text{jjj}}$ . Among the quantities affected by the JAR, the dominant effect is expected in the jet rapidity rather than in the azimuthal angle. This is because the hard scatter vertex disposition along the beam pipe dominates over that in a transverse plane. Therefore, the effect of jet  $\eta$  smearing is explored in the three-jets cross-section measurement. But when measuring the  $Z + \text{jets}$  cross-section, the JAR effects are considered irrelevant since the hard scatter vertex position is well defined by tracks of electrons from the  $Z$ -boson decay.

The JAR is evaluated in the three-jets cross-section measurement using the simulation. The absolute rapidity difference between the closest detector-level and particle-level jets is studied event by event. The JAR is estimated as the width of the Gaussian fit to the distribution of the above differences. As a result, the JAR varies between 0.005 radians and 0.03 radians depending on the jet  $\eta$  and  $p_{\text{T}}$ . Uncertainty is estimated as the difference between the JARs obtained using different event generators. Thus, different physics models are taken into account. The resulting uncertainty is about 10–15% for jets in the  $p_{\text{T}} < 150$  GeV region decreasing to  $\sim 1\%$  in the  $p_{\text{T}} > 400$  GeV region. This uncertainty covers the differences between the data and simulation obtained when the JAR is measured *in situ* [200]. This uncertainty is propagated to the measured three-jets cross-section by smearing the reconstructed jet rapidities.

### 5.7.3.3 Electron energy resolution

The electron energy resolution (EER) affects the  $Z + \text{jets}$  cross-section measurements through the event selection. The EER causes smearing of the  $p_{\text{T}}^e$  and  $m_{ee}$ . Therefore, some events may be accepted or rejected when the reconstructed quantities migrate across the edge of the defined phase space. The EER is measured *in situ* using  $Z \rightarrow ee$  events [162]. In the central detector region, the EER varies between 3% for 20 GeV electrons and 1% for 200 GeV electrons. The simulation describes EER well up to a constant term, which is corrected as described in Section 4.4.5.3. The EER correction does not exceed 1%. The total uncertainty in the correction is within a few per mille. This uncertainty is propagated to the measured  $Z + \text{jets}$  cross-section by smearing the reconstructed electron energies.

## 5.7.4 Mis-modelling of the detector efficiencies

The detector efficiencies represent the probability of detecting an object used in the measurement. Any inefficiency is corrected by the unfolding. However, the unfolding is performed using simulation, so the efficiency mis-modelling distorts the measurement through this correction. The effect of the mis-modelling is reduced by weighting simulated events according to the measured efficiency as discussed in Section [4.4.5.2](#). However, the efficiencies are measured with uncertainty. Thus, it is necessary to propagate this uncertainty to the measured cross-section to account for a potential mis-modelling of the detector efficiency.

The uncertainties are propagated to the measured cross-section by varying the simulated event weight within the uncertainty in the detector efficiency unless otherwise stated.

There are several detector efficiency components whose uncertainties must be propagated to the measurements. These components are discussed along with their uncertainties in this section.

### 5.7.4.1 Reconstruction efficiency

The reconstruction efficiency depends on the detector acceptance. It decreases when the final state objects fall into poorly instrumented detector regions. The reconstructed efficiency is also affected by the dynamic range of the detector. For example, objects whose energy is below the detector sensitivity range are not reconstructed. The reconstruction efficiency mis-modelling must be considered when measuring the cross-section.

The reconstruction is fully efficient for jets with  $p_T$  above 25 GeV [\[149\]](#). The reconstructed jet phase space is constrained within the region of full efficiency. Therefore, there is no associated uncertainty.

The data used for the three-jets cross-section measurement is affected by a failure in a part of the electromagnetic calorimeter. Therefore, reconstructed jets with  $-0.88 < \phi < -0.5$  are rejected. The rejection is performed both in data and simulation to avoid the effect of mis-modelling.

The efficiency of electron reconstruction in the  $Z + \text{jet}$  cross-section measurement is within 95–99% [\[163\]](#). The simulation generally reproduces the reconstruction efficiency in the data well. Therefore, an event weight used in the  $Z + \text{jets}$  simulation to reduce the difference in efficiency compared to the data is within a per cent of one. The reconstruction efficiency is measured within an uncertainty of about one per cent. This uncertainty is propagated to the measured  $Z + \text{jets}$  cross-section.

### 5.7.4.2 Identification efficiency

The electron and jet identification criteria are used to reject backgrounds. However, the background rejection strength is usually achieved at the expense of reduced event selection efficiency. The mis-modelling of this efficiency must be taken into account.

The jet identification in the three-jets cross-section measurement results in the event selection efficiency of more than 99% within the defined phase space [157]. The difference between the data and simulation does not exceed 0.25%. Since three jets are used when measuring cross-section, an uncertainty of 0.75% is assigned directly to the measured cross-section to account for the efficiency mis-modelling.

The same jet identification is used in the  $Z + \text{jets}$  cross-section measurement. However, jets with lower  $p_T$  are used in this measurement. The selection efficiency is within 94–100% for jets in the  $25 \text{ GeV} < p_T^{\text{jet}} < 50 \text{ GeV}$  region. The effect of mis-modelling is estimated using other identification criteria for jets, so the selection efficiency is varied around the nominal. The data-to-simulation ratio between the  $Z + \text{jets}$  yields obtained using the nominal identification is compared to that obtained using other identification criteria. An uncertainty of 1% accounting for the observed differences is assigned directly to the measured  $Z + \text{jets}$  cross-section regardless of jet kinematics.

The electron identification used in the  $Z + \text{jets}$  cross-section measurement results in the selection efficiency of 80–95% depending on electron transverse momentum and rapidity [163]. The simulated efficiency exceeds the data by a few per cent. Event reweighting takes this into account in the  $Z + \text{jets}$  cross-section measurement. A few per cent uncertainty in the measured efficiency is propagated to the measured  $Z + \text{jets}$  cross-section.

### 5.7.4.3 Trigger efficiency

The trigger system makes fast decisions when selecting events at a high rate of  $pp$  collisions. This is achieved using simplified algorithms when reconstructing electrons and jets. The energy and angular resolutions of the final state objects are worse than the nominal. Thus, some properties of the final state objects are smeared outside the phase space defined by the event selection criteria at the trigger. This causes inefficiency in event selection. The mis-modelling of the trigger efficiency is to be propagated to the measured cross-section.

The three-jets cross-section is measured using the collision data pre-selected by several triggers that require at least one jet. The data are then combined within the region of full trigger efficiency. Event selection performed on top of this further restricts the three-jets phase space. Thus, the effect of the trigger efficiency mis-modelling is excluded.

The data for the  $Z + \text{jets}$  cross-section measurement is pre-selected by a trigger requiring two electrons. The measured trigger efficiency is within 97–99% in the  $Z + \text{jets}$  analysis phase-space [173]. The event reweighting accounts for the 1% differences between data and simulation. The uncertainty in the measured efficiency of a per mille level is propagated to the measured cross-section.

### 5.7.5 Mis-modelling of pile-up effects

Pile-up occurs abundantly at the LHC. It complicates many measurements. For example, it results in many jets originating from various vertices adding more complexity to the extraction of the hard scattering final state. Besides this, particles originating from pile-up result in many energy overlays in the calorimeter. Therefore, dealing with high pile-up requires advanced energy reconstruction and pile-up suppression techniques. However, none of them is fully efficient. Thus, a contribution of pile-up is expected in the cross-section measurements. It affects measurements through the simulation-based unfolding if there is a mis-modelling and leads to uncertainty that must be taken into account.

The pile-up originated jets are suppressed by requiring high  $p_T$  jets in the three-jets cross-section measurement. Pile-up jets are generally soft, so their contribution in a sample with jet  $p_T$  above 50 GeV is negligible [143]. Therefore, their mis-modelling does not affect the measurement.

The  $Z + \text{jets}$  cross-section measurement is performed using jets with  $p_T$  above 25 GeV. The pile-up-originated jets are suppressed by restricting the JVF. However, the JVF requirement is not fully efficient, so some pile-up jets can affect the measurement. To account for this, the JVF requirement is varied up and down by 0.03. Thus, the efficiency of pile-up jets suppressions is varied by a few per cent [201]. As a result, the amount of pile-up-originated jets is also varied. These variations are propagated to the measured  $Z + \text{jets}$  cross-section.

The pile-up-originated energy contribution to jets is subtracted when they are calibrated. The associated uncertainty is discussed in Section 5.7.1.3. This uncertainty is validated by studying the three-jets and  $Z + \text{jets}$  yields under different pile-up conditions. For this, the yields are derived in different regions of  $\langle \mu \rangle$  and  $N_{PV}$  in the data. The results agree with the nominal yields within statistical uncertainty. No significant dependence on the pile-up conditions is observed.

Finally, the effect of pile-up conditions mis-modelling is explored. This effect is reduced by event reweighting that improves the agreement between data and simulation in the  $\langle \mu \rangle$  and  $N_{PV}$  distributions as discussed in Section 4.4.5.1. However, the exact match between data and simulation in both distributions simultaneously is impossible, as the  $\langle \mu \rangle$  and  $N_{PV}$  are correlated. So the effect of mis-modelling is evaluated by adjusting the simulation to data in either of the two distributions in turn. These variations are propagated to the measured

cross-section. However, the cross-section changes are not statistically significant. Therefore, they are neglected.

### 5.7.6 Inaccuracy in the background subtraction

Various background processes contributing to the  $Z + \text{jets}$  events are studied when measuring the cross-section. The background contributions are known with uncertainties. When backgrounds are evaluated, they are subtracted from the data. Thus, an inaccurate background estimate affects the measured  $Z + \text{jets}$  yields and, accordingly, the cross-section. Therefore, the uncertainty in the background estimate must be propagated to the measured cross-section.

The backgrounds have their own correlation pattern across the  $Z + \text{jets}$  phase space, so the uncertainty in each is propagated to the measured cross-section separately. To do this, the backgrounds are varied within their uncertainties. The varied backgrounds are subtracted from the data. The other propagations steps are similar to other uncertainties.

The data contamination by the  $Z \rightarrow \tau\tau$ , dibosons,  $t\bar{t}$  and single top-quark backgrounds is estimated using simulation. Each background is normalised by its production cross-section calculated at fixed-order accuracy in QCD. The uncertainties in the calculated cross-sections are propagated to the measurement.

The shape of the backgrounds may vary in case of mis-modelling. Therefore, ensuring that the simulation is consistent with the data is necessary. Good modelling of the  $t\bar{t}$  production is of the greatest importance as it is the dominant background. It was shown previously that the  $t\bar{t}$  simulation describes the shapes of the jet  $p_T$  and  $y$  distributions in data to within a few percent [183]. So, possible shape mis-modellings are covered by the uncertainty in the  $t\bar{t}$  cross-section. The shape mis-modellings in other backgrounds have a negligible effect on the final results. Therefore, the background shape mis-modellings are irrelevant in the  $Z + \text{jets}$  cross-section measurement.

The combined multi-jet plus  $W + \text{jets}$  background is estimated using a data-driven approach. The uncertainty in the background estimation is described by several components. They account for different assumptions to evaluate the background template shape and normalisation. First, the shape of the background depends on the control sample definition. The effect of this dependence is evaluated by redefining the event selection to include more background. To do this, the background electron identification is varied. Instead of the nominal definition, an electron faked by a jet is identified when it satisfies *loose++*, but not *medium++* set of criteria. Thus, a modified background template is obtained. This template is symmetrised against the nominal one to estimate up and down variations within the uncertainty. This uncertainty is propagated to the measured cross-section.

Second, the shape of the template depends on the control sample contamination by other backgrounds. This effect is evaluated by varying the  $Z \rightarrow \tau\tau$ ,

dibosons,  $t\bar{t}$  and single top-quark backgrounds within their uncertainties. The dominant change in the template shape is due to  $t\bar{t}$  cross-section variation, while the effect of other backgrounds is small. Thus, the templates varied within the uncertainty in the  $t\bar{t}$  cross-section are used to propagate this uncertainty into the measurement.

Finally, the template normalisation is affected by the amount of background accessed by the fit. The variation of the template normalisation is thus a source of uncertainty. This uncertainty is evaluated by varying the  $m_{ee}$  range used for fitting. Different background contributions on the sides of the  $m_{ee}$  distribution around the  $Z$ -boson mass peak are probed by fitting in the  $66 \text{ GeV} < m_{ee} < 140 \text{ GeV}$  and  $60 \text{ GeV} < m_{ee} < 116 \text{ GeV}$  regions. The exclusion region of  $80 \text{ GeV} < m_{ee} < 100 \text{ GeV}$  remains untouched in these fits. Therefore, a third variation is obtained by extending the exclusion range to  $70 \text{ GeV} < m_{ee} < 110 \text{ GeV}$  while fitting within the nominal window of  $60 \text{ GeV} < m_{ee} < 140 \text{ GeV}$ . In this case, the  $Z + \text{jets}$  contribution is suppressed harder. As a result, the templates that experienced the largest normalisation changes are used for the uncertainty propagation to the measured cross-section.

### 5.7.7 Inaccuracy in the detector effects correction

Distortions due to the detector effects are corrected in both measurements. Two uncertainties associated with the correction are evaluated. One uncertainty accounts for mis-modelling the shape of the particle-level spectra being measured. Another uncertainty accounts for mis-modelling the particle-level spectral shape in other quantities affecting the detector response, i.e. in hidden variables. The uncertainties are evaluated using the data and simulations. Their evaluation is discussed in Section [5.6.1](#). Since the cross-section affected by these uncertainties can either increase or decrease, they are symmetrised at the cross-section level.

In the three-jets cross-section measurement, the difference between the particle-level spectra in different event generators is not statistically significant, so the associated uncertainty is neglected.

### 5.7.8 Inaccuracy in the collider luminosity measurement

The measured event yields are normalised by the collider luminosity to obtain cross-section. The luminosity is measured using a dedicated beam-separation scan, the van der Meer scan. The integrated luminosity is quoted with uncertainty. The integrated luminosity of the data sample used for the three-jets cross-section measurement is  $4.51 \pm 0.08 \text{ fb}^{-1}$  [\[202\]](#). In the  $Z + \text{jets}$  cross-section measurement, it is  $19.9 \pm 0.4 \text{ fb}^{-1}$  [\[203\]](#). Therefore, the relative uncertainty of 1.8% and 1.9% is assigned to the measured three-jets and  $Z + \text{jets}$  cross-section, respectively.

## 5.7.9 Reducing statistical fluctuations of systematic uncertainties

Each systematic uncertainty has a statistical component due to the finite size of an event sample. Thus, the uncertainties fluctuate around their true values. Each uncertainty estimate can be underestimated or overestimated due to these fluctuations. These fluctuations sometimes lead to sharp variations of uncertainties between adjacent phase-space points even though the underlying uncertainty is smooth. The effect of the fluctuations can be reduced if the statistical component is known. Therefore, evaluating this component is necessary.

The statistical component of each systematic uncertainty is evaluated using the bootstrap technique, see Section [3.3.2](#). So, in addition to the nominal uncertainty, an ensemble of uncertainties describing the same source is derived using pseudo-experiments. A standard deviation calculated over this ensemble quantifies the corresponding statistical component.

The derived statistical components are used to reduce the fluctuations of systematic uncertainties. To do this, the statistical significance of the systematic uncertainty  $u$  per interval  $i$  of the measured spectra is calculated as  $\mathcal{S}_i = u_i/\delta_i$ , where  $\delta_i$  is the corresponding statistical component. If the significance per the interval does not satisfy  $\mathcal{S} > 1.5$ , this interval is combined with the adjacent one, and the uncertainty is recalculated. The combination proceeds iteratively until the required condition is met. To preserve as much information about the shape of the uncertainty as possible, the iterations start on both sides of the spectrum, and the combination resulting in more intervals remaining is kept. The resulting uncertainties are considered statistically significant. The uncertainties determined in the combined intervals are reported in the original intervals of the measured spectra.

In addition, the uncertainties that vary sharply between the adjacent intervals are smoothed using the Gaussian kernel. The weighted average across the spectrum is used to define the smoothed uncertainty in each interval  $i$ , so it is

$$u_i^{\text{smooth}} = \frac{\sum_j u_j w_{ij}}{\sum_j w_{ij}}, \quad (5.14)$$

where

$$w_{ij} = e^{-\left(\frac{x_i - x_j}{f(x_i)}\right)^2}. \quad (5.15)$$

The  $x_i$  and  $x_j$  are the centres of the respective interval of the measurement. The  $f(x_i)$  is a linear function regulating the amount of smoothing. The parameters of the function  $f(x_i)$  are optimised manually so that the smoothed systematic uncertainty is within the statistical component of the original uncertainty.

All uncertainties describe the up and down variations in the cross-section. However, fluctuations sometimes cause variations in the same direction from the

original cross-section. In such cases, the uncertainty is within its statistical component from zero. Therefore, the most significant uncertainty is kept, while the uncertainty in the opposite direction is neglected.

An example demonstrating the performance of the above procedures is shown in Figure 5.15. This example shows the dominant component of the uncertainty due to the inaccuracy in the jet energy scale calibration in the central detector region in the  $Z + \text{jets}$  cross-section measurement. The fluctuations are studied independently in both the up and down components of the uncertainty. The uncertainty is significant for most of each spectrum, except in the  $|y_{\text{jet}}| > 2.6$  region. Therefore, the combination of several intervals of the spectra is performed. Apart from that, one can see sharp variations in the uncertainties between the adjacent  $|y_{\text{jet}}|$  intervals, especially near the spectrum's centre. Therefore, a minimal amount of smoothing is performed. Finally, the up and down components of uncertainty are clearly distinguishable, i.e. there are no co-directional fluctuations of them, so the final uncertainty is the same as the smoothed result.

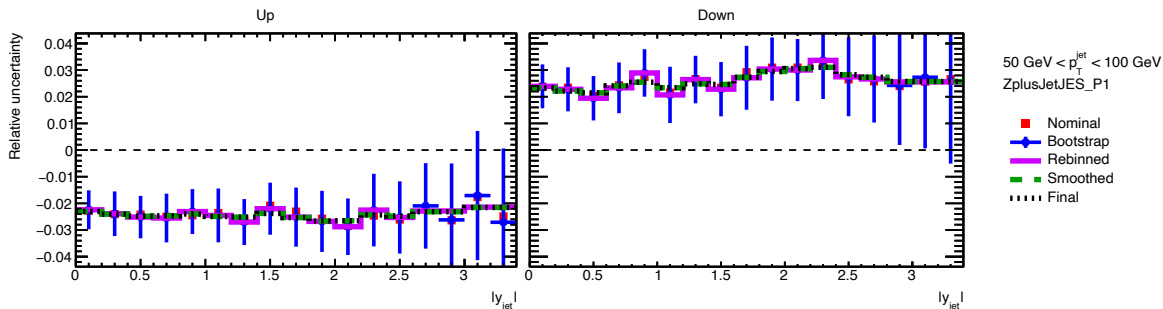


Figure 5.15 — A dominant component of the uncertainty due to the inaccuracy in the jet energy calibration in the central detector region in the  $Z + \text{jets}$  cross-section measurement. The (left) up and (right) down variations are shown. Original uncertainty is shown in red. Blue error bars represent the statistical components of the uncertainty. The error bars are assigned to the mean uncertainty calculated along the pseudo-experiments. A violet solid line represents the statistically significant uncertainty calculated when some adjacent  $|y_{\text{jet}}|$  intervals are combined. A green dashed line is the smoothed uncertainty. The final uncertainty is shown with a black dotted line. The final uncertainty is the same as the smoothed one, as there are no co-directional fluctuations of the uncertainty.

The same procedures for reducing statistical fluctuations apply to most uncertainties. However, the approach is slightly different when evaluating the uncertainty due to the mis-modelling of the detector resolution. To reduce the impact of fluctuations, the reconstructed energy or angle is smeared multiple times for each event. They are used to calculate the average transfer matrix and matching efficiencies, which are less affected by the fluctuations. Instead of using the bootstrap technique, the statistical errors are calculated by considering the original

and smeared cross-section as independent of each other. The smoothing is then performed in the same way as for other uncertainties.

### 5.7.10 Statistical uncertainty

The total statistical uncertainty in the measurement is due to limited statistics in both the data and simulation. This interplay is mainly associated with the transfers of events during the correction of detector effects. The total statistical uncertainty is evaluated using the bootstrap technique. A thousand pseudo-experiment is created with the data and simulation. To calculate the data portion of the uncertainty, the fluctuated data is unfolded using the original transfer matrix and matching efficiencies. The simulation portion is obtained by unfolding the nominal data using the fluctuated transfer matrix and matching efficiencies. Finally, each fluctuated data is unfolded using the fluctuated matrix and matching efficiencies to calculate the total uncertainty. Covariance matrices in all phase space points are calculated for each unfolded data sample. The square root of the diagonal elements of each covariance matrix estimates the respective portion of the total statistical uncertainty.

As an example, the statistical uncertainties calculated in the three-jets cross-section measurement are shown in Figure [5.16](#). The results are compared with the statistical uncertainty in the data calculated using the standard  $1/\sqrt{N}$  law before unfolding. The total statistical uncertainty is dominated by the data portion in most of the points in the phase space. However, in some of them, the simulation portion of the uncertainty becomes similar to the data, so the standard assumption underestimates the statistical uncertainty.

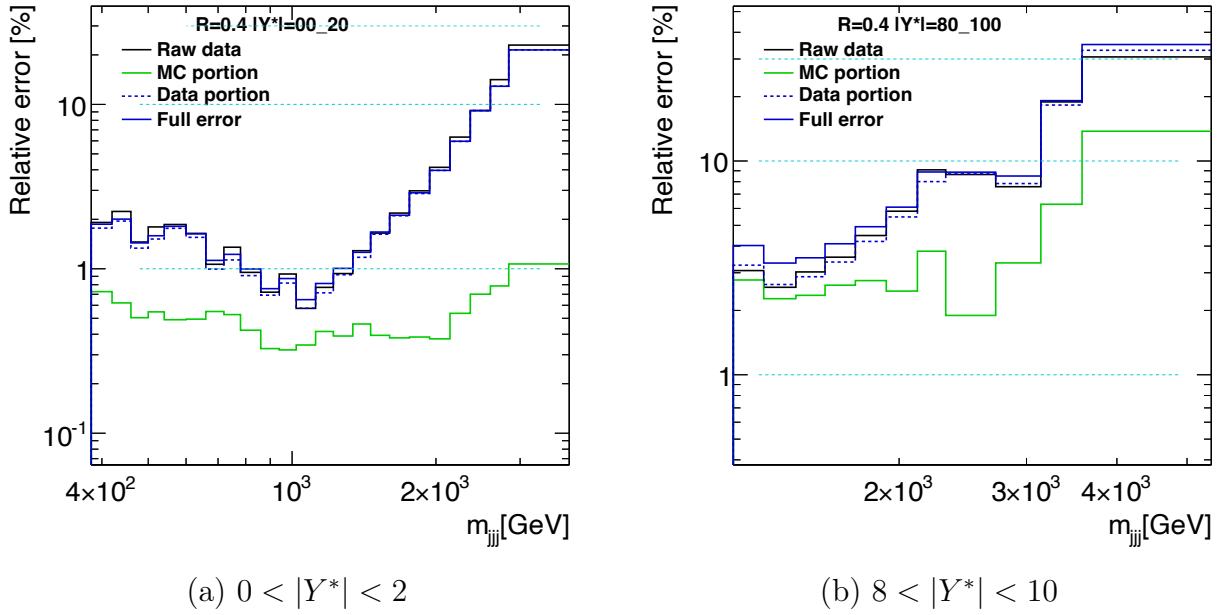


Figure 5.16 — Statistical uncertainty in the three-jets cross-section measurement using anti- $k_t$   $R = 0.4$  jets as a function of  $m_{\text{jjj}}$ . The data portion of the total statistical uncertainty is shown with a blue dotted line. The simulation portion is shown with a green solid line. The total statistical uncertainty is shown with a blue solid line. The statistical uncertainty in the data calculated using the standard  $1/\sqrt{N}$  law before unfolding is shown with a black solid line.

### 5.7.11 Summary on the three-jets cross-section uncertainty

The total systematic uncertainty in the three-jets cross-section measurement is described by a set of 67 components. According to their origin and size, they are classified as:

- Jet energy scale uncertainty:
  - 54 uncertainties due to inaccuracy in the jet energy calibration in the central detector region;
  - 2 uncertainties due to inaccuracy in the jet energy calibration in the forward detector region;
  - 2 uncertainties due to inaccuracy in subtracting pile-up contribution;
  - 2 uncertainties due to the difference between the detector response to quark-initiated and gluon-initiated jets;
  - 1 uncertainty due to inaccuracy in the calibration for jets with the highest transverse momenta;
  - 1 uncertainty due to mis-modelling of close-by jets.

- Jet angular resolution uncertainty.
- Jet energy resolution uncertainty.
- Other uncertainties:
  - 1 uncertainty due to mis-modelling of the jet identification efficiency;
  - 1 uncertainty due to inaccuracy in the detector effects correction.
- Inaccuracy in the collider luminosity measurement.

The total systematic uncertainty in the three-jets cross-section measurement using anti- $k_t$   $R = 0.6$  jets is shown in Figure 5.17. At low  $|Y^*|$ , the uncertainty is in the range of 7–11% at small three-jets masses and increases to 28% at high masses. The dominant uncertainties are due to the inaccuracy in the energy calibration of jets in the central detector regions and the jet flavour-related differences in the detector response. In addition, a substantial contribution is due to the mis-modelling of close-by activity around the jet. The uncertainty increases as a function of  $|Y^*|$ , so at the highest  $|Y^*|$  it is within 18–38%. The inaccuracy in the jet energy calibration in the forward detector region fully dominates the total uncertainty at the highest  $|Y^*|$ . Other systematic uncertainties are relatively small. The same is true for the  $R = 0.4$  jets.

It is interesting to note that a per cent level uncertainty in the jet energy scale calibration translates into the uncertainty of the order of ten per cent in the three-jets cross-section measurement. Therefore, further improvements in jet calibration accuracy are required to reduce the cross-section measurement uncertainty.

Statistical uncertainty is small in most of the  $m_{\text{jjj}}$  except the highest.

A partial decomposition of the uncertainties is provided in Appendix A. The full uncertainty breakdown is provided in the HEPData [204] database.

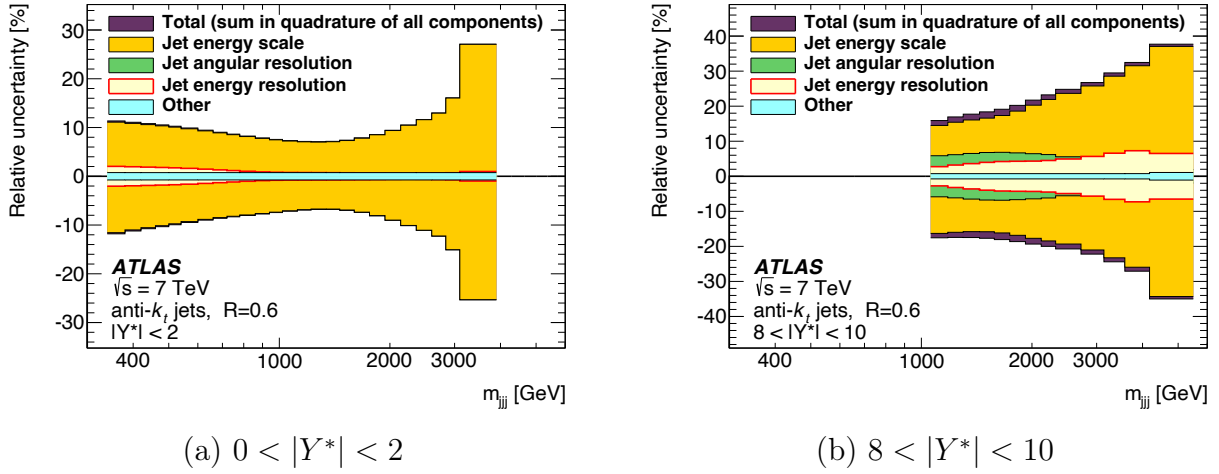


Figure 5.17 — Systematic uncertainties in the three-jets cross-section measurement using anti- $k_t$   $R = 0.6$  jets as a function of  $m_{\text{jjj}}$ . The regions of (a) low and (b) high  $|Y^*|$  are shown. The colour bands show the uncertainties classified as jet energy scale, jet angular resolution, jet energy resolution and other sources. The outer band represents the total systematic uncertainty calculated as the sum in quadrature of all components. Uncertainty of 1.8% due to inaccuracy in the collider luminosity measurement is not shown.

### 5.7.12 Summary on the $Z + \text{jets}$ cross-section uncertainty

The total systematic uncertainty in the  $Z + \text{jets}$  cross-section measurement is described by a set of 39 components. According to their origin and size, they are classified as:

- Jet energy scale uncertainty:
  - 6 effective uncertainties due to inaccuracy in the jet energy calibration in the central detector region;
  - 2 uncertainties due to inaccuracy in the jet energy calibration in the forward detector region;
  - 4 uncertainties due to inaccuracy in subtracting pile-up contribution;
  - 2 uncertainties due to the difference between the detector response to quark-initiated and gluon-initiated jets;
  - 1 uncertainty due to inaccuracy in the calibration for jets with the highest transverse momenta;
  - 1 uncertainty due to mis-modelling of punch-through jets
- Jet energy resolution uncertainty.
- Unfolding uncertainties:

- 2 uncertainties due to inaccuracy in the detector effects correction.
- Other uncertainties:
  - 1 uncertainty due to inaccuracy in the electron energy measurement;
  - 2 uncertainties due to mis-modelling of jet and electron energy resolution;
  - 1 uncertainty due to mis-modelling of jet identification efficiency;
  - 3 uncertainties due to mis-modelling of electron reconstruction, identification and trigger efficiencies;
  - 1 uncertainty due to mis-modelling of pile-up effects;
  - 8 uncertainties due to inaccuracy in the simulation-based background estimation;
  - 3 uncertainties due to inaccuracy in the data-driven background estimation;
- Inaccuracy in the collider luminosity measurement

The total systematic uncertainty in the  $Z + \text{jets}$  cross-section measurement is shown in Figure [5.18](#). The total systematic uncertainty of 7–12% is in the  $25 \text{ GeV} < p_{\text{T}}^{\text{jet}} < 50 \text{ GeV}$  region. The largest contribution is made by jet energy resolution, jet energy scale and unfolding uncertainties. The jet energy resolution uncertainty decreases significantly in the  $50 \text{ GeV} < p_{\text{T}}^{\text{jet}} < 100 \text{ GeV}$  region, so the total uncertainty is within the 4–8% range. The higher  $p_{\text{T}}^{\text{jet}}$  regions are dominated by the jet energy scale uncertainty, which is mostly within 3–4% across  $|y_{\text{jet}}|$ , although this uncertainty increases up to 16% in the  $|y_{\text{jet}}| > 3.2$  region. Other systematic uncertainties are relatively small.

Statistical uncertainty is small in the  $25 \text{ GeV} < p_{\text{T}}^{\text{jet}} < 100 \text{ GeV}$  region, but it increases as a function of the  $p_{\text{T}}^{\text{jet}}$  and  $|y_{\text{jet}}|$ . In the  $100 \text{ GeV} < p_{\text{T}}^{\text{jet}} < 300 \text{ GeV}$  region, the statistical uncertainty is 3–14%, equal to the systematic uncertainty. In the  $300 \text{ GeV} < p_{\text{T}}^{\text{jet}} < 1050 \text{ GeV}$  region, the statistical uncertainty is 10–40%, which is two to three times higher than the systematic uncertainty.

A partial decomposition of the uncertainties is provided in Appendix [B](#). The full uncertainty breakdown is provided in the HEPData [\[204\]](#) database.

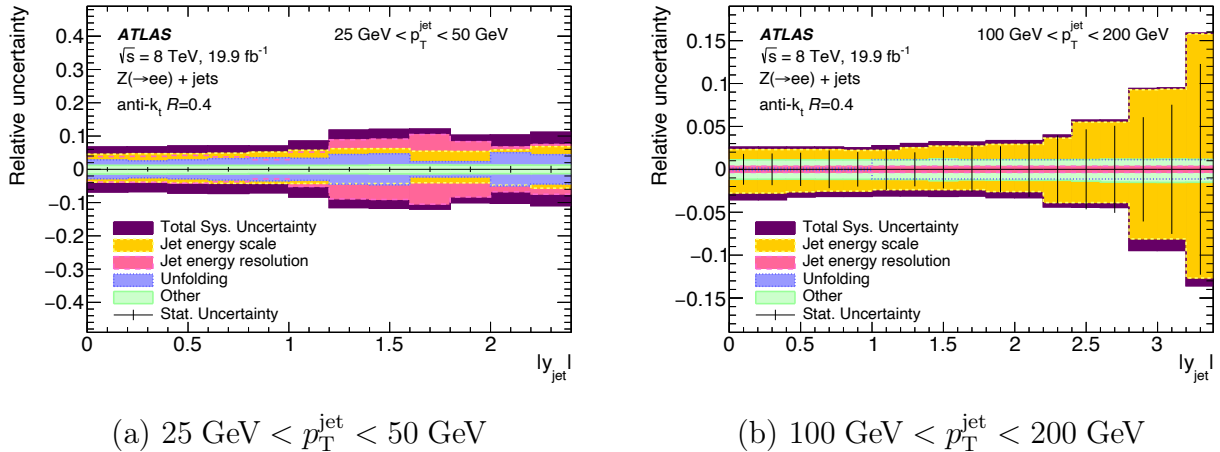


Figure 5.18 — Experimental uncertainties in the  $Z + \text{jets}$  cross-section measurement as a function of  $|y_{\text{jet}}|$ . The regions of (a) low and (b) intermediate  $p_T^{\text{jet}}$  are shown. The colour bands show the uncertainties classified as jet energy scale, jet angular resolution, jet energy resolution and other sources. The outer band represents the total systematic uncertainty calculated as the sum in quadrature of all components. Uncertainty of 1.9% due to inaccuracy in the collider luminosity measurement is not shown. The total statistical uncertainties are shown with vertical error bars.

## 5.8 Theoretical predictions

Testing different theoretical models describing the three-jets and  $Z + \text{jets}$  production is among the goals of the cross-section measurement. The perturbative series expansion is of most interest as it tends to an exact solution when calculating cross-section. Predictions obtained by expanding the total cross-section up to several leading terms in  $\alpha_s$  are currently state-of-the-art. The most accurate calculations available at the time of measurement are used to predict the cross-sections and compare them to the data. These predictions are described in this section.

The calculations are performed at the level of final state partons produced by the hard scattering. However, the cross-section are measured at the level of particles that are detected. Therefore, corrections that bring calculated cross-section to the particle level are computed to allow direct comparison with the measurement.

### 5.8.1 Fixed-order QCD predictions

The three-jets and  $Z + \text{jets}$  cross-sections are calculated at the fixed-order in  $\alpha_s$  for the comparisons with the data. The calculations are performed using different PDF sets to evaluate the sensitivity of the cross-section to them. The

uncertainties in the calculations are estimated to allow for quantitative comparisons.

Several programs are available for cross-section calculations at NLO accuracy. The cross-section of the production of three-jets is calculated using the NLOJET++ [59], while the MCFM [60] is used for the  $Z$  + jets cross-section calculations.

The NNLO calculations for many processes became available in the last decade, so most of them are far less automated than the NLO. Despite this, the  $Z$  + jets cross-section calculated by the NNLOJET [128, 129] is used for the comparisons with data.

The phase space for the three-jets cross-section calculations is constrained by the kinematics of final state jets defined in Table 5.1. The  $Z$  + jets phase space is specified by the kinematics of final state electrons and jets defined in Table 5.2.

The calculations require renormalisation and factorisation scales representing the hard scattering scale well. The scales used in the three-jets cross-section calculations are equal to the three-jets invariant mass, that is

$$\mu_R = \mu_F = m_{\text{jjj}}. \quad (5.16)$$

The scales used in the  $Z$  + jets cross-section calculations are

$$\mu_R = \mu_F = \frac{\sqrt{m_{ee}^2 + p_{T,Z}^2} + \sum p_{T,\text{partons}}}{2}, \quad (5.17)$$

where  $m_{ee}$  is the electron pair's invariant mass,  $p_{T,Z}$  is the transverse momentum of the  $Z$ -boson and  $\sum p_{T,\text{partons}}$  is the sum of the transverse momenta of the partons.

An effect of missing higher-order terms in the cross-section calculations is evaluated by varying the scales by a factor of two. Both scales are varied independently. The case of both scales changing in opposite directions is excluded to avoid the contribution of large logarithmic terms. An envelope of deviations from the nominal cross-section is considered as an uncertainty in the calculations.

The three-jets and  $Z$  + jets cross-sections are calculated using the CT10 [166] and CT14 [205] PDF sets, respectively. The PDFs are known within uncertainty that must be considered when calculating cross-section. The uncertainty accounts for the inaccuracy in the measurements used to derive the PDF and the assumptions made in its construction. The total uncertainty is described by a set of uncorrelated uncertainty components. The up and down variations of the PDF within each uncertainty component are provided as supplementary PDF sets. To propagate the PDF uncertainty to the cross-section, the latter is recalculated using all supplementary PDF sets. Instead of recalculating the cross-section from scratch, a fast convolution of the cross-section with various PDF sets is obtained using the APPLgrid [206] program. The sum in

quadrature of the deviations from the nominal PDF is used as an uncertainty in the cross-section calculations. Since the PDF uncertainty is provided to the 90% confidence level by default, the uncertainty in the cross-section is rescaled to the 68% confidence level by a factor of 1.645 according to the prescription of the PDF4LHC group [207].

There are many other PDF sets. They are evaluated using different data or relying on different assumptions. The three-jets and  $Z + \text{jets}$  cross-sections are recalculated using several other PDF sets for comparisons with data. The sensitivity of each cross-section to various PDF sets is shown in Figure 5.19 and 5.20, respectively. The PDF uncertainties are calculated according to their prescription and provided at the 68% confidence level [207]. The differences between cross-section obtained using different PDF sets reach 20%. Therefore, the measurements have a high potential for further PDF constraints.

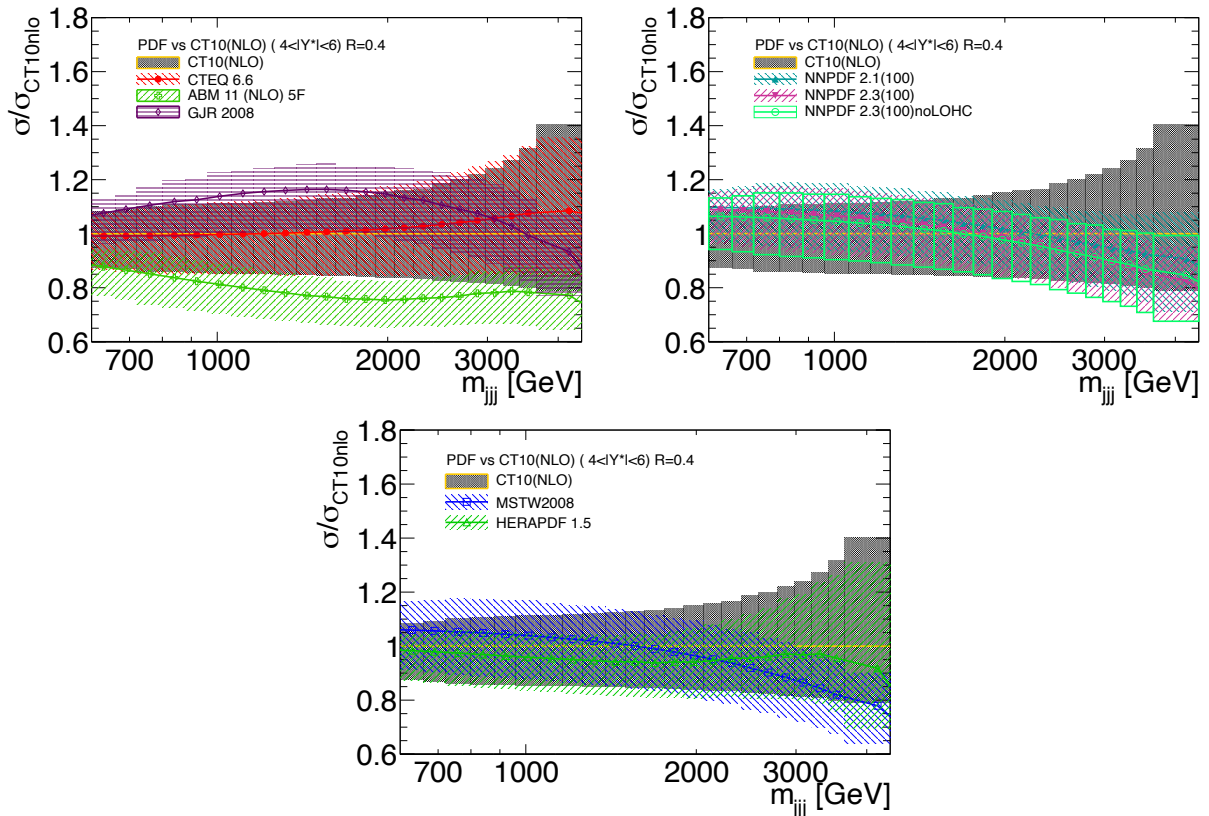


Figure 5.19 – Relative difference between the three-jet cross-section calculated using the CT 10 and other PDF sets. The results are shown as a function of  $m_{jjj}$  in the  $4 < |Y^*| < 6$  region. Different PDFs are shown with coloured markers. The band around each marker represents the corresponding PDF uncertainty.

The PDFs depend on the value of the QCD coupling strength at the  $Z$ -boson mass scale,  $\alpha_S(M_Z)$ . The coupling is known within uncertainty. This uncertainty is propagated to the cross-section using two additional proton PDF sets calculated with  $\alpha_S(M_Z) = 0.116$  and  $\alpha_S(M_Z) = 0.120$  [208]. The deviation from the nominal cross-section is used as an uncertainty in the cross-section calculations. This

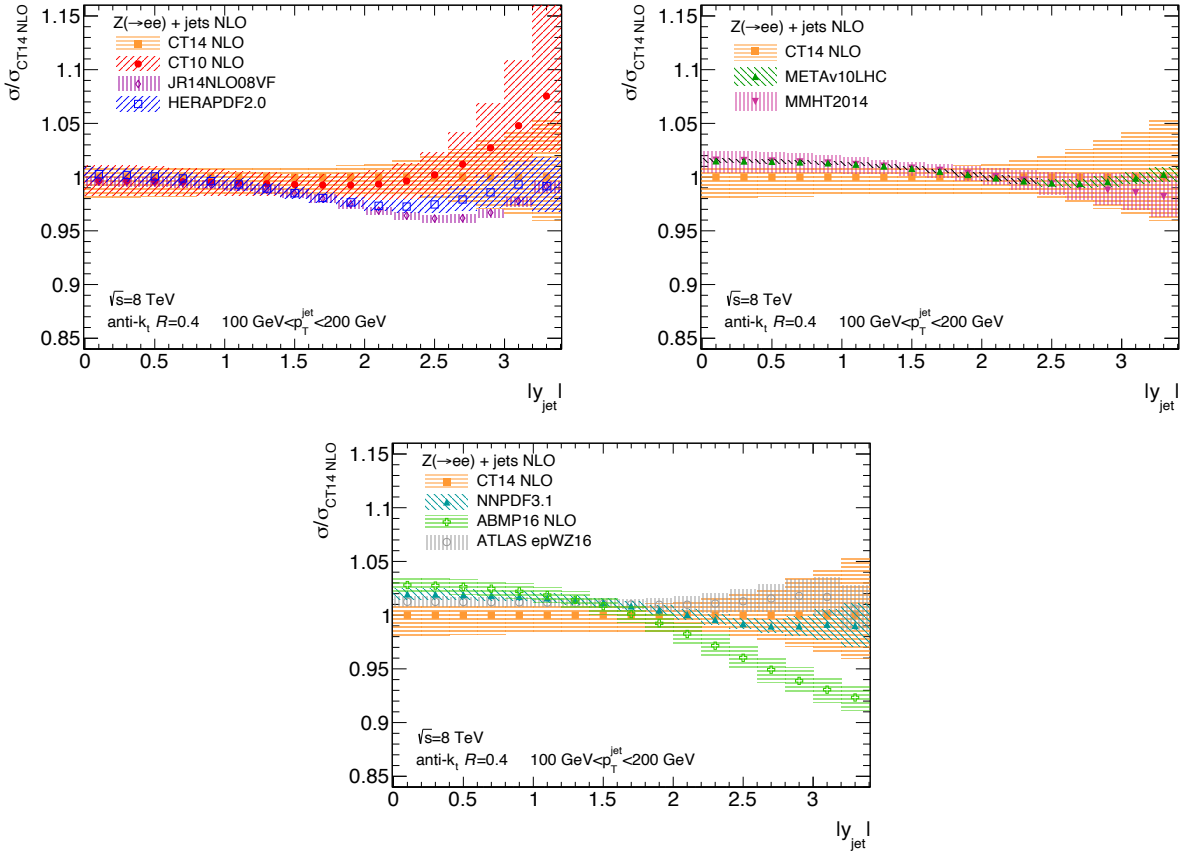


Figure 5.20 — Relative difference between the  $Z + \text{jets}$  cross-section calculated using the CT 14 and other PDF sets. The results are shown as a function of  $|y_{\text{jet}}|$  in the  $100 \text{ GeV} < p_T^{\text{jet}} < 200 \text{ GeV}$  region. Different PDFs are shown with coloured markers. The band around each marker represents the corresponding PDF uncertainty.

uncertainty is scaled to the uncertainty in the world average  $\alpha_S(M_Z) = 0.118 \pm 0.0012$  [207].

The total uncertainty in the calculated cross-section is evaluated as the sum in quadrature of the scale, PDF and  $\alpha_S$  uncertainty components.

The total uncertainty in the three-jets cross-sections calculations for the  $R = 0.4$  and  $R = 0.6$  jets is shown in Figure 5.21. At low  $m_{\text{jjj}}$  the uncertainty is about 10%. The dominant contribution is due to scale uncertainty. The total uncertainty increases as a function of  $m_{\text{jjj}}$  up to 80%. This increase is mainly due to PDF uncertainty, while the scale uncertainty increases slightly. The  $\alpha_S$  uncertainty is about a few per cent. The uncertainty is a few per cent larger for the  $R = 0.6$  than for  $R = 0.4$  due to larger scale uncertainty in the former.

The total uncertainty in the  $Z + \text{jets}$  cross-section calculations at NLO and NNLO accuracy are shown in Figure 5.22. The uncertainty in NLO calculations increases from 7% to 14% as a function of  $|y_{\text{jet}}|$  in the lowest  $p_T^{\text{jet}}$  region. The uncertainty increases as a function of  $p_T^{\text{jet}}$  and is twice as large in the highest  $p_T^{\text{jet}}$  region. The dominant contribution is due to scale uncertainty. However, the

scale uncertainty reduces significantly in the NNLO calculations. So, for small  $p_T^{\text{jet}}$ , the total uncertainty is within 2–5%, where the contributions of all uncertainty components are basically equal. The total uncertainty increases slightly as a function of  $|y_{\text{jet}}|$  and  $p_T^{\text{jet}}$  up to a maximum of 8%. The increase is mainly due to PDF uncertainty. In general, the NNLO predictions are three times more accurate than the NLO.

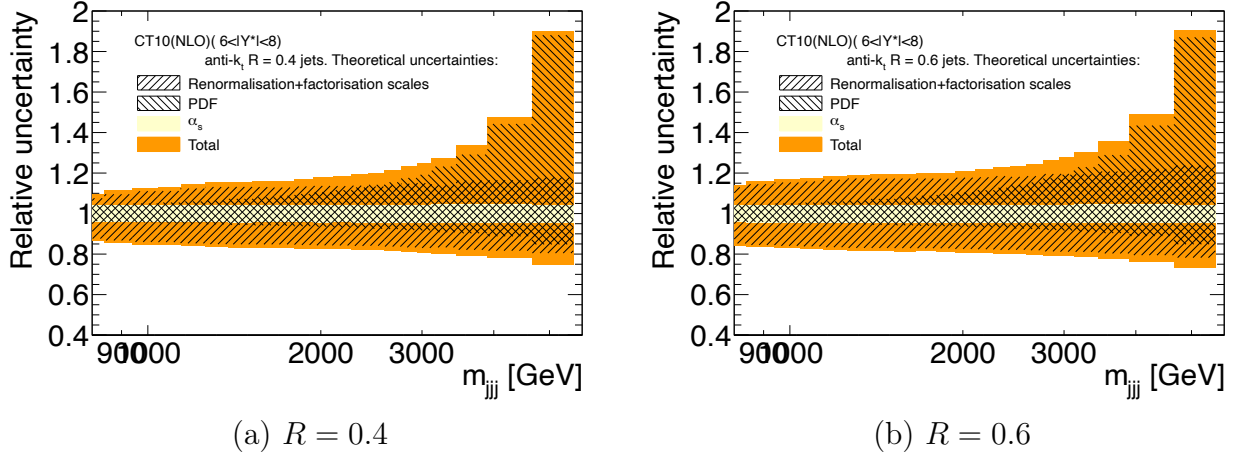


Figure 5.21 — Theory uncertainties in the  $Z + \text{jets}$  cross-section calculation for (a)  $R = 0.4$  and (b)  $R = 0.6$  accuracy. The uncertainty is shown as a function of  $m_{\text{jjj}}$  in the  $4 < |Y^*| < 6$  region. The hatched bands show the scale and PDF uncertainties. The light yellow band is the  $\alpha_s$  uncertainty. The total uncertainty is calculated as a sum in the quadrature over all the individual components. The total uncertainty is shown by the orange band.

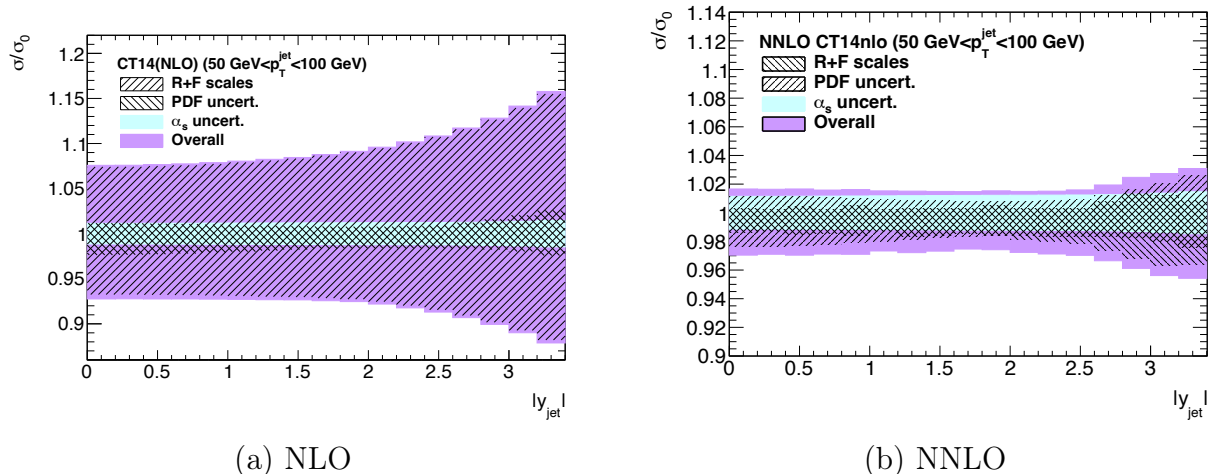


Figure 5.22 — Theory uncertainties in the  $Z + \text{jets}$  cross-section calculation at (a) NLO and (b) NNLO accuracy. The uncertainty is shown as a function of  $|y_{\text{jet}}|$  in the  $50 \text{ GeV} < p_{\text{T}}^{\text{jet}} < 100 \text{ GeV}$  region. The hatched bands show the scale and PDF uncertainties. The light blue band is the  $\alpha_s$  uncertainty. The total uncertainty is calculated as a sum in the quadrature over all the individual components. The total uncertainty is shown by the violet band.

## 5.8.2 Non-perturbative effects and corresponding cross-section correction

The fixed-order predictions are obtained using partons in the final state of the hard scattering. However, these predictions neglect several non-perturbative (NP) effects. One such effect is hadronisation, the process by which the final state partons fragment into particles. These particles define the particle level final state being detected. However, some particles initiated by hard-scatter partons appear outside a cone of a limited radius that defines a jet. So the measured jet energy decreases. Another effect is the underlying event, which refers to the interactions between multiple partons that can occur in a single  $pp$  collision. These interactions lead to additional particles being clustered into jets. So the measured jet energy increases. Influenced by these two effects, the cross-section measured as a function of jet kinematics may deviate from its true value.

The contribution of the NP effects to the measured cross-section can not be computed precisely from the first principles. Instead, phenomenological models tuned to reproduce the key features of the data are used to describe them. Therefore, an NP correction that brings parton level prediction to the particle level is necessary for comparisons with the data.

The NP correction is evaluated using parton shower event generators incorporating the models of hadronisation and underlying event. The generators run

twice to calculate the cross-section with NP effects turned on and off. The ratio between two predictions defines the NP correction.

There are many models of NP effects, but none is known as exact. The uncertainty can be estimated by evaluating the NP correction using different models. They are implemented in different event generators. For example, the PYTHIA generator uses the Lund model of hadronisation by default, while the SHERPA and HERWIG use the cluster model. However, some generators allow the user to choose an alternative hadronisation model. Besides the hadronisation, generators incorporate different underlying event models tuned to different data sets. Therefore, the spread of NP corrections obtained using different models is often used to estimate uncertainty.

The NP corrections to the three-jets cross-section are shown in Figure 5.23. The corrections obtained using jets with  $R = 0.4$  are generally below one. This is because the effect of hadronisation prevails over the underlying event. Energy losses due to the effect of hadronisation decrease at higher  $p_T$  since jets become better collimated. The underlying event is generally soft, so its fractional contribution also decreases for high  $p_T$  jets. As a result, the NP correction is smaller at high  $m_{jij}$ . The high  $m_{jij}$  region is also less affected by the differences between different models of NP effects than the low  $m_{jij}$  region. The largest spread between models is about 10% at the lowest  $m_{jij}$ .

Jets with a larger radius are less affected by the hadronisation effect as more distant radiation is clustered. However, they obtain a larger contribution from the underlying events. As a result, the NP correction for  $R = 0.6$  jets is generally above one in most of the generators.

The NP corrections to the  $Z + \text{jets}$  cross-section are shown in Figure 5.24. The corrections obtained using different generators are within 5% from one. The spread between them increases as a function of  $|y_{\text{jet}}|$ , as the contribution of the underlying event increases. As in the three-jets case, the NP correction decreases as a function of  $p_T^{\text{jet}}$ .

The derived corrections are applied multiplicatively to the fixed-order predictions. The NP correction obtained using the same event generator as for the correction of detector effects is used as the nominal one. The envelope of other corrections is used as the uncertainty. This uncertainty is added in quadrature to other uncertainties in the theoretical predictions.

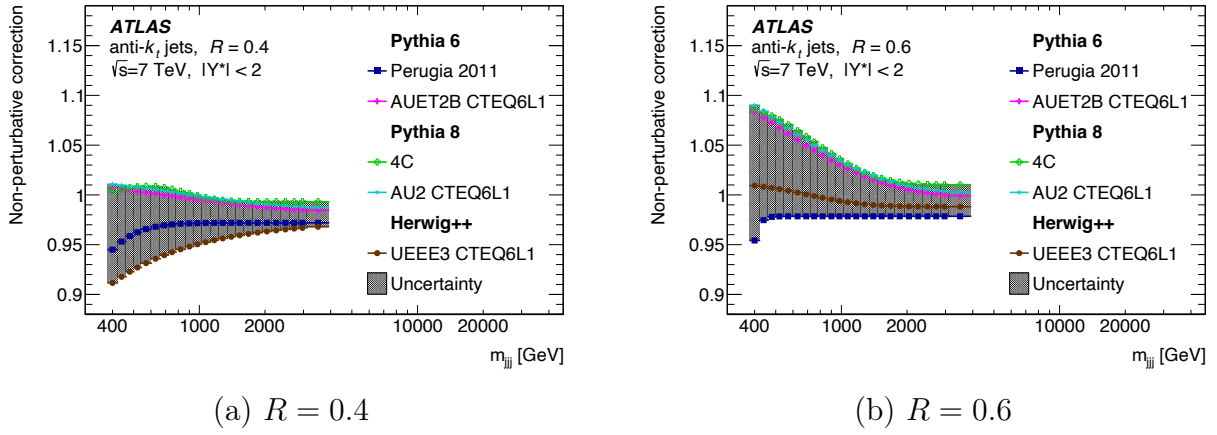


Figure 5.23 — Non-perturbative correction to the three-jets cross-section as the function of  $m_{\text{jjj}}$ . The corrections for the anti- $k_t$  (a)  $R = 0.4$  and (b)  $R = 0.6$  jets are shown. The corrections obtained using various event generators and their tunes are shown with coloured markers. The spread of the corrections is the uncertainty shown with a yellow band.

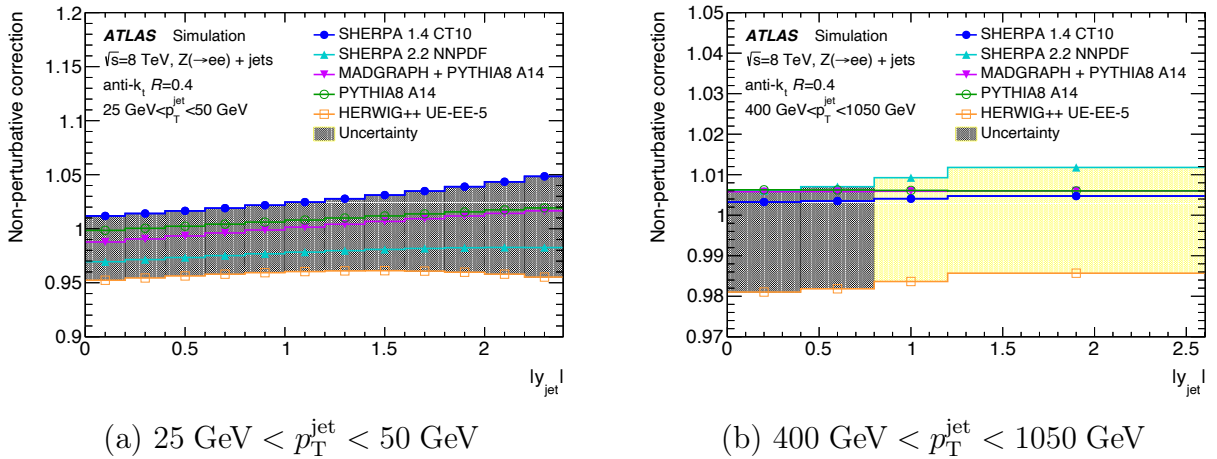


Figure 5.24 — Non-perturbative correction to the  $Z + \text{jets}$  cross-section as the function of  $|y_{\text{jet}}|$ . The corrections obtained in the (a)  $25 \text{ GeV} < p_T^{\text{jet}} < 50 \text{ GeV}$  and (b)  $400 \text{ GeV} < p_T^{\text{jet}} < 1050 \text{ GeV}$  regions are shown. The corrections obtained using various event generators and their tunes are shown with coloured markers. The spread of the corrections is the uncertainty shown with a yellow band.

### 5.8.3 QED radiation effects and corresponding cross-section correction

The  $Z + \text{jets}$  data are unfolded to the level of dressed electrons. That is, only the four-momenta of radiated photons within a cone of  $\Delta R = 0.1$  around the electron axis are added to the electron four-momentum. That is the energy carried by out the QED radiation is partially recovered for these electrons. However, the predictions used for comparison with the data are obtained at the lowest order in QED. That is, the QED radiation is disabled, so the electrons are at the born

level. Therefore, a correction that brings electrons from the born to dressed level is necessary.

The correction is evaluated using the event generators that allow turning the QED radiation on and off. The event generators run twice to obtain the  $Z + \text{jets}$  predictions at the level of dressed and born electrons. The ratio between two predictions defines the correction.

The derived correction is shown in Figure 5.25. The correction is within a few per cent below one because the number of selected dressed electrons is lower than that of born electrons. This correction is generally uniform across  $|y_{\text{jet}}|$  in most of the  $p_{\text{T}}^{\text{jet}}$  regions as the jet kinematics is independent of that of electrons. There is a slight dependence on  $|y_{\text{jet}}|$  at its edge at low  $p_{\text{T}}^{\text{jet}}$  due to event migrations across the phase space limits. The correction is well described by two different event generators. The spread between them is treated as uncertainty that accounts for the difference in the implementation of QED radiation effects.

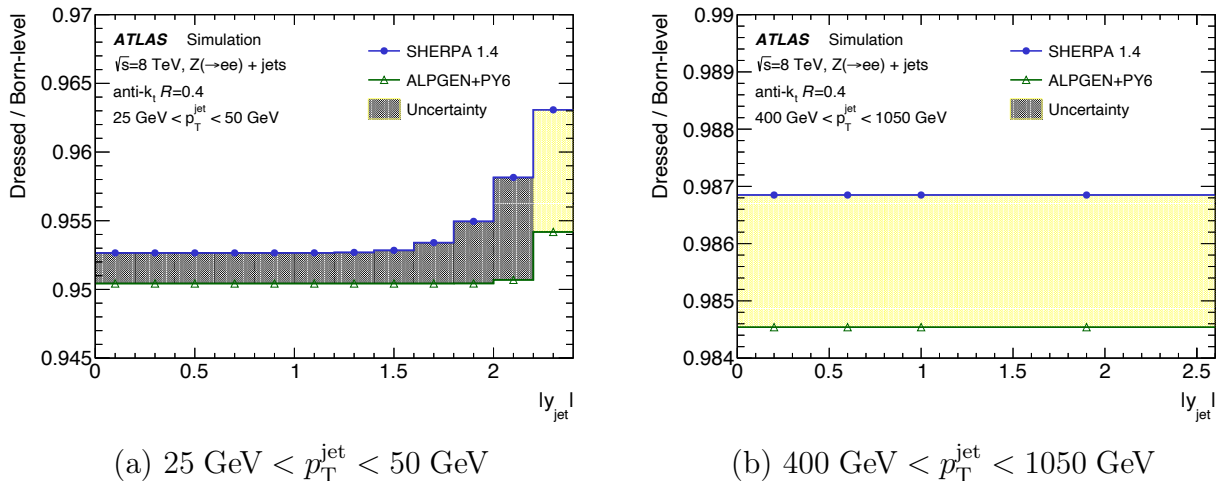


Figure 5.25 — QED radiation correction to the  $Z + \text{jets}$  cross-section as a function of  $|y_{\text{jet}}|$  in the (a)  $25 \text{ GeV} < p_{\text{T}}^{\text{jet}} < 50 \text{ GeV}$  and (b)  $400 \text{ GeV} < p_{\text{T}}^{\text{jet}} < 1050 \text{ GeV}$  regions. The corrections obtained using different event generators are shown with coloured markers. The spread of corrections is the uncertainty shown with a yellow band.

## 5.9 Results of the three-jets cross-section measurement

The double differential three-jets cross-section is measured using 7 TeV  $pp$  collisions data as a function of  $m_{\text{jjj}}$  and  $|Y^*|$ . The measurement is performed using the anti- $k_t$  jets with  $R = 0.4$  and  $R = 0.6$ . The data are corrected for detector effects and provided on the particle level. The results of the measurement are shown in Figure 5.26. The phase space of the measurement is defined within

the  $380 \text{ GeV} < m_{\text{jjj}} < 5500 \text{ GeV}$  and  $|Y^*| < 10$  range. The measured cross-section spans almost seven orders of magnitude, decreasing rapidly as a function of  $m_{\text{jjj}}$ . The results are well described by the NLO QCD predictions corrected for non-perturbative effects.

The measured cross-section are provided along with systematic and statistical uncertainties in Appendix [A](#). The measured cross-sections with the full breakdown of all uncertainties are provided in the HEPData database.

Qualitative comparisons between the measured three-jets cross-section for jets with  $R = 0.4$  and theoretical predictions are shown in Figure [5.27](#). The most modern PDF sets available at the time of the measurement are probed. The cross-section predictions obtained using most of them agree with the data within uncertainties over the full kinematic range. The exception is the ABM 11 PDF set, which results in about 20% lower cross-section than in the data. Thus, this PDF set requires improvements.

The predictions for jets with  $R = 0.6$  are systematically below the data, as shown in Figure [5.28](#). The difference between central values is 10–20% across the measurement kinematics. However, most of these differences are within the experimental and theoretical uncertainties. Since none of the PDFs leads to cross-section predictions that match the data, the measurement provides important input for their improvement.

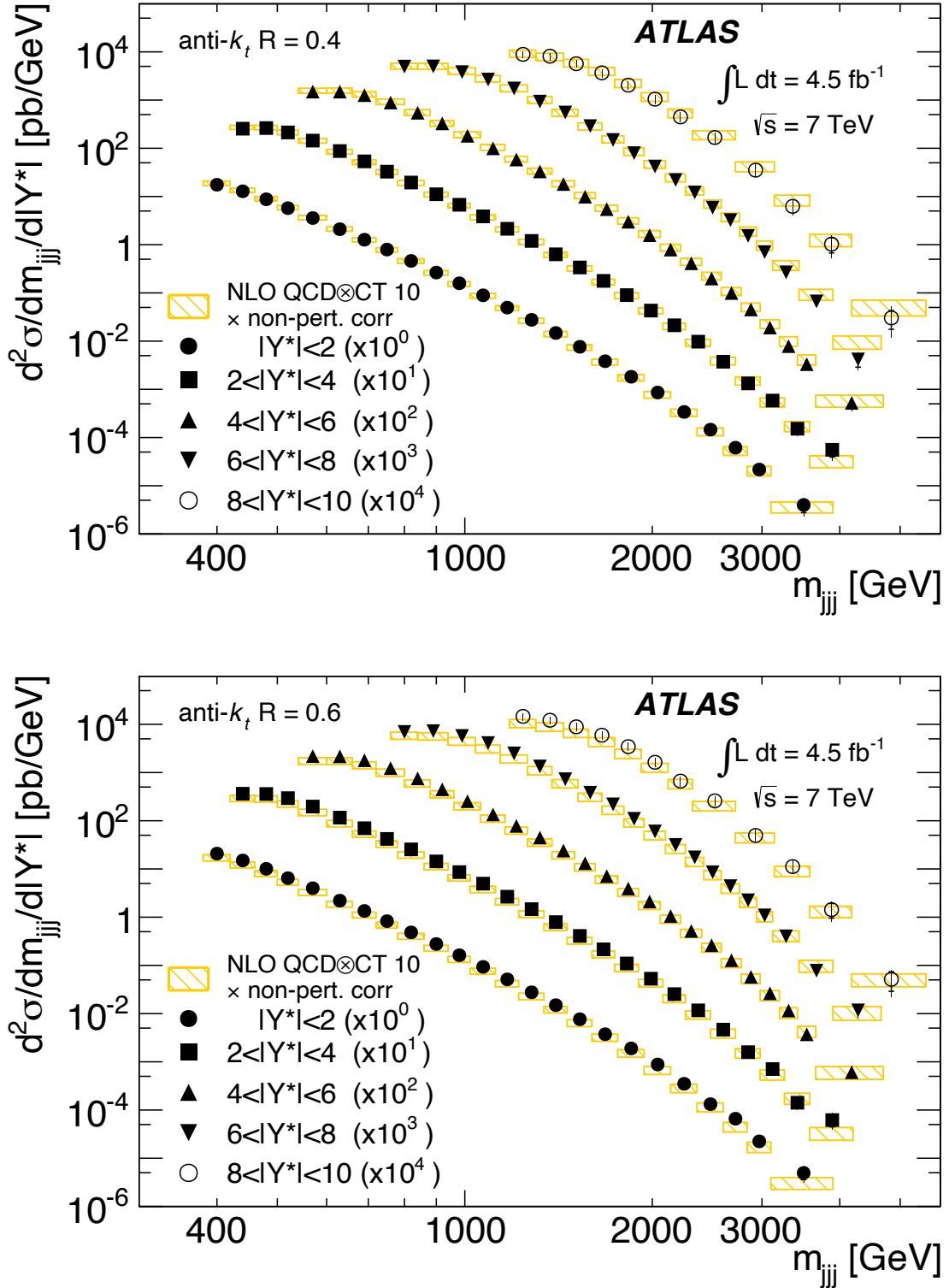


Figure 5.26 — The double differential three-jets cross-section measured as a function of  $m_{jjj}$  in regions of  $|Y^*|$ . The jets are identified using the anti- $k_t$  algorithm. The cross-sections for anti- $k_t$  jets with  $R = 0.4$  (top) and  $R = 0.6$  (bottom) are shown. For convenience, the cross-sections are multiplied by the factors indicated in the legend. The statistical uncertainties are smaller than the size of the markers. Where visible, the sum in quadrature of the statistical and experimental systematic uncertainties is plotted. The data are compared to the NLO QCD prediction obtained using the CT10 PDF set and corrected for non-perturbative effects. The theoretical uncertainties are shown with shaded bands.

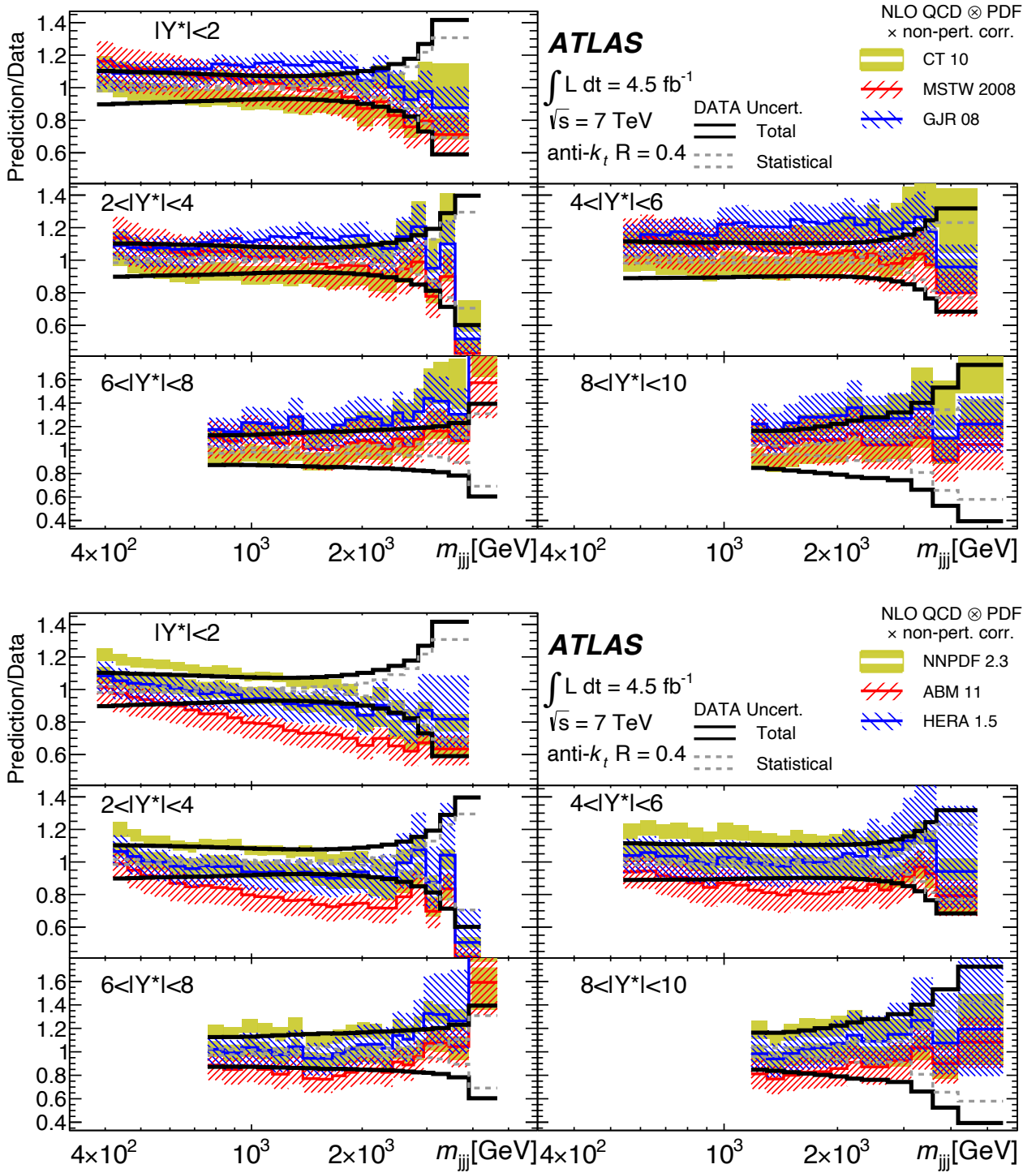


Figure 5.27 — The ratio of NLO QCD predictions, obtained with different PDF sets and corrected for non-perturbative effects, to data as a function of  $m_{jjj}$  in regions of  $|Y^*|$ , as denoted in the legend. The ratios are for anti- $k_t$  jets with  $R = 0.4$ . The experimental error bands are centred at one and designate the relative statistical (thin dashed line) and total (statistical and systematic uncertainties added in quadrature) experimental uncertainties (thick solid line). Thick lines with the hatched or filled band around them represent the theoretical predictions with the corresponding theoretical uncertainties.

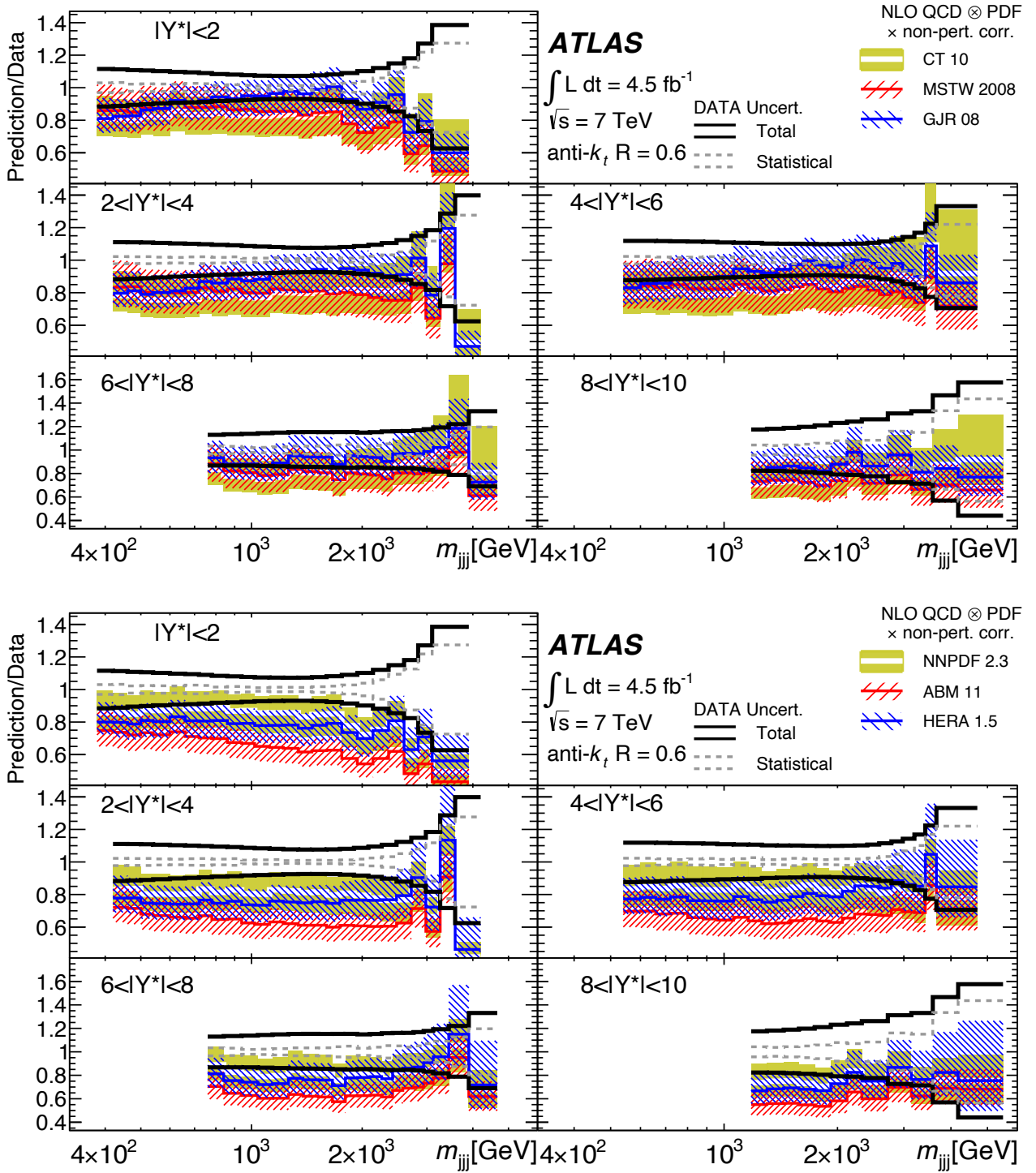


Figure 5.28 — The ratio of NLO QCD predictions, obtained with different PDF sets and corrected for non-perturbative effects, to data as a function of  $m_{jjj}$  in regions of  $|Y^*|$ , as denoted in the legend. The ratios are for anti- $k_t$  jets with  $R = 0.6$ . The experimental error bands are centred at one and designate the relative statistical (thin dashed line) and total (statistical and systematic uncertainties added in quadrature) experimental uncertainties (thick solid line). Thick lines with the hatched or filled band around them represent the theoretical predictions with the corresponding theoretical uncertainties.

## 5.10 Results of the $Z + \text{jets}$ cross-section measurement

The double differential  $Z + \text{jets}$  cross-section is measured using 8 TeV  $pp$  collisions data as a function of jet rapidity and transverse momentum. The measurement is performed using the anti- $k_t$  jets with  $R = 0.4$ . All background events are subtracted from the data. The data are corrected for detector effects and provided on the particle level. The measurement results are shown in Figure 5.29. The phase space of the measurement is defined within the  $|y_{\text{jet}}| < 3.4$  and  $25 \text{ GeV} < p_{\text{T}}^{\text{jet}} < 1050 \text{ GeV}$  range. The measured cross-section covers five orders of magnitude and falls steeply as a function of  $|y_{\text{jet}}|$  and  $p_{\text{T}}^{\text{jet}}$ .

The measured cross-section are provided along with systematic and statistical uncertainties in Appendix B. The measured cross-sections with the full breakdown of all uncertainties are provided in the HEPData database.

The comparisons with the theoretical predictions are shown in Figure 5.29. The fixed-order QCD predictions are corrected for the non-perturbative and QED radiation effects. The predictions obtained at the NLO accuracy are lower than the data by approximately 5%–10%. However, this difference is covered by uncertainties. The calculations obtained at the NNLO accuracy agree with the data much better, so their central cross-section values match in many phase space regions. The predictions obtained using the parton-shower event generators describe well the shape of the  $|y_{\text{jet}}|$  distribution, but there is a dependence on the  $p_{\text{T}}^{\text{jet}}$  in some of them. The predictions from different generators match the data in different regions of the phase space. Therefore, improved precision is required for these predictions.

In addition to the default predictions, a comparison to the most modern one obtained using the SHERPA v. 2.2 is performed. In this prediction, the matrix elements are calculated with the NLO accuracy for the inclusive  $Z$  production process with up to two additional partons in the final state, and with the LO accuracy in the final states with up to four partons. The matrix elements are convolved with the NNPDF 3.0 [209] PDFs. The matrix elements are merged with the SHERPA parton shower using the ME+PS@NLO [210] prescription, which avoids double counting between them. This prediction shows the best agreement with data in all bins of the measurement.

Qualitative comparisons between the measured  $Z + \text{jets}$  cross-section and the NLO QCD predictions obtained using different PDFs are shown in Figure 5.30. None of the PDFs results in a significant improvement in the agreement between the data and predictions. The difference between predictions obtained using different PDFs is within the theoretical uncertainty. This uncertainty is compatible with the experimental uncertainty in the measurement. The precision of the predictions improves significantly in the case of NNLO calculations. However, the

difference between predictions obtained with the two most widespread PDFs is comparable to the size of the uncertainty as shown in Figure 5.31. Therefore, further improvements are required to match the predictions to the data.

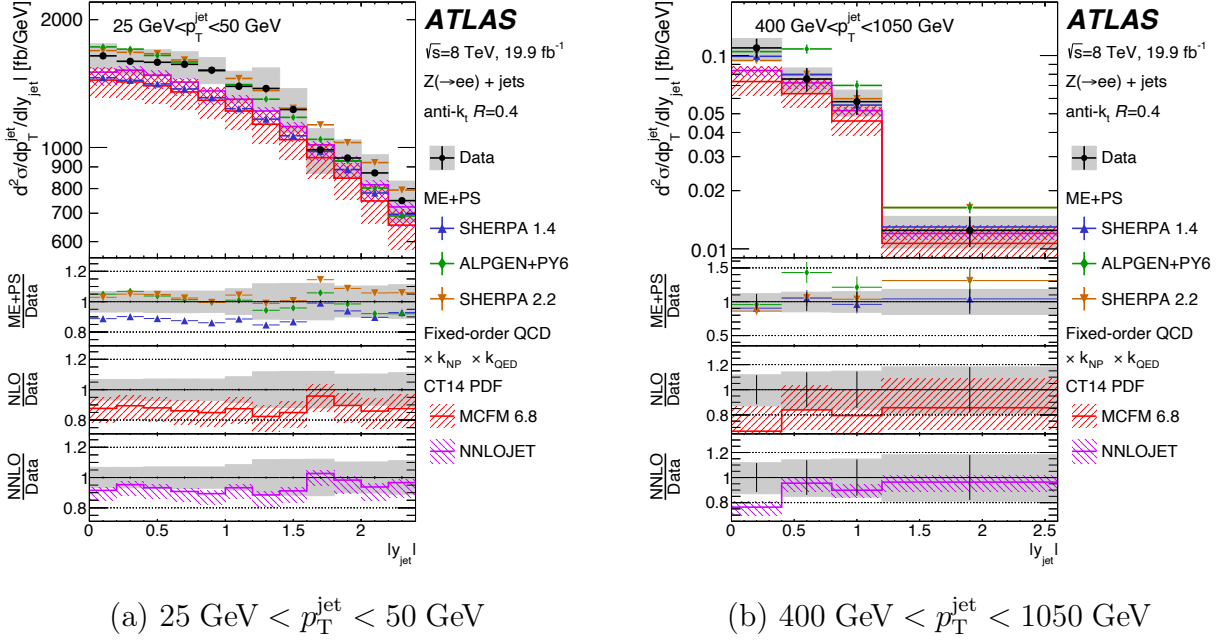


Figure 5.29 — The double differential  $Z + \text{jets}$  production cross-section as a function of  $|y_{\text{jet}}|$  measured in (a) low and (b) high  $p_T^{\text{jet}}$  regions. The jets are identified using the anti- $k_t$  algorithm with  $R = 0.4$ . The data are compared to the parton-shower event generator predictions and the fixed-order QCD prediction obtained at NLO and NNLO accuracy. The former predictions imply that parton showers (PS) supplement the multi-leg matrix element (ME) calculations, so they are referred to as the ME+PS predictions. The fixed-order QCD predictions are corrected for the non-perturbative and QED radiation effects. The statistical uncertainties are shown with error bars. The total uncertainties in the measurement and fixed-order QCD predictions are shown with shaded bands. The luminosity uncertainty of 1.9% is not included in the experimental uncertainty. The lower panels show the ratios between the predictions and data.

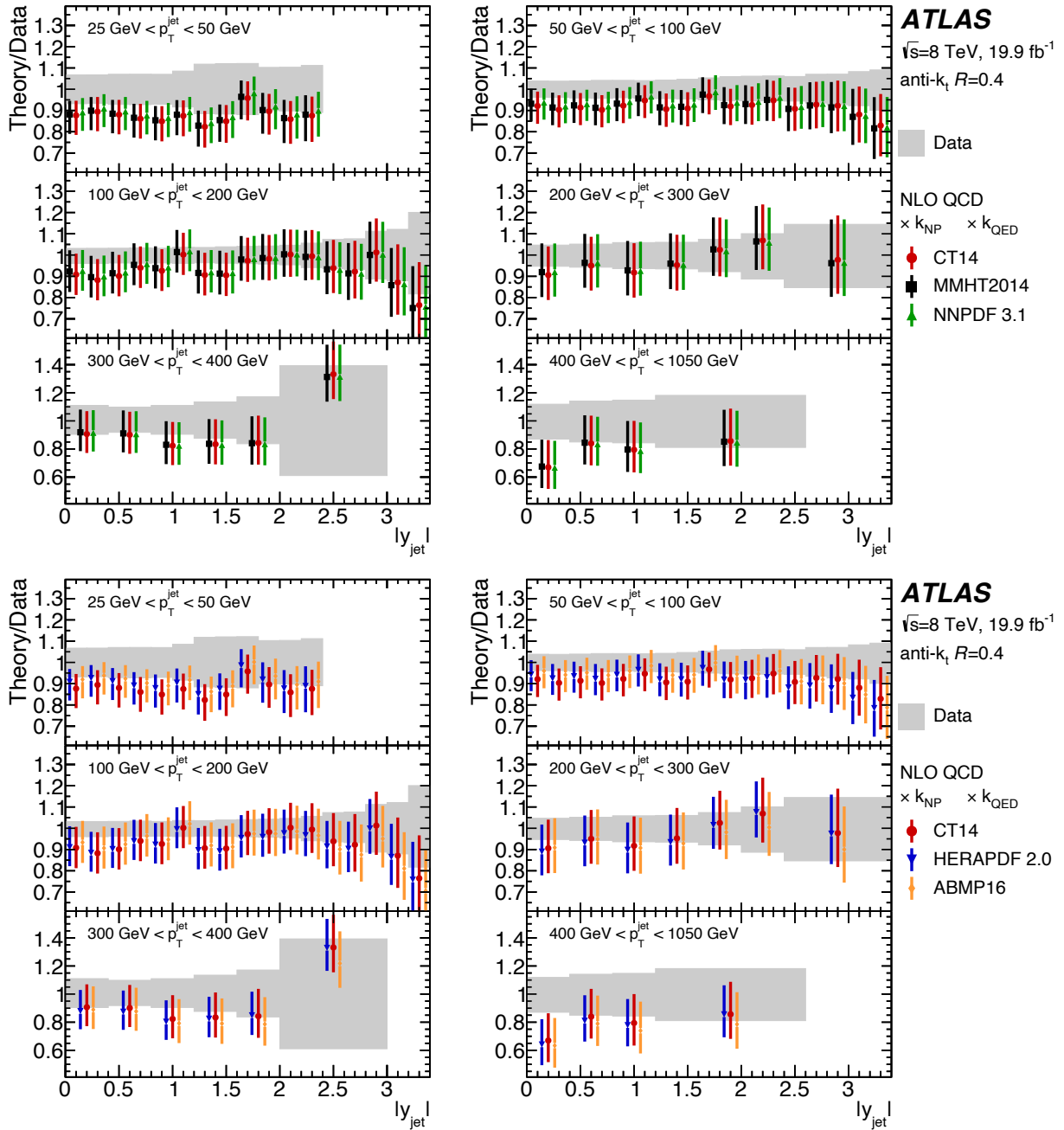


Figure 5.30 — The ratio of the measured  $Z + \text{jets}$  cross-section and the NLO QCD predictions as a function of  $|y_{\text{jet}}|$  and  $p_{\text{T}}^{\text{jet}}$ . The predictions are corrected for the non-perturbative and QED radiation effects. Theoretical predictions are calculated using different PDF sets and shown with coloured markers. The bars represent the total theoretical uncertainty. The grey band shows the sum in quadrature of the statistical and systematic uncertainties in the measurement except for the luminosity uncertainty of 1.9%.

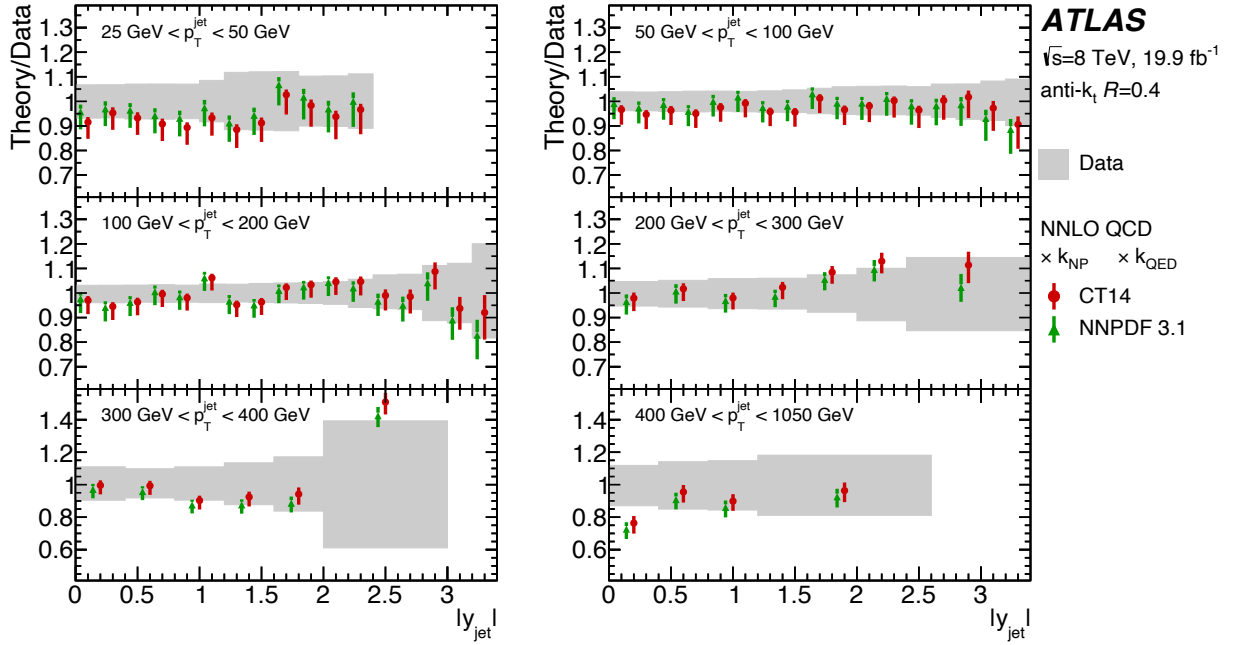


Figure 5.31 — The ratio of the measured  $Z + \text{jets}$  cross-section and the NNLO QCD predictions as a function of  $|y_{\text{jet}}|$  and  $p_{\text{T}}^{\text{jet}}$ . The predictions are corrected for the non-perturbative and QED radiation effects. Theoretical predictions are calculated using different PDF sets and shown with coloured markers. The bars represent the total theoretical uncertainty. The grey band shows the sum in quadrature of the statistical and systematic uncertainties in the measurement except for the luminosity uncertainty of 1.9%.

## 5.11 Quantitative comparison to theoretical predictions

There are many PDF sets constructed on different assumptions or using different data. Identifying which leads to the best data predictions is necessary to improve the others. However, a qualitative comparison between the measured cross-sections and theoretical predictions obtained using different PDF sets does not reveal the best one. Some of the predictions are better in different kinematic regions, and none match the data across the full range of the measurement. Therefore, a quantitative statement about their agreement is required.

A quantitative comparison between the data and theoretical predictions is performed using a  $\chi^2$  function that accounts for both experimental and theoretical uncertainties and their correlations. That is

$$\begin{aligned} \chi^2(\beta^{\text{data}}, \beta^{\text{theory}}) = & \sum_{i=1}^{N_{\text{bins}}} \frac{(\sigma_i^{\text{data}} + \sum_{\mu} \beta_{\mu}^{\text{data}} \Delta_{i\mu}^{\text{data}} - \sigma_i^{\text{theory}} - \sum_{\nu} \beta_{\nu}^{\text{theory}} \Delta_{i\nu}^{\text{theory}})^2}{\delta_i^2} + \\ & + \sum_{\mu} (\beta_{\mu}^{\text{data}})^2 + \sum_{\nu} (\beta_{\nu}^{\text{theory}})^2, \end{aligned} \quad (5.18)$$

where  $\sigma_i^{\text{data}}$  and  $\sigma_i^{\text{theory}}$  are the measured and computed cross-sections in a given kinematic region  $i$ , respectively. The  $\beta_{\mu}^{\text{data}}$  is a nuisance parameter of an amplitude  $\Delta_{i\mu}^{\text{data}}$  of a given experimental uncertainty component  $\mu$ . The  $\beta_{\nu}^{\text{theory}}$  and  $\Delta_{i\nu}^{\text{theory}}$  describe a given component  $\nu$  of the theoretical uncertainty, correspondingly. All systematic and theoretical uncertainties are assumed to be independent of each other and fully correlated across the measurement kinematics. Their nuisance parameters are assumed to be normally distributed. The correlations of the statistical uncertainty  $\delta_i^2$  are not taken into account. Minimising the  $\chi^2$  function quantifies the compatibility between the data and theoretical predictions.

The minimisation of the  $\chi^2$  function, for the case of symmetric systematic uncertainties, results in a system of linear equations for shifts of systematic uncertainties,  $\beta_{\rho}$ . However, most systematic and theoretical uncertainties are asymmetric. These asymmetries are accounted for using an iterative procedure. At each iteration, the amplitudes  $\Delta_{i\rho}$  are recalculated as

$$\Delta_{i\rho} \rightarrow \Delta_{i\rho} + \beta_{\rho} \nabla_{i\rho}, \quad (5.19)$$

where  $\Delta_{i\rho} = (\Delta_{i\rho}^+ - \Delta_{i\rho}^-)/2$  and  $\nabla_{i\rho} = (\Delta_{i\rho}^+ + \Delta_{i\rho}^-)/2$  are defined using the positive  $\Delta_{i\rho}^+$  and negative  $\Delta_{i\rho}^-$  components of systematic uncertainties.

Correlated shifts of nuisance parameters after minimisation, represented by the second and third terms of the  $\chi^2$  function, are usually referred to as the  $\chi_{\text{corr}}^2$ , while the  $\chi_{\text{uncorr}}^2$  notation is used for the first term.

The minimisation of the  $\chi^2$  between the measured and computed three-jets cross-sections is summarised in Table 5.4. The NLO predictions obtained with different PDF sets and corrected for the non-perturbative effects are used in the comparisons. The PDF sets leading to the cross-section predictions most consistent with the data are selected for this comparison. The  $\chi^2$  minimisation is performed globally in all bins of the measurement. The total  $\chi^2$  is slightly above 120 for the anti- $k_t$   $R = 0.4$  jets. This indicates a good agreement between the data and predictions, considering that the number of degrees of freedom (n.d.f.) is 105. The predictions resulting in the  $\chi^2/\text{n.d.f.}$  closest to one are the most consistent with the data. The agreement is significantly worse when the anti- $k_t$   $R = 0.6$  jets are used. The total  $\chi^2$  at the same n.d.f. exceeds 160 for the considered PDF sets, as the predictions systematically underestimate the data. However, the predictions obtained using the MSTW 2008 PDF are the most consistent with the data regardless of the jet radius. But the other PDF sets are not significantly worse.

Table 5.4. — Values of  $\chi^2$  evaluated from the comparisons of the NLO QCD predictions corrected for non-perturbative effects and measured three-jets cross-section. The predictions are obtained using different PDF sets. The  $\chi_{\text{total}}^2$  is the sum of  $\chi_{\text{uncorr}}^2$  and  $\chi_{\text{corr}}^2$ . The  $\chi^2$  minimisations are performed globally in all kinematic regions of the measurement.

	$ Y^* $ region	CT 10		NNPDF 2.1		MSTW 2008	
		R=0.4	R=0.6	R=0.4	R=0.6	R=0.4	R=0.6
$\chi_{\text{uncorr}}^2$	$ Y^*  < 2$	13.30	39.66	14.21	42.53	14.03	41.04
	$2 <  Y^*  < 4$	41.08	61.31	40.97	60.32	40.49	61.12
	$4 <  Y^*  < 6$	29.44	19.07	26.36	19.18	25.75	19.36
	$6 <  Y^*  < 8$	19.42	10.74	22.80	12.58	22.33	12.98
	$8 <  Y^*  < 10$	6.97	6.51	5.90	6.56	5.73	6.63
$\chi_{\text{corr}}^2$		13.85	26.73	15.08	24.55	12.34	19.19
$\chi_{\text{total}}^2$		124.07	164.03	125.32	165.72	120.68	160.32
n.d.f.		105	105	105	105	105	105
$\chi_{\text{total}}^2/\text{n.d.f.}$		1.18	1.56	1.19	1.58	1.15	1.53

The quantitative comparisons of the  $Z$  + jets cross-section are summarised in Table 5.5. The data are compared to the NNLO QCD predictions obtained with different PDF sets and corrected for non-perturbative and QED radiation effects. The improved versions of the PDF sets compared to the three-jets study are used. In addition, the ABMP16 PDF leading to the best agreement with data is shown. The total  $\chi^2$  is above 120 when the minimisation is performed globally in all bins of the measurement. Since the n.d.f. is 63, the agreement between the data and the theory is twice worse than in the case of three-jets. The largest difference between the data and predictions is in the lowest  $p_T^{\text{jet}}$  regions, so the minimisation

Table 5.5. — Values of  $\chi^2$  evaluated from the comparisons of the NNLO QCD predictions corrected for non-perturbative effects and measured  $Z + \text{jets}$  cross-section. The predictions are obtained using different PDF sets. The  $\chi_{\text{total}}^2$  is the sum of  $\chi_{\text{uncorr}}^2$  and  $\chi_{\text{corr}}^2$ . The  $\chi^2$  minimisations are performed globally in all kinematic regions of the measurement within several  $p_{\text{T}}^{\text{jet}}$  ranges.

	$p_{\text{T}}^{\text{jet}}$ region [ GeV ]	CT 14	NNPDF 3.1	MMHT 2014	ABMP 16
$p_{\text{T}}^{\text{jet}} > 25$ GeV					
$\chi_{\text{uncorr}}^2$	$25 < p_{\text{T}}^{\text{jet}} < 50$	40.5	42.3	41.3	38.7
	$50 < p_{\text{T}}^{\text{jet}} < 100$	33.0	37.5	39.2	31.6
	$100 < p_{\text{T}}^{\text{jet}} < 200$	27.8	31.0	31.7	27.8
	$200 < p_{\text{T}}^{\text{jet}} < 300$	6.3	5.1	5.6	4.1
	$300 < p_{\text{T}}^{\text{jet}} < 400$	3.0	2.9	3.1	2.5
	$400 < p_{\text{T}}^{\text{jet}} < 1050$	2.4	2.2	2.3	1.7
$\chi_{\text{corr}}^2$		19.8	19.3	18.7	17.8
$\chi_{\text{total}}^2$		132.6	140.0	141.9	124.3
n.d.f.		63	63	63	63
$\chi_{\text{total}}^2/\text{n.d.f.}$		2.1	2.2	2.3	2.0
$p_{\text{T}}^{\text{jet}} > 50$ GeV					
$\chi_{\text{uncorr}}^2$	$50 < p_{\text{T}}^{\text{jet}} < 100$	24.8	26.9	27.1	24.8
	$100 < p_{\text{T}}^{\text{jet}} < 200$	24.6	26.6	27.7	22.7
	$200 < p_{\text{T}}^{\text{jet}} < 300$	4.2	4.4	4.7	3.4
	$300 < p_{\text{T}}^{\text{jet}} < 400$	2.8	3.0	3.1	2.5
	$400 < p_{\text{T}}^{\text{jet}} < 1050$	4.0	3.8	3.9	2.9
$\chi_{\text{corr}}^2$		4.7	4.3	5.1	4.1
$\chi_{\text{total}}^2$		65.2	69.0	71.6	60.4
n.d.f.		51	51	51	51
$\chi_{\text{total}}^2/\text{n.d.f.}$		1.3	1.4	1.4	1.2
$p_{\text{T}}^{\text{jet}} > 100$ GeV					
$\chi_{\text{uncorr}}^2$	$100 < p_{\text{T}}^{\text{jet}} < 200$	25.0	25.9	26.6	22.4
	$200 < p_{\text{T}}^{\text{jet}} < 300$	3.3	4.1	4.4	3.3
	$300 < p_{\text{T}}^{\text{jet}} < 400$	2.8	3.0	3.1	2.6
	$400 < p_{\text{T}}^{\text{jet}} < 1050$	3.8	3.6	3.6	3.3
$\chi_{\text{corr}}^2$		3.7	2.7	4.1	2.3
$\chi_{\text{total}}^2$		38.5	39.3	41.8	33.8
n.d.f.		34	34	34	34
$\chi_{\text{total}}^2/\text{n.d.f.}$		1.1	1.2	1.2	1.0

excluding the first and the first two  $p_{\text{T}}^{\text{jet}}$  regions is performed. As a result, a very good agreement between the data and predictions is obtained already when the first  $p_{\text{T}}^{\text{jet}}$  region is excluded, with further improvements when the second one is excluded. However, these exclusions lead to the loss of experimental information if the same is performed to improve PDF. Therefore, improved predictions in the low  $p_{\text{T}}^{\text{jet}}$  regions are necessary.

## 5.12 Summary and outlook

The double differential three-jets and  $Z + \text{jets}$  cross-sections are measured using the data on  $pp$  collisions with the centre of mass energy of 7 and 8 TeV collected by the ATLAS experiment. The measurements are performed as a function of jet kinematics in the TeV regime. The results are unfolded to the particle level, which is necessary for direct comparisons with the fixed-order theory predictions. The cross-sections are provided with detailed information about the systematic uncertainty, described by almost 70 independent components. The results agree with theoretical predictions in most of the probed kinematics regions. However, there are cases when improved predictions are required. For example, the three-jet cross-section predictions for the anti- $k_t$  jets with  $R = 0.6$  systematically underestimate the data by up to 20%. In the  $Z + \text{jets}$  case, some tension exists with predictions at low  $p_T^{\text{jet}}$  regions, where better theory predictions may be required. Nevertheless, the uncertainty in theoretical predictions is almost the same as the experimental uncertainty, so predictions with improved precision are necessary. Among the dominant theoretical uncertainties is the one associated with the non-perturbative effects, so its reduction is required. The results of the measurement provide a means for these improvements. In addition, they provide important input to constrain the parton distribution functions, especially the gluon contribution.

# Summary and conclusions

Studies of jet production in collider experiments is a vibrant topic. The first observations of jets in particle collisions led to the discovery of quarks and gluons. Since then, jets have become one of the key tools for studying the Standard Model physics and searching for new phenomena. The use cases of jets include studies of the structure of hadrons and measurements of the coupling of strong interactions. These studies stimulate the development of the theory of fundamental interactions and elementary constituents of matter.

The Large Hadron Collider is the most modern device for such studies. In proton–proton collisions at the LHC, jets are produced abundantly. The centre-of-mass energy of such collisions exceeds that of previous colliders. Thus, the studies at the LHC, especially those using jets, explore new energy frontiers.

In the course of the studies, jets are considered from three perspectives. The first one considers the objects necessary to reconstruct jets in the experiment. These objects are calorimeter energy deposits, the main input to jet reconstruction. Particles that deposit energy in the calorimeter often originate from many simultaneous  $pp$  interactions, whose number can exceed 200 in the LHC upgrade scenarios. The overlay of their energy deposits affects the jet energy measurements. The effect of such overlay is treated as pile-up noise, whose magnitude is measured in cells of the hadronic Tile Calorimeter. For this purpose, a method has been developed that accounts for pile-up noise dependence on the collider luminosity. The method has been adopted as the default for measuring pile-up noise in the Tile Calorimeter. In this context, the pile-up noise measurement using the  $pp$  collisions data with  $\sqrt{s} = 8$  TeV is reported. The results are shown to be underestimated by the simulation by about 10%. Thus, improved soft physics modelling may be required to provide a better description of the hadron shower development. The measured noise is loaded into the ATLAS software database and used by the jet reconstruction algorithm to suppress the energy contribution associated with the pile-up noise. Such a suppression improves the jet energy resolution in the ATLAS experiment.

The second perspective considers reconstructed jets whose energy needs to be calibrated to ensure the most precise measurements in any physics analysis using jets in the ATLAS experiment. The calibration is performed *in situ* using the  $pp$  collisions data with  $\sqrt{s} = 13$  TeV. The jets are calibrated against the  $Z$ -boson decaying into an electron and a positron, whose energies are measured

precisely. As a result, jets with transverse momenta in the range from about 20 GeV to 500 GeV are calibrated with an accuracy of up to 1.5%. The results are combined with calibrations measured in other jet transverse momenta regions and provided as recommendations for all ATLAS studies. The derived calibration is particularly important for jet cross-section measurements, which are very sensitive to jet energy measurement inaccuracy.

The third perspective uses reconstructed and calibrated jets to probe predictions of perturbative Quantum Chromodynamics. For this purpose, the cross-sections of the three-jets productions and the production of jets associated with a  $Z$ -boson are measured using the  $pp$  collision data with  $\sqrt{s} = 7$  TeV and 8 TeV, respectively. The three-jets cross-section is measured double-differentially as a function of  $m_{\text{jjj}}$  and  $|Y^*|$ , where the  $m_{\text{jjj}}$  reaches up to 5 TeV. The  $Z + \text{jets}$  cross-section is measured as a function of  $|y_{\text{jet}}|$  and  $p_{\text{T}}^{\text{jet}}$ , where the  $p_{\text{T}}^{\text{jet}}$  reaches up to about 1 TeV. Such energy scales exceed the reach of previous experiments. The measured cross-section spans up to seven orders of magnitude. The results of both measurements are corrected for detector effects and provided on the particle level. The results are supplied with thoroughly studied systematic uncertainties, among which the jet energy measurement uncertainty dominates most of the probed jet kinematics regions. The accuracy in the three-jet cross-section measurement is consistent with that of the NLO predictions. The accuracy in the  $Z + \text{jets}$  cross-section measurements exceeds that of the NLO predictions and is comparable to that of the NNLO predictions, which first appeared just at the time of measurement. Within the uncertainties, the measured cross-section agree with theoretical predictions corrected for non-perturbative effects. Quantitative comparisons to theoretical predictions obtained with different PDFs show little difference. However, to study more subtle effects, increased accuracy in predictions may be required.

Apart from probing theoretical predictions, the measured cross-sections provide accurate input for constraining PDFs and  $\alpha_{\text{S}}$ . The results were shown to be particularly sensitive to the quark sea and gluon PDFs. Considering the new energy scales explored experimentally, the measured cross-sections have great potential for improving the description of theoretical unknowns. This allows a step towards a better understanding of fundamental interactions and elementary constituents of matter.

## References

1. *ATLAS Collaboration*. The ATLAS Collaboration Software and Firmware / ATLAS Collaboration. — 2021. — URL: <https://cds.cern.ch/record/2767187>. ATL-SOFT-PUB-2021-001.
2. *Hrynevich, A.* Performance of the ATLAS Tile Calorimeter / A. Hrynevich // J. of Instrumentation. — 2017. — Vol. 12, no. C06021. — P. 8.
3. *ATLAS Collaboration*. Operation and performance of the ATLAS Tile Calorimeter in Run 1 / ATLAS Collaboration // Eur. Phys. J. C. — 2018. — Vol. 78. — P. 987. — arXiv: [1806.02129 \[hep-ex\]](https://arxiv.org/abs/1806.02129).
4. *Karnevskiy, M.* Measurement of the Z Boson production with the ATLAS Experiment at the LHC / M. Karnevskiy // PhD thesis. — Universität Hamburg, 2012.
5. *Sedov, G.* Measurement of Z Boson production using  $Z \rightarrow ee$  decays with one of the electrons detected in the forward calorimeters of the ATLAS detector using  $4.6 \text{ fb}^{-1}$  of data collected at  $\sqrt{s} = 7 \text{ TeV}$  / G. Sedov // PhD thesis. — Universität Hamburg, 2016.
6. *ATLAS Collaboration*. Jet energy scale measurements and their systematic uncertainties in proton–proton collisions at  $\sqrt{s} = 13 \text{ TeV}$  with the ATLAS detector / ATLAS Collaboration // Phys. Rev. D. — 2017. — Vol. 96. — P. 072002. — arXiv: [1703.09665 \[hep-ex\]](https://arxiv.org/abs/1703.09665).
7. *Hrynevich, A.* ATLAS jet and missing energy reconstruction, calibration and performance in LHC Run-2 / A. Hrynevich // J. of Instrumentation. — 2017. — Vol. 12, no. C06038. — P. 7.
8. *Hrynevich, A.* Jet Energy Scale Calibration and Uncertainties with 13 TeV [Electronic resource] / A. Hrynevich // 125 LHC Experiments Committee Meeting, Geneva, Switzerland, 2 – 3 March 2016. — 2016. — Mode of access: <https://indico.cern.ch/event/491582/contributions/1168890/attachments/1236380/1815614/ATL-PHYS-SLIDE-2016-104.pdf>. — Date of acces: 28.09.2018.
9. *ATLAS Collaboration*. Measurement of three-jet production cross-sections in  $pp$  collisions at 7 TeV centre-of-mass energy using the ATLAS detector / ATLAS Collaboration // Eur. Phys. J. C. — 2015. — Vol. 75. — P. 228. — arXiv: [1411.1855 \[hep-ex\]](https://arxiv.org/abs/1411.1855).

10. *Kondrashova, N.* Measurement of Z boson plus jet production cross section using  $\sqrt{s} = 8$  TeV data and studies of jet quark-gluon decomposition / N. Kondrashova // PhD thesis. — Universität Hamburg, 2016.
11. *ATLAS Collaboration.* Measurement of the inclusive cross-section for the production of jets in association with a Z boson in proton–proton collisions at 8 TeV using the ATLAS detector / ATLAS Collaboration // Eur. Phys. J. C. — 2019. — Vol. 79. — P. 847. — arXiv: [1907.06728 \[hep-ex\]](https://arxiv.org/abs/1907.06728).
12. *ATLAS Collaboration.* ATLAS Tile Calorimeter Phase-II Upgrade: Technical Design Report : ATLAS-TDR-028; CERN-LHCC-2017-019 / ATLAS Collaboration. — 2017. — URL: <https://cds.cern.ch/record/2285583>.
13. *ATLAS Collaboration.* Measurement of the inclusive jet cross-section in proton–proton collisions at  $\sqrt{s} = 7$  TeV using  $4.5 \text{ fb}^{-1}$  of data with the ATLAS detector / ATLAS Collaboration // JHEP. — 2015. — Vol. 02. — P. 153. — arXiv: [1410.8857 \[hep-ex\]](https://arxiv.org/abs/1410.8857). — Erratum: // JHEP. 2015. Vol. 09. P. 141.
14. *ATLAS Collaboration.* Determination of the parton distribution functions of the proton from ATLAS measurements of differential  $W^\pm$  and Z boson production in association with jets / ATLAS Collaboration // JHEP. — 2021. — Vol. 07. — P. 223. — arXiv: [2101.05095 \[hep-ex\]](https://arxiv.org/abs/2101.05095).
15. Evidence for Jet Structure in Hadron Production by  $e^+e^-$  Annihilation / G. Hanson [et al.] // Phys. Rev. Lett. — 1975. — Dec. — Vol. 35, issue 24. — P. 1609–1612. — URL: <https://link.aps.org/doi/10.1103/PhysRevLett.35.1609>.
16. *Ali, A.* Jets and QCD: A Historical Review of the Discovery of the Quark and Gluon Jets and its Impact on QCD / A. Ali, G. Kramer // Eur. Phys. J. H. — 2010. — Vol. 36. — P. 245–326.
17. *Evans, L.* LHC Machine / L. Evans, P. Bryant // JINST. — 2008. — Vol. 3. — S08001.
18. *ATLAS Collaboration.* The ATLAS Experiment at the CERN Large Hadron Collider / ATLAS Collaboration // JINST. — 2008. — Vol. 3. — S08003.
19. *CMS Collaboration.* The CMS Experiment at the CERN LHC / CMS Collaboration // JINST. — 2008. — Vol. 3. — S08004.
20. *LHCb Collaboration.* The LHCb Detector at the LHC / LHCb Collaboration // JINST. — 2008. — Vol. 3. — S08005.
21. *ALICE Collaboration.* The ALICE experiment at the CERN LHC / ALICE Collaboration // JINST. — 2008. — Vol. 3. — S08002.

22. *Burgess, C.* The Standard Model: A Primer / C. Burgess, G. Moore. — Cambridge University Press, 2012. — P. 560.
23. *Okun, L. B.* Physics of elementary particles / L. B. Okun. — M. : Nauka, 1988. — P. 272.
24. *Okun, L. B.* Leptons and quarks / L. B. Okun. — M. : Nauka, 1990. — P. 346.
25. *Weinberg, S.* A Model of Leptons / S. Weinberg // Phys. Rev. Lett. — 1967. — Nov. — Vol. 19, issue 21. — P. 1264–1266. — URL: <https://link.aps.org/doi/10.1103/PhysRevLett.19.1264>.
26. *Higgs, P.* Broken symmetries, massless particles and gauge fields / P. Higgs // Physics Letters. — 1964. — Vol. 12, no. 2. — P. 132–133. — URL: <https://www.sciencedirect.com/science/article/pii/0031916364911369>.
27. *Higgs, P. W.* Broken Symmetries and the Masses of Gauge Bosons / P. W. Higgs // Phys. Rev. Lett. — 1964. — Oct. — Vol. 13, issue 16. — P. 508–509. — URL: <https://link.aps.org/doi/10.1103/PhysRevLett.13.508>.
28. *Englert, F.* Broken Symmetry and the Mass of Gauge Vector Mesons / F. Englert, R. Brout // Phys. Rev. Lett. — 1964. — Aug. — Vol. 13, issue 9. — P. 321–323. — URL: <https://link.aps.org/doi/10.1103/PhysRevLett.13.321>.
29. *Guralnik, G. S.* Global Conservation Laws and Massless Particles / G. S. Guralnik, C. R. Hagen, T. W. B. Kibble // Phys. Rev. Lett. — 1964. — Nov. — Vol. 13, issue 20. — P. 585–587. — URL: <https://link.aps.org/doi/10.1103/PhysRevLett.13.585>.
30. *Kibble, T. W. B.* Symmetry Breaking in Non-Abelian Gauge Theories / T. W. B. Kibble // Phys. Rev. — 1967. — Mar. — Vol. 155, issue 5. — P. 1554–1561. — URL: <https://link.aps.org/doi/10.1103/PhysRev.155.1554>.
31. *ATLAS Collaboration.* Observation of a new particle in the search for the Standard Model Higgs boson with the ATLAS detector at the LHC / ATLAS Collaboration // Phys. Lett. B. — 2012. — Vol. 716. — P. 1. — arXiv: [1207.7214](https://arxiv.org/abs/1207.7214) [hep-ex].
32. *CMS Collaboration.* Observation of a new boson at a mass of 125 GeV with the CMS experiment at the LHC / CMS Collaboration // Phys. Lett. B. — 2012. — Vol. 716. — P. 30. — arXiv: [1207.7235](https://arxiv.org/abs/1207.7235) [hep-ex].
33. Standard Model [Electronic resource] // Wikipedia. — Mode of access: [https://en.wikipedia.org/wiki/Standard\\_Model](https://en.wikipedia.org/wiki/Standard_Model). — Date of access: 04.10.2022.
34. *Pesking, M.* An Introduction To Quantum Field Theory / M. Pesking, D. Schroeder. — Boulder, CO : Westview, 1995.

35. *Halzen, F.* Quarks and Leptons: An Introductory Course in Modern Particle Physics / F. Halzen, A. Martin. — New York : Wiley, 1984.
36. *Dissertori, G.* Quantum Chromodynamics: High Energy Experiments and Theory / G. Dissertori, G. Knowles, M. Schmelling. — Oxford University Press, 2009. — P. 560.
37. *Mangano, M. L.* QCD and the physics of hadronic collisions / M. L. Mangano // Phys.–Usp. — 2010. — Vol. 53:109. — P. 109–132.
38. *Mangano, M. L.* Introduction to QCD / M. L. Mangano // European School on High-Energy Physics. — 1998. — P. 44.
39. *Skands, P. Z.* QCD for Collider Physics / P. Z. Skands // European School of High Energy Physics, Raseborg, Finland, 20 June – 3 July 2010. — CERN, Theory department, 2011. — P. 48.
40. *Sjöstrand, T.* Monte Carlo Generators / T. Sjöstrand // European School of High Energy Physics, Aronsborg, Sweden, 18 June – 1 July 2006. — CERN, Theory department, 2006. — P. 23.
41. General-purpose event generators for LHC physics / A. Buckley [et al.] // Phys. Rep. — 2011. — Vol. 504. — P. 145–233.
42. *Gross, D. J.* Ultraviolet Behavior of Non-Abelian Gauge Theories / D. J. Gross, F. Wilczek // Phys. Rev. Lett. — 1973. — June. — Vol. 30, issue 26. — P. 1343–1346. — URL: <https://link.aps.org/doi/10.1103/PhysRevLett.30.1343>.
43. *Politzer, H. D.* Reliable Perturbative Results for Strong Interactions? / H. D. Politzer // Phys. Rev. Lett. — 1973. — June. — Vol. 30, issue 26. — P. 1346–1349. — URL: <https://link.aps.org/doi/10.1103/PhysRevLett.30.1346>.
44. Review of Particle Physics / Particle Data Group // Progress of Theoretical and Experimental Physics. — 2022. — Vol. 72. — P. 1849.
45. *Salam, G. P.* Elements of QCD for hadron colliders / G. P. Salam. — 2010. — arXiv: [1011.5131 \[hep-ph\]](https://arxiv.org/abs/1011.5131).
46. *Gribov, V. N.* Deep inelastic  $ep$  scattering in perturbation theory / V. N. Gribov, L. N. Lipatov // Sov. J. Nucl. Phys. — 1972. — Vol. 15. — P. 438–450.
47. *Lipatov, L. N.* The parton model and perturbation theory / L. N. Lipatov // Sov. J. Nucl. Phys. — 1975. — Vol. 20. — P. 94–102.
48. *Altarelli, G.* Asymptotic freedom in parton language / G. Altarelli, G. Parisi // Nucl. Phys. B. — 1977. — Vol. 126. — P. 298–318.

49. *Dokshitzer, Y. L.* Calculation of the structure functions for deep inelastic scattering and  $e^+e^-$  annihilation by perturbation theory in quantum chromodynamics / Y. L. Dokshitzer // Sov. Phys. JETP. — 1977. — Vol. 46. — P. 641–653.
50. *De Roeck, A.* Structure functions / A. De Roeck, R. Thorne // Progress in Particle and Nuclear Physics. — 2011. — Vol. 66. — P. 727–781.
51. New CTEQ global analysis of quantum chromodynamics with high-precision data from the LHC / T.-J. Hou [et al.] // Physical Review D. — 2021. — Jan. — Vol. 103, no. 1. — P. 116. — arXiv: [1912.10053 \[hep-ph\]](#).
52. Parton distributions from LHC, HERA, Tevatron and fixed target data: MSHT20 PDFs / S. Bailey [et al.] // The European Physical Journal C. — 2021. — Apr. — Vol. 81, no. 4. — P. 140. — arXiv: [2012.04684 \[hep-ph\]](#).
53. Parton distributions from high-precision collider data / R. D. Ball [et al.] // The European Physical Journal C. — 2017. — Oct. — Vol. 77, no. 10. — P. 86. — arXiv: [1002.4407 \[hep-ph\]](#).
54. Combination of measurements of inclusive deep inelastic  $e^\pm p$  scattering cross sections and QCD analysis of HERA data / H1 and ZEUS Collaborations // Eur. Phys. J. C. — 2015. — Vol. 75:580. — P. 98.
55. Parton distribution functions,  $\alpha_s$  and heavy-quark masses for LHC Run II / S. Alekhin [et al.] // Phys. Rev. D. — 2017. — Vol. 96:014011. — P. 48.
56. *Jimenez-Delgado, P.* Delineating parton distributions and the strong coupling / P. Jimenez-Delgado, E. Reya // Phys. Rev. D. — 2014. — Vol. 89:074049. — P. 17.
57. *Kinoshita, T.* Mass singularities of feynman amplitudes / T. Kinoshita // J. Math. Phys. — 1962. — Vol. 3. — P. 650.
58. *Lee, T.* Degenerate systems and mass singularities / T. Lee, M. Nauenberg // Phys. Rev. B. — 1964. — Vol. 133. — P. 1549.
59. *Nagy, Z.* Next-to-leading order calculations of three jet observables in hadron hadron collisions / Z. Nagy // Phys. Rev. D. — 2003. — Vol. 68:094002. — P. 11.
60. *Campbell, J.* MCFM for the Tevatron and the LHC / J. Campbell, R. Ellis // Nucl. Phys. Proc. Suppl. — 2010. — Vol. 205–206. — P. 6.
61. *Sjöstrand, T.* PYTHIA 6.4 physics and manual / T. Sjöstrand, S. Mrenna, P. Z. Skands // JHEP. — 2006. — Vol. 05. — P. 026. — arXiv: [hep-ph/0603175](#).
62. *Sjöstrand, T.* A brief introduction to PYTHIA 8.1 / T. Sjöstrand, S. Mrenna, P. Skands // Comput. Phys. Commun. — 2008. — Vol. 178. — P. 852–867. — arXiv: [0710.3820 \[hep-ph\]](#).

63. An introduction to PYTHIA 8.2 / T. Sjöstrand [et al.] // Comput. Phys. Commun. — 2015. — Vol. 191. — P. 159. — arXiv: [1410.3012 \[hep-ph\]](#).
64. HERWIG 6: an event generator for hadron emission reactions with interfering gluons (including supersymmetric processes) / G. Corcella [et al.] // JHEP. — 2001. — Vol. 01. — P. 010. — arXiv: [hep-ph/0011363](#).
65. Herwig++ physics and manual / M. Bähr [et al.] // Eur. Phys. J. C. — 2008. — Vol. 58. — P. 639. — arXiv: [0803.0883 \[hep-ph\]](#).
66. Herwig 7.0/Herwig++ 3.0 release note / J. Bellm [et al.] // Eur. Phys. J. C. — 2016. — Vol. 76, no. 4. — P. 196. — arXiv: [1512.01178 \[hep-ph\]](#).
67. Herwig 7.1 Release Note / J. Bellm [et al.]. — 2017. — arXiv: [1705.06919 \[hep-ph\]](#).
68. Event generation with SHERPA 1.1 / T. Gleisberg [et al.] // JHEP. — 2009. — Vol. 02. — P. 007. — arXiv: [0811.4622 \[hep-ph\]](#).
69. Event generation with Sherpa 2.2 / E. Bothmann [et al.] // SciPost Phys. — 2019. — Vol. 7, no. 3. — P. 034. — arXiv: [1905.09127 \[hep-ph\]](#).
70. QCD Matrix Elements + Parton Showers / S. Catani [et al.] // JHEP. — 2001. — Vol. 11. — P. 063. — arXiv: [hep-ph/0109231](#).
71. *Lönnblad, L.* Correcting the Colour-Dipole Cascade Model with Fixed Order Matrix Elements / L. Lönnblad // JHEP. — 2002. — Vol. 05. — P. 046. — arXiv: [hep-ph/0112284](#).
72. Matching matrix elements and shower evolution for top-quark production in hadronic collisions / M. L. Mangano [et al.] // J. High Energy Phys. — 2006. — Vol. 01. — P. 22.
73. *Frixione, S.* Matching NLO QCD computations and parton shower simulations / S. Frixione, B. R. Webber // JHEP. — 2002. — Vol. 06. — P. 029. — arXiv: [hep-ph/0204244](#).
74. *Nason, P.* A new method for combining NLO QCD with shower Monte Carlo algorithms / P. Nason // JHEP. — 2004. — Vol. 11. — P. 040. — arXiv: [hep-ph/0409146](#).
75. *Frixione, S.* Matching NLO QCD computations with parton shower simulations: the POWHEG method / S. Frixione, P. Nason, C. Oleari // JHEP. — 2007. — Vol. 11. — P. 070. — arXiv: [0709.2092 \[hep-ph\]](#).
76. *Hamilton, K.* Improving NLO-parton shower matched simulations with higher order matrix elements / K. Hamilton, P. Nason // J. High Energy Phys. — 2010. — Vol. 06:039. — P. 38.
77. Parton Fragmentation and String Dynamics / B. Andersson [et al.] // Phys. Rept. — 1983. — Vol. 97. — P. 31–145.

78. *Andersson, B.* The Lund model / B. Andersson // Camb. Monogr. Part. Phys. Nucl. Phys. Cosmol. — 1997. — Vol. 77. — P. 1–471.
79. *Amati, D.* Preconfinement as a Property of Perturbative QCD / D. Amati, G. Veneziano // Phys. Lett. B. — 1979. — Vol. 83. — P. 87.
80. *Huth, J. E.* Toward a standartization of jet definitions / J. E. Huth // 1990 DPF Summer Study on High-Energy Physics : Research Directions for the Decade (Snowmass 90) Snowmass, Colorado, June 25 - July 13. — 1990. — P. 134–136.
81. *Marzani, S.* Looking Inside Jets. An Introduction to Jet Substructure and Boosted-object Phenomenology / S. Marzani, G. Soyez, M. Spannowsky // Lecture Notes in Physics. — 2019. — Vol. 958. — P. 208.
82. *Salam, G. P.* Towards Jetography / G. P. Salam // Eur. Phys. J. C. — 2010. — Vol. 67. — P. 95.
83. *Sterman, G.* Jets from Quantum Chromodynamics / G. Sterman, S. Weinberg // Phys. Rev. Lett. — 1977. — Vol. 39. — P. 4.
84. *Salam, G. P.* A practical Seedless Infrared-Safe Cone jet algorithm / G. P. Salam, G. Soyez // J. High Energy Phys. — 2007. — Vol. 0705. — P. 42.
85. *Cacciari, M.* The anti- $k_t$  jet clustering algorithm / M. Cacciari, G. P. Salam, G. Soyez // JHEP. — 2008. — Vol. 04. — P. 063. — arXiv: [0802.1189](https://arxiv.org/abs/0802.1189) [hep-ph].
86. Longitudinally-invariant  $k_t$ -clustering algorithms for hadron-hadron collisions / S. Catani [et al.] // Nucl. Phys. B. — 1993. — Vol. 406. — P. 187–224.
87. *Ellis, S. D.* Successive combination jet algorithm for hadron collisions / S. D. Ellis, D. E. Soper // Phys. Rev. D. — 1993. — Vol. 48. — P. 3160–3166.
88. Better jet clustering algorithms / Y. L. Dokshitzer [et al.] // J. High Energy Phys. — 1997. — Vol. 08. — P. 3.
89. *Wobisch, M.* Hadronization correctinos to jet cross-sections in deep inelastic scattering / M. Wobisch, T. Wengler // Workshop on Monte Carlo Generators for HERA Physics. — 1999. — P. 10.
90. Evidence for Jet Structure in Hadron Production by  $e^+e^-$  Annihilation / G. Hanson [et al.] // Phys. Rev. Lett. — 1975. — Vol. 35. — P. 1609–1612.
91. Evidence for Planar Events in  $e^+e^-$  Annihilation at High-Energies / R. Brandelik [et al.] // Phys. Lett. B. — 1979. — Vol. 86. — P. 243–249.
92. Discovery of Three Jet Events and a Test of Quantum Chromodynamics at PETRA Energies / D. P. Barber [et al.] // Phys. Rev. Lett. — 1979. — Vol. 43. — P. 830.

93. Evidence for Gluon Bremsstrahlung in  $e^+e^-$  Annihilations at High-Energies / C. Berger [et al.] // Phys. Lett. B. — 1979. — Vol. 86. — P. 418–425.
94. Observation of Planar Three Jet Events in  $e^+e^-$  Annihilation and Evidence for Gluon Bremsstrahlung / W. Bartel [et al.] // Phys. Lett. B. — 1980. — Vol. 91. — P. 142–147.
95. *Bethke, S.* QCD studies at LEP / S. Bethke // Physics Reports. — 2004. — Vol. 403/404. — P. 203–220.
96. High  $p_T$  Hadrons as Leading Particles in Jets Produced at the ISR. 1. Momentum Distribution of Secondaries in the Trigger Jet / A. Breakstone [et al.] // Z. Phys. C. — 1984. — Vol. 23. — P. 9.
97. *Scott, W. G.* Jets in the UA1 Experiment / W. G. Scott // 4th Topical Workshop on Proton-Antiproton Collider Physics. — 1985. — P. 6–19.
98. An NLO QCD analysis of inclusive cross-section and jet-production data from the zeus experiment / S. Chekanov [et al.] // Eur. Phys. J. C. — 2005. — Vol. 42. — P. 1–16. — arXiv: [hep-ph/0503274](https://arxiv.org/abs/hep-ph/0503274).
99. Measurement of inclusive jet production in deep-inelastic scattering at high  $Q^2$  and determination of the strong coupling / A. Aktas [et al.] // Phys. Lett. B. — 2007. — Vol. 653. — P. 134–144. — arXiv: [0706.3722](https://arxiv.org/abs/0706.3722) [[hep-ex](#)].
100. *Campagnari, C.* The Discovery of the top quark / C. Campagnari, M. Franklin // Rev. Mod. Phys. — 1997. — Vol. 69. — P. 137–212. — arXiv: [hep-ex/9608003](https://arxiv.org/abs/hep-ex/9608003).
101. A detailed map of Higgs boson interactions by the ATLAS experiment ten years after the discovery // Nature. — 2022. — Vol. 607, no. 7917. — P. 52–59. — arXiv: [2207.00092](https://arxiv.org/abs/2207.00092) [[hep-ex](#)].
102. Standard Model Summary Plots February 2022 [Electronic resource] // ATLAS Collaboration. — 2022. — Mode of access: <https://cds.cern.ch/record/2804061>. — Date of acces: 05.10.2020.
103. Measurement of three-jet differential cross section  $d\sigma_{3\text{jet}}/dM_{3\text{jet}}$  in  $p\bar{p}$  collisions at  $\sqrt{s} = 1.96$  TeV / D0 collaboration // Phys. Lett. B. — 2011. — Vol. 704:434. — P. 10.
104. *ATLAS Collaboration.* Measurement of the inclusive jet cross section in  $pp$  collisions at  $\sqrt{s} = 2.76$  TeV and comparison to the inclusive jet cross section at  $\sqrt{s} = 7$  TeV using the ATLAS detector / ATLAS Collaboration // Eur. Phys. J. C. — 2013. — Vol. 73. — P. 2509. — arXiv: [1304.4739](https://arxiv.org/abs/1304.4739) [[hep-ex](#)].

105. *ATLAS Collaboration*. Measurement of inclusive jet and dijet cross sections in proton–proton collisions at 7 TeV centre-of-mass energy with the ATLAS detector / ATLAS Collaboration // Eur. Phys. J. C. — 2011. — Vol. 71. — P. 1512. — arXiv: [1009.5908 \[hep-ex\]](#).
106. *ATLAS Collaboration*. Measurement of inclusive jet and dijet production in  $pp$  collisions at  $\sqrt{s} = 7$  TeV using the ATLAS detector / ATLAS Collaboration // Phys. Rev. D. — 2012. — Vol. 86. — P. 014022. — arXiv: [1112.6297 \[hep-ex\]](#).
107. *ATLAS Collaboration*. Measurement of dijet cross sections in  $pp$  collisions at 7 TeV centre-of-mass energy using the ATLAS detector / ATLAS Collaboration // JHEP. — 2014. — Vol. 05. — P. 059. — arXiv: [1312.3524 \[hep-ex\]](#).
108. *ATLAS Collaboration*. Measurement of the inclusive jet cross-sections in proton–proton collisions at  $\sqrt{s} = 8$  TeV with the ATLAS detector / ATLAS Collaboration // JHEP. — 2017. — Vol. 09. — P. 020. — arXiv: [1706.03192 \[hep-ex\]](#).
109. *ATLAS Collaboration*. Measurement of inclusive jet and dijet cross-sections in proton–proton collisions at  $\sqrt{s} = 13$  TeV with the ATLAS detector / ATLAS Collaboration // JHEP. — 2018. — Vol. 05. — P. 195. — arXiv: [1711.02692 \[hep-ex\]](#).
110. *CMS Collaboration*. Measurement of the ratio of inclusive jet cross sections using the anti- $k_T$  algorithm with radius parameters  $R = 0.5$  and  $0.7$  in  $pp$  collisions at  $\sqrt{s} = 7$  TeV / CMS Collaboration // Phys. Rev. D. — 2014. — Vol. 90. — P. 072006. — arXiv: [1406.0324 \[hep-ex\]](#).
111. *CMS Collaboration*. Measurement of the ratio of the inclusive 3-jet cross section to the inclusive 2-jet cross section in  $pp$  collisions at  $\sqrt{s} = 7$  TeV and first determination of the strong coupling constant in the TeV range / CMS Collaboration // Eur. Phys. J. C. — 2013. — Vol. 73. — P. 2604. — arXiv: [1304.7498 \[hep-ex\]](#).
112. *ATLAS Collaboration*. Measurement of multi-jet cross sections in proton–proton collisions at a 7 TeV center-of-mass energy / ATLAS Collaboration // Eur. Phys. J. C. — 2011. — Vol. 71. — P. 1763. — arXiv: [1107.2092 \[hep-ex\]](#).
113. *CMS Collaboration*. Measurement of four-jet production in proton–proton collisions at  $\sqrt{s} = 7$  TeV / CMS Collaboration // Phys. Rev. D. — 2014. — Vol. 89. — P. 092010. — arXiv: [1312.6440 \[hep-ex\]](#).

114. *CDF Collaboration*. Measurement of Inclusive Jet Cross Sections in  $Z/\gamma^*(\rightarrow e^+e^-)+jets$  Production in  $p\bar{p}$  Collisions at  $\sqrt{s} = 1.96$  TeV / CDF Collaboration // Phys. Rev. Lett. — 2008. — Vol. 100. — P. 102001. — arXiv: [0711.3717 \[hep-ex\]](#).
115. *D0 Collaboration*. Measurement of differential cross section of  $Z/\gamma^*+jets+X$  events in  $p\bar{p}$  collisions at  $\sqrt{s} = 1.96$  TeV / D0 Collaboration // Phys. Lett. B. — 2009. — Vol. 678. — P. 45–54. — arXiv: [0903.1748 \[hep-ex\]](#).
116. *D0 Collaboration*. Measurement of  $Z/\gamma^*+jets+X$  angular distributions in  $p\bar{p}$  collisions at  $\sqrt{s} = 1.96$  TeV / D0 Collaboration // Phys. Lett. B. — 2010. — Vol. 682. — P. 370–380. — arXiv: [0907.4286 \[hep-ex\]](#).
117. *CDF Collaboration*. Measurement of differential production cross sections for  $Z/\gamma^*$  bosons in association with jets in  $p\bar{p}$  collisions at  $\sqrt{s} = 1.96$  TeV / CDF Collaboration // Phys. Rev. D. — 2015. — Vol. 91. — P. 012002. — arXiv: [1409.4359 \[hep-ex\]](#).
118. *ATLAS Collaboration*. Measurement of the production cross section for  $Z/\gamma^*$  in association with jets in  $pp$  collisions at  $\sqrt{s} = 7$  TeV with the ATLAS detector / ATLAS Collaboration // Phys. Rev. D. — 2012. — Vol. 85. — P. 032009. — arXiv: [1111.2690 \[hep-ex\]](#).
119. *ATLAS Collaboration*. Measurement of the production cross section of jets in association with a  $Z$  boson in  $pp$  collisions at  $\sqrt{s} = 7$  TeV with the ATLAS detector / ATLAS Collaboration // JHEP. — 2013. — Vol. 07. — P. 032. — arXiv: [1304.7098 \[hep-ex\]](#).
120. *ATLAS Collaboration*. Measurements of the production cross section of a  $Z$  boson in association with jets in  $pp$  collisions at  $\sqrt{s} = 13$  TeV with the ATLAS detector / ATLAS Collaboration // Eur. Phys. J. C. — 2017. — Vol. 77. — P. 361. — arXiv: [1702.05725 \[hep-ex\]](#).
121. *CMS Collaboration*. Rapidity distributions in exclusive  $Z+jet$  and  $\gamma+jet$  events in  $pp$  collisions at  $\sqrt{s} = 7$  TeV / CMS Collaboration // Phys. Rev. D. — 2013. — Vol. 88. — P. 112009. — arXiv: [1310.3082 \[hep-ex\]](#).
122. *CMS Collaboration*. Measurements of jet multiplicity and differential production cross sections of  $Z+jets$  events in proton–proton collisions at  $\sqrt{s} = 7$  TeV / CMS Collaboration // Phys. Rev. D. — 2015. — Vol. 91. — P. 052008. — arXiv: [1408.3104 \[hep-ex\]](#).
123. *CMS Collaboration*. Measurements of the differential production cross sections for a  $Z$  boson in association with jets in  $pp$  collisions at  $\sqrt{s} = 8$  TeV / CMS Collaboration // JHEP. — 2017. — Vol. 04. — P. 022. — arXiv: [1611.03844 \[hep-ex\]](#).

124. *CMS Collaboration*. Measurement of differential cross sections for  $Z$  boson production in association with jets in proton–proton collisions at  $\sqrt{s} = 13$  TeV / CMS Collaboration // Eur. Phys. J. C. — 2018. — Vol. 78. — P. 965. — arXiv: [1804.05252 \[hep-ex\]](#).
125. *CMS Collaboration*. Measurement of differential cross sections for  $Z$  boson pair production in association with jets at  $\sqrt{s} = 8$  TeV and 13 TeV / CMS Collaboration // Phys. Lett. B. — 2019. — Vol. 789. — P. 19. — arXiv: [1806.11073 \[hep-ex\]](#).
126. *LHCb Collaboration*. Study of forward  $Z$  + jet production in pp collisions at  $\sqrt{s} = 7$  TeV / LHCb Collaboration // JHEP. — 2014. — Vol. 01. — P. 033. — arXiv: [1310.8197 \[hep-ex\]](#).
127. *LHCb Collaboration*. Measurement of forward  $W$  and  $Z$  boson production in association with jets in proton-proton collisions at  $\sqrt{s} = 8$  TeV / LHCb Collaboration // JHEP. — 2016. — Vol. 05. — P. 131. — arXiv: [arXiv: 1605.00951 \[hep-ex\]](#).
128. Precise QCD Predictions for the Production of a  $Z$  Boson in Association with a Hadronic Jet / A. Gehrmann-De Ridder [et al.] // Phys. Rev. Lett. — 2016. — Vol. 117:022001. — P. 5.
129.  $Z$ -Boson Production in Association with a Jet at Next-To-Next-To-Leading Order in Perturbative QCD / R. Boughezal [et al.] // Phys. Rev. Lett. — 2016. — Vol. 116:152001. — P. 6.
130. *ATLAS Collaboration*. ATLAS data quality operations and performance for 2015–2018 data-taking / ATLAS Collaboration // JINST. — 2020. — Vol. 15. — P04003. — arXiv: [1911.04632 \[physics.ins-det\]](#).
131. Luminosity Public Results [Electronic resource] // ATLAS Collaboration. — Mode of access: <https://twiki.cern.ch/twiki/bin/view/AtlasPublic/LuminosityPublicResults>. — Date of access: 16.07.2020.
132. Luminosity Public Results Run 2 [Electronic resource] // ATLAS Collaboration. — Mode of access: <https://twiki.cern.ch/twiki/bin/view/AtlasPublic/LuminosityPublicResultsRun2>. — Date of access: 16.07.2020.
133. *ATLAS Collaboration*. ATLAS Detector and Physics Performance: Technical Design Report, Volume 2 : ATLAS-TDR-15; CERN-LHCC-99-015 / ATLAS Collaboration. — 1999. — URL: <https://cds.cern.ch/record/391177>.
134. *ATLAS Collaboration*. Performance of the ATLAS Trigger System in 2010 / ATLAS Collaboration // Eur. Phys. J. C. — 2012. — Vol. 72. — P. 1849. — arXiv: [1110.1530 \[hep-ex\]](#).
135. *ATLAS Collaboration*. Performance of the ATLAS trigger system in 2015 / ATLAS Collaboration // Eur. Phys. J. C. — 2017. — Vol. 77. — P. 317. — arXiv: [1611.09661 \[hep-ex\]](#).

136. *ATLAS Collaboration*. Operation of the ATLAS trigger system in Run 2 / ATLAS Collaboration // JINST. — 2020. — Vol. 15. — P10004. — arXiv: [2007.12539 \[hep-ex\]](https://arxiv.org/abs/2007.12539).
137. *ATLAS Collaboration*. The ATLAS Simulation Infrastructure / ATLAS Collaboration // Eur. Phys. J. C. — 2010. — Vol. 70. — P. 823. — arXiv: [1005.4568 \[physics.ins-det\]](https://arxiv.org/abs/1005.4568).
138. GEANT4 – a simulation toolkit / GEANT4 Collaboration, S. Agostinelli, [et al.] // Nucl. Instrum. Meth. A. — 2003. — Vol. 506. — P. 250.
139. *ATLAS Collaboration*. Readiness of the ATLAS Tile Calorimeter for LHC collisions / ATLAS Collaboration // Eur. Phys. J. C. — 2010. — Vol. 70. — P. 1193. — arXiv: [1007.5423 \[hep-ex\]](https://arxiv.org/abs/1007.5423).
140. *ATLAS Collaboration*. Performance of missing transverse momentum reconstruction in proton–proton collisions at  $\sqrt{s} = 7$  TeV with ATLAS / ATLAS Collaboration // Eur. Phys. J. C. — 2012. — Vol. 72. — P. 1844. — arXiv: [1108.5602 \[hep-ex\]](https://arxiv.org/abs/1108.5602).
141. *Cleland, W.* Signal processing considerations for liquid ionization calorimeters in a high rate environment / W. Cleland, E. Stern // Nucl. Instr. Meth. — 1994. — Vol. A 338. — P. 467–497.
142. *ATLAS Collaboration*. Topological cell clustering in the ATLAS calorimeters and its performance in LHC Run 1 / ATLAS Collaboration // Eur. Phys. J. C. — 2017. — Vol. 77. — P. 490. — arXiv: [1603.02934 \[hep-ex\]](https://arxiv.org/abs/1603.02934).
143. *ATLAS Collaboration*. Performance of pile-up mitigation techniques for jets in  $pp$  collisions at  $\sqrt{s} = 8$  TeV using the ATLAS detector / ATLAS Collaboration // Eur. Phys. J. C. — 2016. — Vol. 76. — P. 581. — arXiv: [1510.03823 \[hep-ex\]](https://arxiv.org/abs/1510.03823).
144. Testbeam studies of production modules of the ATLAS Tile Calorimeter / P. Adragna [et al.] // Nuclear Instruments and Methods in Physics Research Section A: Accelerators, Spectrometers, Detectors and Associated Equipment. — 2009. — Vol. 606, no. 3. — P. 362–394.
145. *ATLAS Collaboration*. ATLAS Tile Calorimeter: Technical Design Report : ATLAS-TDR-3; CERN-LHCC-96-042 / ATLAS Collaboration. — 1996. — URL: <https://cds.cern.ch/record/331062>.
146. *ATLAS Collaboration*. Measurement of the Inelastic Proton–Proton Cross Section at  $\sqrt{s} = 13$  TeV with the ATLAS Detector at the LHC / ATLAS Collaboration // Phys. Rev. Lett. — 2016. — Vol. 117. — P. 182002. — arXiv: [1606.02625 \[hep-ex\]](https://arxiv.org/abs/1606.02625).
147. *Bohm, G.* Introduction to Statistics and Data Analysis for Physicists / G. Bohm, G. Zech. — Verlag Deutsches Elektronen-Synchrotron, 2017. — P. 488.

148. *ATLAS Collaboration*. Evaluating statistical uncertainties and correlations using the bootstrap method / ATLAS Collaboration. — 2021. — URL: <https://cds.cern.ch/record/2759945>. ATL-PHYS-PUB-2021-011.
149. *ATLAS Collaboration*. Jet energy measurement with the ATLAS detector in proton–proton collisions at  $\sqrt{s} = 7$  TeV / ATLAS Collaboration // Eur. Phys. J. C. — 2013. — Vol. 73. — P. 2304. — arXiv: [1112.6426 \[hep-ex\]](https://arxiv.org/abs/1112.6426).
150. *ATLAS Collaboration*. Jet energy measurement and its systematic uncertainty in proton–proton collisions at  $\sqrt{s} = 7$  TeV with the ATLAS detector / ATLAS Collaboration // Eur. Phys. J. C. — 2015. — Vol. 75. — P. 17. — arXiv: [1406.0076 \[hep-ex\]](https://arxiv.org/abs/1406.0076).
151. *ATLAS Collaboration*. Determination of jet calibration and energy resolution in proton–proton collisions at  $\sqrt{s} = 8$  TeV using the ATLAS detector / ATLAS Collaboration // Eur. Phys. J. C. — 2020. — Vol. 80. — P. 1104. — arXiv: [1910.04482 \[hep-ex\]](https://arxiv.org/abs/1910.04482).
152. *ATLAS Collaboration*. Jet energy scale and resolution measured in proton–proton collisions at  $\sqrt{s} = 13$  TeV with the ATLAS detector / ATLAS Collaboration // Eur. Phys. J. C. — 2020. — Vol. 81. — P. 689. — arXiv: [2007.02645 \[hep-ex\]](https://arxiv.org/abs/2007.02645).
153. *ATLAS Collaboration*. Jet reconstruction and performance using particle flow with the ATLAS Detector / ATLAS Collaboration // Eur. Phys. J. C. — 2017. — Vol. 77. — P. 466. — arXiv: [1703.10485 \[hep-ex\]](https://arxiv.org/abs/1703.10485).
154. Local Hadronic Calibration [Electronic resource] // ATLAS Collaboration. — 2008. — Mode of access: <https://cds.cern.ch/record/1112035>. — Date of acces: 28.09.2018.
155. *Cacciari, M.* Pileup subtraction using jet areas / M. Cacciari, G. P. Salam // Phys. Lett. B. — 2008. — Vol. 659. — P. 12.
156. *Cacciari, M.* The catchment area of jets / M. Cacciari, G. P. Salam, G. Soyez // JHEP. — 2008. — Vol. 04. — P. 42.
157. *ATLAS Collaboration*. Selection of jets produced in proton–proton collisions with the ATLAS detector using 2011 data / ATLAS Collaboration. — 2012. — URL: <https://cds.cern.ch/record/1430034>. ATLAS-CONF-2012-020.
158. *ATLAS Collaboration*. Electron and photon energy calibration with the ATLAS detector using 2015–2016 LHC proton–proton collision data / ATLAS Collaboration // JINST. — 2019. — Vol. 14. — P03017. — arXiv: [1812.03848 \[hep-ex\]](https://arxiv.org/abs/1812.03848).

159. *Cukierman, A.* Mathematical properties of numerical inversion for jet calibrations / A. Cukierman, B. Nachman // Nuclear Instruments and Methods in Physics Research Section A: Accelerators, Spectrometers, Detectors and Associated Equipment. — 2017. — Vol. 858. — P. 1–11. — URL: <https://www.sciencedirect.com/science/article/pii/S0168900217303789>.
160. *ATLAS Collaboration.* Electron reconstruction and identification in the ATLAS experiment using the 2015 and 2016 LHC proton–proton collision data at  $\sqrt{s} = 13$  TeV / ATLAS Collaboration // Eur. Phys. J. C. — 2019. — Vol. 79. — P. 639. — arXiv: [1902.04655 \[hep-ex\]](https://arxiv.org/abs/1902.04655).
161. *ATLAS Collaboration.* Electron performance measurements with the ATLAS detector using the 2010 LHC proton–proton collision data / ATLAS Collaboration // Eur. Phys. J. C. — 2012. — Vol. 72. — P. 1909. — arXiv: [1110.3174 \[hep-ex\]](https://arxiv.org/abs/1110.3174).
162. *ATLAS Collaboration.* Electron and photon energy calibration with the ATLAS detector using LHC Run 1 data / ATLAS Collaboration // Eur. Phys. J. C. — 2014. — Vol. 74. — P. 3071. — arXiv: [1407.5063 \[hep-ex\]](https://arxiv.org/abs/1407.5063).
163. *ATLAS Collaboration.* Electron efficiency measurements with the ATLAS detector using 2012 LHC proton–proton collision data / ATLAS Collaboration // Eur. Phys. J. C. — 2017. — Vol. 77. — P. 195. — arXiv: [1612.01456 \[hep-ex\]](https://arxiv.org/abs/1612.01456).
164. Calorimeter Clustering Algorithms: Description and Performance / W. Lampl [et al.]. — 2008. — URL: <https://cds.cern.ch/record/1099735>. ATL-LARG-PUB-2008-002.
165. A general framework for implementing NLO calculations in shower Monte Carlo programs: the POWHEG BOX / S. Alioli [et al.] // JHEP. — 2010. — Vol. 06. — P. 043. — arXiv: [1002.2581 \[hep-ph\]](https://arxiv.org/abs/1002.2581).
166. New parton distributions for collider physics / H.-L. Lai [et al.] // Phys. Rev. D. — 2010. — Vol. 82. — P. 074024. — arXiv: [1007.2241 \[hep-ph\]](https://arxiv.org/abs/1007.2241).
167. *ATLAS Collaboration.* Example ATLAS tunes of PYTHIA8, PYTHIA6 and POWHEG to an observable sensitive to  $Z$  boson transverse momentum / ATLAS Collaboration. — 2013. — URL: <https://cds.cern.ch/record/1629317>. ATL-PHYS-PUB-2013-017.
168. *ATLAS Collaboration.* Summary of ATLAS Pythia 8 tunes / ATLAS Collaboration. — 2012. — URL: <https://cds.cern.ch/record/1474107>. ATL-PHYS-PUB-2012-003.
169. Energy Linearity and Resolution of the ATLAS Electromagnetic Barrel Calorimeter in an Electron Test-Beam / M. Aharrouche [et al.] // Nucl. Instrum. Meth. A. — 2006. — Vol. 568. — P. 601–623. — arXiv: [physics/0608012 \[hep-ex\]](https://arxiv.org/abs/physics/0608012).

170. Global QCD analysis of parton structure of the nucleon: CTEQ5 parton distributions / H. L. Lai [et al.] // Eur. Phys. J. C. — 2000. — Vol. 12. — P. 375. — arXiv: [hep-ph/9903282](https://arxiv.org/abs/hep-ph/9903282).
171. New Generation of Parton Distributions with Uncertainties from Global QCD Analysis / J. Pumplin [et al.] // JHEP. — 2002. — Vol. 07. — P. 012. — arXiv: [hep-ph/0201195](https://arxiv.org/abs/hep-ph/0201195).
172. Parton distributions with LHC data / R. D. Ball [et al.] // Nucl. Phys. B. — 2013. — Vol. 867:244. — P. 56.
173. *ATLAS Collaboration*. Performance of the ATLAS Electron and Photon Trigger in  $pp$  Collisions at  $\sqrt{s} = 7$  TeV in 2011 / ATLAS Collaboration. — 2012. — URL: <https://cds.cern.ch/record/1450089>. ATLAS-CONF-2012-048.
174. *ATLAS Collaboration*. Performance of the ATLAS Silicon Pattern Recognition Algorithm in Data and Simulation at  $\sqrt{s} = 7$  TeV / ATLAS Collaboration. — 2010. — URL: <https://cds.cern.ch/record/1281363>. ATLAS-CONF-2010-072.
175. *ATLAS Collaboration*. Reconstruction of primary vertices at the ATLAS experiment in Run 1 proton–proton collisions at the LHC / ATLAS Collaboration // Eur. Phys. J. C. — 2017. — Vol. 77. — P. 332. — arXiv: [1611.10235](https://arxiv.org/abs/1611.10235) [[hep-ex](https://arxiv.org/abs/hep-ex)].
176. *ATLAS Collaboration*. Performance of the ATLAS Inner Detector Track and Vertex Reconstruction in High Pile-Up LHC Environment / ATLAS Collaboration. — 2012. — URL: <https://cds.cern.ch/record/1435196>. ATLAS-CONF-2012-042.
177. *Frixione, S.* Jet photoproduction at HERA / S. Frixione, G. Ridolfi // Nucl. Phys. B. — 1997. — Vol. 507. — P. 18.
178. *ATLAS Collaboration*. Determination of the jet energy scale and resolution at ATLAS using  $Z/\gamma$ -jet events in data at  $\sqrt{s} = 8$  TeV / ATLAS Collaboration. — 2015. — URL: <https://cds.cern.ch/record/2059846>. ATLAS-CONF-2015-057.
179. *ATLAS Collaboration*. Single Boson and Diboson Production Cross Sections in  $pp$  Collisions at  $\sqrt{s} = 7$  TeV / ATLAS Collaboration. — 2010. — URL: <https://cds.cern.ch/record/1287902>. ATL-COM-PHYS-2010-695.
180. *ATLAS Collaboration*. Measurement of  $W^+W^-$  production cross section in  $pp$  collisions at  $\sqrt{s} = 8$  TeV with the ATLAS detector / ATLAS Collaboration. — 2014. — URL: <https://cds.cern.ch/record/1728248>. ATLAS-CONF-2014-033.

181. *ATLAS Collaboration*. A Measurement of  $W^\pm Z$  Production in Proton–Proton Collisions at  $\sqrt{s} = 8$  TeV with the ATLAS Detector / ATLAS Collaboration. — 2013. — URL: <https://cds.cern.ch/record/1525557>. ATLAS-CONF-2013-021.
182. *ATLAS Collaboration*. Measurement of the total  $ZZ$  production cross section in proton–proton collisions at  $\sqrt{s} = 8$  TeV in  $20 \text{ fb}^{-1}$  with the ATLAS detector / ATLAS Collaboration. — 2013. — URL: <https://cds.cern.ch/record/1525555>. ATLAS-CONF-2013-020.
183. *ATLAS Collaboration*. Measurement of the  $t\bar{t}$  production cross-section using  $e\mu$  events with  $b$ -tagged jets in  $pp$  collisions at  $\sqrt{s} = 7$  and 8 TeV with the ATLAS detector / ATLAS Collaboration // Eur. Phys. J. C. — 2014. — Vol. 74. — P. 3109. — arXiv: [1406.5375 \[hep-ex\]](https://arxiv.org/abs/1406.5375).
184. *ATLAS Collaboration*. Search for  $s$ -channel single top-quark production in proton–proton collisions at  $\sqrt{s} = 8$  TeV with the ATLAS detector / ATLAS Collaboration // Phys. Lett. B. — 2015. — Vol. 740. — P. 118. — arXiv: [1410.0647 \[hep-ex\]](https://arxiv.org/abs/1410.0647).
185. *ATLAS Collaboration*. Measurement of the cross-section for associated production of a top quark and a  $W$  boson at  $\sqrt{s} = 8$  TeV with the ATLAS detector / ATLAS Collaboration. — 2013. — URL: <https://cds.cern.ch/record/1600799>. ATLAS-CONF-2013-100.
186. *ATLAS Collaboration*. Measurement of the Inclusive and Fiducial Cross-Section of Single Top-Quark  $t$ -Channel Events in  $pp$  Collisions at  $\sqrt{s} = 8$  TeV / ATLAS Collaboration. — 2014. — URL: <https://cds.cern.ch/record/1668960>. ATLAS-CONF-2014-007.
187. *Skands, P. Z.* Tuning Monte Carlo generators: The Perugia tunes / P. Z. Skands // Phys. Rev. D. — 2010. — Vol. 82. — P. 074018. — arXiv: [1005.3457 \[hep-ph\]](https://arxiv.org/abs/1005.3457).
188. ALPGEN, a generator for hard multiparton processes in hadronic collisions / M. L. Mangano [et al.] // JHEP. — 2003. — Vol. 07. — P. 001. — arXiv: [hep-ph/0206293](https://arxiv.org/abs/hep-ph/0206293).
189. High-precision QCD at hadron colliders: Electroweak gauge boson rapidity distributions at next-to-next-to leading order / C. Anastasiou [et al.] // Phys. Rev. D. — 2004. — Vol. 69. — P. 094008. — arXiv: [hep-ph/0312266](https://arxiv.org/abs/hep-ph/0312266).
190. *Melnikov, K.* Electroweak gauge boson production at hadron colliders through  $\mathcal{O}(\alpha_s^2)$  / K. Melnikov, F. Petriello // Phys. Rev. D. — 2006. — Vol. 74. — P. 114017. — arXiv: [hep-ph/0609070](https://arxiv.org/abs/hep-ph/0609070).
191. FEWZ 2.0: A code for hadronic  $Z$  production at next-to-next-to-leading order / R. Gavin [et al.]. — 2010. — arXiv: [1011.3540 \[hep-ph\]](https://arxiv.org/abs/1011.3540).

192. *Golonka, P.* PHOTOS Monte Carlo: a precision tool for QED corrections in  $Z$  and  $W$  decays / P. Golonka, Z. Was // Eur. Phys. J. C. — 2006. — Vol. 45. — P. 97–107. — arXiv: [hep-ph/0506026](https://arxiv.org/abs/hep-ph/0506026).
193. The  $\tau$  decay library TAUOLA, version 2.4 / S. Jadach [et al.] // Computer Physics Communications. — 1993. — Vol. 76, no. 3. — P. 361–380.
194. *Cowan, G.* Statistical data analysis / G. Cowan. — Oxford University Press, 1998. — P. 197.
195. *ATLAS Collaboration.* Proposal for particle-level object and observable definitions for use in physics measurements at the LHC / ATLAS Collaboration. — 2015. — URL: <https://cds.cern.ch/record/2022743>. ATL-PHYS-PUB-2015-013.
196. *Hoecker, A.* SVD Approach to Data Unfolding / A. Hoecker, V. Kartvelishvili // Nucl. Instrum. Meth. — 1996. — Vol. 372. — P. 22.
197. *D'Agostini, G.* A multidimensional unfolding method based on Bayes' theorem / G. D'Agostini // Nucl. Instrum. Meth. A. — 1995. — Vol. 362. — P. 12.
198. *Malaescu, B.* An Iterative, Dynamically Stabilized (IDS) Method of Data Unfolding / B. Malaescu // PHYSTAT 2011, CERN, Geneva, Switzerland, January 2011. — 2011. — P. 5.
199. *ATLAS Collaboration.* Jet energy resolution in proton–proton collisions at  $\sqrt{s} = 7$  TeV recorded in 2010 with the ATLAS detector / ATLAS Collaboration // Eur. Phys. J. C. — 2013. — Vol. 73. — P. 2306. — arXiv: [1210.6210](https://arxiv.org/abs/1210.6210) [hep-ex].
200. Azimuthal Decorrelations in Dijet Events at  $\sqrt{s} = 7$  TeV // ATLAS Collaboration. — Mode of access: <https://cds.cern.ch/record/1290956>. — Date of access: 27.12.2022.
201. *ATLAS Collaboration.* Pile-up subtraction and suppression for jets in ATLAS / ATLAS Collaboration. — 2013. — URL: <https://cds.cern.ch/record/1570994>. ATLAS-CONF-2013-083.
202. *ATLAS Collaboration.* Improved luminosity determination in  $pp$  collisions at  $\sqrt{s} = 7$  TeV using the ATLAS detector at the LHC / ATLAS Collaboration // Eur. Phys. J. C. — 2013. — Vol. 73. — P. 2518. — arXiv: [1302.4393](https://arxiv.org/abs/1302.4393) [hep-ex].
203. *ATLAS Collaboration.* Luminosity determination in  $pp$  collisions at  $\sqrt{s} = 8$  TeV using the ATLAS detector at the LHC / ATLAS Collaboration // Eur. Phys. J. C. — 2016. — Vol. 76. — P. 653. — arXiv: [1608.03953](https://arxiv.org/abs/1608.03953) [hep-ex].

204. Repository for publication-related High-Energy Physics data // HEP-Data. — <https://www.hepdata.net>.
205. New parton distribution functions from a global analysis of quantum chromodynamics / S. Dulat [et al.] // Phys. Rev. D. — 2016. — Vol. 93, no. 3. — P. 033006. — arXiv: [1506.07443 \[hep-ph\]](https://arxiv.org/abs/1506.07443).
206. A posteriori inclusion of parton density functions in NLO QCD final-state calculations at hadron colliders: The APPLGRID Project / T. Carli [et al.] // Eur. Phys. J. C. — 2010. — Vol. 66:503. — P. 22.
207. PDF4LHC recommendations for LHC Run II / J. Butterworth [et al.] // J. Phys. G. — 2016. — Vol. 43. — P. 023001. — arXiv: [1510.03865 \[hep-ph\]](https://arxiv.org/abs/1510.03865).
208. Uncertainty induced by QCD coupling in the CTEQ global analysis of parton distributions / H.-L. Lai [et al.] // Phys. Rev. D. — 2010. — Vol. 82:054021. — P. 25.
209. Parton distributions for the LHC run II / R. D. Ball [et al.] // JHEP. — 2015. — Vol. 04. — P. 040. — arXiv: [1410.8849 \[hep-ph\]](https://arxiv.org/abs/1410.8849).
210. QCD matrix elements + parton showers. The NLO case / S. Höche [et al.] // JHEP. — 2013. — Vol. 04. — P. 027. — arXiv: [1207.5030 \[hep-ph\]](https://arxiv.org/abs/1207.5030).

## Appendix A

### The measured three-jets production cross-sections

The three-jets cross-section is measured as a function of the three highest- $p_T$  jets invariant mass in six equidistant regions of the absolute rapidity separation. The cross-section measured using the anti- $k_t$  jets with  $R = 0.4$  and  $R = 0.6$  are shown in Tables [A.1–A.5](#) and Tables [A.6–A.10](#), respectively. The measured cross-sections are quoted along with statistical and systematic uncertainties.

Table A.1. — Measured double-differential three-jets cross-section,  $\sigma$ , for  $R = 0.4$  jets and  $|Y^*| < 2$ , along with uncertainties in the measurement. All uncertainties are given in %, where  $\delta_{\text{stat}}^{\text{data}}$  ( $\delta_{\text{stat}}^{\text{MC}}$ ) are the statistical uncertainties in the data (MC simulation). The  $\gamma$  components are the uncertainty in the jet energy calibration from the *in situ*, the pile-up, the close-by jet, and the flavour components. The  $u$  components show the uncertainty in the jet energy and angular resolution, the unfolding, the jet identification, and the luminosity. While all columns are uncorrelated with each other, the *in situ*, pile-up, and flavour uncertainties shown here are the sum in quadrature of multiple uncorrelated components.

N <sup>o</sup>	$m_{\text{jjj-range}}$ [TeV]	$\sigma$ [pb/GeV]	$\delta_{\text{stat}}^{\text{data}}$ [%]	$\delta_{\text{stat}}^{\text{MC}}$ [%]	$\gamma_{\text{in situ}}$ [%]	$\gamma_{\text{pile-up}}$ [%]	$\gamma_{\text{close-by}}$ [%]	$\gamma_{\text{flavour}}$ [%]	$u_{\text{JER}}$ [%]	$u_{\text{JAR}}$ [%]	$u_{\text{unfold}}$ [%]	$u_{\text{ID}}$ [%]	$u_{\text{lumi}}$ [%]
1	0.38 – 0.42	17.5	1.8	0.73	+6.4 -6.3	+0.4 -2.7	+3.3 -3.4	+7.0 -6.6	0.7	0.0	0.0	0.75	1.8
2	0.42 – 0.46	12.8	2.0	0.62	+6.2 -6.1	+0.3 -1.9	+3.2 -3.2	+6.7 -6.3	0.8	0.0	0.0	0.75	1.8
3	0.46 – 0.50	8.75	1.3	0.50	+6.1 -6.0	+0.2 -1.4	+3.2 -3.2	+6.5 -6.2	0.8	0.0	0.0	0.75	1.8
4	0.50 – 0.54	5.72	1.5	0.55	+6.0 -5.9	+0.1 -1.2	+3.2 -3.2	+6.3 -6.0	0.8	0.0	0.0	0.75	1.8
5	0.54 – 0.60	3.57	1.8	0.49	+5.9 -5.7	+0.1 -1.1	+3.2 -3.2	+6.0 -5.7	0.8	0.0	0.0	0.75	1.8
6	0.60 – 0.66	2.09	1.6	0.49	+5.7 -5.6	+0.3 -1.1	+3.3 -3.2	+5.7 -5.4	0.7	0.0	0.0	0.75	1.8
7	0.66 – 0.72	1.27	1.0	0.55	+5.5 -5.4	+0.4 -1.1	+3.3 -3.3	+5.4 -5.2	0.7	0.0	0.0	0.75	1.8
8	0.72 – 0.78	$7.93 \cdot 10^{-1}$	1.1	0.53	+5.4 -5.3	+0.4 -1.1	+3.3 -3.2	+5.1 -4.9	0.6	0.0	0.0	0.75	1.8
9	0.78 – 0.86	$4.61 \cdot 10^{-1}$	0.91	0.42	+5.3 -5.2	+0.5 -1.0	+3.2 -3.1	+4.9 -4.7	0.6	0.0	0.0	0.75	1.8
10	0.86 – 0.94	$2.64 \cdot 10^{-1}$	0.69	0.33	+5.2 -5.1	+0.4 -0.9	+3.0 -2.9	+4.7 -4.5	0.6	0.0	0.0	0.75	1.8
11	0.94 – 1.02	$1.58 \cdot 10^{-1}$	0.82	0.32	+5.2 -5.1	+0.3 -0.8	+2.8 -2.7	+4.4 -4.3	0.6	0.0	0.0	0.75	1.8
12	1.02 – 1.12	$8.91 \cdot 10^{-2}$	0.58	0.34	+5.2 -5.1	+0.2 -0.6	+2.4 -2.4	+4.2 -4.1	0.6	0.0	0.0	0.75	1.8
13	1.12 – 1.22	$4.96 \cdot 10^{-2}$	0.71	0.42	+5.4 -5.2	+0.2 -0.5	+2.1 -2.0	+4.0 -3.9	0.6	0.0	0.0	0.75	1.8
14	1.22 – 1.34	$2.76 \cdot 10^{-2}$	0.92	0.39	+5.6 -5.4	+0.2 -0.4	+1.8 -1.8	+3.9 -3.7	0.6	0.0	0.0	0.75	1.8
15	1.34 – 1.46	$1.48 \cdot 10^{-2}$	1.2	0.46	+5.9 -5.7	+0.2 -0.4	+1.6 -1.5	+3.7 -3.6	0.6	0.0	0.0	0.75	1.8
16	1.46 – 1.60	$7.63 \cdot 10^{-3}$	1.6	0.39	+6.3 -6.1	+0.2 -0.4	+1.3 -1.3	+3.6 -3.5	0.5	0.0	0.0	0.75	1.8
17	1.60 – 1.76	$3.83 \cdot 10^{-3}$	2.1	0.38	+6.9 -6.7	+0.1 -0.4	+1.2 -1.2	+3.5 -3.4	0.6	0.0	0.0	0.75	1.8
18	1.76 – 1.94	$1.82 \cdot 10^{-3}$	2.9	0.38	+7.7 -7.5	+0.1 -0.3	+1.0 -1.0	+3.4 -3.3	0.6	0.0	0.0	0.75	1.8
19	1.94 – 2.14	$8.60 \cdot 10^{-4}$	4.0	0.37	+8.7 -8.4	+0.0 -0.2	+0.9 -0.9	+3.4 -3.2	0.6	0.0	0.0	0.75	1.8
20	2.14 – 2.36	$3.40 \cdot 10^{-4}$	6.0	0.54	+9.8 -9.4	+0.0 -0.1	+0.9 -0.8	+3.3 -3.1	0.6	0.0	0.0	0.75	1.8
21	2.36 – 2.60	$1.46 \cdot 10^{-4}$	9.1	0.70	+10.8 -10.4	+0.0 -0.1	+0.8 -0.8	+3.2 -3.1	0.7	0.0	0.0	0.75	1.8
22	2.60 – 2.84	$6.16 \cdot 10^{-5}$	13	0.79	+11.9 -11.8	+0.0 -0.1	+0.8 -0.8	+3.1 -3.1	0.7	0.0	0.0	0.75	1.8
23	2.84 – 3.10	$2.17 \cdot 10^{-5}$	22	1.1	+15.4 -15.5	+0.0 -0.1	+0.8 -0.7	+3.0 -3.1	0.8	0.0	0.0	0.75	1.8
24	3.10 – 3.90	$4.00 \cdot 10^{-6}$	31	0.87	+27.9 -26.9	+0.0 -0.1	+0.7 -0.7	+3.0 -3.1	1.3	0.0	0.3	0.75	1.8

Table A.2. — Measured double-differential three-jets cross-section,  $\sigma$ , for  $R = 0.4$  jets and  $2 < |Y^*| < 4$ , along with uncertainties in the measurement. All uncertainties are given in %, where  $\delta_{\text{stat}}^{\text{data}}$  ( $\delta_{\text{stat}}^{\text{MC}}$ ) are the statistical uncertainties in the data (MC simulation). The  $\gamma$  components are the uncertainty in the jet energy calibration from the *in situ*, the pile-up, the close-by jet, and the flavour components. The  $u$  components show the uncertainty in the jet energy and angular resolution, the unfolding, the jet identification, and the luminosity. While all columns are uncorrelated with each other, the *in situ*, pile-up, and flavour uncertainties shown here are the sum in quadrature of multiple uncorrelated components.

N <sub>s</sub>	$m_{\text{jjj-range}}$ [TeV]	$\sigma$ [pb/GeV]	$\delta_{\text{stat}}^{\text{data}}$ [%]	$\delta_{\text{stat}}^{\text{MC}}$ [%]	$\gamma_{\text{in situ}}$ [%]	$\gamma_{\text{pile-up}}$ [%]	$\gamma_{\text{close-by}}$ [%]	$\gamma_{\text{flavour}}$ [%]	$u_{\text{JER}}$ [%]	$u_{\text{JAR}}$ [%]	$u_{\text{unfold}}$ [%]	$u_{\text{ID}}$ [%]	$u_{\text{lumi}}$ [%]
1	0.42 – 0.46	25.5	1.4	0.83	+6.6 –6.5	+0.2 –4.1	+2.9 –2.8	+7.0 –6.2	0.6	0.2	0.0	0.75	1.8
2	0.46 – 0.50	26.3	1.4	0.66	+6.6 –6.5	+0.2 –3.2	+2.8 –2.7	+6.9 –6.2	0.7	0.2	0.0	0.75	1.8
3	0.50 – 0.54	21.3	0.90	0.60	+6.7 –6.4	+0.2 –2.4	+2.8 –2.7	+6.7 –6.1	0.7	0.2	0.0	0.75	1.8
4	0.54 – 0.60	14.4	0.85	0.43	+6.7 –6.4	+0.2 –1.8	+2.8 –2.7	+6.5 –5.9	0.8	0.1	0.0	0.75	1.8
5	0.60 – 0.66	8.76	1.0	0.38	+6.6 –6.4	+0.1 –1.4	+2.8 –2.7	+6.2 –5.8	0.8	0.1	0.0	0.75	1.8
6	0.66 – 0.72	5.35	1.3	0.39	+6.5 –6.3	+0.1 –1.2	+2.9 –2.7	+5.9 –5.6	0.8	0.1	0.0	0.75	1.8
7	0.72 – 0.78	3.27	1.6	0.46	+6.4 –6.2	+0.1 –1.1	+2.9 –2.8	+5.6 –5.3	0.8	0.1	0.0	0.75	1.8
8	0.78 – 0.86	1.95	1.3	0.45	+6.3 –6.1	+0.2 –1.1	+2.9 –2.8	+5.4 –5.1	0.8	0.0	0.0	0.75	1.8
9	0.86 – 0.94	1.11	0.96	0.47	+6.1 –6.0	+0.4 –1.1	+2.8 –2.8	+5.1 –4.9	0.7	0.0	0.0	0.75	1.8
10	0.94 – 1.02	$6.73 \cdot 10^{-1}$	1.1	0.44	+6.0 –5.9	+0.5 –1.2	+2.8 –2.7	+4.9 –4.7	0.7	0.0	0.0	0.75	1.8
11	1.02 – 1.12	$3.87 \cdot 10^{-1}$	0.57	0.39	+5.9 –5.8	+0.6 –1.1	+2.6 –2.6	+4.7 –4.4	0.7	0.0	0.0	0.75	1.8
12	1.12 – 1.22	$2.14 \cdot 10^{-1}$	0.65	0.34	+5.9 –5.7	+0.5 –1.0	+2.4 –2.4	+4.5 –4.2	0.7	0.0	0.0	0.75	1.8
13	1.22 – 1.34	$1.20 \cdot 10^{-1}$	0.75	0.30	+6.0 –5.7	+0.4 –0.7	+2.2 –2.1	+4.3 –4.0	0.7	0.0	0.0	0.75	1.8
14	1.34 – 1.46	$6.32 \cdot 10^{-2}$	0.59	0.33	+6.1 –5.9	+0.3 –0.5	+1.9 –1.9	+4.1 –3.9	0.7	0.0	0.0	0.75	1.8
15	1.46 – 1.60	$3.37 \cdot 10^{-2}$	0.77	0.34	+6.3 –6.1	+0.3 –0.4	+1.7 –1.6	+4.0 –3.8	0.6	0.0	0.0	0.75	1.8
16	1.60 – 1.74	$1.78 \cdot 10^{-2}$	0.98	0.41	+6.6 –6.4	+0.3 –0.4	+1.4 –1.4	+3.8 –3.6	0.6	0.0	0.0	0.75	1.8
17	1.74 – 1.90	$9.00 \cdot 10^{-3}$	1.4	0.45	+7.0 –6.9	+0.4 –0.4	+1.2 –1.2	+3.7 –3.5	0.6	0.0	0.0	0.75	1.8
18	1.90 – 2.08	$4.30 \cdot 10^{-3}$	1.9	0.43	+7.6 –7.5	+0.3 –0.4	+1.1 –1.1	+3.6 –3.4	0.6	0.0	0.0	0.75	1.8
19	2.08 – 2.26	$2.13 \cdot 10^{-3}$	2.6	0.42	+8.4 –8.2	+0.3 –0.3	+0.9 –1.0	+3.5 –3.4	0.7	0.0	0.0	0.75	1.8
20	2.26 – 2.48	$9.74 \cdot 10^{-4}$	3.5	0.44	+9.4 –9.2	+0.3 –0.2	+0.9 –0.9	+3.4 –3.3	0.7	0.0	0.0	0.75	1.8
21	2.48 – 2.72	$3.74 \cdot 10^{-4}$	5.4	0.56	+10.7 –10.4	+0.2 –0.2	+0.8 –0.8	+3.3 –3.2	0.8	0.0	0.0	0.75	1.8
22	2.72 – 2.98	$1.33 \cdot 10^{-4}$	8.8	0.72	+12.1 –11.6	+0.3 –0.2	+0.8 –0.8	+3.2 –3.2	0.8	0.0	0.0	0.75	1.8
23	2.98 – 3.26	$5.84 \cdot 10^{-5}$	13	0.77	+13.9 –13.2	+0.5 –0.2	+0.7 –0.7	+3.2 –3.1	0.8	0.0	0.1	0.75	1.8
24	3.26 – 3.58	$1.52 \cdot 10^{-5}$	23	1.4	+17.2 –16.9	+0.5 –0.2	+0.7 –0.7	+3.2 –3.0	0.9	0.0	0.1	0.75	1.8
25	3.58 – 4.20	$5.57 \cdot 10^{-6}$	29	1.2	+26.2 –26.6	+0.7 –0.2	+0.6 –0.6	+2.6 –2.8	2.1	0.0	0.3	0.75	1.8

Table A.3. — Measured double-differential three-jets cross-section,  $\sigma$ , for  $R = 0.4$  jets and  $4 < |Y^*| < 6$ , along with uncertainties in the measurement. All uncertainties are given in %, where  $\delta_{\text{stat}}^{\text{data}}$  ( $\delta_{\text{stat}}^{\text{MC}}$ ) are the statistical uncertainties in the data (MC simulation). The  $\gamma$  components are the uncertainty in the jet energy calibration from the *in situ*, the pile-up, the close-by jet, and the flavour components. The  $u$  components show the uncertainty in the jet energy and angular resolution, the unfolding, the jet identification, and the luminosity. While all columns are uncorrelated with each other, the *in situ*, pile-up, and flavour uncertainties shown here are the sum in quadrature of multiple uncorrelated components.

N <sup>o</sup>	$m_{\text{jjj-range}}$ [TeV]	$\sigma$ [pb/GeV]	$\delta_{\text{stat}}^{\text{data}}$ [%]	$\delta_{\text{stat}}^{\text{MC}}$ [%]	$\gamma_{\text{in situ}}$ [%]	$\gamma_{\text{pile-up}}$ [%]	$\gamma_{\text{close-by}}$ [%]	$\gamma_{\text{flavour}}$ [%]	$u_{\text{JER}}$ [%]	$u_{\text{JAR}}$ [%]	$u_{\text{unfold}}$ [%]	$u_{\text{ID}}$ [%]	$u_{\text{lumi}}$ [%]
1	0.54 – 0.60	15.0	1.6	1.0	+8.2 -7.6	+0.0 -4.1	+2.7 -2.5	+7.2 -6.4	0.2	0.1	0.0	0.75	1.8
2	0.60 – 0.66	15.0	1.6	0.81	+8.2 -7.8	+0.0 -3.2	+2.7 -2.6	+6.8 -6.3	0.4	0.1	0.0	0.75	1.8
3	0.66 – 0.72	12.7	1.3	0.74	+8.2 -8.0	+0.1 -2.4	+2.7 -2.6	+6.5 -6.2	0.6	0.1	0.0	0.75	1.8
4	0.72 – 0.80	8.89	0.98	0.62	+8.3 -8.2	+0.2 -1.8	+2.7 -2.7	+6.3 -6.1	0.7	0.1	0.0	0.75	1.8
5	0.80 – 0.88	5.46	1.2	0.57	+8.4 -8.3	+0.2 -1.4	+2.7 -2.7	+6.1 -5.9	0.8	0.1	0.0	0.75	1.8
6	0.88 – 0.96	3.28	1.5	0.57	+8.5 -8.3	+0.2 -1.3	+2.7 -2.7	+5.9 -5.7	0.8	0.1	0.0	0.75	1.8
7	0.96 – 1.06	1.82	1.8	0.52	+8.5 -8.3	+0.3 -1.3	+2.8 -2.7	+5.7 -5.4	0.8	0.1	0.0	0.75	1.8
8	1.06 – 1.16	$9.98 \cdot 10^{-1}$	1.4	0.61	+8.6 -8.2	+0.5 -1.3	+2.8 -2.7	+5.5 -5.2	0.8	0.1	0.0	0.75	1.8
9	1.16 – 1.26	$5.84 \cdot 10^{-1}$	1.1	0.65	+8.5 -8.2	+0.6 -1.3	+2.8 -2.7	+5.2 -4.9	0.8	0.1	0.0	0.75	1.8
10	1.26 – 1.38	$3.31 \cdot 10^{-1}$	1.4	0.66	+8.5 -8.2	+0.7 -1.3	+2.8 -2.6	+5.0 -4.8	0.8	0.1	0.0	0.75	1.8
11	1.38 – 1.50	$1.81 \cdot 10^{-1}$	1.3	0.64	+8.6 -8.2	+0.7 -1.3	+2.7 -2.6	+4.8 -4.6	0.8	0.1	0.0	0.75	1.8
12	1.50 – 1.62	$9.89 \cdot 10^{-2}$	0.92	0.66	+8.7 -8.2	+0.7 -1.2	+2.6 -2.5	+4.7 -4.5	0.8	0.0	0.0	0.75	1.8
13	1.62 – 1.76	$5.46 \cdot 10^{-2}$	1.1	0.60	+8.9 -8.3	+0.6 -1.1	+2.5 -2.3	+4.6 -4.3	0.9	0.0	0.0	0.75	1.8
14	1.76 – 1.90	$2.99 \cdot 10^{-2}$	1.4	0.57	+9.0 -8.4	+0.4 -0.9	+2.3 -2.1	+4.5 -4.2	0.9	0.0	0.0	0.75	1.8
15	1.90 – 2.06	$1.57 \cdot 10^{-2}$	1.1	0.60	+9.2 -8.6	+0.2 -0.7	+2.1 -1.9	+4.3 -4.1	0.9	0.0	0.0	0.75	1.8
16	2.06 – 2.22	$7.92 \cdot 10^{-3}$	1.4	0.67	+9.4 -8.9	+0.2 -0.5	+1.8 -1.7	+4.2 -4.0	0.9	0.0	0.0	0.75	1.8
17	2.22 – 2.40	$4.12 \cdot 10^{-3}$	1.8	0.76	+9.8 -9.3	+0.2 -0.3	+1.6 -1.5	+4.1 -3.9	1.0	0.0	0.0	0.75	1.8
18	2.40 – 2.58	$1.99 \cdot 10^{-3}$	2.7	0.98	+10.4 -9.9	+0.3 -0.2	+1.4 -1.3	+3.9 -3.8	1.1	0.0	0.0	0.75	1.8
19	2.58 – 2.78	$9.95 \cdot 10^{-4}$	3.6	1.0	+11.1 -10.5	+0.3 -0.1	+1.3 -1.2	+3.9 -3.7	1.2	0.0	0.0	0.75	1.8
20	2.78 – 2.98	$4.54 \cdot 10^{-4}$	5.2	1.2	+12.1 -11.2	+0.3 -0.1	+1.2 -1.1	+3.8 -3.6	1.3	0.0	0.0	0.75	1.8
21	2.98 – 3.20	$1.91 \cdot 10^{-4}$	7.7	1.5	+13.0 -12.0	+0.3 -0.1	+1.1 -1.1	+3.8 -3.6	1.4	0.0	0.0	0.75	1.8
22	3.20 – 3.42	$7.88 \cdot 10^{-5}$	12	1.6	+14.0 -12.7	+0.3 -0.0	+1.0 -1.0	+3.8 -3.5	1.5	0.0	0.0	0.75	1.8
23	3.42 – 3.66	$3.33 \cdot 10^{-5}$	19	1.7	+15.0 -13.5	+0.3 -0.0	+1.0 -1.0	+3.9 -3.5	1.6	0.0	0.0	0.75	1.8
24	3.66 – 4.70	$5.24 \cdot 10^{-6}$	23	1.6	+21.4 -21.1	+0.3 -0.0	+0.8 -0.7	+3.8 -3.7	2.4	0.0	0.0	0.75	1.8

Table A.4. — Measured double-differential three-jets cross-section,  $\sigma$ , for  $R = 0.4$  jets and  $6 < |Y^*| < 8$ , along with uncertainties in the measurement. All uncertainties are given in %, where  $\delta_{\text{stat}}^{\text{data}}$  ( $\delta_{\text{stat}}^{\text{MC}}$ ) are the statistical uncertainties in the data (MC simulation). The  $\gamma$  components are the uncertainty in the jet energy calibration from the *in situ*, the pile-up, the close-by jet, and the flavour components. The  $u$  components show the uncertainty in the jet energy and angular resolution, the unfolding, the jet identification, and the luminosity. While all columns are uncorrelated with each other, the *in situ*, pile-up, and flavour uncertainties shown here are the sum in quadrature of multiple uncorrelated components.

N <sup>o</sup>	$m_{\text{jjj-range}}$ [TeV]	$\sigma$ [pb/GeV]	$\delta_{\text{stat}}^{\text{data}}$ [%]	$\delta_{\text{stat}}^{\text{MC}}$ [%]	$\gamma_{\text{in situ}}$ [%]	$\gamma_{\text{pile-up}}$ [%]	$\gamma_{\text{close-by}}$ [%]	$\gamma_{\text{flavour}}$ [%]	$u_{\text{JER}}$ [%]	$u_{\text{JAR}}$ [%]	$u_{\text{unfold}}$ [%]	$u_{\text{ID}}$ [%]	$u_{\text{lumi}}$ [%]
1	0.76 – 0.84	4.95	2.4	1.6	+9.8 -9.9	+0.3 -4.1	+2.5 -2.7	+6.7 -6.3	0.3	0.7	0.0	0.75	1.8
2	0.84 – 0.94	5.00	2.1	1.2	+10.2 -10.1	+0.3 -3.2	+2.5 -2.7	+6.5 -6.1	0.6	0.6	0.0	0.75	1.8
3	0.94 – 1.04	3.80	1.4	1.1	+10.7 -10.5	+0.3 -2.4	+2.6 -2.6	+6.3 -6.0	0.8	0.5	0.0	0.75	1.8
4	1.04 – 1.14	2.67	1.4	1.2	+11.4 -10.9	+0.2 -1.8	+2.6 -2.7	+6.1 -6.0	1.0	0.4	0.0	0.75	1.8
5	1.14 – 1.26	1.74	1.7	1.1	+12.2 -11.4	+0.2 -1.5	+2.7 -2.7	+6.0 -5.8	1.1	0.3	0.0	0.75	1.8
6	1.26 – 1.38	$9.30 \cdot 10^{-1}$	2.2	1.1	+12.8 -11.8	+0.1 -1.5	+2.7 -2.7	+5.8 -5.5	1.2	0.3	0.0	0.75	1.8
7	1.38 – 1.52	$5.52 \cdot 10^{-1}$	2.7	1.1	+13.4 -12.2	+0.4 -1.7	+2.8 -2.7	+5.6 -5.2	1.3	0.2	0.0	0.75	1.8
8	1.52 – 1.66	$2.88 \cdot 10^{-1}$	4.0	1.2	+13.8 -12.6	+0.6 -1.8	+2.8 -2.7	+5.4 -5.0	1.3	0.2	0.0	0.75	1.8
9	1.66 – 1.80	$1.49 \cdot 10^{-1}$	2.1	1.3	+14.2 -13.0	+0.8 -1.9	+2.8 -2.8	+5.2 -4.9	1.3	0.2	0.0	0.75	1.8
10	1.80 – 1.94	$7.94 \cdot 10^{-2}$	2.5	1.5	+14.6 -13.3	+1.0 -1.8	+2.8 -2.8	+5.1 -4.7	1.2	0.1	0.0	0.75	1.8
11	1.94 – 2.10	$4.19 \cdot 10^{-2}$	3.0	1.5	+15.0 -13.6	+1.1 -1.7	+2.8 -2.8	+5.0 -4.6	1.3	0.1	0.0	0.75	1.8
12	2.10 – 2.26	$2.20 \cdot 10^{-2}$	3.8	1.7	+15.6 -14.0	+1.2 -1.5	+2.8 -2.8	+4.9 -4.5	1.3	0.1	0.0	0.75	1.8
13	2.26 – 2.42	$1.21 \cdot 10^{-2}$	2.4	1.8	+16.0 -14.3	+1.2 -1.3	+2.8 -2.7	+4.9 -4.5	1.4	0.0	0.0	0.75	1.8
14	2.42 – 2.58	$5.86 \cdot 10^{-3}$	2.8	2.4	+16.5 -14.8	+1.1 -1.1	+2.7 -2.6	+4.9 -4.5	1.6	0.0	0.0	0.75	1.8
15	2.58 – 2.76	$3.24 \cdot 10^{-3}$	3.8	2.1	+16.9 -15.2	+1.0 -0.9	+2.6 -2.5	+4.8 -4.6	1.7	0.0	0.0	0.75	1.8
16	2.76 – 2.94	$1.53 \cdot 10^{-3}$	4.8	1.5	+17.3 -15.7	+0.8 -0.7	+2.5 -2.4	+4.7 -4.7	1.7	0.0	0.0	0.75	1.8
17	2.94 – 3.12	$7.02 \cdot 10^{-4}$	4.5	2.2	+17.8 -16.2	+0.6 -0.5	+2.4 -2.3	+4.7 -4.7	1.8	0.0	0.0	0.75	1.8
18	3.12 – 3.44	$2.67 \cdot 10^{-4}$	5.6	2.1	+18.5 -16.9	+0.3 -0.4	+2.3 -2.2	+4.6 -4.7	2.0	0.0	0.0	0.75	1.8
19	3.44 – 3.90	$6.67 \cdot 10^{-5}$	10	2.8	+19.8 -18.2	+0.0 -0.2	+2.1 -2.0	+4.4 -4.5	2.1	0.0	0.0	0.75	1.8
20	3.90 – 4.66	$4.17 \cdot 10^{-6}$	30	5.0	+24.1 -24.4	+0.0 -0.5	+1.2 -0.7	+3.2 -3.0	2.8	0.0	0.0	0.75	1.8

Table A.5. — Measured double-differential three-jets cross-section,  $\sigma$ , for  $R = 0.4$  jets and  $8 < |Y^*| < 10$ , along with uncertainties in the measurement. All uncertainties are given in %, where  $\delta_{\text{stat}}^{\text{data}}$  ( $\delta_{\text{stat}}^{\text{MC}}$ ) are the statistical uncertainties in the data (MC simulation). The  $\gamma$  components are the uncertainty in the jet energy calibration from the *in situ*, the pile-up, the close-by jet, and the flavour components. The  $u$  components show the uncertainty in the jet energy and angular resolution, the unfolding, the jet identification, and the luminosity. While all columns are uncorrelated with each other, the *in situ*, pile-up, and flavour uncertainties shown here are the sum in quadrature of multiple uncorrelated components.

$N_{\text{s}}$	$m_{\text{jjj-range}}$ [TeV]	$\sigma$ [pb/GeV]	$\delta_{\text{stat}}^{\text{data}}$ [%]	$\delta_{\text{stat}}^{\text{MC}}$ [%]	$\gamma_{\text{in situ}}$ [%]	$\gamma_{\text{pile-up}}$ [%]	$\gamma_{\text{close-by}}$ [%]	$\gamma_{\text{flavour}}$ [%]	$u_{\text{JER}}$ [%]	$u_{\text{JAR}}$ [%]	$u_{\text{unfold}}$ [%]	$u_{\text{ID}}$ [%]	$u_{\text{lumi}}$ [%]
1	1.18 – 1.30	$8.88 \cdot 10^{-1}$	3.3	2.8	+14.4 -13.3	+0.2 -2.7	+2.2 -2.1	+5.8 -5.2	1.0	0.8	0.0	0.75	1.8
2	1.30 – 1.44	$8.13 \cdot 10^{-1}$	2.6	2.3	+14.6 -14.4	+0.1 -2.3	+2.3 -2.3	+5.5 -5.5	1.0	0.8	0.0	0.75	1.8
3	1.44 – 1.58	$5.67 \cdot 10^{-1}$	2.9	2.4	+15.4 -15.6	+0.1 -2.0	+2.4 -2.5	+5.4 -5.7	1.0	0.8	0.0	0.75	1.8
4	1.58 – 1.74	$3.67 \cdot 10^{-1}$	3.4	2.6	+16.7 -16.8	+0.2 -1.8	+2.5 -2.6	+5.3 -5.6	1.0	0.7	0.0	0.75	1.8
5	1.74 – 1.92	$2.04 \cdot 10^{-1}$	4.2	2.8	+18.5 -17.9	+0.4 -1.7	+2.6 -2.6	+5.3 -5.4	1.0	0.6	0.0	0.75	1.8
6	1.92 – 2.12	$1.04 \cdot 10^{-1}$	5.5	2.5	+20.6 -19.1	+0.5 -1.7	+2.7 -2.7	+5.3 -5.1	1.0	0.4	0.0	0.75	1.8
7	2.12 – 2.32	$4.48 \cdot 10^{-2}$	8.0	3.8	+22.6 -20.2	+0.4 -1.7	+2.8 -2.8	+5.4 -4.9	1.1	0.3	0.0	0.75	1.8
8	2.32 – 2.72	$1.67 \cdot 10^{-2}$	8.7	1.9	+25.6 -21.4	+0.1 -1.7	+3.0 -3.0	+5.4 -4.4	1.6	0.2	0.0	0.75	1.8
9	2.72 – 3.14	$3.52 \cdot 10^{-3}$	7.9	3.3	+30.2 -23.6	+0.2 -1.7	+3.4 -3.2	+5.1 -3.6	2.7	0.1	0.0	0.75	1.8
10	3.14 – 3.58	$6.24 \cdot 10^{-4}$	18	6.3	+34.7 -27.2	+0.2 -1.8	+3.6 -3.5	+4.8 -3.2	3.7	0.1	0.0	0.75	1.8
11	3.58 – 4.18	$1.03 \cdot 10^{-4}$	32	14	+39.9 -32.1	+0.2 -1.8	+3.9 -3.8	+4.6 -3.6	4.4	0.1	0.1	0.75	1.8
12	4.18 – 5.50	$3.03 \cdot 10^{-6}$	40	14	+58.5 -42.4	+0.2 -1.9	+5.4 -4.1	+4.3 -8.2	5.0	0.1	0.7	0.75	1.8

Table A.6. — Measured double-differential three-jets cross-section,  $\sigma$ , for  $R = 0.6$  jets and  $|Y^*| < 2$ , along with uncertainties in the measurement. All uncertainties are given in %, where  $\delta_{\text{stat}}^{\text{data}}$  ( $\delta_{\text{stat}}^{\text{MC}}$ ) are the statistical uncertainties in the data (MC simulation). The  $\gamma$  components are the uncertainty in the jet energy calibration from the *in situ*, the pile-up, the close-by jet, and the flavour components. The  $u$  components show the uncertainty in the jet energy and angular resolution, the unfolding, the jet identification, and the luminosity. While all columns are uncorrelated with each other, the *in situ*, pile-up, and flavour uncertainties shown here are the sum in quadrature of multiple uncorrelated components.

N <sup>o</sup>	$m_{\text{jjj-range}}$ [TeV]	$\sigma$ [pb/GeV]	$\delta_{\text{stat}}^{\text{data}}$ [%]	$\delta_{\text{stat}}^{\text{MC}}$ [%]	$\gamma_{\text{in situ}}$ [%]	$\gamma_{\text{pile-up}}$ [%]	$\gamma_{\text{close-by}}$ [%]	$\gamma_{\text{flavour}}$ [%]	$u_{\text{JER}}$ [%]	$u_{\text{JAR}}$ [%]	$u_{\text{unfold}}$ [%]	$u_{\text{ID}}$ [%]	$u_{\text{lumi}}$ [%]
1	0.38 – 0.42	20.8	2.9	0.91	+6.6 -6.6	+0.1 -3.4	+5.0 -4.6	+7.0 -6.6	2.0	0.7	0.0	0.75	1.8
2	0.42 – 0.46	15.0	3.1	0.81	+6.5 -6.5	+0.1 -2.6	+4.8 -4.4	+6.8 -6.5	1.9	0.6	0.0	0.75	1.8
3	0.46 – 0.50	10.1	2.1	0.60	+6.4 -6.4	+0.1 -2.2	+4.6 -4.3	+6.7 -6.3	1.8	0.5	0.0	0.75	1.8
4	0.50 – 0.54	6.44	2.4	0.59	+6.3 -6.2	+0.1 -1.9	+4.4 -4.1	+6.5 -6.0	1.7	0.4	0.0	0.75	1.8
5	0.54 – 0.60	3.99	2.2	0.49	+6.2 -5.9	+0.2 -1.6	+4.3 -3.9	+6.2 -5.8	1.6	0.3	0.0	0.75	1.8
6	0.60 – 0.66	2.20	2.1	0.53	+6.0 -5.7	+0.4 -1.3	+4.1 -3.8	+5.9 -5.4	1.5	0.2	0.0	0.75	1.8
7	0.66 – 0.72	1.35	2.6	0.63	+5.8 -5.5	+0.5 -1.1	+3.9 -3.7	+5.5 -5.2	1.3	0.1	0.0	0.75	1.8
8	0.72 – 0.78	$8.27 \cdot 10^{-1}$	2.4	0.67	+5.6 -5.4	+0.6 -1.1	+3.7 -3.6	+5.2 -4.9	1.2	0.1	0.0	0.75	1.8
9	0.78 – 0.86	$4.83 \cdot 10^{-1}$	1.4	0.57	+5.4 -5.3	+0.6 -1.1	+3.5 -3.4	+4.9 -4.7	1.0	0.0	0.0	0.75	1.8
10	0.86 – 0.94	$2.78 \cdot 10^{-1}$	1.8	0.45	+5.3 -5.3	+0.6 -1.1	+3.2 -3.1	+4.6 -4.4	0.9	0.0	0.0	0.75	1.8
11	0.94 – 1.02	$1.62 \cdot 10^{-1}$	1.5	0.43	+5.3 -5.2	+0.6 -1.1	+2.9 -2.9	+4.4 -4.2	0.8	0.0	0.0	0.75	1.8
12	1.02 – 1.12	$9.31 \cdot 10^{-2}$	1.0	0.38	+5.3 -5.2	+0.5 -1.1	+2.6 -2.5	+4.1 -3.9	0.8	0.0	0.0	0.75	1.8
13	1.12 – 1.22	$5.12 \cdot 10^{-2}$	1.4	0.44	+5.4 -5.2	+0.3 -0.9	+2.3 -2.2	+3.9 -3.7	0.8	0.0	0.0	0.75	1.8
14	1.22 – 1.34	$2.77 \cdot 10^{-2}$	1.3	0.47	+5.7 -5.4	+0.2 -0.7	+2.0 -1.9	+3.6 -3.5	0.8	0.0	0.0	0.75	1.8
15	1.34 – 1.46	$1.50 \cdot 10^{-2}$	1.2	0.49	+5.9 -5.6	+0.1 -0.5	+1.7 -1.7	+3.4 -3.2	0.7	0.0	0.0	0.75	1.8
16	1.46 – 1.60	$7.63 \cdot 10^{-3}$	1.6	0.50	+6.4 -6.0	+0.2 -0.3	+1.6 -1.5	+3.3 -3.1	0.7	0.0	0.0	0.75	1.8
17	1.60 – 1.76	$3.73 \cdot 10^{-3}$	2.0	0.44	+7.0 -6.6	+0.2 -0.3	+1.4 -1.4	+3.1 -2.9	0.7	0.0	0.0	0.75	1.8
18	1.76 – 1.94	$1.90 \cdot 10^{-3}$	2.8	0.38	+7.8 -7.4	+0.3 -0.2	+1.3 -1.2	+3.0 -2.8	0.7	0.0	0.0	0.75	1.8
19	1.94 – 2.14	$8.81 \cdot 10^{-4}$	3.9	0.40	+8.8 -8.5	+0.4 -0.2	+1.2 -1.1	+2.9 -2.8	0.6	0.0	0.0	0.75	1.8
20	2.14 – 2.36	$3.50 \cdot 10^{-4}$	5.9	0.58	+10.0 -9.7	+0.4 -0.2	+1.1 -1.1	+2.9 -2.7	0.6	0.0	0.0	0.75	1.8
21	2.36 – 2.60	$1.32 \cdot 10^{-4}$	9.4	0.70	+11.2 -10.7	+0.4 -0.2	+1.0 -1.0	+2.8 -2.6	0.6	0.0	0.0	0.75	1.8
22	2.60 – 2.84	$6.60 \cdot 10^{-5}$	13	0.83	+12.6 -11.9	+0.4 -0.2	+1.0 -1.0	+2.8 -2.6	0.7	0.0	0.0	0.75	1.8
23	2.84 – 3.10	$2.24 \cdot 10^{-5}$	22	1.2	+15.8 -14.8	+0.4 -0.2	+1.0 -1.0	+2.8 -2.5	0.7	0.0	0.0	0.75	1.8
24	3.10 – 3.90	$4.95 \cdot 10^{-6}$	27	0.93	+26.9 -25.2	+0.4 -0.2	+1.0 -0.9	+2.6 -2.4	1.0	0.0	0.0	0.75	1.8

Table A.7. — Measured double-differential three-jets cross-section,  $\sigma$ , for  $R = 0.6$  jets and  $2 < |Y^*| < 4$ , along with uncertainties in the measurement. All uncertainties are given in %, where  $\delta_{\text{stat}}^{\text{data}}$  ( $\delta_{\text{stat}}^{\text{MC}}$ ) are the statistical uncertainties in the data (MC simulation). The  $\gamma$  components are the uncertainty in the jet energy calibration from the *in situ*, the pile-up, the close-by jet, and the flavour components. The  $u$  components show the uncertainty in the jet energy and angular resolution, the unfolding, the jet identification, and the luminosity. While all columns are uncorrelated with each other, the *in situ*, pile-up, and flavour uncertainties shown here are the sum in quadrature of multiple uncorrelated components.

N <sub>2</sub>	$m_{\text{jjj-range}}$ [TeV]	$\sigma$ [pb/GeV]	$\delta_{\text{stat}}^{\text{data}}$ [%]	$\delta_{\text{stat}}^{\text{MC}}$ [%]	$\gamma_{\text{in situ}}$ [%]	$\gamma_{\text{pile-up}}$ [%]	$\gamma_{\text{close-by}}$ [%]	$\gamma_{\text{flavour}}$ [%]	$u_{\text{JER}}$ [%]	$u_{\text{JAR}}$ [%]	$u_{\text{unfold}}$ [%]	$u_{\text{ID}}$ [%]	$u_{\text{lumi}}$ [%]
1	0.42 – 0.46	36.3	2.1	0.90	+7.0 -7.2	+0.7 -4.4	+4.0 -4.0	+6.9 -6.8	1.8	0.8	0.0	0.75	1.8
2	0.46 – 0.50	35.9	2.0	0.76	+7.0 -7.1	+0.5 -3.3	+4.0 -3.9	+6.8 -6.6	1.9	0.8	0.0	0.75	1.8
3	0.50 – 0.54	29.5	2.1	0.76	+6.9 -7.0	+0.4 -2.5	+3.9 -3.8	+6.7 -6.5	1.9	0.8	0.0	0.75	1.8
4	0.54 – 0.60	19.7	1.8	0.59	+6.9 -6.9	+0.4 -1.9	+3.8 -3.7	+6.5 -6.3	1.8	0.7	0.0	0.75	1.8
5	0.60 – 0.66	11.6	1.7	0.51	+6.8 -6.7	+0.3 -1.6	+3.7 -3.6	+6.2 -6.0	1.7	0.6	0.0	0.75	1.8
6	0.66 – 0.72	6.99	2.0	0.40	+6.7 -6.5	+0.3 -1.4	+3.6 -3.4	+6.0 -5.7	1.6	0.5	0.0	0.75	1.8
7	0.72 – 0.78	4.20	2.0	0.47	+6.5 -6.3	+0.4 -1.4	+3.5 -3.3	+5.8 -5.4	1.5	0.4	0.0	0.75	1.8
8	0.78 – 0.86	2.55	1.7	0.42	+6.4 -6.1	+0.5 -1.3	+3.4 -3.1	+5.5 -5.2	1.4	0.3	0.0	0.75	1.8
9	0.86 – 0.94	1.43	2.0	0.47	+6.3 -6.0	+0.5 -1.3	+3.2 -3.0	+5.3 -4.9	1.3	0.3	0.0	0.75	1.8
10	0.94 – 1.02	$8.60 \cdot 10^{-1}$	1.0	0.47	+6.1 -5.9	+0.6 -1.4	+3.0 -2.8	+5.0 -4.7	1.2	0.2	0.0	0.75	1.8
11	1.02 – 1.12	$4.96 \cdot 10^{-1}$	1.2	0.41	+6.0 -5.8	+0.6 -1.4	+2.8 -2.6	+4.7 -4.5	1.1	0.2	0.0	0.75	1.8
12	1.12 – 1.22	$2.66 \cdot 10^{-1}$	1.5	0.37	+5.9 -5.7	+0.7 -1.4	+2.5 -2.4	+4.4 -4.2	1.0	0.1	0.0	0.75	1.8
13	1.22 – 1.34	$1.47 \cdot 10^{-1}$	0.79	0.32	+5.9 -5.8	+0.7 -1.2	+2.2 -2.2	+4.1 -4.0	0.9	0.1	0.0	0.75	1.8
14	1.34 – 1.46	$7.89 \cdot 10^{-2}$	0.95	0.32	+6.0 -5.8	+0.6 -1.0	+2.0 -1.9	+3.9 -3.8	0.9	0.1	0.0	0.75	1.8
15	1.46 – 1.60	$4.08 \cdot 10^{-2}$	1.1	0.34	+6.2 -6.0	+0.4 -0.7	+1.7 -1.7	+3.7 -3.5	0.9	0.0	0.0	0.75	1.8
16	1.60 – 1.74	$2.15 \cdot 10^{-2}$	0.90	0.39	+6.6 -6.3	+0.3 -0.5	+1.5 -1.4	+3.5 -3.3	0.9	0.0	0.0	0.75	1.8
17	1.74 – 1.90	$1.09 \cdot 10^{-2}$	1.2	0.46	+7.1 -6.8	+0.2 -0.3	+1.3 -1.3	+3.3 -3.2	0.8	0.0	0.0	0.75	1.8
18	1.90 – 2.08	$5.29 \cdot 10^{-3}$	1.7	0.49	+7.7 -7.4	+0.2 -0.2	+1.2 -1.1	+3.2 -3.0	0.8	0.0	0.0	0.75	1.8
19	2.08 – 2.26	$2.53 \cdot 10^{-3}$	2.4	0.53	+8.5 -8.1	+0.2 -0.1	+1.1 -1.0	+3.1 -2.9	0.9	0.0	0.0	0.75	1.8
20	2.26 – 2.48	$1.17 \cdot 10^{-3}$	3.2	0.48	+9.5 -9.2	+0.1 -0.1	+1.0 -0.9	+3.0 -2.9	0.9	0.0	0.0	0.75	1.8
21	2.48 – 2.72	$4.65 \cdot 10^{-4}$	5.1	0.50	+10.7 -10.5	+0.1 -0.1	+0.9 -0.9	+2.9 -2.9	0.9	0.0	0.0	0.75	1.8
22	2.72 – 2.98	$1.58 \cdot 10^{-4}$	7.9	0.61	+12.2 -11.9	+0.1 -0.1	+0.9 -0.8	+3.0 -2.9	0.9	0.0	0.0	0.75	1.8
23	2.98 – 3.26	$7.07 \cdot 10^{-5}$	12	0.75	+13.8 -13.6	+0.1 -0.1	+0.8 -0.8	+3.0 -2.9	0.8	0.0	0.0	0.75	1.8
24	3.26 – 3.58	$1.42 \cdot 10^{-5}$	22	1.6	+17.4 -16.8	+0.1 -0.1	+0.8 -0.7	+3.1 -3.0	0.8	0.0	0.0	0.75	1.8
25	3.58 – 4.20	$6.19 \cdot 10^{-6}$	28	1.2	+28.3 -25.0	+0.1 -0.1	+0.9 -0.7	+3.6 -3.3	2.8	0.0	0.0	0.75	1.8

Table A.8. — Measured double-differential three-jets cross-section,  $\sigma$ , for  $R = 0.6$  jets and  $4 < |Y^*| < 6$ , along with uncertainties in the measurement. All uncertainties are given in %, where  $\delta_{\text{stat}}^{\text{data}}$  ( $\delta_{\text{stat}}^{\text{MC}}$ ) are the statistical uncertainties in the data (MC simulation). The  $\gamma$  components are the uncertainty in the jet energy calibration from the *in situ*, the pile-up, the close-by jet, and the flavour components. The  $u$  components show the uncertainty in the jet energy and angular resolution, the unfolding, the jet identification, and the luminosity. While all columns are uncorrelated with each other, the *in situ*, pile-up, and flavour uncertainties shown here are the sum in quadrature of multiple uncorrelated components.

N <sup>o</sup>	$m_{\text{jjj-range}}$ [TeV]	$\sigma$ [pb/GeV]	$\delta_{\text{stat}}^{\text{data}}$ [%]	$\delta_{\text{stat}}^{\text{MC}}$ [%]	$\gamma_{\text{in situ}}$ [%]	$\gamma_{\text{pile-up}}$ [%]	$\gamma_{\text{close-by}}$ [%]	$\gamma_{\text{flavour}}$ [%]	$u_{\text{JER}}$ [%]	$u_{\text{JAR}}$ [%]	$u_{\text{unfold}}$ [%]	$u_{\text{ID}}$ [%]	$u_{\text{lumi}}$ [%]
1	0.54 – 0.60	21.9	2.2	0.98	+7.9 –8.1	+0.3 –5.2	+3.6 –3.6	+7.1 –6.6	2.2	1.8	0.0	0.75	1.8
2	0.60 – 0.66	21.7	2.2	0.85	+8.0 –8.2	+0.3 –3.7	+3.6 –3.6	+6.9 –6.5	2.2	1.8	0.0	0.75	1.8
3	0.66 – 0.72	18.0	1.8	0.81	+8.2 –8.2	+0.3 –2.6	+3.6 –3.6	+6.7 –6.4	2.2	1.7	0.0	0.75	1.8
4	0.72 – 0.80	12.3	1.4	0.61	+8.2 –8.2	+0.3 –1.8	+3.6 –3.6	+6.5 –6.2	2.1	1.6	0.0	0.75	1.8
5	0.80 – 0.88	7.56	1.7	0.61	+8.3 –8.1	+0.3 –1.4	+3.6 –3.5	+6.2 –6.0	2.1	1.4	0.0	0.75	1.8
6	0.88 – 0.96	4.49	2.1	0.65	+8.2 –8.0	+0.3 –1.3	+3.5 –3.4	+6.0 –5.7	2.0	1.2	0.0	0.75	1.8
7	0.96 – 1.06	2.54	1.5	0.47	+8.2 –8.0	+0.5 –1.3	+3.3 –3.2	+5.7 –5.5	1.9	1.1	0.0	0.75	1.8
8	1.06 – 1.16	1.35	1.9	0.50	+8.1 –7.9	+0.7 –1.5	+3.2 –3.1	+5.4 –5.2	1.8	0.9	0.0	0.75	1.8
9	1.16 – 1.26	$7.82 \cdot 10^{-1}$	2.6	0.60	+8.0 –7.8	+0.8 –1.6	+3.1 –3.0	+5.2 –5.0	1.7	0.7	0.0	0.75	1.8
10	1.26 – 1.38	$4.48 \cdot 10^{-1}$	1.3	0.62	+8.0 –7.7	+0.9 –1.7	+3.0 –2.8	+5.0 –4.7	1.7	0.6	0.0	0.75	1.8
11	1.38 – 1.50	$2.40 \cdot 10^{-1}$	1.6	0.67	+8.0 –7.6	+1.0 –1.6	+2.8 –2.7	+4.8 –4.5	1.6	0.5	0.0	0.75	1.8
12	1.50 – 1.62	$1.31 \cdot 10^{-1}$	2.1	0.69	+8.1 –7.6	+1.1 –1.5	+2.6 –2.5	+4.6 –4.3	1.6	0.4	0.0	0.75	1.8
13	1.62 – 1.76	$7.10 \cdot 10^{-2}$	1.8	0.64	+8.1 –7.6	+1.1 –1.4	+2.5 –2.3	+4.5 –4.1	1.6	0.3	0.0	0.75	1.8
14	1.76 – 1.90	$3.92 \cdot 10^{-2}$	1.3	0.60	+8.2 –7.7	+1.1 –1.1	+2.2 –2.1	+4.3 –4.0	1.6	0.3	0.0	0.75	1.8
15	1.90 – 2.06	$2.11 \cdot 10^{-2}$	1.7	0.52	+8.4 –7.9	+1.0 –0.9	+2.0 –1.9	+4.1 –3.8	1.6	0.3	0.0	0.75	1.8
16	2.06 – 2.22	$1.05 \cdot 10^{-2}$	1.9	0.63	+8.6 –8.3	+0.8 –0.7	+1.8 –1.7	+3.9 –3.7	1.6	0.3	0.0	0.75	1.8
17	2.22 – 2.40	$5.18 \cdot 10^{-3}$	1.7	0.74	+9.0 –8.8	+0.6 –0.5	+1.6 –1.6	+3.7 –3.7	1.6	0.3	0.0	0.75	1.8
18	2.40 – 2.58	$2.62 \cdot 10^{-3}$	2.3	0.98	+9.5 –9.4	+0.4 –0.3	+1.4 –1.4	+3.6 –3.6	1.7	0.2	0.0	0.75	1.8
19	2.58 – 2.78	$1.28 \cdot 10^{-3}$	3.2	1.1	+10.1 –10.3	+0.3 –0.2	+1.3 –1.3	+3.5 –3.5	1.9	0.2	0.0	0.75	1.8
20	2.78 – 2.98	$5.77 \cdot 10^{-4}$	4.7	1.4	+10.9 –11.3	+0.2 –0.2	+1.2 –1.2	+3.4 –3.5	2.0	0.2	0.0	0.75	1.8
21	2.98 – 3.20	$2.64 \cdot 10^{-4}$	6.7	1.5	+11.8 –12.3	+0.1 –0.2	+1.1 –1.1	+3.4 –3.6	2.2	0.2	0.0	0.75	1.8
22	3.20 – 3.42	$1.16 \cdot 10^{-4}$	10	1.7	+12.8 –13.3	+0.1 –0.1	+1.1 –1.1	+3.4 –3.6	2.3	0.2	0.0	0.75	1.8
23	3.42 – 3.66	$3.72 \cdot 10^{-5}$	17	1.9	+13.9 –14.2	+0.1 –0.1	+1.0 –1.0	+3.5 –3.6	2.5	0.2	0.0	0.75	1.8
24	3.66 – 4.70	$6.07 \cdot 10^{-6}$	22	1.3	+24.1 –18.9	+0.1 –0.1	+0.9 –0.7	+4.9 –3.6	2.9	0.1	0.0	0.75	1.8

Table A.9. — Measured double-differential three-jets cross-section,  $\sigma$ , for  $R = 0.6$  jets and  $6 < |Y^*| < 8$ , along with uncertainties in the measurement. All uncertainties are given in %, where  $\delta_{\text{stat}}^{\text{data}}$  ( $\delta_{\text{stat}}^{\text{MC}}$ ) are the statistical uncertainties in the data (MC simulation). The  $\gamma$  components are the uncertainty in the jet energy calibration from the *in situ*, the pile-up, the close-by jet, and the flavour components. The  $u$  components show the uncertainty in the jet energy and angular resolution, the unfolding, the jet identification, and the luminosity. While all columns are uncorrelated with each other, the *in situ*, pile-up, and flavour uncertainties shown here are the sum in quadrature of multiple uncorrelated components.

N <sup>o</sup>	$m_{\text{jjj-range}}$ [TeV]	$\sigma$ [pb/GeV]	$\delta_{\text{stat}}^{\text{data}}$ [%]	$\delta_{\text{stat}}^{\text{MC}}$ [%]	$\gamma_{\text{in situ}}$ [%]	$\gamma_{\text{pile-up}}$ [%]	$\gamma_{\text{close-by}}$ [%]	$\gamma_{\text{flavour}}$ [%]	$u_{\text{JER}}$ [%]	$u_{\text{JAR}}$ [%]	$u_{\text{unfold}}$ [%]	$u_{\text{ID}}$ [%]	$u_{\text{lumi}}$ [%]
1	0.76 – 0.84	6.96	3.3	1.4	+8.9 –8.8	+0.4 –5.0	+3.7 –3.6	+6.5 –6.0	2.7	3.6	0.0	0.75	1.8
2	0.84 – 0.94	7.23	3.0	1.2	+9.6 –9.3	+0.4 –3.8	+3.8 –3.5	+6.5 –5.9	2.9	3.6	0.0	0.75	1.8
3	0.94 – 1.04	5.74	1.8	1.0	+10.3 –9.8	+0.4 –2.8	+3.8 –3.5	+6.5 –5.8	2.9	3.5	0.0	0.75	1.8
4	1.04 – 1.14	4.09	2.1	1.2	+11.1 –10.3	+0.4 –2.2	+3.8 –3.5	+6.5 –5.7	2.9	3.4	0.0	0.75	1.8
5	1.14 – 1.26	2.50	2.5	1.2	+11.7 –10.8	+0.4 –2.0	+3.8 –3.5	+6.3 –5.7	3.0	3.2	0.0	0.75	1.8
6	1.26 – 1.38	1.34	3.2	1.2	+12.3 –11.2	+0.6 –1.8	+3.8 –3.5	+6.1 –5.6	3.0	3.0	0.0	0.75	1.8
7	1.38 – 1.52	$7.28 \cdot 10^{-1}$	3.2	1.1	+12.6 –11.6	+1.0 –1.7	+3.7 –3.5	+5.9 –5.5	2.9	2.7	0.0	0.75	1.8
8	1.52 – 1.66	$3.81 \cdot 10^{-1}$	3.2	1.2	+12.7 –11.9	+1.2 –1.5	+3.6 –3.4	+5.6 –5.4	2.8	2.3	0.0	0.75	1.8
9	1.66 – 1.80	$2.19 \cdot 10^{-1}$	4.2	1.0	+12.8 –12.2	+1.4 –1.4	+3.4 –3.4	+5.3 –5.3	2.7	2.0	0.0	0.75	1.8
10	1.80 – 1.94	$1.10 \cdot 10^{-1}$	4.6	1.3	+12.8 –12.4	+1.6 –1.4	+3.2 –3.4	+5.0 –5.3	2.7	1.6	0.0	0.75	1.8
11	1.94 – 2.10	$6.00 \cdot 10^{-2}$	2.8	1.4	+13.0 –12.5	+1.7 –1.5	+3.0 –3.4	+4.8 –5.2	2.7	1.4	0.0	0.75	1.8
12	2.10 – 2.26	$3.15 \cdot 10^{-2}$	3.6	1.7	+13.2 –12.6	+1.8 –1.8	+2.9 –3.3	+4.7 –5.1	2.8	1.1	0.0	0.75	1.8
13	2.26 – 2.42	$1.74 \cdot 10^{-2}$	4.9	2.0	+13.5 –12.8	+1.9 –2.0	+2.8 –3.1	+4.7 –5.0	3.0	0.9	0.0	0.75	1.8
14	2.42 – 2.58	$8.55 \cdot 10^{-3}$	4.5	2.2	+13.9 –13.0	+2.1 –2.1	+2.7 –3.0	+4.7 –4.9	3.1	0.8	0.0	0.75	1.8
15	2.58 – 2.76	$4.40 \cdot 10^{-3}$	3.5	1.9	+14.3 –13.3	+2.3 –2.2	+2.6 –2.8	+4.7 –4.8	3.3	0.8	0.0	0.75	1.8
16	2.76 – 2.94	$2.24 \cdot 10^{-3}$	4.8	1.9	+14.7 –13.6	+2.5 –2.1	+2.5 –2.7	+4.7 –4.8	3.4	0.7	0.0	0.75	1.8
17	2.94 – 3.12	$1.09 \cdot 10^{-3}$	6.8	1.9	+15.0 –13.9	+2.6 –2.0	+2.4 –2.5	+4.8 –4.7	3.6	0.7	0.0	0.75	1.8
18	3.12 – 3.44	$4.01 \cdot 10^{-4}$	8.8	1.9	+15.6 –14.5	+2.8 –1.9	+2.2 –2.3	+4.7 –4.6	3.9	0.7	0.0	0.75	1.8
19	3.44 – 3.90	$7.76 \cdot 10^{-5}$	12	2.7	+16.7 –15.7	+3.0 –1.7	+2.0 –2.1	+4.7 –4.3	4.6	0.6	0.0	0.75	1.8
20	3.90 – 4.66	$1.17 \cdot 10^{-5}$	19	4.3	+24.1 –21.6	+3.3 –1.4	+1.3 –1.1	+5.6 –3.1	9.7	0.6	0.0	0.75	1.8

Table A.10. — Measured double-differential three-jets cross-section,  $\sigma$ , for  $R = 0.6$  jets and  $8 < |Y^*| < 10$ , along with uncertainties in the measurement. All uncertainties are given in %, where  $\delta_{\text{stat}}^{\text{data}}$  ( $\delta_{\text{stat}}^{\text{MC}}$ ) are the statistical uncertainties in the data (MC simulation). The  $\gamma$  components are the uncertainty in the jet energy calibration from the *in situ*, the pile-up, the close-by jet, and the flavour components. The  $u$  components show the uncertainty in the jet energy and angular resolution, the unfolding, the jet identification, and the luminosity. While all columns are uncorrelated with each other, the *in situ*, pile-up, and flavour uncertainties shown here are the sum in quadrature of multiple uncorrelated components.

N <sup>a</sup>	$m_{\text{jjj-range}}$ [TeV]	$\sigma$ [pb/GeV]	$\delta_{\text{stat}}^{\text{data}}$ [%]	$\delta_{\text{stat}}^{\text{MC}}$ [%]	$\gamma_{\text{in situ}}$ [%]	$\gamma_{\text{pile-up}}$ [%]	$\gamma_{\text{close-by}}$ [%]	$\gamma_{\text{flavour}}$ [%]	$u_{\text{JER}}$ [%]	$u_{\text{JAR}}$ [%]	$u_{\text{unfold}}$ [%]	$u_{\text{ID}}$ [%]	$u_{\text{lumi}}$ [%]
1	1.18 – 1.30	1.46	3.8	2.3	+13.6 –13.5	+0.5 –5.0	+4.1 –3.7	+6.0 –5.9	3.2	6.2	0.0	0.75	1.8
2	1.30 – 1.44	1.21	3.4	2.1	+14.3 –13.7	+0.5 –3.8	+4.2 –3.7	+6.0 –5.8	3.6	6.5	0.0	0.75	1.8
3	1.44 – 1.58	$8.88 \cdot 10^{-1}$	3.9	2.3	+15.0 –14.0	+0.6 –2.9	+4.1 –3.8	+5.8 –5.6	4.0	6.8	0.0	0.75	1.8
4	1.58 – 1.74	$5.94 \cdot 10^{-1}$	4.5	2.4	+15.9 –14.6	+0.8 –2.2	+4.0 –3.8	+5.6 –5.4	4.2	6.8	0.0	0.75	1.8
5	1.74 – 1.92	$3.44 \cdot 10^{-1}$	5.5	2.4	+17.3 –15.4	+1.0 –1.8	+4.0 –3.9	+5.6 –5.4	4.3	6.7	0.0	0.75	1.8
6	1.92 – 2.12	$1.63 \cdot 10^{-1}$	7.2	3.0	+19.0 –16.3	+1.0 –1.6	+4.1 –3.9	+5.7 –5.4	4.3	6.4	0.0	0.75	1.8
7	2.12 – 2.32	$6.64 \cdot 10^{-2}$	6.5	2.9	+20.7 –17.1	+0.7 –1.5	+4.1 –3.9	+5.9 –5.4	4.5	6.2	0.0	0.75	1.8
8	2.32 – 2.72	$2.59 \cdot 10^{-2}$	8.1	1.7	+22.6 –18.1	+0.4 –1.4	+3.8 –3.9	+5.9 –5.4	4.9	5.6	0.0	0.75	1.8
9	2.72 – 3.14	$4.95 \cdot 10^{-3}$	16	3.3	+24.8 –19.7	+0.1 –1.3	+3.7 –4.1	+5.8 –5.9	5.7	4.3	0.0	0.75	1.8
10	3.14 – 3.58	$1.12 \cdot 10^{-3}$	14	5.7	+27.7 –22.0	+0.0 –0.8	+3.7 –4.3	+5.7 –6.1	6.6	3.2	0.0	0.75	1.8
11	3.58 – 4.18	$1.44 \cdot 10^{-4}$	33	9.7	+30.8 –25.0	+0.0 –0.2	+3.4 –4.0	+5.7 –5.5	7.3	2.5	0.1	0.75	1.8
12	4.18 – 5.50	$5.14 \cdot 10^{-6}$	43	9.8	+36.0 –34.1	+1.2 –0.2	+1.4 –2.8	+8.6 –2.8	6.5	1.9	0.8	0.75	1.8

## Appendix B

### The measured $Z + \text{jets}$ production cross-sections

The  $Z + \text{jets}$  cross-section is measured as a function of the absolute jet rapidity in six regions of the jet transverse momentum. The cross-section is measured using the anti- $k_t$  jets with  $R = 0.4$ . The results are shown in Tables [B.1](#)–[B.6](#). The measured cross-sections are quoted along with statistical and systematic uncertainties.

Table B.1. — Measured double-differential  $Z + \text{jets}$  production cross-sections as a function of  $|y_{\text{jet}}|$  in the  $25 \text{ GeV} < p_{\text{T}}^{\text{jet}} < 50 \text{ GeV}$  region.  $\delta_{\text{stat}}^{\text{data}}$  and  $\delta_{\text{stat}}^{\text{MC}}$  are the statistical uncertainties in the data and MC simulation, respectively.  $\gamma_{\text{tot}}^{\text{sys}}$  is the total systematic uncertainty and includes the following components: uncertainties due to electron reconstruction ( $\gamma_{\text{rec}}^{\text{el}}$ ), identification ( $\gamma_{\text{ID}}^{\text{el}}$ ) and trigger ( $\gamma_{\text{trig}}^{\text{el}}$ ) efficiencies; electron energy scale ( $\gamma_{\text{EES}}^{\text{el}}$ ) and energy resolution ( $\gamma_{\text{EER}}^{\text{el}}$ ) uncertainties; a sum in quadrature of the uncertainties associated with the absolute *in situ* JES calibration ( $\gamma_{\text{in situ}}^{\text{jet}}$ ); a sum in quadrature of the uncertainties associated with the  $\eta$ -intercalibration ( $\gamma_{\eta\text{-int}}^{\text{jet}}$ ); an uncertainty in the high- $p_{\text{T}}$  jet JES calibration ( $\gamma_{\text{high-}p_{\text{T}}}^{\text{jet}}$ ); MC non-closure uncertainty ( $\gamma_{\text{closure}}^{\text{jet}}$ ); a sum in quadrature of the uncertainties due to pile-up corrections of the jet kinematics ( $\gamma_{\text{pile-up}}^{\text{jet}}$ ); a sum in quadrature of the flavour-based uncertainties ( $\gamma_{\text{flavour}}^{\text{jet}}$ ); punch-through uncertainty ( $\gamma_{\text{pthr}}^{\text{jet}}$ ); JER uncertainty ( $\gamma_{\text{JER}}^{\text{jet}}$ ); pile-up jet suppression efficiency uncertainty ( $\gamma_{\text{JVVF}}^{\text{jet}}$ ); a sum in quadrature of the unfolding uncertainties ( $\gamma_{\text{unfold}}$ ); a sum in quadrature of the uncertainties due to MC generated backgrounds normalisation ( $\gamma_{\text{MC}}^{\text{bg}}$ ); a sum in quadrature of the uncertainty due to combined multijet and  $W + \text{jets}$  backgrounds ( $\gamma_{\text{data}}^{\text{bg}}$ ); uncertainty due to jet quality selection ( $\gamma_{\text{ID}}^{\text{jet}}$ ). All uncertainties are given in %. The luminosity uncertainty of 1.9% is not shown and is not included in the total uncertainty and its components.

$ y_{\text{jet}} $	$\frac{d^2\sigma}{d y_{\text{jet}} dp_{\text{T}}^{\text{jet}}}$	$\delta_{\text{stat}}^{\text{data}}$	$\delta_{\text{stat}}^{\text{MC}}$	$\gamma_{\text{tot}}^{\text{sys}}$	$\gamma_{\text{rec}}^{\text{el}}$	$\gamma_{\text{ID}}^{\text{el}}$	$\gamma_{\text{trig}}^{\text{el}}$	$\gamma_{\text{EES}}^{\text{el}}$	$\gamma_{\text{EER}}^{\text{el}}$	$\gamma_{\text{in situ}}^{\text{jet}}$	$\gamma_{\eta\text{-int}}^{\text{jet}}$	$\gamma_{\text{high-}p_{\text{T}}}^{\text{jet}}$	$\gamma_{\text{closure}}^{\text{jet}}$	$\gamma_{\text{pile-up}}^{\text{jet}}$	$\gamma_{\text{flavour}}^{\text{jet}}$	$\gamma_{\text{pthr}}^{\text{jet}}$	$\gamma_{\text{JER}}^{\text{jet}}$	$\gamma_{\text{JVVF}}^{\text{jet}}$	$\gamma_{\text{unfold}}$	$\gamma_{\text{MC}}^{\text{bg}}$	$\gamma_{\text{data}}^{\text{bg}}$	$\gamma_{\text{ID}}^{\text{jet}}$	
range	[fb/ GeV ]	[%]	[%]	[%]	[%]	[%]	[%]	[%]	[%]	[%]	[%]	[%]	[%]	[%]	[%]	[%]	[%]	[%]	[%]	[%]	[%]	[%]	[%]
0.0–0.2	1643.603	0.42	0.51	+6.70	+0.08	+0.23	+0.31	−0.16	+0.01	+3.04	+0.30	+0.00	+0.01	+1.63	+2.95	+0.00	−3.83	+0.47	+2.84	+0.06	+0.14	+1.00	
					−6.80	−0.08	−0.27	−0.44	+0.14	−0.01	−3.04	−0.49	−0.01	−0.01	−1.68	−3.04	−0.02	+3.83	−0.72	−2.84	−0.05	−0.38	−1.00
0.2–0.4	1595.690	0.34	0.60	+6.72	+0.08	+0.23	+0.31	−0.16	+0.01	+3.16	+0.30	+0.00	+0.01	+1.65	+3.04	+0.00	−3.89	+0.47	+2.55	+0.06	+0.14	+1.00	
					−6.70	−0.08	−0.27	−0.44	+0.14	−0.01	−3.02	−0.49	−0.01	−0.01	−1.60	−3.05	−0.02	+3.89	−0.72	−2.55	−0.05	−0.39	−1.00
0.4–0.6	1587.440	0.37	0.60	+7.01	+0.08	+0.23	+0.31	−0.16	+0.01	+3.17	+0.30	+0.00	+0.01	+1.59	+3.08	+0.00	−4.17	+0.46	+2.86	+0.06	+0.15	+1.00	
					−7.14	−0.08	−0.27	−0.44	+0.14	−0.01	−3.14	−0.49	−0.01	−0.01	−1.72	−3.23	−0.02	+4.17	−0.67	−2.86	−0.05	−0.39	−1.00
0.6–0.8	1569.884	0.38	0.60	+7.02	+0.08	+0.23	+0.31	−0.16	+0.01	+3.19	+0.30	+0.00	+0.01	+1.62	+3.26	+0.00	−3.74	+0.46	+3.22	+0.05	+0.15	+1.00	
					−7.24	−0.08	−0.27	−0.44	+0.14	−0.01	−3.25	−0.49	−0.01	−0.01	−1.82	−3.46	−0.02	+3.74	−0.67	−3.22	−0.05	−0.40	−1.00
0.8–1.0	1520.883	0.36	0.59	+6.98	+0.08	+0.23	+0.31	−0.16	+0.01	+3.33	+0.30	+0.00	+0.01	+1.80	+3.54	+0.00	−2.88	+0.46	+3.48	+0.05	+0.15	+1.00	
					−7.04	−0.08	−0.27	−0.33	+0.14	−0.01	−3.25	−0.49	−0.01	−0.01	−1.88	−3.61	−0.02	+2.88	−0.56	−3.48	−0.05	−0.39	−1.00
1.0–1.2	1393.139	0.38	0.64	+8.32	+0.08	+0.23	+0.31	−0.16	+0.01	+3.60	+0.76	+0.00	+0.01	+1.97	+3.93	+0.00	−5.18	+0.46	+3.32	+0.05	+0.16	+1.00	
					−8.32	−0.08	−0.27	−0.33	+0.14	−0.01	−3.35	−0.49	−0.01	−0.01	−1.81	−3.87	−0.02	+5.18	−0.56	−3.32	−0.05	−0.41	−1.00
1.2–1.4	1377.328	0.47	0.57	+11.78	+0.08	+0.23	+0.31	−0.16	+0.01	+3.69	+0.76	+0.00	+0.01	+2.04	+4.49	+0.00	−8.88	+0.46	+4.47	+0.05	+0.17	+1.00	
					−11.50	−0.08	−0.27	−0.33	+0.14	−0.01	−3.29	−0.69	−0.01	−0.01	−1.78	−4.14	−0.02	+8.88	−0.56	−4.47	−0.05	−0.41	−1.00
1.4–1.6	1228.213	0.42	0.60	+12.01	+0.08	+0.23	+0.31	−0.16	+0.01	+3.65	+1.44	+0.00	+0.01	+2.00	+4.37	+0.00	−9.07	+0.71	+4.67	+0.05	+0.18	+1.00	
					−11.69	−0.08	−0.27	−0.33	+0.14	−0.01	−3.22	−1.14	−0.01	−0.01	−1.74	−4.02	−0.02	+9.07	−0.69	−4.67	−0.05	−0.42	−1.00
1.6–1.8	987.654	0.48	0.64	+12.09	+0.08	+0.23	+0.31	−0.16	+0.01	+3.37	+1.42	+0.00	+0.01	+1.83	+3.60	+0.00	−10.46	+0.71	+2.32	+0.06	+0.17	+1.00	
					−11.95	−0.08	−0.27	−0.33	+0.14	−0.01	−3.10	−1.25	−0.01	−0.01	−1.62	−3.51	−0.02	+10.46	−0.69	−2.32	−0.05	−0.43	−1.00
1.8–2.0	944.560	0.45	0.65	+10.24	+0.08	+0.23	+0.40	−0.16	+0.01	+3.38	+1.58	+0.00	+0.01	+1.90	+3.38	+0.00	−8.31	+0.55	+2.32	+0.05	+0.16	+1.00	
					−10.02	−0.08	−0.27	−0.33	+0.14	−0.01	−3.09	−1.25	−0.01	−0.01	−1.66	−3.23	−0.02	+8.31	−0.55	−2.32	−0.05	−0.43	−1.00
2.0–2.2	871.035	0.49	0.85	+10.30	+0.08	+0.23	+0.40	−0.16	+0.01	+3.65	+1.96	+0.00	+0.01	+2.05	+3.56	+0.00	−6.74	+0.55	+5.01	+0.05	+0.17	+1.00	
					−10.18	−0.08	−0.27	−0.33	+0.14	−0.01	−3.41	−1.74	−0.01	−0.01	−1.94	−3.60	−0.02	+6.74	−0.55	−5.01	−0.05	−0.43	−1.00
2.2–2.4	749.498	0.54	0.80	+11.14	+0.08	+0.23	+0.40	−0.16	+0.01	+4.23	+2.57	+0.00	+0.01	+2.70	+3.91	+0.00	−7.48	+0.55	+4.42	+0.05	+0.18	+1.00	
					−10.92	−0.08	−0.27	−0.33	+0.14	−0.01	−3.95	−2.33	−0.01	−0.01	−2.50	−3.85	−0.02	+7.48	−0.55	−4.42	−0.05	−0.42	−1.00

Table B.2. — Measured double-differential  $Z + \text{jets}$  production cross-sections as a function of  $|y_{\text{jet}}|$  in the  $50 \text{ GeV} < p_{\text{T}}^{\text{jet}} < 100 \text{ GeV}$  region.  $\delta_{\text{stat}}^{\text{data}}$  and  $\delta_{\text{stat}}^{\text{MC}}$  are the statistical uncertainties in the data and MC simulation, respectively.  $\gamma_{\text{tot}}^{\text{sys}}$  is the total systematic uncertainty and includes the following components: uncertainties due to electron reconstruction ( $\gamma_{\text{rec}}^{\text{el}}$ ), identification ( $\gamma_{\text{ID}}^{\text{el}}$ ) and trigger ( $\gamma_{\text{trig}}^{\text{el}}$ ) efficiencies; electron energy scale ( $\gamma_{\text{EES}}^{\text{el}}$ ) and energy resolution ( $\gamma_{\text{EER}}^{\text{el}}$ ) uncertainties; a sum in quadrature of the uncertainties associated with the absolute *in situ* JES calibration ( $\gamma_{\text{in situ}}^{\text{jet}}$ ); a sum in quadrature of the uncertainties associated with the  $\eta$ -intercalibration ( $\gamma_{\eta\text{-int}}^{\text{jet}}$ ); an uncertainty in the high- $p_{\text{T}}$  jet JES calibration ( $\gamma_{\text{high-}p_{\text{T}}}^{\text{jet}}$ ); MC non-closure uncertainty ( $\gamma_{\text{closure}}^{\text{jet}}$ ); a sum in quadrature of the uncertainties due to pile-up corrections of the jet kinematics ( $\gamma_{\text{pile-up}}^{\text{jet}}$ ); a sum in quadrature of the flavour-based uncertainties ( $\gamma_{\text{flavour}}^{\text{jet}}$ ); punch-through uncertainty ( $\gamma_{\text{pthr}}^{\text{jet}}$ ); JER uncertainty ( $\gamma_{\text{JER}}^{\text{jet}}$ ); pile-up jet suppression efficiency uncertainty ( $\gamma_{\text{JVf}}^{\text{jet}}$ ); a sum in quadrature of the unfolding uncertainties ( $\gamma_{\text{unfold}}$ ); a sum in quadrature of the uncertainties due to MC generated backgrounds normalisation ( $\gamma_{\text{MC}}^{\text{bg}}$ ); a sum in quadrature of the uncertainty due to combined multijet and  $W + \text{jets}$  backgrounds ( $\gamma_{\text{data}}^{\text{bg}}$ ); uncertainty due to jet quality selection ( $\gamma_{\text{ID}}^{\text{jet}}$ ). All uncertainties are given in %. The luminosity uncertainty of 1.9% is not shown and is not included in the total uncertainty and its components.

$ y_{\text{jet}} $	$\frac{d^2\sigma}{d y_{\text{jet}} dp_{\text{T}}^{\text{jet}}}$	$\delta_{\text{stat}}^{\text{data}}$	$\delta_{\text{stat}}^{\text{MC}}$	$\gamma_{\text{tot}}^{\text{sys}}$	$\gamma_{\text{rec}}^{\text{el}}$	$\gamma_{\text{ID}}^{\text{el}}$	$\gamma_{\text{trig}}^{\text{el}}$	$\gamma_{\text{EES}}^{\text{el}}$	$\gamma_{\text{EER}}^{\text{el}}$	$\gamma_{\text{in situ}}^{\text{jet}}$	$\gamma_{\eta\text{-int}}^{\text{jet}}$	$\gamma_{\text{high-}p_{\text{T}}}^{\text{jet}}$	$\gamma_{\text{closure}}^{\text{jet}}$	$\gamma_{\text{pile-up}}^{\text{jet}}$	$\gamma_{\text{flavour}}^{\text{jet}}$	$\gamma_{\text{pthr}}^{\text{jet}}$	$\gamma_{\text{JER}}^{\text{jet}}$	$\gamma_{\text{JVf}}^{\text{jet}}$	$\gamma_{\text{unfold}}$	$\gamma_{\text{MC}}^{\text{bg}}$	$\gamma_{\text{data}}^{\text{bg}}$	$\gamma_{\text{ID}}^{\text{jet}}$
range	[fb/ GeV]	[%]	[%]	[%]	[%]	[%]	[%]	[%]	[%]	[%]	[%]	[%]	[%]	[%]	[%]	[%]	[%]	[%]	[%]	[%]	[%]	[%]
0.0–0.2	349.964	0.56	0.80	+3.75 −3.71	+0.03 −0.08	+0.15 −0.21	+0.24 −0.29	−0.25 +0.19	+0.00 −0.05	+2.67 −2.61	+0.31 −0.26	+0.00 −0.03	+0.00 −0.02	+1.02 −0.92	+0.81 −0.77	+0.00 −0.02	−1.47 +1.47	−0.46 +0.49	+1.28 −1.28	+0.17 −0.15	+0.15 −0.42	+1.00 −1.00
0.2–0.4	352.217	0.71	0.80	+3.68 −3.77	+0.03 −0.08	+0.15 −0.21	+0.24 −0.29	−0.25 +0.19	+0.00 −0.05	+2.56 −2.70	+0.31 −0.26	+0.00 −0.03	+0.00 −0.02	+1.02 −0.92	+0.81 −0.77	+0.00 −0.02	−1.47 +1.47	−0.46 +0.49	+1.28 −1.28	+0.16 −0.15	+0.15 −0.42	+1.00 −1.00
0.4–0.6	338.924	0.74	0.81	+3.78 −3.99	+0.03 −0.08	+0.15 −0.21	+0.24 −0.29	−0.25 +0.19	+0.00 −0.05	+2.52 −2.86	+0.31 −0.26	+0.00 −0.03	+0.00 −0.02	+1.07 −0.92	+0.81 −0.77	+0.00 −0.02	−1.60 +1.60	−0.46 +0.49	+1.43 −1.43	+0.16 −0.15	+0.15 −0.43	+1.00 −1.00
0.6–0.8	328.606	0.72	0.93	+3.99 −4.15	+0.03 −0.08	+0.15 −0.21	+0.24 −0.29	−0.25 +0.19	+0.00 −0.05	+2.75 −2.86	+0.31 −0.26	+0.00 −0.03	+0.00 −0.02	+1.07 −1.08	+1.28 −1.44	+0.00 −0.02	−1.47 +1.47	−0.46 +0.49	+1.41 −1.41	+0.16 −0.14	+0.16 −0.43	+1.00 −1.00
0.8–1.0	303.475	0.69	0.87	+4.05 −3.89	+0.03 −0.08	+0.15 −0.21	+0.24 −0.29	−0.25 +0.19	+0.00 −0.05	+2.98 −2.76	+0.31 −0.26	+0.00 −0.03	+0.00 −0.02	+1.07 −1.08	+1.50 −1.44	+0.00 −0.02	−1.21 +1.21	−0.46 +0.49	+1.07 −1.07	+0.15 −0.14	+0.17 −0.45	+1.00 −1.00
1.0–1.2	274.407	0.71	1.05	+3.85 −4.09	+0.03 −0.08	+0.15 −0.21	+0.24 −0.29	−0.25 +0.19	+0.00 −0.05	+2.74 −2.83	+0.31 −0.26	+0.00 −0.03	+0.00 −0.02	+1.01 −1.19	+1.49 −1.44	+0.00 −0.02	−1.21 +1.21	−0.46 +0.49	+1.07 −1.07	+0.15 −0.14	+0.19 −0.46	+1.00 −1.00
1.2–1.4	261.553	0.81	0.84	+4.14 −4.31	+0.03 −0.08	+0.15 −0.21	+0.24 −0.29	−0.25 +0.19	+0.00 −0.05	+2.86 −2.86	+1.25 −0.96	+0.00 −0.03	+0.00 −0.02	+1.01 −1.19	+1.54 −1.94	+0.00 −0.02	−1.21 +1.21	−0.46 +0.49	+1.07 −1.07	+0.14 −0.13	+0.21 −0.49	+1.00 −1.00
1.4–1.6	233.170	0.75	1.02	+4.48 −4.38	+0.03 −0.08	+0.15 −0.21	+0.24 −0.29	−0.25 +0.19	+0.00 −0.05	+2.82 −2.74	+1.25 −0.96	+0.00 −0.03	+0.00 −0.02	+1.01 −1.05	+1.78 −1.69	+0.00 −0.02	−1.42 +1.42	−0.46 +0.40	+1.73 −1.73	+0.13 −0.12	+0.37 −0.60	+1.00 −1.00
1.6–1.8	192.405	0.92	1.16	+5.11 −4.80	+0.03 −0.08	+0.15 −0.21	+0.24 −0.29	−0.25 +0.19	+0.00 −0.05	+3.09 −2.92	+2.10 −1.97	+0.00 −0.03	+0.00 −0.02	+1.34 −1.05	+2.01 −1.69	+0.00 −0.02	−1.42 +1.42	−0.46 +0.40	+1.73 −1.73	+0.13 −0.12	+0.19 −0.51	+1.00 −1.00
1.8–2.0	174.081	0.90	1.18	+5.75 −5.14	+0.03 −0.08	+0.15 −0.21	+0.24 −0.29	−0.25 +0.19	+0.00 −0.05	+3.38 −3.05	+2.61 −2.27	+0.00 −0.03	+0.00 −0.02	+1.34 −1.05	+2.25 −1.66	+0.00 −0.02	−1.89 +1.89	−0.34 +0.40	+1.73 −1.73	+0.12 −0.11	+0.20 −0.55	+1.00 −1.00
2.0–2.2	145.578	0.94	1.11	+5.92 −5.31	+0.03 −0.08	+0.15 −0.21	+0.24 −0.29	−0.25 +0.19	+0.00 −0.05	+3.48 −3.02	+2.80 −2.36	+0.00 −0.03	+0.00 −0.02	+1.40 −0.92	+1.91 −1.66	+0.00 −0.02	−1.89 +1.89	−0.34 +0.40	+2.16 −2.16	+0.11 −0.10	+0.20 −0.56	+1.00 −1.00
2.2–2.4	117.333	1.08	1.37	+5.99 −5.18	+0.03 −0.08	+0.15 −0.21	+0.24 −0.29	−0.25 +0.19	+0.00 −0.05	+3.56 −2.83	+2.78 −2.23	+0.00 −0.03	+0.00 −0.02	+1.40 −0.92	+1.91 −1.66	+0.00 −0.02	−0.76 +0.76	−0.34 +0.40	+2.83 −2.83	+0.11 −0.10	+0.21 −0.58	+1.00 −1.00
2.4–2.6	98.813	1.31	1.42	+5.65 −5.25	+0.03 −0.08	+0.15 −0.21	+0.24 −0.29	−0.25 +0.19	+0.00 −0.05	+3.32 −2.87	+2.56 −2.20	+0.00 −0.03	+0.00 −0.02	+0.87 −0.92	+1.91 −1.82	+0.00 −0.02	−0.76 +0.76	−0.34 +0.40	+2.83 −2.83	+0.11 −0.10	+0.23 −0.64	+1.00 −1.00
2.6–2.8	75.900	1.47	1.67	+6.65 −6.11	+0.03 −0.08	+0.15 −0.21	+0.24 −0.29	−0.25 +0.19	+0.00 −0.05	+3.21 −2.85	+2.88 −2.20	+0.00 −0.03	+0.00 −0.02	+0.87 −0.92	+2.25 −1.82	+0.00 −0.02	−0.76 +0.76	−0.34 +0.40	+4.23 −4.23	+0.10 −0.10	+0.24 −0.67	+1.00 −1.00
2.8–3.0	58.038	1.59	2.21	+6.49 −6.76	+0.03 −0.08	+0.15 −0.21	+0.24 −0.29	−0.25 +0.19	+0.00 −0.05	+3.08 −2.85	+2.88 −3.79	+0.00 −0.03	+0.00 −0.02	+0.87 −0.92	+2.25 −1.82	+0.00 −0.02	−0.76 +0.76	−0.34 +0.40	+4.08 −4.08	+0.10 −0.09	+0.25 −0.69	+1.00 −1.00
3.0–3.2	44.324	1.58	2.56	+7.78 −7.26	+0.03 −0.08	+0.15 −0.21	+0.24 −0.29	−0.25 +0.19	+0.00 −0.05	+3.08 −2.72	+4.36 −3.79	+0.00 −0.03	+0.00 −0.02	+0.87 −0.92	+2.25 −1.82	+0.00 −0.02	−0.76 +0.76	−0.34 +0.40	+4.94 −4.94	+0.09 −0.09	+0.26 −0.70	+1.00 −1.00
3.2–3.4	32.909	2.09	2.91	+8.34 −9.23	+0.03 −0.08	+0.15 −0.21	+0.24 −0.29	−0.25 +0.19	+0.00 −0.05	+3.08 −2.72	+4.91 −6.55	+0.00 −0.03	+0.00 −0.02	+0.87 −0.92	+2.25 −1.82	+0.00 −0.02	−0.76 +0.76	−0.34 +0.40	+5.32 −5.32	+0.09 −0.09	+0.25 −0.70	+1.00 −1.00

Table B.3. — Measured double-differential  $Z + \text{jets}$  production cross-sections as a function of  $|y_{\text{jet}}|$  in the  $100 \text{ GeV} < p_{\text{T}}^{\text{jet}} < 200 \text{ GeV}$  region.  $\delta_{\text{stat}}^{\text{data}}$  and  $\delta_{\text{stat}}^{\text{MC}}$  are the statistical uncertainties in the data and MC simulation, respectively.  $\gamma_{\text{tot}}^{\text{sys}}$  is the total systematic uncertainty and includes the following components: uncertainties due to electron reconstruction ( $\gamma_{\text{rec}}^{\text{el}}$ ), identification ( $\gamma_{\text{ID}}^{\text{el}}$ ) and trigger ( $\gamma_{\text{trig}}^{\text{el}}$ ) efficiencies; electron energy scale ( $\gamma_{\text{EES}}^{\text{el}}$ ) and energy resolution ( $\gamma_{\text{EER}}^{\text{el}}$ ) uncertainties; a sum in quadrature of the uncertainties associated with the absolute *in situ* JES calibration ( $\gamma_{\text{in situ}}^{\text{jet}}$ ); a sum in quadrature of the uncertainties associated with the  $\eta$ -intercalibration ( $\gamma_{\eta\text{-int}}^{\text{jet}}$ ); an uncertainty in the high- $p_{\text{T}}$  jet JES calibration ( $\gamma_{\text{high-}p_{\text{T}}}^{\text{jet}}$ ); MC non-closure uncertainty ( $\gamma_{\text{closure}}^{\text{jet}}$ ); a sum in quadrature of the uncertainties due to pile-up corrections of the jet kinematics ( $\gamma_{\text{pile-up}}^{\text{jet}}$ ); a sum in quadrature of the flavour-based uncertainties ( $\gamma_{\text{flavour}}^{\text{jet}}$ ); punch-through uncertainty ( $\gamma_{\text{pthr}}^{\text{jet}}$ ); JER uncertainty ( $\gamma_{\text{JER}}^{\text{jet}}$ ); pile-up jet suppression efficiency uncertainty ( $\gamma_{\text{JVf}}^{\text{jet}}$ ); a sum in quadrature of the unfolding uncertainties ( $\gamma_{\text{unfold}}$ ); a sum in quadrature of the uncertainties due to MC generated backgrounds normalisation ( $\gamma_{\text{MC}}^{\text{bg}}$ ); a sum in quadrature of the uncertainty due to combined multijet and  $W + \text{jets}$  backgrounds ( $\gamma_{\text{data}}^{\text{bg}}$ ); uncertainty due to jet quality selection ( $\gamma_{\text{ID}}^{\text{jet}}$ ). All uncertainties are given in %. The luminosity uncertainty of 1.9% is not shown and is not included in the total uncertainty and its components.

$ y_{\text{jet}} $ range	$\frac{d^2\sigma}{d y_{\text{jet}} dp_{\text{T}}^{\text{jet}}}$ [fb/ GeV]	$\delta_{\text{stat}}^{\text{data}}$ [%]	$\delta_{\text{stat}}^{\text{MC}}$ [%]	$\gamma_{\text{tot}}^{\text{sys}}$ [%]	$\gamma_{\text{rec}}^{\text{el}}$ [%]	$\gamma_{\text{ID}}^{\text{el}}$ [%]	$\gamma_{\text{trig}}^{\text{el}}$ [%]	$\gamma_{\text{EES}}^{\text{el}}$ [%]	$\gamma_{\text{EER}}^{\text{el}}$ [%]	$\gamma_{\text{in situ}}^{\text{jet}}$ [%]	$\gamma_{\eta\text{-int}}^{\text{jet}}$ [%]	$\gamma_{\text{high-}p_{\text{T}}}^{\text{jet}}$ [%]	$\gamma_{\text{closure}}^{\text{jet}}$ [%]	$\gamma_{\text{pile-up}}^{\text{jet}}$ [%]	$\gamma_{\text{flavour}}^{\text{jet}}$ [%]	$\gamma_{\text{pthr}}^{\text{jet}}$ [%]	$\gamma_{\text{JER}}^{\text{jet}}$ [%]	$\gamma_{\text{JVf}}^{\text{jet}}$ [%]	$\gamma_{\text{unfold}}$ [%]	$\gamma_{\text{MC}}^{\text{bg}}$ [%]	$\gamma_{\text{data}}^{\text{bg}}$ [%]	$\gamma_{\text{ID}}^{\text{jet}}$ [%]
0.0–0.2	45.769	1.28	1.29	+2.58 −3.54	−0.04 +0.00	+0.02 −0.08	+0.11 −0.15	−0.29 +0.38	+0.06 +0.00	+1.44 −2.11	+0.50 −0.67	+0.00 −0.06	+0.00 −0.03	+0.83 −1.13	+1.51 −2.20	+0.00 −0.06	−0.36 +0.36	−0.04 +0.00	+0.14 −0.14	+0.19 −0.18	+0.18 −0.43	+1.00 −1.00
0.2–0.4	46.342	1.22	1.39	+2.58 −3.54	−0.04 +0.00	+0.02 −0.08	+0.11 −0.15	−0.29 +0.38	+0.06 +0.00	+1.44 −2.11	+0.50 −0.67	+0.00 −0.06	+0.00 −0.03	+0.83 −1.13	+1.51 −2.20	+0.00 −0.06	−0.36 +0.36	−0.04 +0.00	+0.14 −0.14	+0.18 −0.17	+0.18 −0.44	+1.00 −1.00
0.4–0.6	43.964	1.25	1.47	+2.58 −3.21	−0.04 +0.00	+0.02 −0.08	+0.11 −0.15	−0.29 +0.38	+0.06 +0.00	+1.44 −1.93	+0.50 −0.67	+0.00 −0.06	+0.00 −0.03	+0.83 −1.13	+1.51 −1.84	+0.00 −0.06	−0.36 +0.36	−0.04 +0.00	+0.14 −0.14	+0.19 −0.17	+0.17 −0.43	+1.00 −1.00
0.6–0.8	40.076	1.40	1.67	+2.58 −3.15	−0.04 +0.00	+0.02 −0.08	+0.11 −0.15	−0.29 +0.38	+0.06 +0.00	+1.44 −1.93	+0.50 −0.67	+0.00 −0.06	+0.00 −0.03	+0.83 −1.13	+1.51 −1.73	+0.00 −0.06	−0.36 +0.36	−0.04 +0.00	+0.14 −0.14	+0.18 −0.17	+0.20 −0.47	+1.00 −1.00
0.8–1.0	37.981	1.40	1.38	+2.50 −3.15	−0.04 +0.00	+0.02 −0.08	+0.11 −0.15	−0.29 +0.38	+0.06 +0.00	+1.44 −1.93	+0.50 −0.67	+0.00 −0.06	+0.00 −0.03	+0.83 −1.13	+1.37 −1.73	+0.00 −0.06	−0.36 +0.36	−0.04 +0.00	+0.14 −0.14	+0.17 −0.16	+0.17 −0.46	+1.00 −1.00
1.0–1.2	32.122	1.63	1.68	+2.74 −3.08	−0.04 +0.00	+0.02 −0.08	+0.11 −0.15	−0.29 +0.38	+0.06 +0.00	+1.44 −1.82	+0.50 −0.67	+0.00 −0.06	+0.00 −0.03	+0.83 −0.92	+1.37 −1.45	+0.00 −0.06	−0.36 +0.36	−0.04 +0.00	+1.13 −1.13	+0.18 −0.16	+0.18 −0.48	+1.00 −1.00
1.2–1.4	31.772	1.33	1.53	+2.99 −3.09	−0.04 +0.00	+0.02 −0.08	+0.11 −0.15	−0.29 +0.38	+0.06 +0.00	+1.87 −1.82	+0.50 −0.67	+0.00 −0.06	+0.00 −0.03	+0.83 −0.92	+1.37 −1.45	+0.00 −0.06	−0.36 +0.36	−0.04 +0.00	+1.13 −1.13	+0.17 −0.15	+0.19 −0.53	+1.00 −1.00
1.4–1.6	27.737	1.34	1.85	+3.19 −3.15	−0.04 +0.00	+0.02 −0.08	+0.11 −0.15	−0.29 +0.38	+0.06 +0.00	+1.87 −1.82	+0.50 −0.67	+0.00 −0.06	+0.00 −0.03	+0.83 −0.92	+1.70 −1.45	+0.00 −0.06	−0.36 +0.36	−0.04 +0.00	+1.13 −1.13	+0.17 −0.16	+0.52 −0.79	+1.00 −1.00
1.6–1.8	21.873	1.85	2.01	+3.16 −3.10	−0.04 +0.00	+0.02 −0.08	+0.11 −0.15	−0.29 +0.38	+0.06 +0.00	+1.87 −1.82	+0.50 −0.67	+0.00 −0.06	+0.00 −0.03	+0.83 −0.92	+1.70 −1.45	+0.00 −0.06	−0.36 +0.36	−0.04 +0.00	+1.13 −1.13	+0.16 −0.15	+0.24 −0.60	+1.00 −1.00
1.8–2.0	17.806	1.88	2.00	+3.33 −3.29	−0.04 +0.00	+0.02 −0.08	+0.11 −0.15	−0.29 +0.38	+0.06 +0.00	+1.98 −1.95	+0.50 −0.67	+0.00 −0.06	+0.00 −0.03	+0.83 −0.92	+1.70 −1.66	+0.00 −0.06	−0.36 +0.36	−0.04 +0.00	+1.13 −1.13	+0.15 −0.14	+0.26 −0.68	+1.00 −1.00
2.0–2.2	13.820	2.26	2.26	+3.33 −3.30	−0.04 +0.00	+0.02 −0.08	+0.11 −0.15	−0.29 +0.38	+0.06 +0.00	+1.98 −1.95	+0.50 −0.67	+0.00 −0.06	+0.00 −0.03	+1.17 −0.92	+1.70 −1.66	+0.00 −0.06	−0.36 +0.36	−0.04 +0.00	+1.13 −1.13	+0.15 −0.14	+0.26 −0.70	+1.00 −1.00
2.2–2.4	10.613	2.55	2.81	+3.98 −4.38	−0.04 +0.00	+0.02 −0.08	+0.11 −0.15	−0.29 +0.38	+0.06 +0.00	+2.23 −1.95	+0.50 −2.96	+0.00 −0.06	+0.00 −0.03	+1.17 −0.92	+2.57 −1.66	+0.00 −0.06	−0.36 +0.36	−0.04 +0.00	+1.13 −1.13	+0.15 −0.14	+0.25 −0.70	+1.00 −1.00
2.4–2.6	8.152	3.12	2.94	+5.72 −4.41	−0.04 +0.00	+0.02 −0.08	+0.11 −0.15	−0.29 +0.38	+0.06 +0.00	+2.23 −1.95	+4.14 −2.96	+0.00 −0.06	+0.00 −0.03	+1.17 −0.92	+2.57 −1.66	+0.00 −0.06	−0.36 +0.36	−0.04 +0.00	+1.13 −1.13	+0.15 −0.14	+0.32 −0.87	+1.00 −1.00
2.6–2.8	5.663	3.22	3.91	+5.73 −4.45	−0.04 +0.00	+0.02 −0.08	+0.11 −0.15	−0.29 +0.38	+0.06 +0.00	+2.23 −1.95	+4.14 −2.96	+0.00 −0.06	+0.00 −0.03	+1.17 −0.92	+2.57 −1.66	+0.00 −0.06	−0.36 +0.36	−0.04 +0.00	+1.13 −1.13	+0.17 −0.16	+0.44 −1.04	+1.00 −1.00
2.8–3.0	3.248	3.91	4.78	+9.42 −9.46	−0.04 +0.00	+0.02 −0.08	+0.11 −0.15	−0.29 +0.38	+0.06 +0.00	+2.23 −1.95	+8.54 −7.71	+0.00 −0.06	+0.00 −0.03	+1.17 −0.92	+2.57 −4.65	+0.00 −0.06	−0.36 +0.36	−0.04 +0.00	+1.13 −1.13	+0.18 −0.17	+0.40 −1.07	+1.00 −1.00
3.0–3.2	2.169	5.43	5.73	+9.48 −9.46	−0.04 +0.00	+0.02 −0.08	+0.11 −0.15	−0.29 +0.38	+0.06 +0.00	+2.47 −1.95	+8.54 −7.71	+0.00 −0.06	+0.00 −0.03	+1.17 −0.92	+2.57 −4.65	+0.00 −0.06	−0.36 +0.36	−0.04 +0.00	+1.13 −1.13	+0.18 −0.17	+0.46 −1.09	+1.00 −1.00
3.2–3.4	1.234	7.36	9.27	+15.87 −13.57	−0.04 +0.00	+0.02 −0.08	+0.11 −0.15	−0.29 +0.38	+0.06 +0.00	+2.47 −1.95	+15.33 −12.42	+0.00 −0.06	+0.00 −0.03	+1.17 −0.92	+2.57 −4.65	+0.00 −0.06	−0.36 +0.36	−0.04 +0.00	+1.13 −1.13	+0.15 −0.13	+0.41 −1.07	+1.00 −1.00

Table B.4. — Measured double-differential  $Z + \text{jets}$  production cross-sections as a function of  $|y_{\text{jet}}|$  in the  $200 \text{ GeV} < p_{\text{T}}^{\text{jet}} < 300 \text{ GeV}$  region.  $\delta_{\text{stat}}^{\text{data}}$  and  $\delta_{\text{stat}}^{\text{MC}}$  are the statistical uncertainties in the data and MC simulation, respectively.  $\gamma_{\text{tot}}^{\text{sys}}$  is the total systematic uncertainty and includes the following components: uncertainties due to electron reconstruction ( $\gamma_{\text{rec}}^{\text{el}}$ ), identification ( $\gamma_{\text{ID}}^{\text{el}}$ ) and trigger ( $\gamma_{\text{trig}}^{\text{el}}$ ) efficiencies; electron energy scale ( $\gamma_{\text{EES}}^{\text{el}}$ ) and energy resolution ( $\gamma_{\text{EER}}^{\text{el}}$ ) uncertainties; a sum in quadrature of the uncertainties associated with the absolute *in situ* JES calibration ( $\gamma_{\text{in situ}}^{\text{jet}}$ ); a sum in quadrature of the uncertainties associated with the  $\eta$ -intercalibration ( $\gamma_{\eta\text{-int}}^{\text{jet}}$ ); an uncertainty in the high- $p_{\text{T}}$  jet JES calibration ( $\gamma_{\text{high-}p_{\text{T}}}^{\text{jet}}$ ); MC non-closure uncertainty ( $\gamma_{\text{closure}}^{\text{jet}}$ ); a sum in quadrature of the uncertainties due to pile-up corrections of the jet kinematics ( $\gamma_{\text{pile-up}}^{\text{jet}}$ ); a sum in quadrature of the flavour-based uncertainties ( $\gamma_{\text{flavour}}^{\text{jet}}$ ); punch-through uncertainty ( $\gamma_{\text{pthr}}^{\text{jet}}$ ); JER uncertainty ( $\gamma_{\text{JER}}^{\text{jet}}$ ); pile-up jet suppression efficiency uncertainty ( $\gamma_{\text{JVf}}^{\text{jet}}$ ); a sum in quadrature of the unfolding uncertainties ( $\gamma_{\text{unfold}}$ ); a sum in quadrature of the uncertainties due to MC generated backgrounds normalisation ( $\gamma_{\text{MC}}^{\text{bg}}$ ); a sum in quadrature of the uncertainty due to combined multijet and  $W + \text{jets}$  backgrounds ( $\gamma_{\text{data}}^{\text{bg}}$ ); uncertainty due to jet quality selection ( $\gamma_{\text{ID}}^{\text{jet}}$ ). All uncertainties are given in %. The luminosity uncertainty of 1.9% is not shown and is not included in the total uncertainty and its components.

$ y_{\text{jet}} $	$\frac{d^2\sigma}{d y_{\text{jet}} dp_{\text{T}}^{\text{jet}}}$	$\delta_{\text{stat}}^{\text{data}}$	$\delta_{\text{stat}}^{\text{MC}}$	$\gamma_{\text{tot}}^{\text{sys}}$	$\gamma_{\text{rec}}^{\text{el}}$	$\gamma_{\text{ID}}^{\text{el}}$	$\gamma_{\text{trig}}^{\text{el}}$	$\gamma_{\text{EES}}^{\text{el}}$	$\gamma_{\text{EER}}^{\text{el}}$	$\gamma_{\text{in situ}}^{\text{jet}}$	$\gamma_{\eta\text{-int}}^{\text{jet}}$	$\gamma_{\text{high-}p_{\text{T}}}^{\text{jet}}$	$\gamma_{\text{closure}}^{\text{jet}}$	$\gamma_{\text{pile-up}}^{\text{jet}}$	$\gamma_{\text{flavour}}^{\text{jet}}$	$\gamma_{\text{pthr}}^{\text{jet}}$	$\gamma_{\text{JER}}^{\text{jet}}$	$\gamma_{\text{JVf}}^{\text{jet}}$	$\gamma_{\text{unfold}}$	$\gamma_{\text{MC}}^{\text{bg}}$	$\gamma_{\text{data}}^{\text{bg}}$	$\gamma_{\text{ID}}^{\text{jet}}$
range	[fb/ GeV ]	[%]	[%]	[%]	[%]	[%]	[%]	[%]	[%]	[%]	[%]	[%]	[%]	[%]	[%]	[%]	[%]	[%]	[%]	[%]	[%]	[%]
0.0–0.4	5.561	2.50	2.63	+3.55 −4.33	−0.05 +0.04	+0.12 +0.00	+0.10 −0.01	−0.18 +0.18	−0.06 +0.05	+2.62 −3.10	+0.39 −0.77	+0.04 +0.00	+0.15 +0.00	+0.36 −0.75	+1.40 −2.08	+0.20 −0.06	−0.58 +0.58	−0.04 +0.09	+1.40 −1.40	+0.09 −0.08	+0.28 −0.54	+1.00 −1.00
0.4–0.8	4.889	2.36	2.93	+3.55 −4.33	−0.05 +0.04	+0.12 +0.00	+0.10 −0.01	−0.18 +0.18	−0.06 +0.05	+2.62 −3.10	+0.39 −0.77	+0.04 +0.00	+0.15 +0.00	+0.36 −0.75	+1.40 −2.08	+0.20 −0.06	−0.58 +0.58	−0.04 +0.09	+1.40 −1.40	+0.10 −0.09	+0.25 −0.55	+1.00 −1.00
0.8–1.2	4.260	3.18	3.41	+3.54 −4.33	−0.05 +0.04	+0.12 +0.00	+0.10 −0.01	−0.18 +0.18	−0.06 +0.05	+2.62 −3.10	+0.39 −0.77	+0.04 +0.00	+0.15 +0.00	+0.36 −0.75	+1.40 −2.08	+0.20 −0.06	−0.58 +0.58	−0.04 +0.09	+1.40 −1.40	+0.11 −0.10	+0.21 −0.57	+1.00 −1.00
1.2–1.6	3.055	3.61	3.17	+3.55 −4.35	−0.05 +0.04	+0.12 +0.00	+0.10 −0.01	−0.18 +0.18	−0.06 +0.05	+2.62 −3.10	+0.39 −0.77	+0.04 +0.00	+0.15 +0.00	+0.36 −0.75	+1.40 −2.08	+0.20 −0.06	−0.58 +0.58	−0.04 +0.09	+1.40 −1.40	+0.14 −0.13	+0.27 −0.71	+1.00 −1.00
1.6–2.0	1.780	4.43	4.42	+3.56 −4.38	−0.05 +0.04	+0.12 +0.00	+0.10 −0.01	−0.18 +0.18	−0.06 +0.05	+2.62 −3.10	+0.39 −0.77	+0.04 +0.00	+0.15 +0.00	+0.36 −0.75	+1.40 −2.08	+0.20 −0.06	−0.58 +0.58	−0.04 +0.09	+1.40 −1.40	+0.17 −0.16	+0.39 −0.84	+1.00 −1.00
2.0–2.4	0.831	6.45	7.17	+3.60 −6.26	−0.05 +0.04	+0.12 +0.00	+0.10 −0.01	−0.18 +0.18	−0.06 +0.05	+2.62 −5.37	+0.39 −0.77	+0.04 +0.00	+0.15 +0.00	+0.36 −0.75	+1.40 −2.08	+0.20 −0.06	−0.58 +0.58	−0.04 +0.09	+1.40 −1.40	+0.22 −0.20	+0.65 −1.19	+1.00 −1.00
2.4–3.4	0.136	9.48	11.75	+3.58 −6.25	−0.05 +0.04	+0.12 +0.00	+0.10 −0.01	−0.18 +0.18	−0.06 +0.05	+2.62 −5.37	+0.39 −0.77	+0.04 +0.00	+0.15 +0.00	+0.36 −0.75	+1.40 −2.08	+0.20 −0.06	−0.58 +0.58	−0.04 +0.09	+1.40 −1.40	+0.32 −0.29	+0.42 −1.12	+1.00 −1.00

Table B.5. — Measured double-differential  $Z + \text{jets}$  production cross-sections as a function of  $|y_{\text{jet}}|$  in the  $300 \text{ GeV} < p_{\text{T}}^{\text{jet}} < 400 \text{ GeV}$  region.  $\delta_{\text{stat}}^{\text{data}}$  and  $\delta_{\text{stat}}^{\text{MC}}$  are the statistical uncertainties in the data and MC simulation, respectively.  $\gamma_{\text{tot}}^{\text{sys}}$  is the total systematic uncertainty and includes the following components: uncertainties due to electron reconstruction ( $\gamma_{\text{rec}}^{\text{el}}$ ), identification ( $\gamma_{\text{ID}}^{\text{el}}$ ) and trigger ( $\gamma_{\text{trig}}^{\text{el}}$ ) efficiencies; electron energy scale ( $\gamma_{\text{EES}}^{\text{el}}$ ) and energy resolution ( $\gamma_{\text{EER}}^{\text{el}}$ ) uncertainties; a sum in quadrature of the uncertainties associated with the absolute *in situ* JES calibration ( $\gamma_{\text{in situ}}^{\text{jet}}$ ); a sum in quadrature of the uncertainties associated with the  $\eta$ -intercalibration ( $\gamma_{\eta\text{-int}}^{\text{jet}}$ ); an uncertainty in the high- $p_{\text{T}}$  jet JES calibration ( $\gamma_{\text{high-}p_{\text{T}}}^{\text{jet}}$ ); MC non-closure uncertainty ( $\gamma_{\text{closure}}^{\text{jet}}$ ); a sum in quadrature of the uncertainties due to pile-up corrections of the jet kinematics ( $\gamma_{\text{pile-up}}^{\text{jet}}$ ); a sum in quadrature of the flavour-based uncertainties ( $\gamma_{\text{flavour}}^{\text{jet}}$ ); punch-through uncertainty ( $\gamma_{\text{pthr}}^{\text{jet}}$ ); JER uncertainty ( $\gamma_{\text{JER}}^{\text{jet}}$ ); pile-up jet suppression efficiency uncertainty ( $\gamma_{\text{JVf}}^{\text{jet}}$ ); a sum in quadrature of the unfolding uncertainties ( $\gamma_{\text{unfold}}$ ); a sum in quadrature of the uncertainties due to MC generated backgrounds normalisation ( $\gamma_{\text{MC}}^{\text{bg}}$ ); a sum in quadrature of the uncertainty due to combined multijet and  $W + \text{jets}$  backgrounds ( $\gamma_{\text{data}}^{\text{bg}}$ ); uncertainty due to jet quality selection ( $\gamma_{\text{ID}}^{\text{jet}}$ ). All uncertainties are given in %. The luminosity uncertainty of 1.9% is not shown and is not included in the total uncertainty and its components.

$ y_{\text{jet}} $	$\frac{d^2\sigma}{d y_{\text{jet}} dp_{\text{T}}^{\text{jet}}}$	$\delta_{\text{stat}}^{\text{data}}$	$\delta_{\text{stat}}^{\text{MC}}$	$\gamma_{\text{tot}}^{\text{sys}}$	$\gamma_{\text{rec}}^{\text{el}}$	$\gamma_{\text{ID}}^{\text{el}}$	$\gamma_{\text{trig}}^{\text{el}}$	$\gamma_{\text{EES}}^{\text{el}}$	$\gamma_{\text{EER}}^{\text{el}}$	$\gamma_{\text{in situ}}^{\text{jet}}$	$\gamma_{\eta\text{-int}}^{\text{jet}}$	$\gamma_{\text{high-}p_{\text{T}}}^{\text{jet}}$	$\gamma_{\text{closure}}^{\text{jet}}$	$\gamma_{\text{pile-up}}^{\text{jet}}$	$\gamma_{\text{flavour}}^{\text{jet}}$	$\gamma_{\text{pthr}}^{\text{jet}}$	$\gamma_{\text{JER}}^{\text{jet}}$	$\gamma_{\text{JVf}}^{\text{jet}}$	$\gamma_{\text{unfold}}$	$\gamma_{\text{MC}}^{\text{bg}}$	$\gamma_{\text{data}}^{\text{bg}}$	$\gamma_{\text{ID}}^{\text{jet}}$
range	[fb/ GeV ]	[%]	[%]	[%]	[%]	[%]	[%]	[%]	[%]	[%]	[%]	[%]	[%]	[%]	[%]	[%]	[%]	[%]	[%]	[%]	[%]	[%]
0.0–0.4	1.190	5.83	6.75	+5.95	+0.74	+0.56	+0.00	+0.00	+0.76	+4.03	+1.41	+0.68	+0.46	+2.42	+2.24	+0.54	-1.16	+0.79	+0.08	+0.10	+0.30	+1.00
				-2.33	+0.00	+0.00	+0.51	+0.72	+0.00	-1.63	+0.00	+0.00	-0.13	+0.00	+0.00	+0.00	+0.00	+0.00	+1.16	+0.00	-0.08	-0.09
0.4–0.8	1.083	5.52	5.50	+5.94	+0.74	+0.56	+0.00	+0.00	+0.76	+4.03	+1.41	+0.68	+0.46	+2.42	+2.24	+0.54	-1.16	+0.79	+0.08	+0.11	+0.23	+1.00
				-2.30	+0.00	+0.00	+0.51	+0.72	+0.00	-1.63	+0.00	+0.00	-0.13	+0.00	+0.00	+0.00	+0.00	+1.16	+0.00	-0.08	-0.10	-0.55
0.8–1.2	0.946	6.68	6.87	+5.95	+0.74	+0.56	+0.00	+0.00	+0.76	+4.03	+1.41	+0.68	+0.46	+2.42	+2.24	+0.54	-1.16	+0.79	+0.08	+0.12	+0.30	+1.00
				-2.34	+0.00	+0.00	+0.51	+0.72	+0.00	-1.63	+0.00	+0.00	-0.13	+0.00	+0.00	+0.00	+0.00	+1.16	+0.00	-0.08	-0.11	-0.68
1.2–1.6	0.628	8.15	8.34	+5.96	+0.74	+0.56	+0.00	+0.00	+0.76	+4.03	+1.41	+0.68	+0.46	+2.42	+2.24	+0.54	-1.16	+0.79	+0.08	+0.19	+0.45	+1.00
				-2.43	+0.00	+0.00	+0.51	+0.72	+0.00	-1.63	+0.00	+0.00	-0.13	+0.00	+0.00	+0.00	+0.00	+1.16	+0.00	-0.08	-0.17	-0.95
1.6–2.0	0.322	11.56	11.42	+5.97	+0.74	+0.56	+0.00	+0.00	+0.76	+4.03	+1.41	+0.68	+0.46	+2.42	+2.24	+0.54	-1.16	+0.79	+0.08	+0.26	+0.51	+1.00
				-2.46	+0.00	+0.00	+0.51	+0.72	+0.00	-1.63	+0.00	+0.00	-0.13	+0.00	+0.00	+0.00	+0.00	+1.16	+0.00	-0.08	-0.24	-1.00
2.0–3.0	0.032	26.98	24.63	+6.01	+0.74	+0.56	+0.00	+0.00	+0.76	+4.03	+1.41	+0.68	+0.46	+2.42	+2.24	+0.54	-1.16	+0.79	+0.08	+0.69	+0.63	+1.00
				-2.64	+0.00	+0.00	+0.51	+0.72	+0.00	-1.63	+0.00	+0.00	-0.13	+0.00	+0.00	+0.00	+0.00	+1.16	+0.00	-0.08	-0.63	-1.25

Table B.6. — Measured double-differential  $Z + \text{jets}$  production cross-sections as a function of  $|y_{\text{jet}}|$  in the  $400 \text{ GeV} < p_{\text{T}}^{\text{jet}} < 1050 \text{ GeV}$  region.  $\delta_{\text{stat}}^{\text{data}}$  and  $\delta_{\text{stat}}^{\text{MC}}$  are the statistical uncertainties in the data and MC simulation, respectively.  $\gamma_{\text{tot}}^{\text{sys}}$  is the total systematic uncertainty and includes the following components: uncertainties due to electron reconstruction ( $\gamma_{\text{rec}}^{\text{el}}$ ), identification ( $\gamma_{\text{ID}}^{\text{el}}$ ) and trigger ( $\gamma_{\text{trig}}^{\text{el}}$ ) efficiencies; electron energy scale ( $\gamma_{\text{EES}}^{\text{el}}$ ) and energy resolution ( $\gamma_{\text{EER}}^{\text{el}}$ ) uncertainties; a sum in quadrature of the uncertainties associated with the absolute *in situ* JES calibration ( $\gamma_{\text{in situ}}^{\text{jet}}$ ); a sum in quadrature of the uncertainties associated with the  $\eta$ -intercalibration ( $\gamma_{\eta\text{-int}}^{\text{jet}}$ ); an uncertainty in the high- $p_{\text{T}}$  jet JES calibration ( $\gamma_{\text{high-}p_{\text{T}}}^{\text{jet}}$ ); MC non-closure uncertainty ( $\gamma_{\text{closure}}^{\text{jet}}$ ); a sum in quadrature of the uncertainties due to pile-up corrections of the jet kinematics ( $\gamma_{\text{pile-up}}^{\text{jet}}$ ); a sum in quadrature of the flavour-based uncertainties ( $\gamma_{\text{flavour}}^{\text{jet}}$ ); punch-through uncertainty ( $\gamma_{\text{pthr}}^{\text{jet}}$ ); JER uncertainty ( $\gamma_{\text{JER}}^{\text{jet}}$ ); pile-up jet suppression efficiency uncertainty ( $\gamma_{\text{JVf}}^{\text{jet}}$ ); a sum in quadrature of the unfolding uncertainties ( $\gamma_{\text{unfold}}$ ); a sum in quadrature of the uncertainties due to MC generated backgrounds normalisation ( $\gamma_{\text{MC}}^{\text{bg}}$ ); a sum in quadrature of the uncertainty due to combined multijet and  $W + \text{jets}$  backgrounds ( $\gamma_{\text{data}}^{\text{bg}}$ ); uncertainty due to jet quality selection ( $\gamma_{\text{ID}}^{\text{jet}}$ ). All uncertainties are given in %. The luminosity uncertainty of 1.9% is not shown and is not included in the total uncertainty and its components.

$ y_{\text{jet}} $	$\frac{d^2\sigma}{d y_{\text{jet}} dp_{\text{T}}^{\text{jet}}}$	$\delta_{\text{stat}}^{\text{data}}$	$\delta_{\text{stat}}^{\text{MC}}$	$\gamma_{\text{tot}}^{\text{sys}}$	$\gamma_{\text{rec}}^{\text{el}}$	$\gamma_{\text{ID}}^{\text{el}}$	$\gamma_{\text{trig}}^{\text{el}}$	$\gamma_{\text{EES}}^{\text{el}}$	$\gamma_{\text{EER}}^{\text{el}}$	$\gamma_{\text{in situ}}^{\text{jet}}$	$\gamma_{\eta\text{-int}}^{\text{jet}}$	$\gamma_{\text{high-}p_{\text{T}}}^{\text{jet}}$	$\gamma_{\text{closure}}^{\text{jet}}$	$\gamma_{\text{pile-up}}^{\text{jet}}$	$\gamma_{\text{flavour}}^{\text{jet}}$	$\gamma_{\text{pthr}}^{\text{jet}}$	$\gamma_{\text{JER}}^{\text{jet}}$	$\gamma_{\text{JVf}}^{\text{jet}}$	$\gamma_{\text{unfold}}$	$\gamma_{\text{MC}}^{\text{bg}}$	$\gamma_{\text{data}}^{\text{bg}}$	$\gamma_{\text{ID}}^{\text{jet}}$
range	[fb/ GeV ]	[%]	[%]	[%]	[%]	[%]	[%]	[%]	[%]	[%]	[%]	[%]	[%]	[%]	[%]	[%]	[%]	[%]	[%]	[%]	[%]	[%]
0.0–0.4	0.110	6.84	8.88	+2.79	−0.34	+0.00	+0.00	−0.82	−0.41	+2.01	+0.22	+0.00	+0.00	+0.10	+0.33	+0.13	−0.14	+0.01	+1.47	+0.15	+0.59	+1.00
				−5.82	+0.00	−0.26	−0.43	+0.00	+0.00	−4.74	−0.50	−0.36	−0.33	−0.91	−2.13	−0.58	+0.14	−0.32	−1.47	−0.14	−0.84	−1.00
0.4–0.8	0.076	9.45	9.66	+2.76	−0.34	+0.00	+0.00	−0.82	−0.41	+2.01	+0.22	+0.00	+0.00	+0.10	+0.33	+0.13	−0.14	+0.01	+1.47	+0.18	+0.42	+1.00
				−5.81	+0.00	−0.26	−0.43	+0.00	+0.00	−4.74	−0.50	−0.36	−0.33	−0.91	−2.13	−0.58	+0.14	−0.32	−1.47	−0.16	−0.71	−1.00
0.8–1.2	0.058	11.67	11.68	+2.78	−0.34	+0.00	+0.00	−0.82	−0.41	+2.01	+0.22	+0.00	+0.00	+0.10	+0.33	+0.13	−0.14	+0.01	+1.47	+0.21	+0.54	+1.00
				−5.83	+0.00	−0.26	−0.43	+0.00	+0.00	−4.74	−0.50	−0.36	−0.33	−0.91	−2.13	−0.58	+0.14	−0.32	−1.47	−0.20	−0.86	−1.00
1.2–2.6	0.012	12.84	13.36	+2.84	−0.34	+0.00	+0.00	−0.82	−0.41	+2.01	+0.22	+0.00	+0.00	+0.10	+0.33	+0.13	−0.14	+0.01	+1.47	+0.37	+0.73	+1.00
				−5.90	+0.00	−0.26	−0.43	+0.00	+0.00	−4.74	−0.50	−0.36	−0.33	−0.91	−2.13	−0.58	+0.14	−0.32	−1.47	−0.34	−1.24	−1.00